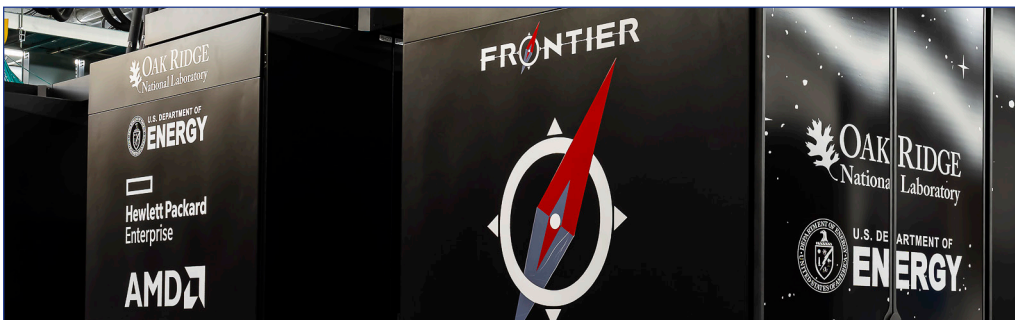




Italian National Agency for New Technologies,
Energy and Sustainable Economic Development

High Performance Computing on CRESCO infrastructure: research activity and results 2022



December 2023



Italian National Agency for New Technologies,
Energy and Sustainable Economic Development

High Performance Computing on CRESCO Infrastructure: research activity and results 2022

December 2023

High Performance Computing on CRESCO Infrastructure: research activity and results 2022

Contributions provided by a selection of users of the CRESCO infrastructure

Scientific Editor: Beatrice Calosso, ENEA, TERIN-ICT-HPC

Cover: Amedeo Trolese, ENEA, TERIN-ICT, CR Frascati

ISBN: 978-88-8286-458-3

Summary

Foreword.....	5
ENERGY EFFICIENCY OF PARALLEL ALGORITHMS IN HETEROGENEOUS COMPUTING ARCHITECTURES RELEVANT FOR EXASCALE SYSTEMS	7
F.Iannone,P.Palazzari and <i>CRESKO team</i>	7
KNOWLEDGE SHARING IN AGRICULTURE 4.0	33
Daniela Alderuccio , Rossana Cotroneo	33
ENEA-REG (v2.0), A REGIONAL EARTH SYSTEM MODEL FOR DYNAMICAL DOWNSCALING OF CMIP6 MODELS OVER THE MED-CORDEX REGION.....	37
Alessandro Anav, Marta Antonelli, Sandro Calmanti, Adriana Carillo, Franco Catalano, Alessandro Dell’Aquila, Roberto Iacono, Salvatore Marullo, Ernesto Napolitano, Massimiliano Palma, Giovanna Pisacane, Gianmaria Sannino, Maria Vittoria Struglia	37
FROM MOSCAB TO MILCHAM TO MEASURE ATMOSPHERIC NEUTRONS: THE MODELLING OF THE NEW ANSWER FUNCTION USING FLUKA AND PHITHS CODES ON CRESKO.....	43
Nunzio Burgio, Alfonso Santagata.....	43
CRITICAL REVIEW OF RESULTS ON THE HEAT CAPACITY AND MELTING TEMPERATURE OF PUO ₂	47
Rolando Calabrese	47
LES OF A H ₂ /Air CYCLONIC COMBUSTOR UNDER MILD REGIME	51
Donato Cecere, Simone Carpenella, Eugenio Giacomazzi, Ilaria Quaranta	51
EVALUATION OF MCNPX CORRECTION FACTORS FOR PRE-CHARACTERIZATION ANALYSES OF MATERIALS FROM THE DECOMMISSIONING OF THE FRASCATI TOKAMAK UPGRADE FUSION FACILITY	55
Nadia Cherubini, Giada Gandolfo, Luigi Lepore, Giuseppe Augusto Marzo	55
STRUCTURAL, ELECTRONIC AND VIBRATIONAL PROPERTIES OF B ₂₄ N ₂₄ NANOCAPSULES: NOVEL ANODES FOR MAGNESIUM BATTERIES	61
Domenico Corona, Francesco Buonocore, Massimo Celino and Olivia Pulci.....	61
PRELIMINARY CFD INVESTIGATION OF A TURBULENT FLOW IN A 19-PIN WIRE WRAPPED FUEL BUNDLE.....	65
Roberto Da Vià, Daniele Panico, Francesco Lodi, Giacomo Grasso	65
NANOCOMPARTMENTALIZATION STRUCTURES FROM BACTERIA’S LIPIDS....	69
Antonio De Nicola.....	69
CFD-PBE FRAMEWORK FOR ASSESSING CLOSE CONTACT SARS-COV-2 TRANSMISSION.....	73
Valerio D’Alessandro, Matteo Falone, Luca Giammichele and Renato Ricci.....	73
A DFT INVESTIGATION OF LEAD-FREE PEROVSKITE FASIBR ₃ (CH (NH ₂) ₂ SIBR ₃) USING GGA-PBESOL APPROXIMATION FOR PHOTOVOLTAIC APPLICATION	77
Youssef El Arfaoui, Mohammed Khenfouch, Nabil Habiballah.....	77

INTERPRETATION OF OUT-OF-CONTROL SIGNALS IN MULTIPLE STREAM PROCESS CONTROL CHARTS USING ARTIFICIAL NEURAL NETWORKS	83
Antonio Lepore, Biagio Palumbo, Gianluca Sposito	83
AN AUTOMATED WORKFLOW APPROACH FOR NUMERICAL SCREENING OF FUNCTIONALIZED SILICON SURFACES.....	87
Sara Marchio, Francesco Buonocore, Simone Giusepponi, Barbara Ferrucci, Claudio Ronchetti and Massimo Celino.....	87
ARTIFICIAL INTELLIGENCE PROJECTS ON CRESCO PLATFORM.....	91
Angelo Mariano, Claudio Ronchetti, Serena D’Onofrio and Nicola Quercioli	91
FAST-PETASE: A MOLECULAR DYNAMICS STUDY	97
Carla Orlando, Mario Prejanò, Nino Russo and Tiziana Marino	97
PRELIMINARY CFD INVESTIGATION OF BARE FUEL BUNDLE FOR LMFR APPLICATIONS.....	101
Daniele Panico, Roberto Da Vià, Giacomo Grasso.....	101
AB-INITIO STUDY OF VINYLENE CARBONATE REACTIVITY AT LITHIUM METAL INTERFACE	105
Michele Pavone, Francesca Fasulo, Ana B. Muñoz-García, Arianna Massaro.....	105
AB-INITIO STUDY OF THE CHARGE DYNAMICS AT THE SPIRO-MEOTAD/ LEAD HALIDE PEROVSKITES INTERFACE.....	109
Adriana Pecoraro, Francesca Fasulo, Michele Pavone and Ana Belén Muñoz-García.....	109
RADIATION DAMAGE ANALYSIS OF THE LFR-AS-30 CORE.....	113
Roberto Pergreffì, Francesco Lodi, Giacomo Grasso, Alessia Di Francesco, Giorgia Mantovani.....	113
MOLECULAR DYNAMICS SIMULATIONS OF ACID B-GLUCOSIDASE ENZYME: DYNAMICAL AND STRUCTURAL EFFECT OF A PARKINSON’S-ASSOCIATED MUTATION.....	117
Davide Pietrafesa, Alessia Casamassa, Massimo Santoro, Claudia Consales, Jessica Diana Rosati and Caterina Arcangeli	117
JOINT UNIFI-ENEA PARTICIPATION TO THE INTERNATIONAL SAMPL9 BLIND CHALLENGE FOR PREDICTING TOLUENE-WATER LOGP PARTITION COEFFICIENTS USING MASSIVELY PARALLEL NON EQUILIBRIUM ALCHEMICAL SIMULATIONS	123
Piero Procacci, Guido Guarnieri.....	123
EVALUATION OF PHTHALOCYANINE AND HYPERICIN AS NOVEL ENTRY INHIBITORS AGAINST SARS-COV-2.....	127
Alice Romeo, Federico Iacovelli and Mattia Falconi	127
MATERIALS SCIENCE USING MACHINE LEARNING	133
Claudio Ronchetti, Marco Puccini, Sergio Ferlito, Simone Giusepponi, Filippo Palombi, Francesco Buonocore and Massimo Celino	133
ATOMISTIC SIMULATIONS OF QUANTUM DOTS	137
Gabriele Saleh, Juliette Zito and Ivan Infante	137

MCNP ANALYSES FOR THE NIORT® TREATMENT OF SOLID CANCERS BY A COMPACT NEUTRON GENERATOR.....	141
Massimo Sarotto, Maurizio Martellini	141
MAGNETOHYDRODYNAMIC MODELLING OF LIQUID METAL WATER-COOLED BREEDING BLANKETS FOR NUCLEAR FUSION APPLICATIONS.....	145
Alessandro Tassone and Simone Siriano.....	145
COMPUTER SIMULATIONS OF POLYMER MODELS OF CHROMOSOME FOLDING ARE TESTED AGAINST SINGLE-CELL MICROSCOPY DATA IN HUMAN CELLS..	149
Francesca Vercellone, Andrea Esposito, Simona Bianco, Andrea Maria Chiariello, Andrea Fontana, Florinda Di Pierno, and Mattia Conte.....	149
THRUST COMPUTATION USING EXPERIMENTAL OPTICAL AND MORPHOLOGICAL PROPERTIES OF SOLAR PHOTON SAILS	157
Danilo Zola, Salvatore Scaglione, Rocco C. Pellegrini, Enrico Cavallini, Christian Circi	157
HYBRID COVE-EDGED GRAPHENE NANORIBBONS FOR ATOMISTIC PROTEIN SEQUENCING.....	161
Giuseppe Zollo, Tommaso Civitarese	161

Foreword

During the year 2022, the CRESCO high performance computing clusters have provided 129 million hours of “core” computing time, at a high availability rate, to about 170 users, supporting ENEA research and development activities in many relevant scientific and technological domains. In the framework of joint programs with ENEA researchers and technologists, computational services have been provided also to academic and industrial communities. The slight decrease in computing power delivered in 2022 compared to 2021 highlights the aging of the current CRESCO HPC systems and the need for a technological upgrade.

This report, the thirty-first of a series started in 2008, is a collection of thirty papers illustrating the main results obtained during 2022 using the CRESCO/ENEAGRID HPC facilities. The significant number of contributions proves the importance of the HPC facilities in ENEA for the research community. The topics cover various fields of research, such as materials science, efficient combustion, climate research, nuclear technology, plasma physics, biotechnology, aerospace, complex systems physics, geophysical flow, renewable energies, environmental issues, HPC technology. The report shows the wide spectrum of applications of high-performance computing, which has become an all-round enabling technology for science and engineering.

Since 2008, the main ENEA computational resources are located near Naples, in Portici Research Centre. This is a result of the CRESCO Project (Computational Centre for Research on Complex Systems), co-funded, in the framework of the 2001-2006 PON (European Regional Development Funds Program), by the Italian Ministry of Education, University and Research (MIUR).

The CRESCO Project provided the financial resources to set up the first HPC x86_64 Linux cluster in ENEA; a major computing installation for both the Italian and the International context: it ranked 126 in the HPC Top 500 June 2008 world list, with 17.1 Tflops and 2504 cpu cores. It was later decided to keep CRESCO as the name for all the Linux clusters in the ENEAGRID infrastructure, which integrates all ENEA scientific computing systems, and is currently distributed in six Italian sites.

CRESCO computing resources were later upgraded in the framework of PON 2007-2013 with the project TEDAT and the cluster CRESCO4, 100 Tflops computing power. In 2020 the ENEAGRID computational resources consist of ~25000 computing cores and a raw data storage of about 5 PB.

In 2015 ENEA and CINECA, the main HPC institution in Italy, signed a collaboration agreement to promote joint activities and projects in HPC. In this framework, CINECA and ENEA are providing HPC services for the nuclear fusion researcher community until 2023. In this framework, the new system MARCONI-FUSION started operation in July 2016 with 1 Pflops computation power level which has been increased to 5 Pflops in 2017 and the HPC services of MARCONI Fusion have been extend until 2023 with a power peak of 8 PFlops of conventional processors Intel Skylake and 2 PFlops of accelerated GPU partition of CINECA Marconi 100.

The ENEA-CINECA agreement was the key basis for ENEA HPC developments in the past. The CRESCO6 cluster has been installed in 2018 and its own 1.4 PFlops peak computing power, ranked 420th in November 2018 Top500 list. CRESCO6 has been a challenge in HPC co-design system thanks to implement a multi-fabric network able for working Infiniband and Omni-Path on a single GPFS cluster using the same storage systems of CRESCO data centre. New project opportunities will need to be seized in 2023 to provide for the technological upgrade of the CRESCO HPC systems.

The success and the quality of the results produced by CRESCO stress the role that HPC facilities can play in supporting science and technology for all ENEA activities, national and international collaborations, and the ongoing renewal of the infrastructure provides the basis for an upkeep of this role in the forthcoming years.

*Dipartimento Tecnologie Energetiche e Fonti Rinnovabili,
Divisione per lo Sviluppo di Sistemi per l'Informatica e l'ICT - CRESCO Team*

ENERGY EFFICIENCY OF PARALLEL ALGORITHMS IN HETEROGENEOUS COMPUTING ARCHITECTURES RELEVANT FOR EXASCALE SYSTEMS

F.Iannone*, P.Palazzari and *CRESCO team*:

L.Acampora, D.Alderuccio, E.Andreassi, F.Ambrosino, G.Baldassarre, T.Bastianelli, R.Bertini, G.Bracco, L.Bucci, F.Buonocore, M.Caiazzo, B.Calosso, G.Cannataro, M.Caporicci, G.Carretto, M.Celino, M.Chinnici, R.Clemente, M.De Rosa, D.Di Mattia, S.Ferriani, G.Ferro, M.Fratarcangeli, A.Funel, S.Giusepponi, G.Guarnieri, M.Gusso, W.Lusani, M.Marano, S.Marchio, A.Mariano, S.Migliori, M.Mongelli, F.Palombi, S.Pecoraro, S.Pierattini, G.Ponti, G.Santomauro, A.Scalise, F.Simoni, M.Steffè,

Energy Technologies & Renewable Sources Department - Information Communication Technologies, Lungotevere Thaon di Revel, 76, 00196 Rome Italy

* Corresponding author. E-mail: francesco.iannone@enea.it

ABSTRACT. High-performance computing (HPC) has emerged as a critical component in various domains, ranging from scientific research to artificial intelligence. As the demand for computational power continues to grow, novel architectures are being explored to enhance the performance and energy efficiency of HPC systems. Currently all the pre/exascale HPC systems deployed have heterogeneous architectures GPU based in order to operate with a sustainable power consuming as well as being capable a huge number of FLOPs. On the other hand, the new HPC systems with heterogeneous architectures must efficiently run both traditional parallel numerical modelling applications, such as the HPL test based on numerical linear algebra, and new AI applications, sometimes characterized by embarrassingly parallel workloads. This paper aims to compare energy efficiency and performances of GPU vs FPGA by means the benchmark tests of BLAS/GEMM and image processing algorithms.

1 Introduction

Electric power is the main limiting factor for exascale systems. The first HPC systems in the June 2023 TOP500 list has consumed electric power greater than 22 MW to run ground-breaking scientific workloads and simulations at very large-scale. Deployment of such large-scale HPC systems are typically limited in scaling by the power capacity available to the data center as well as the cooling infrastructure constrains. As the HPC industry marches towards exascale-class systems, there is more and more of a focus on the peak power consumption of these large-scale systems. HPC designers must give consideration for the available power/cooling and how to measure and enforce these power policies at the data center to achieve exascale performance. To support with this power-limited challenge, CPU manufacturers provide several levels of power management ranging from CPU clock gating and power-capping to managing the power budget at the data center rack-level.

Nowadays HPC data center is used a metric called *Performance Per Watt* (PPW) or FLOPS/s per Watt as a measure of the energy efficiency of a particular HPC system. FLOPS/s per Watt measures the rate of computation (typically floating-point operations per second) that can be delivered by a HPC system for every Watt of power consumed. As a software developer, FLOPS/s is used as a measure of the computational performance of a parallel workload. PPW is how much energy or power a HPC system needs to spend in order to reach a computation performance. In other words, PPW is how much power in watts does HPC system have to dissipate in order to get some number of FLOPS/s

out of the system. Therefore the $PPW = Performance (FLOPS/s) / Electric Power (Watt)$. The problem is how to compute the number of floating operations in compute algorithms. Usually the computing performance can be expressed in terms of floating point operations or FLOPS required to find the solution. The FLOPS serves as a basic unit of computation, which could denote one addition, subtraction, multiplication or division of floating point numbers. Note that, the FLOPS count is just a rough measure of how expensive an algorithm can be. Many more aspects need to be taken into account to accurately estimate practical runtime. The following base principle applies: In practical situations, we're interested in rough, not exact FLOPS counts to measure the complexity of operations.

Traditionally for many scientific applications in HPC, linear algebra operations are the most important computational tasks, indeed the HPL benchmark, that solves a random linear system: $Ax=b$, is used to build the TOP500 list ranking the world's most powerful supercomputers. The HPL benchmark is considered a typical compute-bound task, unlike the HPCG benchmark, which is also used in the TOP500 list, and it is instead a memory-bound task able to solve sparse linear systems using iterative methods.

The need for energy-efficient supercomputers is driving heterogeneous architectures towards specialized accelerators, such as GPUs and FPGAs that has emerged as keystone element in various domains, ranging from scientific applications to artificial intelligence able to exploit parallel computing techniques based on linear algebra and tensor arithmetic. These techniques are commonly used to address numerical problems in parallel. They serve as an excellent starting point for studying parallel computing on reprogrammable processor units like FPGAs. It's widely acknowledged that FPGAs offer comparable computational power for floating-point operations as CPUs [1]. However, due to data transmission overheads and the challenging and time-consuming design process, FPGAs are seldom utilized for floating-point intensive computations.

On the other hand, FPGAs find frequent application in image processing, where limited bit-width (8 or 16-bit) integer operations are commonly used. Additionally, for Digital Signal Processing (DSP) integer operations, especially 16-bit or lower, FPGAs significantly outperform CPUs in computational power. Recently, FPGAs have garnered interest in the high-performance computing community due to their potential to minimize data movement compared to typical load-store architectures. Nevertheless, they tend to be slow for memory-bound operations due to limited memory performance. To address this limitation, major FPGA companies have begun integrating High-Bandwidth Memory (HBM) into their devices. HBM, or High Bandwidth Memory, is essentially a 3D stack of multiple DRAMs with independent memory interfaces. This configuration allows for reduced I/O energy consumption and achieves very high memory bandwidth by efficiently distributing data across all HBM memories and accessing it in parallel. Several FPGAs, including the Xilinx Alveo U280 FPGA, have incorporated this technology, leading to significantly improved efficiency for memory-bound operations on these FPGAs. However, one prominent challenge is finding effective methods to distribute data across the HBM banks and manage the complexity of dealing with a large number of different data locations.

2 Parallel architectures for computing linear algebra

The most basic model capable of implementing a parallel architecture for computing linear algebra involves a network of processor units interconnected in a linear array. An illustration of a linear array is presented in Fig.1.

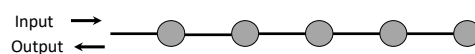


Fig.1: a 5-cell linear array

In this system, each node serves as a processor unit and is connected in a linear array with bidirectional links to both its left and right neighbors. The outermost processors may have only one

connection each, and they can act as input/output points for the entire network. A linear array represents the simplest form of a fixed-connection network.

Every processor node in the array has its own local program control and local storage space. The complexity of the local program control and the size of the local storage may vary, but for our purposes, we will assume that the local control is simple, involving only a few operations, and that the local storage is limited, capable of holding only a few words of data.

During each step of operation, each processor node performs the following tasks:

- Receives input from its neighboring nodes.
- Inspects its local storage.
- Executes computations based on its local control.
- Generates output for its neighboring nodes.
- Updates its local storage.

Time is divided into discrete steps by a global clock, ensuring that the entire array operates synchronously. This mode of computation is often referred to as systemic operation because data flows through the network in a manner reminiscent of how blood circulates through the body. When a linear array is employed in this manner, it is commonly known as a systolic array.

Parallel algorithm performance

There are several ways to measure the performance of a parallel algorithm. Most obviously, we can count the total time taken T and the number of processors used P .

It is also interesting to compare the speed attained by the parallel algorithm to that of the best sequential algorithm. In particular the Speedup S of a parallel algorithm is defined to be the ratio of the running time Γ of the fastest sequential algorithm for the problem to the running time T of the parallel algorithm (i.e., $S = \Gamma / T$).

In general, we would like to develop parallel algorithms that have as much speedup as possible. In particular, given P processors, we would like our parallel algorithm to run P times as fast as the best sequential algorithm. When we can obtain such performance (i.e., when $S = P$, or even when $S = \Theta(P)$), we say that the parallel algorithm achieves linear speedup. Unfortunately, this is often hard to do. Note that a parallel algorithm can never obtain greater than linear speedup. In other words, S is always at most P .

Another important measure of the performance of a parallel algorithm is the work performed by the algorithm. More specifically, the work W of a parallel algorithm is defined to be the product of its running time and the number of processors used (i.e., $W = T \cdot P$). The notion of work measures the total processing efforts needed for an algorithm, and it accounts for insufficiencies caused by one or more processors being idle (or performing no useful task) during the computation. The notion of work can also be used to measure the efficiency with which the processors are utilised. More precisely, the efficiency E of a parallel algorithm is defined to be the ratio of the running time of the best sequential algorithm (Γ) to the work of the parallel algorithm (i.e., $E = \Gamma / W$). Alternatively, the efficiency of a parallel algorithm can be expressed as the ratio of the speedup to the number of the processors used. These measures are equivalent because:

$$E = \Gamma / W = \Gamma / (T \cdot P) = S / P$$

Network model

There are a plethora of networks models beyond the linear array. Most of the networks share several common properties. These common properties form the basis of the fixed-connection network model of parallel computing. The properties are partitioned into three categories: properties of the processors, properties of the interconnections, and properties of the input/output protocol. The following properties of network model is simple enough to be practical, yet robust enough to be completely general in a mathematical sense. Indeed, most all of relevant research in parallel computing on reprogrammable device, such as FPGA, can be nicely expressed within this model.

Processors' properties

Each processor will be allowed to have only local control. In particular the function performed by any processor can only depend on its local storage and local inputs. The complexity of the local control and local storage may vary, however. For example, a processor might or might not be provided with knowledge of its address, the topology and/or size of the network, and/or a clock to keep track of time. Usually the local memory has constant size, but occasionally there are situations in which the size of the local memory is a growing function of the size of the network.

The complexity of a processor will also vary in terms of the scale of operation that can be performed in a single step. For example, a bit processor will be allowed to perform a constant number of bit operations in a single step, whereas a byte processor can perform a constant number of byte operations in a single step, and so on for float and double processors.

Interconnections' properties

Connections between pairs of processors defined by the network (e.g., a complete linear array) are not allowed to vary with time. Hence the term of fixed connection network.

In one time step, a constant amount of communication can occur through any connection. Depending on the data type and kind of processor, this communication could be in form of bit, byte, float or double.

Usually each processor has only a constant number (often three or four excluding star networks) of connections to other processors (I.e., that the network is a bounded-degree network), although we will occasionally consider networks in which each processor is connected to $\mathcal{O}(\log N)$ other processors where N is the size of the network. The size of the network will usually be a polynomial function (often linear) of the size of the problem being solved.

The choice of a network topology for linking processors is a fundamental design requirement involving a trade-off between performance and cost. An ideal solution provides to connect every processors with a direct link, but it is very expensive as the number of processors grow. Therefore the number of link has to be reduced, yet providing low communication overhead, as well as allowing simple routing strategies to keep high reliability in the case of faulty processors or link.

In general given n generic processors, a complete network topology, the so called complete graph K_n , connects every pair of processors by direct link between them. There are $n(n-1)/2$ links in K_n and it's very expensive to adopt this topology for large number of processors. In parallel computing architectures is needed to design the cheapest topology, such as: linear (systolic) array, meshes, trees, tori, butterflies, hypercube or complete graph, for making nodes communicate as fast as possible. Interconnection networks use undirected graphs theory to design high performance topologies. Therefore let $G=(V,E)$ be a finite undirected graph, where:

$$V \equiv \{x_i : i=1..n\} \text{ and } E \equiv \{(x_i \leftrightarrow x_j) \neq \emptyset : i \neq j : i, j=1..n\}$$

the vertex and edges sets of G , respectively, the most important topological properties including the following:

- Vertex or Node (V): represents a processor. $N=|V|$ is the number of nodes or size of the graph.
- Edge (E): is a communication link between two nodes. $L=|E|$ is the cost or the number of links among the nodes. Simply put, more wires mean faster communication between nodes.
- Vertex or Node degree (d): number of channels connected to one node.
- Diameter (D): the maximum distance between any pair of nodes. Sometimes it is a lower bound on the time which it takes to perform all to all node communication.
- Bisection width (B): to bisect a network means split it in two parts, each one containing roughly the same number of nodes. The bisection width is the minimum number of links removed in order to bisect a network. A larger bisection width enables faster information exchange
- I/O bandwidth (S): the number of input/output lines in the network.
- Symmetry: the network seems the same from any nodes.

- Recursive level: the network is built by connecting smaller topologies of the same network. It makes scalable the problem solution.

The Fig.2 shows a summary of the topological properties of the simplest interconnection networks for parallel computation.

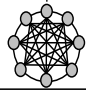

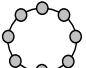
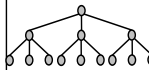
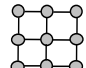
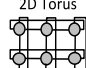

Topology Size: n	Node degree	Edges	Diameter	Bisection width
complete 	$n-1$	$\frac{n(n-1)}{2}$	1	$\left(\frac{n}{2}\right)^2$
1D Array 	2	$n-1$	$n-1$	1
1D Torus 	2	n	$\left\lfloor \frac{n}{2} \right\rfloor$	2
k-ary h-Tree 	k $n = \frac{k^{(h+1)} - 1}{k - 1}$	$\sum_{i=0}^{h-1} k^{(h-i)}$	$2 \log_k(nk - n) - 2$	$k \text{ even} \rightarrow 1$ $k \text{ odd} \rightarrow ?$
2D Mesh 	4	$2n - 2\sqrt{n}$	$2(\sqrt{n} - 1)$	\sqrt{n}
2D Torus 	4	$2n - 2\sqrt{n} + 6$	$n^{\frac{1}{2}}$	$2\sqrt{n}$
k-ary, hypercube 	k $n = 2^t$	$k \cdot 2^{(k-1)}$	$\log_2 n$	$\frac{n}{2}$

Fig.2: network topology

To generate new network topologies the cross product of two graph is used. The formal mathematical representation is, given two graphs:

$$G_1 = (V_1 \equiv \{x_i : i=1..n\}, E_1 \equiv \{(x_i \leftrightarrow x_j) \neq \emptyset : i \neq j : i, j=1..n\})$$

$$G_2 = (V_2 \equiv \{y_k : k=1..m\}, E_2 \equiv \{(y_k \leftrightarrow y_h) \neq \emptyset : k \neq h : h, k=1..m\})$$

then the cross product $G = G_1 \otimes G_2 = G(V, E)$, where:

$$V = \{ \langle x_i, y_j \rangle \mid x_i \in V_1, y_j \in V_2 \}$$

and

$$E = \{ (\langle x_i, y_k \rangle \leftrightarrow \langle x_j, y_k \rangle) : (x_i \leftrightarrow x_j) \in E_1 \} \cup \{ (\langle x_i, y_k \rangle \leftrightarrow \langle x_i, y_h \rangle) : (y_k \leftrightarrow y_h) \in E_2 \}$$

Fig.3 depicts an example of cross product. Note that the $G = G_1 \otimes G_2$ can be viewed as being constructed from $|V_1|$ copies of G_2 or $|V_2|$ copies of G_1 connecting pairs of nodes whose labels are identical.

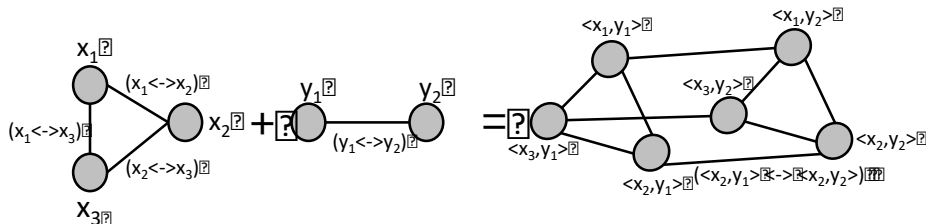


Fig.3: cross product between 1D torus and 1D Array

Input/Output protocols' properties

The most stringent constrain on the input/output protocol is that each input be provided just once. Of course, any processor of the network can store any input and distribute its value to other processors, but this will cost time and space. The point of forbidding multiple inputs of the same data is to gain a complete measure of the computation and communication which must be performed by a network to solve a problem. Among the things, this measure should include the cost of saving, replicating and distributing data. Indeed, the development of efficient methods for performing these tasks is central to the development of efficient parallel computation.

In other words, the I/O protocol specify $(p_k, p_k', t_k, t_k' \mid k=1,2,\dots)$ where input k is provided to processor p_k at time t_k , and output ok will be contained in processor p_k' at time t_k' for all k .

Linear algebra algorithms

The numerical linear algebra algorithms are easy to implement on linear arrays networks consisting of simple Byte, Float or Double processors (I.e., adders, multipliers and occasionally dividers). For the most part, the algorithms are also efficient in the sense they achieve near optimal speedups over the corresponding sequential algorithms. Basically the matrix-vector and matrix-matrix multiplication were among the first systolic algorithms discovered and serve as the basis for many tensor applications. They are also particularly well suited for use on arrays, ring and tori.

There are so many other algorithms and approaches to solving linear algebra problems that will not cover in this work, however the algorithms and techniques reported in this work provide a representative landscape of the methods used to efficiently parallelise linear algebra algorithms for use on linear arrays networks and the form the building blocks from which substantially more complex applications can be developed.

The number of multiplications and summations required for linear algebra arithmetic allows to define *FLOPS* needs to the PPW metric. Therefore a list linear algebra operations is provided as follow:

- *Vector-vector operations:*
Given vector $a, b \in \mathbb{R}^n$:
 - Addition $a + b$: requires n FLOPS for n element-wise additions.
 - Scalar multiplication $c \cdot a$: requires n FLOPS for n element-wise multiplications.
 - Inner product $a^T b$: requires approximately $2n$ FLOPS for n multiplications and $n - 1$ additions.
- *Matrix-vector operations:*
Given $A \in \mathbb{R}^{m \times n}$, $b \in \mathbb{R}^n$ consider Ab :
 - In general, $Ab = (a_1^T, a_2^T, \dots, a_m^T)^T b = (a_1^T b, a_2^T b, \dots, a_m^T b)^T$, each row takes $2n$ FLOPS, then m rows, take $2mn$ FLOPS in total.
 - If A is s -sparse matrix, the i 'th element of Ab is $Ab(i) = \sum_j a_j b_j \in S$ where S is the index set of non-zero elements in A . Since $|S| = s$, the total FLOPS count is $2s$. (The worst case is that all the non-zero elements are in the same row)
 - If $A \in \mathbb{R}^{n \times n}$ is a k -banded, the non-zero elements of each row is $2k$, then the total FLOPS count of n row is $2nk$.
 - If $A = \sum_{i=1}^r u_i u_i^T$, $Ab = \sum_{i=1}^r u_i (u_i^T b)$. Calculate $m_i = u_i^T b, i = 1, \dots, r$ costs $2nr$ FLOPS. Then scalar multiplication takes mr FLOPS, finally the sum takes mr FLOPS count is $2r(m+n)$.
 - If $A \in \mathbb{R}^{n \times n}$ is a permutation matrix, it takes 0 FLOPS to reorder elements in b .
- *Matrix-matrix product:*
Given $A \in \mathbb{R}^{m \times n}$, $B \in \mathbb{R}^{n \times p}$, consider AB :
 - In general, $AB = A(b_1, b_2, \dots, b_p) = (Ab_1, \dots, Ab_p)$. For each b_i the product cost $2mn$ FLOPS, then the total FLOPS is $2mnp$.
 - If A is s -sparse matrix the cost is $2sp$ FLOPS. The cost can be further reduced if B is also sparse.
- *Matrix-matrix-vector product:*
Given $A \in \mathbb{R}^{m \times n}$, $B \in \mathbb{R}^{n \times p}$, $c \in \mathbb{R}^p$ consider ABC :

- If product is done properly, that is $ABC = A(BC)$, the total cost is $2np+2mn$. Else if done improperly, i.e., $ABC=(AB)c$, the cost is $2mnp+2mp!$

- *Linear systems:*

Given a non-singular square matrix $A \in \mathbb{R}^{n \times n}$, and a vector $b \in \mathbb{R}^n$, consider solving the linear equation, $Ax=b$. In other words it means to determine the cost of computing $x=A^{-1}b$.

- In general, it costs n^3 FLOPS. This can be a very expensive cost when n is a large number. However, the complexity of solving linear systems can be reduced for some matrices having special properties.
- If A is diagonal, it just cost n FLOPS, one each for element-wise divisions. $x_i=b/a_i, i=1, \dots, n$
- If A is lower triangular ($A_{ij}=0, j > i$), it costs about n^2 FLOPS by forward substitution.

$$\begin{aligned} x_1 &= b_1/A_{11} \\ x_2 &= (b_2 - A_{21}x_1)/A_{22} \\ &\dots \dots \dots \\ x_n &= (b_n - A_{n,n-1}x_{n-1} - \dots - A_{n1}x_1)/A_{nn} \end{aligned}$$

- If A is upper triangular ($A_{ij}=0, i > j$), it costs about n^2 FLOPS by backward substitution.
- If A is s -sparse, it often costs $\ll n^3$ FLOPS. However, it is hard to determine the exact order of FLOPS. It heavily depends on the sparsity structure of the matrix.
- If A is a k -banded, it costs about nk^2 FLOPS.
- If A is a permutation matrix, which means that $A^{-1}=A^T$, then $x = A^T b$ costs 0 FLOPS since each row of A has only one element and x can be obtained from n assignment operations that are free of cost.

To solve a linear system $Ax=b$, instead of doing $A \setminus b$ or compute A^{-1} directly, it is useful to factorize A into product of some structured (orthogonal, triangular, diagonal, or permutation matrices that are easier to compute inverse). Useful alternatives are the QR , Cholesky and LU decomposition.

- In QR decomposition assuming:

$$\begin{aligned} A &= QR \text{ is non-singular and square, where} \\ Q &\in \mathbb{R}^{m \times n}, Q^T Q = I_n \text{ (orthogonal)} \\ R &\in \mathbb{R}^{m \times n}, Q^T Q = I_n \text{ (upper triangular)} \end{aligned}$$

$Ax=b$ is solved:

$$\begin{aligned} &\text{Compute } QR \text{ factorization in } 2mn^2 \text{ FLOPS} \\ &\text{Compute } y = Q^T b \text{ in } 2mn \text{ FLOPS} \\ &\text{Solve } Rx = y \text{ in } n^2 \text{ FLOPS (backward substitution)} \\ &\text{Total is : } 2mn^2 + 2mn + n^2 \approx 2mn^2 \text{ for large } m, n \end{aligned}$$

- In Cholesky decomposition assuming:

$$\begin{aligned} A &= LL^T, \text{ symmetric and positive . It is a special case of Gaussian elimination for} \\ &\text{the positive matrices that requires } n^3/3 \text{ FLOPS} \\ L &\in \mathbb{R}^{n \times n}, \text{ non-singular upper triangular} \end{aligned}$$

$Ax=b$ is solved:

$$\begin{aligned} &\text{Compute } A=LL^T \text{ in } n^3/3 \text{ FLOPS} \\ &\text{Compute } y = L^{-1}b \text{ by forward substitution in } n^2 \text{ FLOPS} \\ &\text{Solve } x = (L^T)^{-1} y \text{ by backward substitution in } n^2 \text{ FLOPS} \\ &\text{Total is : } n^3/3 + 2n^2 \approx n^3/3 \text{ for large } n \end{aligned}$$

- In LU decomposition assuming:

$$\begin{aligned} A &= PLU \text{ with:} \\ P &\in \mathbb{R}^{n \times n} \text{ a permutation matrix} \\ L &\in \mathbb{R}^{n \times n}, \text{ non-singular lower triangular} \\ U &\in \mathbb{R}^{n \times n}, \text{ non-singular upper triangular} \end{aligned}$$

$Ax=b$ is solved:

$$\begin{aligned} &\text{Compute } A=PLU \text{ factorization is } 2/3n^3 \text{ FLOPS} \\ &\text{Compute } y_1 = P^T b \text{ by permutation in zero FLOPS} \\ &\text{Compute } Ly_2 = y_1 \text{ by forward substitution in } n^2 \text{ FLOPS} \end{aligned}$$

Compute $Ux = y_2$ by backward substitution in n^2 FLOPS
 Total is: $2/3n^3 + 2n^2 \approx 2/3n^3$ FLOPS

Elementary matrix multiplications

The simplest sequential method for doing matrix multiplication takes $2N^2 - N$ steps: N multiplications and $N - 1$ adds for each $y(i)$. Using an N -cell linear array, however the entire multiplication can be calculated in $2N - 1$ multiply/add steps, thereby providing a reasonably efficient speedup over the naive sequential algorithm. The algorithm for matrix-vector multiplication on a linear array is quite simple. The x_j 's are input one-per-step (clock cycle) from the left end of the array (starting with x_1, x_2, \dots) and a_{ij} 's are input from the top of the array as shown in Fig.4.

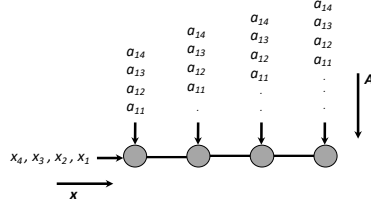


Fig.4: matrix-vector product $y = Ax$. The i^{th} cell computes y_i by adding the product $a_{ij}x_j$ to the memory at step $i + j - 1$

The i^{th} cell of the linear array computes y_i by multiplying the x -value input from the left by the A -value input from the top, and adding the product to i^{st} local memory at each step. Note that x_j and a_{ij} arrive in the cell i^{th} at the same time (specifically. At step $i + j - 1$) so that the value computed at the i^{th} cell is precisely $y_i = \sum_{j=1}^N a_{ij} x_j$. The computation of y_i is completed at step $N + i - 1$, after which it may be output. Hence, all values are computed after $2N - 1$ steps of clock cycle.

The algorithm for matrix-vector multiplication on a linear array can be easily extended to multiply two matrices on a two-dimensional array (or mesh). In particular, given two matrices $A = (a_{ij})$ and $B = (b_{ij})$, the product row per column matrix $C = AB$ where $C = (c_{ij})$ and

$$c_{ij} = \sum_{k=1}^N a_{ik} b_{kj}$$

can be computed in $3N - 2$ steps on an $N \times N$ array. As with matrix-vector multiplication, the i^{th} row of A is input to the i^{th} column of the array from the top, starting with a_{i1} at step i . Similarly, the j^{th} column of B is input to the j^{th} row of the array from the left, starting with b_{1j} at step j . The values of a_{ik} and b_{kj} arrive at cell (i,j) of the array simultaneously at step $i + j + k - 2$, whereupon they are multiplied and passed downward and rightward respectively. The product $a_{ik}b_{kj}$ is added to the local memory and the (i,j) cell of the array will have computed exactly:

$$c_{ij} = \sum_{k=1}^N a_{ik} b_{kj}$$

after $i + j + N - 2$ steps. The entire matrix product is calculated after a total of $3N - 2$ steps. For example, Fig. 5 shows the start arrangement of data for a 4×4 matrix product with the details of the processor. The Fig.6 shows the first 4 steps of runtime evolution of the 4×4 matrix product of Fig.5.

Both the previous algorithms achieve a speedup over their sequential counterparts that is linear in the number of processors, which is the best possible (up to constant factors). In the case of matrix multiplication, we might hope to do better by using a parallelized version of $\mathcal{O}(N^3)$ -step sequential algorithm, but such algorithms are very complicated and cannot be efficiently implemented on an array. It is possible to improve efficiency of the algorithms starting with the data already in the network and adding wraparound wires in the arrays, both the algorithms can be made to run in N steps, not counting the I/O. For example, consider the linear array with a wraparound wire (or ring) by starting with the value of x_j in the cell $N - j + 1$ for $1 \leq j \leq N$, and imputing the value of a_{ij} to cell i during step $i + j$ or $i + j - N$ (whichever is between 1 and N , inclusive), we can compute y_i in cell i ($1 \leq i \leq N$) in N steps by simply passing the values of x rightward after each multiply/add step.

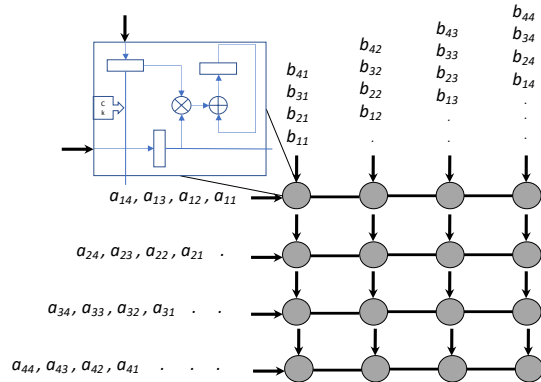


Fig.5: Start arrangement of data and details of the processor for the 4×4 matrix product

A similar approach can be used to multiply two matrices in N steps using $N \times N$ two-dimensional array with wraparound wires in the rows and columns (e.g. 2D torus). A torus is a simple 2D-mesh with wraparound wires in the rows and columns. In this case, cell (j, i) initially contains the values of a_{ik} and b_{jk} where k equals $N + 2 - i - j$ or $2N + 2 - i - j$ (whichever is positive). The values of A move downward and the values of B move rightward after each multiply/add/step. The value c_{ij} is computed in the cell (j, i) after N steps.

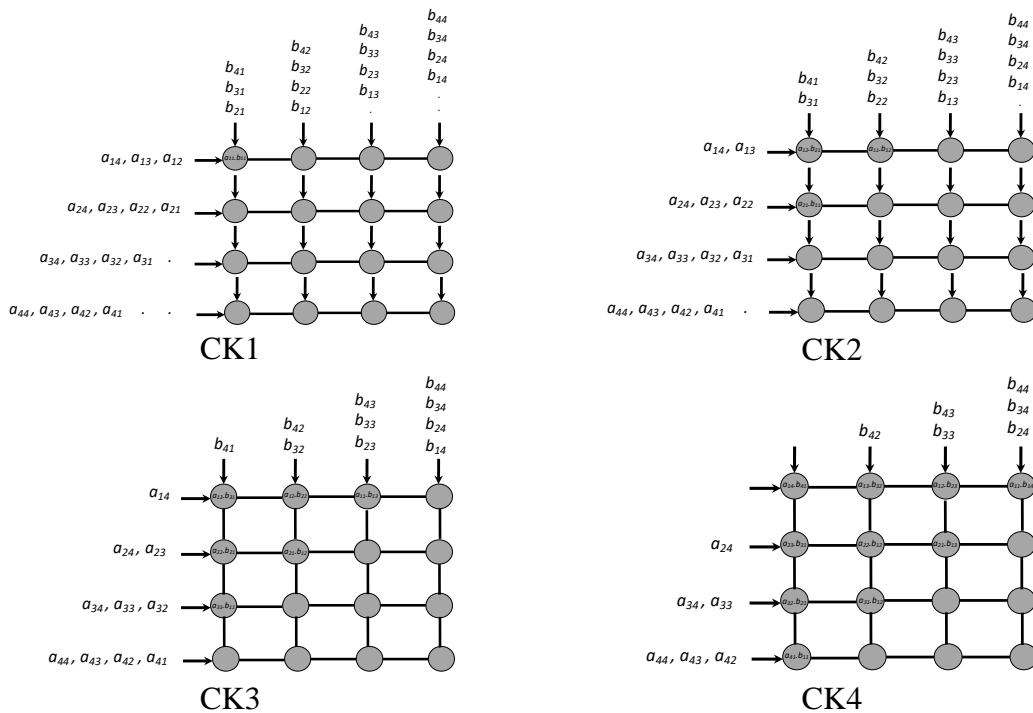


Fig.6: The first four steps for the 4×4 matrix product

3 The Xilinx Vitis BLAS Library

The BLAS (Basic Linear Algebra Subprograms) [2] are routines that provide standard building blocks for performing basic vector and matrix operations. The Level 1 BLAS perform scalar, vector and vector-vector operations, the Level 2 BLAS perform matrix-vector operations, and the Level 3 BLAS perform matrix-matrix operations. Because the BLAS are efficient, portable, and widely available, they are commonly used in the development of high quality linear algebra software, LAPACK [3] for example.

Xilinx provides the VITIS unified software platform including a set of open-source, performance-optimized libraries that offer offloading acceleration on Xilinx FPGA Alveo devices. Common Vitis accelerated-libraries, including Solver, Basic Linear Algebra Subroutines (BLAS), Sparse, DSP, and Utilities, offer a set of core functionality for a wide range of diverse applications.

Xilinx offers a unified software platform, called Vitis, to develop FPGA applications. Vitis includes a rich set of hardware-accelerated open-source libraries optimized for Xilinx FPGA and the Xilinx Runtime library (XRT) to facilitate communication between the host application (running on the host CPU) and the accelerator deployed on the reconfigurable portion of the card, which is connected via PCIeExpress. It also includes user-space libraries and APIs, kernel drivers, and board utilities that can be used to measure performance and monitor power consumption. In this work, we aim to automate the generation of CU descriptions and the associated configuration file directly on top of the existing Xilinx libraries.

In order to specify the FPGA performance, floating-point operations for Matrix to Matrix multiplication is used as reference in this benchmarks since Xilinx Vitis BLAS Library is available including benchmarks on Xilinx Alveo U200. Usually DGEMM function is relevant to stress important system properties or generate workloads that is similar to relevant applications. Some benchmarks were carried out in [4] implementing the GEMM matrix-matrix multiplication function of the BLAS library in a kernel function for U280 PCIe FPGA. The GEMM Cannon's Matrix Multiplication Algorithm used in the benchmark, is 8192×8192 matrices for the calculation based on 4×4 and 16×16 matrices block, so the kernel can initialize respectively: 1024 and 8192 Floating-point single precision (FP32) multiplications and additions per clock cycle. The board U280 with DDR and HBM usage is about 200 GFLOPS/s with a clock frequency of 250 MHz. It's difficult to establish a performance limit for DGEMM function because it depends on the algorithm. In [5] the implementation of DGEMM on Xilinx Alveo U200 card performed a benchmark of 350 GFLOPS/s in single precision (FP32) with a clock of 300 MHz. The best performance of a GEMM single precision on Xilinx U200 is 409 GFLOPS/s [6] using ~90% of the LUT resources. The aims of our benchmarks activities are to evaluate the performances of VITIS Library BLAS/DGEMM design on Xilinx Alveo U250 and U280 in order to verify if they achieve at least 0.5 TFLOPS/s in single precision.

Vitis BLAS Library provides three types of function implementations, namely L1 primitive functions, L2 kernel functions and L3 software API functions. L1 primitive functions can be leveraged by FPGA hardware developers. L2 kernel functions are built by integrating L1 primitive functions and data movers, which can be called by host codes with XRT Runtime Library. L3 software API functions provide C, C++ and Python function interfaces to allow pure software developers to offload BLAS operations to AMD platforms without additional hardware related configurations.

In order to follow a co-design approach to heterogeneous architecture for exascale compute node FPGA based, the proof of concept is to evaluate the friendly usage and performance of BLAS/GEMM Matrix Multiplication in Vitis BLAS Library at L3 API level.

The Vitis BLAS L3 Library supports three different versions of APIs to match memory allocation in device. In this proof of concept the restricted memory version is adopted. It requires the input matrix sizes must be multiple of certain configuration values that are used to build the FPGA kernel bitstreams. The Vitis BLAS L3 Library support float datatypes and the basic API functions for Matrix Multiplication $C = A \times B$ are the following:

`xfblasCreate()`: to initialize the BLAS library this function must be called at beginning. It will open the device, download the FPGA image to the device and create context on the selected compute unit. For a multi-kernels `xclbin`, contexts will be opened on the corresponding compute units. The function arguments are:

- *const char* xclbin* : file path to FPGA bitstream
- *string configFile* : file path to *config_info.dat* file. This *config_info* file includes the connectivity map of the kernels in the hardware regions of the FPGA device.
- *const char* logFile* : file path to log file
- *xfblasEngine_t engineName* : Vitis BLAS engine to run (for GEMM is `XFBLAS_ENGINE_GEMM`)
- *unsigned int kernelNumber* : number of kernels that is being used, default is 1
- *unsigned int deviceIndex* : index of device that is being used, default is 0

`xfblasMallocRestricted()` : This function allocates memory for host row-major format matrix on the FPGA device in the restricted memory version API. The function arguments are:

- *int rows* : number of rows in the matrix
- *int cols* : number of cols in the matrix that is being used
- *int elemSize* : number of bytes required to store each element in the matrix
- *void* Matrix* : pointer to the matrix array in the host memory
- *int lda* : leading dimension of the matrix that indicates the total number of cols in the matrix
- *unsigned int kernelIndex* : index of kernel that is being used, default is 0
- *unsigned int deviceIndex* : index of device that is being used, default is 0
- `xfblasSet[Get]MatrixRestricted()` : These functions copie a matrix in host [FPGA] memory to FPGA device [host] memory. The functions arguments are:
 - *void* Matrix* : pointer to the matrix array in the host memory
 - *unsigned int kernelIndex* : index of kernel that is being used, default is 0
 - *unsigned int deviceIndex* : index of device that is being used, default is 0
- `xfblasGemm()` : This function performs the Matrix-Matrix multiplication $C = \alpha(A \times B) + \beta \cdot C$.

The function arguments are:

- *xfblasOperation_t transa* : A matrix with *xfblasOperation_t* data types as follow:
 - `XFBLAS_OP_N` : The non-transpose operation is selected
 - `XFBLAS_OP_T` : The transpose operation is selected
 - `XFBLAS_OP_C` : The conjugate transpose operation is selected
- *xfblasOperation_t transb* : B matrix with *xfblasOperation_t* data types as above
- *int m* : number of rows in matrix A, matrix C
- *int n* : number of cols in matrix B, matrix C
- *int k* : number of cols in matrix A, number of rows in matrix B
- *int alpha* : scalar used for multiplication
- *void* A Matrix* : pointer to matrix A in the host memory
- *int lda* : leading dimension of the matrix that indicates the total number of cols in the matrix A
- *void* B Matrix* : pointer to matrix B in the host memory
- *int ldb* : leading dimension of the matrix that indicates the total number of cols in the matrix B
- *int beta* : scalar used for multiplication
- *int ldc* : leading dimension of the matrix that indicates the total number of cols in the matrix C
- *void* C Matrix* : pointer to matrix C in the host memory
- *unsigned int kernelIndex* : index of kernel that is being used, default is 0
- *unsigned int deviceIndex* : index of device that is being used, default is 0

There are some functions in L3 API that allow to implement flexible algorithms in users applications. They are as follow:

- `xfblasExecute()` : This function starts the kernel and wait until it finishes. The function arguments are:

- *unsigned int kernelIndex* : index of kernel that is being used, default is 0
- *unsigned int deviceIndex* : index of device that is being used, default is 0
- *xfblasExecuteAsync()* : This asynchronous function starts all kernels and wait until them finish. The function arguments are:
 - *unsigned int numkernels* : number of kernels to start
 - *unsigned int deviceIndex* : index of device that is being used, default is 0

An example of L3 API source code is as follow:

```
// INITIALIZE DEVICE
xfblasStatus_t status = xfblasCreate(l_xclbinFile.c_str(), l_configFile, XFBLAS_ENGINE_GEMM, 1);
//MEMORY ALLOC OF DATA TO FPGA
status = xfblasMallocRestricted(m,k,sizeof(*a),a,k, 0);
status = xfblasMallocRestricted(k,n,sizeof(*b),b,n, 0);
status = xfblasMallocRestricted(m,n,sizeof(*c),c,n, 0);
//COPY DATA FROM HOST TO FPGA
status = xfblasSetMatrixRestricted(a, 0);
status = xfblasSetMatrixRestricted(b, 0);
status = xfblasSetMatrixRestricted(c, 0);
//RUN API GEMM
status = xfblasGemm(XFBLAS_OP_N, XFBLAS_OP_N, m, k, n, 1, a, k, b, n, 1, c, n, 0);
//COPY DATA FROM FPGA TO HOST
status = xfblasGetMatrixRestricted(c, 0);
```

4 The Xilinx Alveo FPGA for HPC

Currently there are two Xilinx Alveo FPGA available for HPC systems. The following Tab.1 shows the technical specification of the U250/U280 FPGA board installed in the ENEA FPGA Lab.

	U250	U280
Look-up tables (LUT)	1,728K	1,304K
Registers	3,456K	2,607K
DSO Slices	12,288	9,024
INT8 TOPs Peak	33.3	24.5
DDR memory	4x 16GB 72b	2x 16GB 72b
DDR total capacity	64 GB	32 GB
DDR Max Data Rate	2400 MT/s	2400 MT/s
DDR Total BW	77GB/s	38 GB/s
HBM2 Total Capacity	-	8 GB
HBM2 Total Bandwidth	-	460 GB/s
Internal memory total capacity	57 MB	43 MB
Internal memory total BW	47 TB/s	35 TB/s
PCI Express®	Gen3 x16	2x Gen4 x8, Gen3 x16 with CCIX
Network Interface	2x QSFP28	2x QSFP28
Typical power	110 W	100 W
Maximum power	225 W	225 W

Tab.1: Xilinx Alveo U250 and U280 specifications

In Textarossa project activities, the specifications of a compute node for heterogeneous architectures, are defined adopting a Xilinx Alveo U280 as FPGA accelerator device. The reason for that requirement is the availability of the HBM resources of U280 compared to U250.

HBM is a memory technology, which is standardized by JEDEC [7]. It's essentially a 3D stack of multiple DRAMs that have completely independent memory interfaces, which allows to reduce I/O energy and achieve very high memory bandwidth.

The Xilinx Alveo U280, in all the following parts of this work referred to as U280, is an FPGA-board that belongs to the Virtex UltraScale+ HBM family, which provides HBM as part of the FPGA. In

the case of the U280 there are two HBM-stacks, each containing 4 GB of memory, which leads to a total of 8 GB HBM. Access to the HBM stacks is provided via the AXI HBM Controller. Each stack consists of 8 completely independent memory channels each of which is again split into 2 pseudo channels of 64 bit. This means that on the U280 each memory part accessible by one pseudo-channel contains a total of $4 \text{ GB} / 16 = 256 \text{ MB}$ storage capacity.

The difference between the two Xilinx cards is mainly in the HBM available on the U280. HBM is a novel memory architecture that enables high-performance and adaptability for memory-bound applications.

The Alveo U280 is built on the Xilinx 16nm UltraScale+ architecture and offers a rich set of memory solutions, as shown in Fig. 7. The Alveo U280 card features the XCU280 FPGA, which combines three Super Logic Regions (SLRs). The Tab 2.3, SLR0 integrates an HBM controller to interface with the HBM2 subsystem through 32 pseudo-channels (PCs) each with direct access to 256 MB of storage (8 GB in total). Each 256-bit PC operates at 450 MHz, yielding a maximum bandwidth of 14.4 GB/s. only the SLR0 is connected to the off-chip HBM2 memory banks, and then in this case Super Long Line (SSL) routes can not be avoided for accessing data from logic allocated in SLR1 and SLR2 The full system can thus achieve a theoretical bandwidth of 460.8 GB/s. SLR0 also connects to the host via 16 lanes of the PCI Express (PCIe) interface. Only SLR0 and SLR1 are connected to the 2 off-chip 16 GB DDR memory banks, and then in this case SLL routes can not be avoided for accessing DDRs from logic allocated in SLR2. Finally, each region has up to 8 MB of PLRAM for fast access to small data sets. In the following, we will use the term global memory for the set of memories available on the board. The host must transfer data into the device global memory before they can be accessed by the FPGA logic [8].

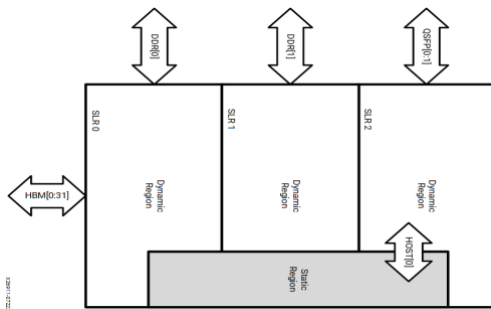


Fig.7. Architecture of XCU280

Resources	SLR0	SLR1	SLR2
HBM	32x256MB	-	-
DDR4 (72 bit)	16GB	16GB	-
PLRAM (512 bit)	2x128K	2x128K	2x128K
CLB LUT	369K	333K	367K
CLB Reg.	746K	675K	729K
Block RAM tile	507	468	512
UltraRAM	320	320	320
DSP	2733	2877	2880

Tab.2: Alveo U280 SLR resources

The target system for the Alveo U280 is composed of multiple compute units (CUs). Each CU is a user-defined hardware module that can be attached to any of the PCs through independent AXI interfaces, while the built-in HBM controller and switch have access to all physical channels. The CU can be described in C++ and synthesized with HLS or specified directly in RTL. Multiple CUs allow parallel execution but must be connected to different HBM channels. The system configuration file describes the connections between the CU ports and the HBM channels. The required logic is automatically generated during system synthesis.

The Alveo U250 accelerator card is custom-built UltraScale+ FPGAs that run optimally (and exclusively) on the Alveo architecture. The Alveo U250 card uses the XCU250 FPGA, both of which use Xilinx stacked silicon interconnect (SSI) technology to deliver breakthrough FPGA capacity, bandwidth, and power efficiency. This technology allows for increased density by combining multiple super logic regions (SLRs). The XCU250 comprises four SLRs. The device connects to 16 lanes of PCI Express® that can operate up to 8 GT/s (Gen3). The device connects to four DDR4 16 GB, 2400 MT/s, 64-bit with error correcting code (ECC) DIMMs for a total of 64 GB of DDR4. The device connect to two QSFP28 connectors with associated clocks generated on board. The following Fig. 8 shows the SLR regions along with the PCIe, DDR4 and QSFP28 connections for the Alveo U250 card, whilst the Tab.3 shows the resources belongs to each of the four SLRs.

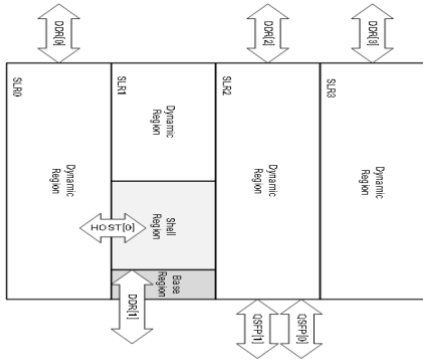


Fig.8. Architecture of XCU250

Resources	SLR0	SLR1	SLR2	SLR3
HBM	-	-	-	-
DDR4 (72 bit)	16GB	16GB	16GB	16GB
PLRAM (512 bit)	2x128K	2x128K	2x128K	2x128K
CLB LUT	419K	205K	410K	424K
CLB Reg.	839K	410K	819K	848K
Block RAM tile	668	384	664	672
UltraRAM	312	128	308	320
DSP	3032	1536	3016	3072

Tab.3: Alveo U250 SLR resources

The FPGA Xilinx U250 is more oriented for computations that require a lot of logic (intensive computations), while the U280, having more I/O bandwidth (2 HBM2 memory banks, 4 GB each, with a global bandwidth of 460 GB/s and 2x Gen4x8 PCIe channels) is more suited for applications memory bounding. Apart from the different characterization depending on the availability of more I/O logic or a larger quantity of “pure computational” logic, both the FPGA boards are well suited for HPC applications, having - both of them - a lot of logic resources (i.e. computational power) connected with internal memory (~50 MB) with a huge bandwidth (~40 TB/s).

5 BLAS Benchmarks

The Xilinx Vitis BLAS library has been tested with the Xilinx Alveo U250/U280 FPGA board. The boards are hosted in X86_64 nodes with 2 x Intel Xeon Haswell CPU and 128 GB RAM, PCIe Gen3x16 and OS CentOS 7.4. The Vitis 2022.2 HLS toolchain to compile the Xilinx BLAS Vitis Library and run the tests.

A first set of benchmarks have been carried out to compare the time to solution of the GEMM L3 Xilinx BLAS library on U280 board using DDR and HBM. The benchmarks perform the GEMM matrix-matrix multiplication of 4096×4096 matrices of float elements in two different cases: *i*) 4×4 matrices blocks (default setting of the library) and *ii*) 16×16 matrices blocks. The 4096×4096 size matrices of float elements is the upper limit of a single HBM channel of 256 MB. The Table 4 shows the benchmarks results as time-to-solution measured from *INITIALIZE DEVICE* to *COPY DATA FROM FPGA TO HOST* as described previously in the L3 API source code example. In terms of FPGA usage resources, the kernels of the BLAS algorithms use ~18.4% of the resources (LUT=218215) for the HBM case, whilst they use ~19.3% of the resources (LUT=220721) for the DDR case. A clock of 300 MHz has been adopted in the high level synthesis to build the bitstream target for the U280 FPGA.

Time-to-solution/FLOPS/s	4×4	16×16
	[sec.]/GFLOPS/s	[sec.]/GFLOPS/s
HBM	7.4 / 18.5	6.8 / 20.2
DDR	10 / 13.7	9.5 / 14.5

Tab.4: Alveo U280 Benchmarks: HBM vs DDR for 4096×4096 matrix-matrix multiplication

The two different matrices blocks setting are not significant for small size matrices (4096×4096), whilst the HBM channel allows better performances of the DDR channel.

A second set of benchmarks have been carried out to compare the time to solution of the GEMM L3 Xilinx BLAS library on U280 and U250 boards using the DDR channel. The benchmarks perform the GEMM matrix-matrix multiplication of 16384×16384 matrices of float elements in two different cases: *i*) 4×4 matrices blocks (default setting the library) and *ii*) 16×16 matrices blocks. The Table 5 shows the benchmarks results as time-to-solution measured like the previously benchmarks. In terms of FPGA usage resources, the kernels of the BLAS algorithms use ~13.5% of the resources

(LUT=219936) for the U250 FPGA boards. In these benchmarks the 16×16 matrices blocks setting produces a significant performance improvement.

Time-to-solution/FLOPS/s	4×4	16×16
	[sec.]/ GFLOPS/s	[sec.]/ GFLOPS/s
U280	98 / 89.7	65 / 135
U250	103 / 85.4	63.5/138.5

Tab.5: Benchmarks of U280 vs. U250 for 16384×16384 matrix-matrix multiplication

The benchmarks results show the performances of the Xilinx U250 and U280 FPGA, achieved with the Vitis BLAS library, is lower than performance results achieved with ad-hoc optimized implementations using much more FPGA LUT resources, however a multi-kernel implementation of the Xilinx BLAS library could achieve higher performance. Indeed a matrix-matrix multiplication of 16384×16384 matrices can be execute parallelly as four matrix-matrix multiplications of 8192×16384 matrices with a time to solution of ~14 sec. on U250 FPGA board, including the time spent to move data from host to FPGA DDR memory and return that is ~0.3 sec. Therefore the parallel execution of 4 kernels could produce a performance of ~600 GFLOPS/s for a matrix-matrix multiplication of 16384×16384 matrices in single precision (float 32 bit).

From an energy efficiency perspective, a set of benchmarks have been carried out using a different hardware configuration consisting of: *i*) a compute node with dual-socket AMD Epyc 7313 CPU, each with 16 cores at 3.0 GHz, *ii*) the same type of compute node with an Nvidia A100 GPU/PCIe board, and *iii*) a third compute node of the same type with a Xilinx Alveo U280 FPGA/PCIe board. This hardware layout allows for the comparison of power efficiency across various CPU architectures. The BLAS libraries adopted in the benchmarks are: *i*) the Intel MKL library (v.2020) in openMP programming model running on dual-socket AMD Epyc 7313 compute node, *ii*) the NVIDIA CUBLAS library in Nvidia Development Kit (v.23.1) and *iii*) the Xilinx BLAS Library in Vitis (2022.2) toolchain. The IPMI tool, sampled every 50 ms, gathers the instantaneous power consumption of the three compute nodes, producing the plot shown in Fig.9.

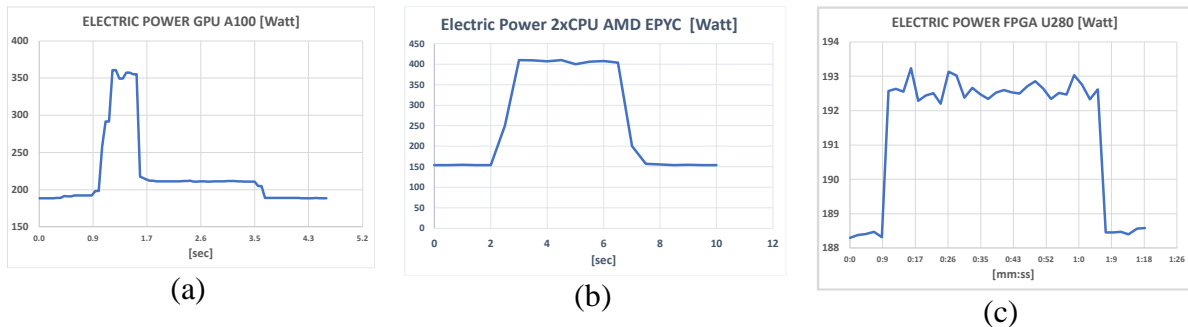


Fig.9: Power consumption of compute node: (a) GPU NVIDIA A100, (b) 2xCPU AMD EPYC, (c) FPGA Xilinx U280

Using the average power consumption of the compute nodes and the performance in GFLOPS/s of the floating-point matrix multiplication algorithm, the energy efficiency as *PPW*, for the three different processor architectures, is depicted in the fig.10.

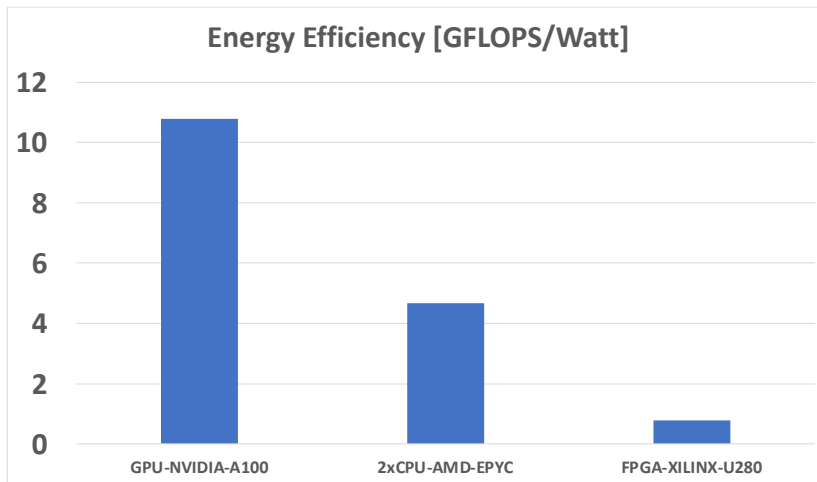


Fig.10: Energy efficiency of: GPU NVIDIA A100, 2xCPU AMD EPYC and FPGA Xilinx U280

The *PPW* analysis shows the current technologies based on FPGAs in parallel linear algebra applications have significantly lower energy efficiency compared to those utilizing GPUs or conventional CPUs.

6 Image processing on FPGA

FPGAs have found widespread utility in the realm of image processing, for their capability to implement in hardware with a dedicated architecture the deep pipelines required by image processing, as well as for the reduced power demands. Several FPGA implementations for image processing are reported in [9]. The methodologies expounded across the papers within [Bailey,2019] can be categorized into four distinct classes: utilization of a Hardware Description Language (HDL) or an HLS flow for algorithm realization, deployment of pre-designed Intellectual Properties (IP) for complex graphical functionality, and design of soft processor cores optimized for image processing. All these approaches harness the versatility characteristic of FPGAs—specifically, their programmable nature and their support for virtually any computing architecture. FPGAs offer a lot of logic elements (such as Flip Flops, Look-up Tables, DSPs) for implementing computing kernels and boast numerous discrete internal memory blocks (BRAM) that collectively deliver remarkably high memory bandwidth.

Conversely, AMD adopts a distinct approach, employing FPGA technology to implement certain OpenCV functionalities [10]. The greatest part of the functionalities processes the input image on a pixel-per-pixel basis, allowing the user to choose whether to process 1 pixel per cycle or 8 pixels per cycle.

An Image Processing Library tailored for Xilinx FPGAs has been devised [11], wherein SDSoc HLS has been harnessed to devise streaming kernels for image processing. These kernels can be combined to execute diverse image-processing tasks. The library seamlessly accommodates varying pixel sizes, enabling parallel computation of 1, 2, 4, or 8 pixels, facilitated through a template-based paradigm. The FPGA Image Processing Library (*FIPLib*) developed by ENEA in C++ employs the Vitis HLS flow to construct the library's kernels for the execution of image processing algorithms, subsequently translating them into bitstreams. Presently, *FIPLib* encompasses nearly 50 functionalities, each conceived with a streaming behavior: data are read from the input streams and are written to the output streams. The width of all streams is controlled by a template parameter that determines both the data path width and the available parallelism. The functionalities within *FIPLib* can be classified as follows:

1. *Stream Management*: Encompasses stream copy, stream split, and stream merge operations.

2. *Data Mover*: Serves as the interface between DDR/HBM and streams.
3. *Parameter Initialization*: Establishes weight values for distinct filters like Sobel, Gaussian, and Box filters.
4. *Pixel-based Operations*: Orchestrates pixel-based operations on input images, yielding output images through operations such as multiplication, subtraction, addition, complementation, logical operations, minimum, maximum, and linear scaling.
5. *Color Space Conversion*: Undertakes pixel-based transformations, converting images from RGB color space to YUV color space and vice versa.
6. *Image Masking*: Executes pixel-based operations that derive output images based on pixel values from either of two input images, based on the binary masking image. Also includes rectangular and circular mask generation.
7. *Line-based Operations*: Requires complete reading of one or more lines prior to initiating the output of processed images. This category encompasses diverse filters (2D convolution with kernels of dimensions 3x3, 5x5, 7x7), median filtering (3x3, 5x5), morphological operators like dilation and erosion, and 2x up-sampling through bilinear interpolation.
8. *Store and Forward Transformations*: Demands full image read before generating the output image. This includes operations such as histogram equalization, contrast maximization, and vertical mirroring.

All functions share a consistent structure, and they encompass the subsequent parameters: Input/Output streams, function specific parameters (such as kernel weights in convolutional filters), image size (comprising the overall image dimensions, including the number of rows and columns), number of images to be processed before the function restarts.

These functions, or tasks, can be interconnected via streams and are invoked within a designated DataFlow section. Tasks within a DataFlow section are executed concurrently, with synchronization achieved through streaming communications. In Fig.11, we provide an excerpt of a basic image-processing kernel, accompanied by its graphical representation within a process network:

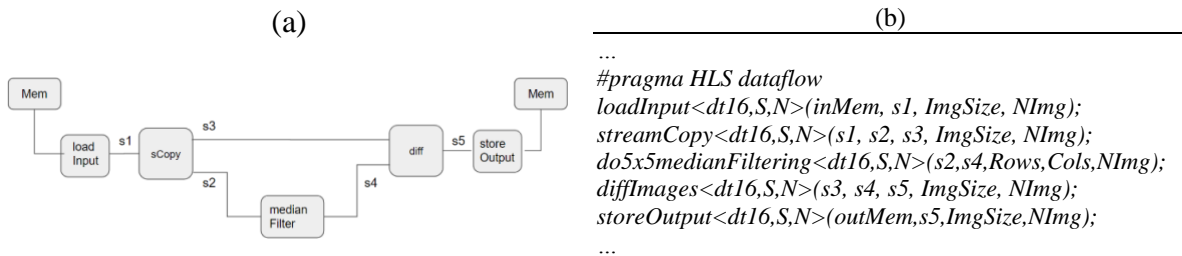


Fig.11: Graphics (a) and Codelet (b) showing a simple image processing kernel

In the preceding codelet, the template values $dt16$, S , and N respectively denote the stream data type (in this case, 16 bytes wide), the pixel component size S (in bits), and the stream width N (in bits) (here, $S=8$ and $N=128$). These parameters afford us control over the degree of parallelism for each function: during each clock cycle, N/S elements are simultaneously read from the stream, processed in parallel, and subsequently written to the output stream, all in a pipelined fashion. In the kernel outlined in Fig.11, data is read from the external memory $inMem$ and directed to stream $s1$. It is then duplicated into streams $s2$ and $s3$. The image conveyed through $s2$ undergoes median filtering (5×5), and the resulting output is subtracted from the original image received via $s3$. This difference image is sent through stream $s5$ to the task $storeOutput$, which in turn writes it to the external memory $outMem$.

Simply changing the template parameters from $dt16$ to $dt32$ and N from 128 to 256, the previous codelet would effectively double the operations per cycle. We tested the library for N values of $\{64, 128, 256, 512\}$. Nevertheless, numerous *FIPLib* functions can potentially function effectively with

varying N values: mainly splitting and merging functions, being connected to data alignment, necessitate tailored design to support different N values.

The key point in achieving optimal FPGA processing performance is the maximization of parallelism, both in data access and data processing. Within *FIPLib*, four distinct types of parallelism are employed:

Spatial Parallelism: This form of parallelism involves the concurrent processing of N/S image components, optimizing the utilization of parallel resources.

Fine-Grain Pipeline Parallelism: Employed in tasks such as stream management, data movers, and pixel-based operations, this type of parallelism operates at the granularity of an individual pixel component.

Medium-Grain Pipeline Parallelism: Implemented in line-based operations, this type of parallelism is centered around processing an entire line of the image, hence the unit of parallelism is one line of the image.

Coarse-Grain Pipeline Parallelism: Observed in store and forward transformations, this parallelism form encompasses the entirety of an image as the unit of parallel processing. However, it is applicable only when processing a sequence of images.

Once the functionalities in *FIPLib* have been coded, they can be composed through the dataflow modality as described previously. In this way, we obtain a top-level kernel whose signature usually contains the input and output memory banks, the image size, the number of rows and columns, and the number of images (this latter value is used only if we need the coarse-grain pipelining).

As reading from an empty stream or writing into a stream with the FIFO full are blocking operations, care must be put when choosing the size of the FIFOs associated with the streams in case there are convergent paths: wrong FIFO sizing could lead to deadlocks [Bharath,2004], [Jiang,2008]. For example, let's refer to the graph in fig.10 in which data arrive at the *diff* kernel through two different paths ($s3$ comes from *sCopy()* and $s4$ from the *medianFilter()*). If the FIFO of $s3$ is not large enough, the kernel would deadlock: *sCopy()*, at each clock cycle, writes N/S components of the input image on $s2$ and $s3$; the median filter will start writing on $s4$ the processed data only after having received $2r+1$ input lines. As the *diff()* kernel reads in parallel, with blocking read, from $s3$ and $s4$, data will not be consumed from $s3$ till data arrive also at $s4$; if $s3$ FIFO is not large enough, *sCopy()* cannot write on $s3$ and, consequently, on $s2$, because the two write operations are done in parallel. The *medianFilter()* does not receive any more input data, so it is blocked and will never provide $s4$ with the data necessary to unblock the read on $s3$. As filtering kernels forward unchanged the first r lines as soon as they are read, $s2$ should be able to store $r+1$ lines to avoid the just described deadlock situation.

In the general case, correct FIFO sizing is still an open problem and there is not yet a definitive solution. Care must be put in by the designer to ensure that the streams have enough room to store incoming data. The size of the FIFO associated with a stream is set through the HLS STREAM pragma, through the depth parameter.

7 Image processing benchmarks

The *FIPLib* has been used to test different image processing algorithms targeting the Xilinx Alveo U280 FPGA board. The board is hosted in one X86_64 node with 2 x Intel Xeon Haswell CPU and 128 GB RAM, PCIe Gen3x16 and OS CentOS 7.4. We used the Vitis 2022.2 HLS toolchain to compile the *FIPLib* and run the tests.

The first benchmark (*ALGO1*) uses a design like the one in fig.10, with an additional last kernel performing the complement of the image. The test processes images (Rows, Cols) with 8bpp (256 levels of grey). In *ALGO1*, we set the stream width to 32 Bytes through the template parameters *dt32*, $S=8$, and $N=256$.

In *ALGO1*, we set the stream width to 32 Bytes through the template parameters *dt32*, $S=8$, and $N=256$.

The number of operations involved is as follow:

- $loadInput()$, $streamCopy()$ and $storeOutput()$ do not perform any computing operation, being only data movers/copiers.
- $Medianfilter()$ 5×5 requires, for each pixel not belonging to the border of the image ($r = 2$), to find the median value among 25 characters. This can be done with 138 comparisons using the even-odd sorting network [12], which is the algorithm used in *FIPLib* to implement the median filter. Counting one comparison as one 8 bit operation, the number of operations performed by the 5×5 median filter is: $N_{MF} = 138 \times (Rows-2) \times (Cols-2)$.
- Similarly, by counting 2 operations/pixel for the $diff()$ kernel (2 operations because the absolute value of the difference is taking into account) and 1 operation/pixel for the $doNegate()$ kernel, the number of operations for those kernel are: $N_{diff} = 2 \times Rows \times Cols$ and $N_{Negate} = Rows \times Cols$.
- Finally the number of operations of the *ALGO1* is:

$$N_{ALGO1} = 138 \times (Rows-2) \times (Cols-2) + 3 \times Rows \times Cols$$

With images 4096×4096 , *ALGO1* processes one image in $T_{exe} = 3.9$ ms, resulting in a sustained speed of:

$$S = N_{ALGO1}/T_{exe} = 597 \text{ GOP/s}$$

In the following fig.12, reporting the timeline view of an *ALGO1* run processing a sequence of images, we show the pipelined behaviour achieved with proper host synchronization: the read of input image i (pink rectangles) is overlapped with the processing of image $i-1$ (green rectangles) and with the write of output image $i-2$ (violet rectangles).

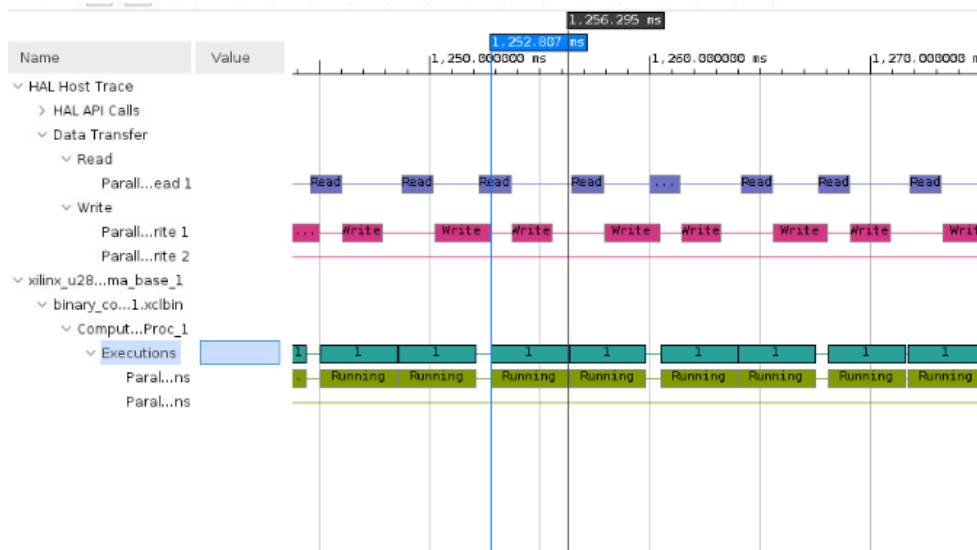


Fig.12: Timeline view of *ALGO1* run

The resources used by the *ALGO1* are reported in Tab.6. *ALGO1* clock frequency is $f_{ck} = 200 \text{ MHz}$. As the number of clock cycles to process one image is $N_{ck} = 7.8 \times 10^4$, *ALGO1* is sustaining:

$$N_{ALGO1}/N_{ck} = 3.2 \times 10^3 \text{ Ops/cycle}$$

	#	%
LUT	70394	6.4%
BRAM	183	10.79%
DSP	12	0.13%

Tab.6: *ALGO1* – Resources used

As *ALGO1* can be fully pipelined, its theoretical minimum execution time is determined by the time required to process the image in an ideal pipeline, where pipeline latency is neglected. This can be calculated using the formula:

$$T_{min} = \frac{Rows \times Cols}{\left(\frac{N}{S}\right)} \times T_{ck} \quad (1)$$

The benchmarks setting are: $Rows=Cols=4096$, $N/S=32$, and $T_{ck}=5ns$ and $T_{min}=2.6 ms$. The *ALGO1* achieves $T_{exe}=3.9 ms$, it demonstrates an efficiency of $\eta=67\%$.

As a second test, the following *ALGO2* has been developed, setting through the template values the stream width to $32B$ and the fine grain parallelism degree $N/S=256/8=32$. The operations performed by the 3 Gaussian filters are given by

$$N_{GF} = 3 \times 97 \times (Rows-3) \times (Cols-3)$$

so that the number of operations of *ALGO2* is:

$$N_{ALGO2} = 291 (Rows-3) \times (Cols-3) + 3 \times Rows \times Cols$$

With images 4096×4096 , *ALGO2* processes one image in 6.9 ms, resulting in a sustained speed:

$$S = N_{ALGO2} / T_{exe} = 714 GOp/s$$

The fig.13 shows *Algo2* graphics and codelet, whilst the usage of the FPGA resources are reported in Tab.7.

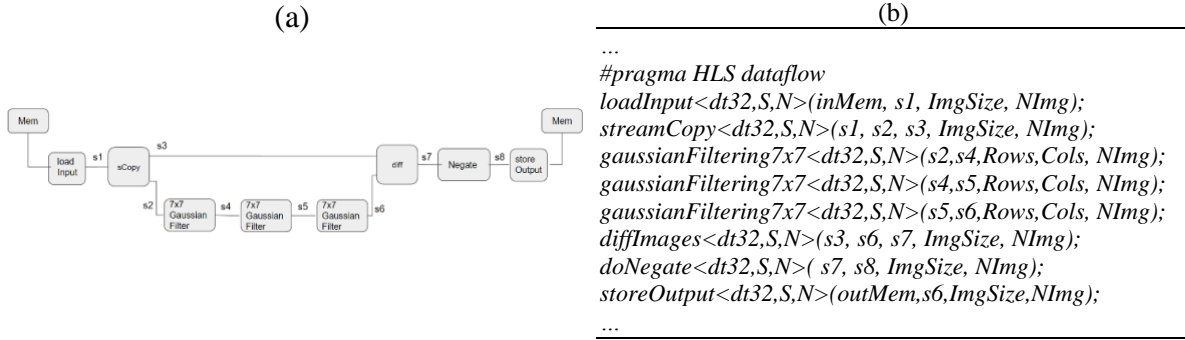


Fig.13: Graphics (a) and Codelet (b) showing *ALGO2*

	#	%
LUT	70977	6.4%
BRAM	1152	67.9%
DSP	6982	77.5%

Tab.7: *ALGO2* – 32B Resources used

Due to the high density of the design (DSP usage close to 80%), *ALGO2* synthesizes at $f_{ck}=100MHz$. As the number of clock cycles to process one image is $N_{ck}=6.9 \times 10^4$, *ALGO2* is sustaining with:

$$N_{ALGO2} / N_{ck} = 7.1 \times 10^3 Ops/cycle$$

To try to increase the clock frequency, *ALGO2* has been configured with the template parameters $dt16$, $S=8$, $N=128$. In this way the streams are narrower (16B instead of 32B) and *BRAM* usage should be reduced as well as the fine grain parallelism degree halves (from 32 to 16), and this should reduce the *DSP* usage. The Tab.8 shows the *ALGO2-16B* FPGA resources used.

	#	%
LUT	42232	3.8%
BRAM	576	34.0%
DSP	3244	36.0%

Tab.8: *ALGO2* – 16B Resources used

As expected, the kernel resource usage nearly halved, and the *ALGO2 – 16B* synthesized at $f_{ck}=200MHz$. In this second case, *ALGO2-16B* processed one 4096×4096 grey image in 7.4 ms, with a slight reduction in performance (7%) but with a significant reduction in the number of resources used. The sustained speed of the *ALGO2-16B* is:

$$S = N_{ALGO2\ 16B} / T_{exe} = 666 GOp/s$$

As ALGO2 can be fully pipelined, its theoretical lower limit for execution time is determined by (1), resulting in $T_{min}=5.2\text{ ms}$ ($Rows=Cols=4096$, $N/S = 16$, $T_{ck}=5ns$). Since *ALGO2-16B* design exhibits $T_{exe}=7.4\text{ ms}$, its efficiency is $\eta=71\%$.

The timeline views in fig. 14 show the overlap between host/FPGA communication and FPGA computation.

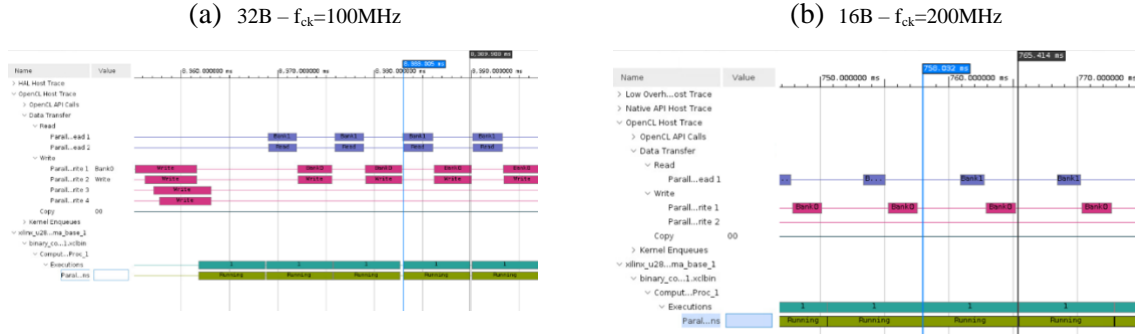


Fig.14: Timeline view of *ALGO2* execution with (a) 32B and (b) 16B configurations

To exploit the unused logic of the 16B implementation of *ALGO2-16B*, two independent replicas of the 16B kernel are instantiated: even if the resource utilization is roughly the same as the 32B kernel, its synthesis is easier, and the two kernels could be synthesized to run at 175 MHz. As we are far from saturating the PCIe bandwidth, two 16B kernels running at $f_2=175\text{ MHz}$ should give a speed-up w.r.t. one 16 B kernel running at $f_1=200\text{ MHz}$ given by:

$$S = 2 \times f_2 / f_1 = 1.5$$

In essence, this replicated configuration should result in a 1.5-fold enhancement in processing speed compared to the scenario of a single 16B kernel running at 200 MHz. The Tab.9 shows the FPGA resources used for *ALGO2-16B* replicated:

	#	%
LUT	94891	8.6%
BRAM	1152	68.7%
DSP	6506	72.2%

Tab.9: *ALGO2* – $2 \times 16B$ replicated Resources used

When running *ALGO2* $2 \times 16B$, the execution time measured is: $T_{Exe\ 2 \times 16B} = 9.2\text{ ms}$ to process two images (images are processed in parallel); the sustained speed of *ALGO2* $2 \times 16B$ is given by:

$$S = 2 \times N_{ALGO2} / T_{Exe\ 2 \times 16B} = 1070\text{ Gop/s}$$

To evaluate the advantages of *FPLib*, two versions of *ALGO1* and *ALGO2* have been implemented on a multicore CPU using OpenCV [13]. The first version processes one image at a time, relying on OpenCV to detect and utilize parallelism; in contrast, the second version explicitly processes 16 images in parallel, thus exposing to the OpenCV library a greater degree of parallelism. To benchmark performance against GPU accelerators, we leveraged the CUDA version of OpenCV to implement *ALGO1* and *ALGO2* on the NVIDIA A100 GPU. Results are summarized in the Tab.10 reporting the execution time to process one 4096×4096 8bpp image (times are derived as the average, computed processing a sequence of 5000 images).

	Execution time (ms)	
	ALGO1	ALGO2
FIPLib	3.9	4.6
OpenCV – 1 image	70.0	137.7
OpenCV – 16 images	6.0	11.1
Cuda openCV	295	5.0

Tab.10: *FIPLib* vs *OpenCV*

It's not clear why the GPU implementation of *Algo1* is performing slowly; this aspect warrants further investigation.

FPGAs are often thought of as computing devices able to reduce power consumption. Let's now try to check

and quantify this aspect through measures on kernels implemented through the *FIPLib*. To quantify the power consumption during a computation, let's consider the energy used by the application to be run, being the energy defined as follow:

$$E_A = \int_0^D P_A(t) dt \quad (2)$$

being D the running time of the application, and

$$P_A(t) = P(t) - P_{Idle}$$

the power used by the application at time t , computed as difference between the node instant power and the power absorbed by the node when no user processing is running. To perform the power measurements, we accessed the Baseboard Management Controllers (BMCs) of the computing node through the Intelligent Platform Management Interface (IPMI): in this way, with a sampling period of 1 s, we can read the instant power absorption of the node.

To evaluate (2), a first estimate of P_{Idle} has been done, measuring the instant power absorbed when there are no user processes running, then we take the instant power measurements, along the application run, to compute E_A .

Fig. 15 reports the measures for $P_A(t)$ obtained when running ALGO2 to process 2000 images: *i*) on CPU one image at a time and in groups of 16 images (all processed in parallel), *ii*) on FPGA with design using 32B streams, $f_{ck}=100$ MHz, design using 16B streams and $f_{ck}=200$ MHz, and the design replicating twice the kernel with 16B streams, each with $f_{ck}=175$ MHz.

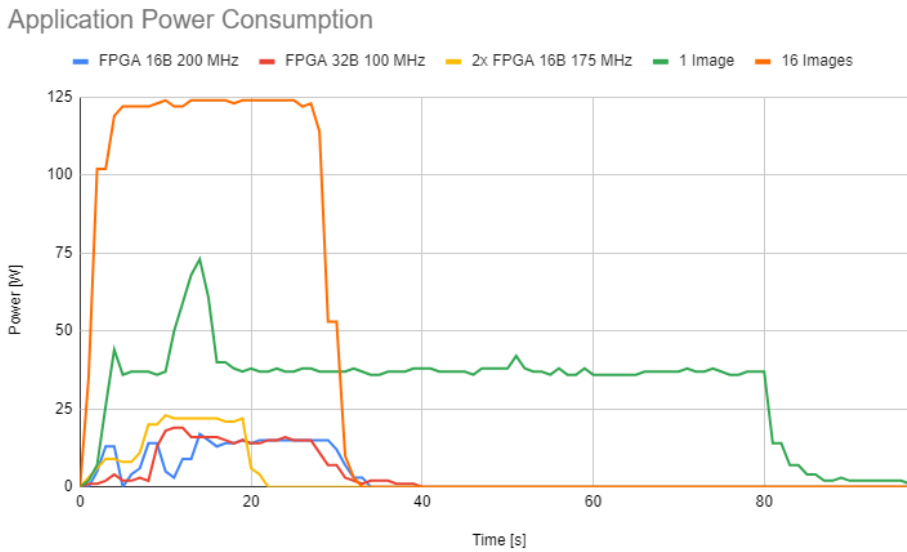


Fig. 15: $P_A(t)$ for ALGO2 executed on 1 or 16 CPU cores and on FPGA using 1 kernel with 32B or 16B streams and 2 16B kernels

The values for E_A and the computing times are reported in Tab.11 (computing time includes FPGA programming time, filesystem accesses, and all the needed initializations). While the three FPGA designs consume roughly the same amount of power, there are notable differences in processing time. Specifically, the design with two kernels clocked at 175 MHz stands out as the fastest. Additionally, FPGA implementations outperform CPU implementations in both energy efficiency and speed, either being faster or at least equal in speed.

	Energy used by ALGO2 run (J)	Time used by ALGO2 run (s)
FIPLib 32B, 100 MHz	353	39
FIPLib 16B, 200 MHz	357	31
FIPLib 2x16B, 175 MHz	323	21
CPU OpenCV – 1 image	3102	97
CPU OpenCV – 16 images	3426	32

Tab.11: Energy and Time to process 2000 images

To compare the different implementations, we use the *Energy Delay Product (EDP)* [14]:

$$EDP = E_A \times D \quad (3)$$

EDP [Js] considers both the energy consumed by the application and its execution time. Using EDP, we can distinguish between two designs that consume the same amount of energy by identifying the faster one. A smaller EDP indicates a more efficient design implementation.

EDP values derived from the measures shown in Tab.11 for *ALGO2* are reported in Tab.12 and are depicted in fig.16.

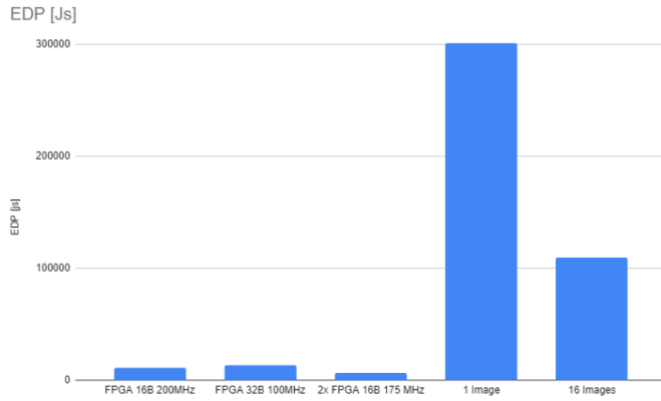


Fig.16: EDP for different implementations of ALGO2

Tab.12: EDO processing 2000 images	
	ALGO2 EDP [Js]
FIPLib 32B, 100 MHz	13767
FIPLib 16B, 200 MHz	11067
FIPLib 2x16B, 175 MHz	6783
OpenCV – 1 image	300894
OpenCV – 16 images	109632

The previous table shows the best FPGA design for *ALGO2* (i.e. 2x16B) improves the best CPU design by a factor:

$$\frac{EDP_{Best\ CPU}}{EDP_{Best\ FPGA}} = \frac{109632}{6783} = 16.2$$

as the best FPGA design uses 10.6 times less energy and is 1.5 faster than the best CPU implementation. FPGA implementations of *ALGO2* clearly outperform the CPU counterparts, as they use less energy and are either faster or comparable in run time.

As aforementioned the FPGA designs for *ALGO2* (32B and 16B) are nearly equivalent in runtime and energy usage, so their *EDPs* are nearly similar. But the two designs are not equivalent, because the two implementations significantly differ in resource usage (see Tabs. 7 and 8). Should this aspect be relevant (some free resources could be used to implement some other functionality), we can introduce the usage of resources in the ranking, being the design implementations targeting the same type of FPGA. Let's indicate with

$$F = 1 - \max(LUT\%, BRAM\%, DSP\%)/100 \quad (4)$$

the free fraction of the most used FPGA resource. Other than energy and computing time, we introduce the fraction of free resources *F* into the ranking, through the *Energy Delay and Free resources Product (EDFP)* depicted in fig.17 for *ALGO2* 16B and 32B:

$$EDFP = E_A \times D \times (1 + F) \quad (5)$$

We sum 1 to F to avoid the ranking going to zero when the design uses very few resources; in fact, the free resource term should play a role only when different FPGA designs have nearly the same EDP value. Using (5) to compare the two FPGA designs of *ALGO2*, the 16B implementation emerges as the preferable, due to its higher fraction of unused logic.

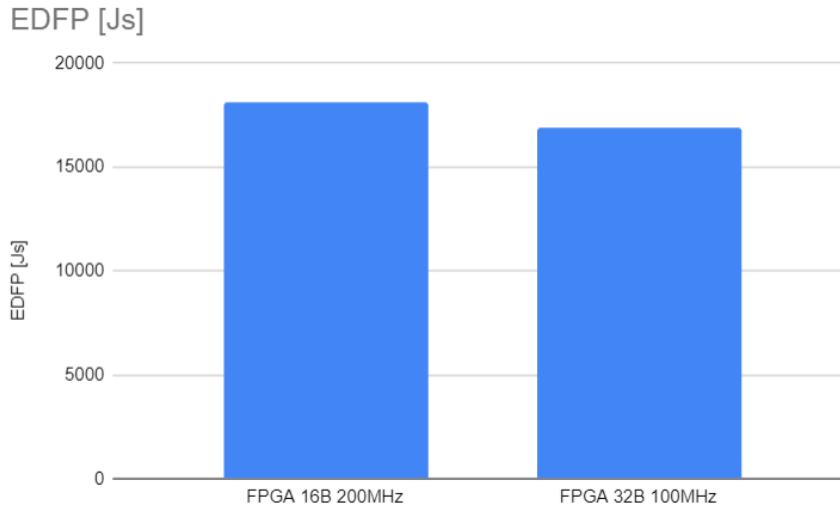


Fig.17: EDPF for the two FPGA implementations of *ALGO2*

The final benchmarks, aimed for comparing the FPGA design to the GPU implementation, we processed 20,000 images with dimensions of 4096×4096 pixels and a color depth of 8 bits per pixel using *ALGO2*. It was implemented on both FPGA with two replicated kernels (*FIPLib* $2 \times 16B$, 175 MHz) and on the GPU using CUDA functions from OpenCV. To ensure a fair comparison and eliminate host node-related differences, only the power consumption of the accelerator boards (ALVEO U280 and NVIDIA A100) has been measured during the processing phases, excluding the FPGA configuration and environment initialization. The fig.18 plots the instant power consumption of both the FPGA and GPU boards during the computation. While the computing times are nearly equivalent (with FPGA being slightly faster), there is a significant difference in energy consumption. Specifically, the GPU board consumes 5.4 kJ, whereas the FPGA board consumes only 0.74 kJ. The EDP values for this case are $EDP_{GPU} = 530$ [kJ/s] and $EDP_{FPGA} = 67$ [kJ/s].



Fig.18 $P_A(t)$ for *ALGO2* executed on FPGA and GPU when processing 20000 4096×4096 8bpp images

We would have liked to compare *FIPLib* with the AMD Vision Library. However, we were unable to compare *ALGO1* and *ALGO2* with the AMD Vision Library because it lacks support for the U280 board. Furthermore, this library only supports pixel parallelism values of 1 and 8. Given our focus on maximizing pixel parallelism, our tests could not align with the library's capabilities.

8 Conclusions

The benchmarks result carried out in this work shows the computing performances of heterogeneous architectures of processors able to improve the energy efficiency of the next generation of the HPC exascale supercomputers. In particular the benchmarks result have shown the low performances in the parallel linear algebra application field of the current technologies of Xilinx FPGA, respect to GPUs and conventional CPUs, whilst that technology is able to support today's demanding HPC data centers in AI application fields, such as image processing, proving to be high-performing and highly energy-efficient.

Acknowledgements

This work is partially supported by the EuroHPC JU and the Italian Ministry MIMIT (ex MiSE) under GA 956831 "Towards EXtreme scale Technologies and Accelerators for euROhpc hw/Sw Supercomputing Applications for exascale (TEXTAROSSA)".

References

- [1] Jamro, Ernest et al. "The Algorithms for FPGA Implementation of Sparse Matrices Multiplication." *Comput. Informatics* 33 (2014): 667-684.
- [2] <https://www.netlib.org/blas/>
- [3] <https://www.netlib.org/lapack/>
- [4] M. Meyer, T. Kenter and C. Plesl, "Evaluating FPGA Accelerator Performance with a Parameterized OpenCL Adaptation of Selected Benchmarks of the HPCChallenge Benchmark Suite," 2020 IEEE/ACM International Workshop on Heterogeneous High-performance Reconfigurable Computing (H2RC), GA, USA, 2020, pp. 10-18, doi: 10.1109/H2RC51942.2020.00007.
- [5] J. M. de Haro, J. Bosch, A. Filgueras, M. Vidal, D. Jiménez-González, C. Álvarez, et al., "OmpSsFPGA framework for high performance FPGA computing", *IEEE Trans. Comput.*, vol. 70, no. 12, pp. 2029-2042, Dec. 2021.
- [6] J.de Fine Licht et al: "Flexible Communication Avoiding Matrix Multiplication on FPGA with High-Level Synthesis", *FPGA '20: Proceedings of the 2020 ACM/SIGDA International Symposium on Field-Programmable Gate Arrays*, February 2020.
- [7] <https://www.jedec.org/standards-documents/docs/jesd235a>
- [8] S. Soldavini, K. F. A. Friebe, M. Tibaldi, G. Hempel, J. Castrillon, and C. Pilato, "Automatic creation of high-bandwidth memory architectures from domain-specific languages: The case of computational fluid dynamics,". *ACM Trans. Reconfigurable Technol. Syst.*, 09 2022.
- [9] Special Issue of the *Journal of Imaging* on "Image Processing Using FPGAs", Special Issue Editor Donald G. Bailey, 2019.
- [10] Vitis Vision Library, https://xilinx.github.io/Vitis_Libraries/vision/2022.1/index.html
- [11] Kalms, L., Podlubne, A., Göhringer, D. (2019). HiFlipVX: An Open Source High-Level Synthesis FPGA Library for Image Processing. In: Hochberger, C., Nelson, B., Koch, A., Woods, R., Diniz, P. (eds) *Applied Reconfigurable Computing. ARC 2019. Lecture Notes in Computer Science()*, vol 11444.
- [12] K.E. Batcher: *Sorting Networks and their Applications*. Proc. AFIPS Spring Joint Comput. Conf., Vol. 32, 307-314 (1968).
- [13] <https://opencv.org/>
- [14] Xizhou Feng, Rong Ge, K.W. Cameron: *Power and Energy Profiling of Scientific Applications on Distributed Systems*. . Proceedings. 19th IEEE International Parallel and Distributed Processing Symposium, 2005.

KNOWLEDGE SHARING IN AGRICULTURE 4.0

Daniela Alderuccio^{1*}, Rossana Cotroneo²

¹ ENEA – TERIN-ICT-HPC – Rome, Italy¹

² ENEA – ISV-MARK- Rome, Italy

ABSTRACT. Knowledge flows across boundaries. The dynamics of knowledge has an interactive nature. Agriculture 4.0 shows different type of knowledge: *Scientific* vs local, tacit, and experiential *Farmer Knowledge*. The two forms of knowledge are related. Their merging is relevant to overcome wariness toward scientific and governmental institutions in achieving farmer adoption of new technologies. The participation and engagement of the farming community (in collaboration, co-designing, and co-construction with scientists, researchers, economists, and regulators) is crucial. Knowledge in Agriculture 4.0 flows from Farmer as first-data producer through intermediary data platforms and returns to Farmer as main user of data and farm-tailored services, in turn producing new data to be implemented. Shifting perspective from stakeholders' traditional roles in the farm-to-fork supply chain to the roles in data supply chain highlights barriers for farmer in data access, control and sharing activities. Neutral intermediary data platforms play a relevant role also in gaining farmers' trust on data sharing and re-use. Trust is one of the key concepts for data altruism for data, information and knowledge sharing. In this paper we also present a case study on demand and supply water management. Results show how a positive feedback loop in the data supply chain generates competitive advantage, respecting all access-seekers' rights, and find solutions to the asymmetry in information access.

1. Introduction

Agriculture is mainly determined by natural and biological factors. The paradigm 4.0 is a strategy relying on digital and ubiquitous connectivity (enabled by various technologies) to transform processes, products, and services through real-time and decentralized decision-making. The term '4.0' has been applied to a variety of fields [1], including Agriculture 4.0, representing the impact of this technological innovation (Artificial Intelligence, Big Data and the Internet of Things). Agriculture 4.0 can be defined as the evolution to connected knowledge-based farm production systems. It also shares technologies and enjoys the benefits arising from knowledge coming from big data.

According to the “Smart Agriculture Market Size, Share Global Analysis Report, 2022 – 2028”², in 2021 the smart agriculture business was estimated at USD 17,392.40 million at worldwide level and it is estimated to grow to USD 29,653.81 million by 2028, with a compound annual growth rate (CAGR) of approximately 9.30% over the forecast period.

The use of knowledge generated by data analytics creates value for the agricultural sector. There is a resistance from micro, small and medium farm to provide data due to the data sharing concerns, access control policies and to high input costs.

Agricultural land use generates impacts on different natural resources. Water is one of these components. Farmer and Land Manager Knowledge is at the basis of designing integrated and sustainable approaches to land management. This tacit knowledge generates large quantities of data. Eliciting this Farmer tacit local-level knowledge enables to generate model rules relating to farm enterprise types and help to discern farming practices likely to impact on rural economy and environmental quality. Valuing farmers' knowledge enables a more integrated approach to land and water management and assists in resolving agriculturally derived issues. The participation and engagement of the farming community, in collaboration, co-designing and co-construction with scientists, researchers, economists and regulators, is vital.

¹ Corresponding author. E-mail: daniela.alderuccio@enea.it

² <https://www.fnfresearch.com/>

2. Agricultural Knowledge

Knowledge has a fluid and interactive nature well defined by the notion of “Knowledge-Cultures” [2] explaining the concept of merging different knowledge forms. Agriculture 4.0 shows different kind of Knowledge: *Scientific* vs local *Farmer Knowledge*. The two forms of knowledge are related. Farmer’s knowledge is embedded in social and cultural relations. Farmers’ knowledge is experiential and is related to and integrated with other form of knowledge (such as scientific knowledge). It is crucial to understand and consider Farmer’s Knowledge to avoid both farmers’ loss of trust in scientific and government institutions, and difficulties for authorities in achieving farmer engagement or adoption. An example of harmonizing Knowledge-cultures is offered by local land knowledge. Problems may arise in the comparison of folk vs scientific classification or denomination, to improve soil classification, mapping, modelling accuracy, and reaching semantic interoperability. Trust is one of the key concepts for data altruism for data and knowledge sharing.

Farmers and Land managers are custodians of tacit local knowledge. This tacit knowledge generates large quantities of data. Their knowledge and experience grounds in everyday land management practices. This expert knowledge at local level is only partially accessible through scientific observation [3] and problems might be missed by specialist scientific knowledge. Local farmer knowledge is different from standard *Scientific Knowledge*: science tends to be independent of social and local contexts, yet agriculture is defined both by its biophysical context and its localized socio-economic and political elements. Farmer knowledge is based upon the interdependent accumulation of local, natural, and socio-economic knowledge resources and practices. It is embedded in local ecosystems and is encoded in local and regional cultures rather than in abstract notions.

3. Big Data in Agriculture 4.0

The digitalization of agricultural data turns raw data in information and then into knowledge. Agriculture data is big data and the main relevant characteristics are *velocity* and *variety* [4] Agriculture 4.0 needs real-time data for real-time decisions, due to the perishability and seasonality of products. It is based on the integration process of quality and accuracy datasets from different official sources (taking into account the type of data and their privacy level): private data (e.g. owners’ private information, farm data); public data (e.g. meteorological data, utilised agricultural area (UAA)³, Agricultural area (AA), agricultural crops [5],[6], including administrative data - income, taxations, etc.- ; product data (production-related data, seasonal production); innovation data (novel techniques, innovation processes, patents, licensing, etc.). None of them alone captures the complexity of creating value through data but how data is characterized points to different regulatory perspectives and outcomes. It needs to underline the data collection process from these different sources also considers different times scales: e.g., meteorological data are filled out continuously, but crop data are filled every year and at municipality level every 10 years during Agricultural Census or through Corine land cover data⁴, or remote sensing data. The end-users (the farmers) need continuous data for their activities; thus the data collection process should be provided to them through technological applications (IoT, devices, drones, etc.).

Accessing data is critical both for farmers and for those generating product/services, training algorithms, etc. Data access problems are mostly related to the exclusive control of farm data and proprietary datasets. There is a problem of trust. In Agriculture 4.0 there is a feedback loop: more data from farmer means better-trained algorithms, and more precise services; more services attract more users, generating additional data sets and better farm-tailored services. The benefits of sharing data and providing agri-business models move into an era of digitally enhanced farming.

Agriculture 4.0 faces the challenge of having connectivity, data exchange and communication standards, linking different systems in a unifying network, covering all aspects of agricultural exploitation. Data exchange and analysis is the key to the success of Agriculture 4.0 (EU Common Agricultural Data Space⁵). It is mandatory that people have awareness of the importance of data. Local Farmers’ willingness to invest in new technologies to innovate their practices of production faces limited investment ability and limited access to credit, in comparison with stronger stakeholder, holding a dominant position in the agricultural economic

³ [https://ec.europa.eu/eurostat/statistics-explained/index.php?title=Glossary:Utilised agricultural area \(UAA\)](https://ec.europa.eu/eurostat/statistics-explained/index.php?title=Glossary:Utilised_agricultural_area_(UAA))

⁴ <https://sdi.eea.europa.eu/catalogue/geoss/api/records/71c95a07-e296-44fc-b22b-415f42acdf0>

⁵ <https://digital-strategy.ec.europa.eu/en/library/common-european-data-spaces-agriculture-and-mobility>

ecosystem. In the EU, data sharing is limited due both to technical obstacle and low trust in data sharing, and re-use of public data and data collection for common good.

4. Case Study on Water

In our case study we analysed Agriculture Knowledge Sharing process applied to demand and supply of water for agroecosystems [7] [8]. This process is showed as follows:

From FARMER (first-data producer) → Intermediary data platform (from data collecting to elaborated data in the platform) ⁶→ to FARMER (main knowledge user through Iot services)

Farmer Knowledge Sharing → Optimising Agricultural Activities → Improving Income

Agriculture Knowledge Sharing leads to a more efficient use of irrigation; its planning is not only based on climatic data (mainly precipitation), but also based on water demanded by the crop considering physic and biologic parameters and technology innovation (e.g., sprinkling vs. drop system). Thus, it should be possible to manage irrigation scheduling efficiently and effectively, maintaining or increasing the irrigation regime appropriately and thus avoiding problems of aridity and soil erosion and moving towards quality production. The research is on-going, and the results will be published in an article.

5. Conclusions

A global socio-technical transition towards digital agricultural information systems is underway. The impact of this transition engages research, agricultural firms, and stakeholders. Sharing Knowledge awareness and negotiation mitigate risks for the future, allowing the interconnected evolution of the network of players/stakeholder in the Agricultural (Digital) Ecosystem, and according to “Altruism” principle in the Digital Governance Act (from 24 September 2023)⁷ that encourages the data sharing for altruistic purposes and regulate the re-use of publicly held protected data. It enhances trust in voluntary data sharing for the benefits of citizens and business and agricultural activities. Neutral Intermediary data platforms play a relevant role also in gaining farmers’ trust on data sharing and re-use. ENEA supports the Italian partners in information services to support farmer activities and decision making, with the Open IACS Project⁸ facilitating end-user access to HPC capabilities.

Farmers request an equal, fair, easy access to their microdata and to new product/services based on agricultural data (cf. case studies on water). Otherwise, unfair competitive advantage may arise due to unequal access to information.

Siloed data depreciate compared to data connected to a supply network; data collecting and sharing benefit every stage of the supply chain, increasing efficiency, lowering costs, and optimising the resources. Data is used to interpret the past and to help predicting the future, to make more timely or accurate decisions, [9].

For farming 4.0 is essential a modern ICT infrastructure in rural areas.

For a successful transformation of agricultural processes toward Agriculture 4.0 essential is the ability to extract knowledge from structured and unstructured data along the agricultural supply chain, connecting real/physical world and its digital representations. It’s a new digital farming model based on the artificial intelligent techniques for data analysis from the entire supply chain, driving precision farming and transforming it into smart agriculture. The farmers must be able to adapt autonomously and in real-time to changes to remain competitive on the market, and to become smart farm.

References

⁶ <https://statswiki.unece.org/display/GSBPM/GSBPM+v5.1>

⁷ <https://digital-strategy.ec.europa.eu/en/policies/data-governance-act>

⁸ ENEA started in 2019 the OpenIACS Project (Open LOD Platform based on HPC capabilities for Integrated Administration and Control System of Common Agrarian Policy). The project will provide an open community platform for sharing solutions in the IACS domain through the Linked Open Data (LOD) Paradigm. a Project, co-financed by the European Union (H2020 Connecting Europe Facility 2014-2020, CEF TELECOM CALL for PROPOSALS 2018, CEF-TC-2018-5). The Project started in September 2019 and lasts 4 years (2019-2023) and has a total cost of about 4.5Meuro: CEF contribution 75%. <https://open-iacs-project.com/>

- [1] Alderuccio D. & Cotroneo R. Data Analytics in Health 4.0: Extracting Knowledge from Big Data in Pandemic Times”. in *High Performance Computing on CRESCO Infrastructure: Research Activities 2021*, pp. 29-33, ENEA, December 2022 – ISBN 978-88-8286-440-8 (2022)
- [2] V. Higgins et al., Ordering Adoption: Materiality, Knowledge, and Farmer engagement with precision agriculture technologies. In *Journal of Rural Studies* 55 (2017) pp. 193-202 (2017) – DOI: <https://doi.org/10.1016/j.jrurstud.2017.08.011> (2017)
- [3] Oliver et al. Valuing local knowledge as a source of expert data: Farmer engagement and the design of decision support systems. In *Environmental Modelling & Software* 36, pp, 76-85 (2012)
- [4] S. Osinga et al. Big Data in Agriculture: Between opportunity and solutions. In *Agricultural Systems* 195 103298 (2022)
- [5] ISTAT. Indicatori Agro-Ambientali (AEIs). Anni 2010-2019 (27 maggio 2021)
- [6] ISTAT. 6° Censimento Generale dell’Agricoltura (2010).
- [7] R. Cotroneo. Valutazione dei servizi ecosistemici idrologici in aree rurali: analisi spazio-temporale in quattro comuni del territorio pontino (Phd. Thesis, 11/11/2016).
- [8] J. Maes et al. Mapping and assessment of ecosystems and their services: An EU wide ecosystem assessment in support of the EU biodiversity strategy. (2020).
- [9] L. Klerkx. A review of social science on digital agriculture, smart farming, and Agriculture 4.0: New contributions and a future research agenda. In *NJAS – Wageningen Journal of Life Sciences* 90-91 100315 (2019)

ENEA-REG (v2.0), A REGIONAL EARTH SYSTEM MODEL FOR DYNAMICAL DOWNSCALING OF CMIP6 MODELS OVER THE MED-CORDEX REGION

Alessandro Anav¹, Marta Antonelli¹, Sandro Calmanti¹, Adriana Carillo¹, Franco Catalano¹,
Alessandro Dell'Aquila¹, Roberto Iacono¹, Salvatore Marullo¹, Ernesto Napolitano¹,
Massimiliano Palma¹, Giovanna Pisacane¹, Gianmaria Sannino¹, Maria Vittoria Struglia¹

¹ *Italian National Agency for New Technologies, Energy and the Environment (ENEA), Rome, Italy.*

ABSTRACT. In the framework of the coordinated regional modeling initiative Med-CORDEX (Coordinated Regional Climate Downscaling Experiment), we present an updated version of the regional Earth System Model ENEA-REG designed to downscale, over the Mediterranean basin, the models used in the Coupled Model Intercomparison Project (CMIP6). The regional ESM includes coupled atmosphere (WRF), ocean (MITgcm), land (Noah-MP, embedded within WRF), and river (HD) components with spatial resolution of 12 km for the atmosphere, 1/12° for the ocean and 0.5° for the river rooting model.

For the present climate, we performed a hindcast (i.e. reanalysis-driven) and a historical simulation (GCM-driven) over the 1980-2014 temporal period. The evaluation shows that the regional ESM reliably reproduces the mean state, spatial and temporal variability of the relevant atmospheric and ocean variables.

1. Introduction

The climate in the Mediterranean region is characterized by the interplay between midlatitude and subtropical circulation regimes with local air–sea interactions that can substantially influence both the regional climate and the Mediterranean Sea circulation.

Despite Earth system models (ESMs) represent an important source of climate information for the regional scale, regional climate models (RCMs) allow to better represent the complex phenomena that emerge at higher resolutions, especially over regions of complex orography or with heterogeneous surface characteristics, such as the Mediterranean basin. As matter of fact, the last IPCC (Intergovernmental Panel on Climate Change) Assessment Report (AR) acknowledged that regional climate information for impacts and risk assessment is increasingly robust and mature to feed climate services and impacts studies with the higher resolution they need. On the other hand, local information on climate change impacts produced by global models should be considered with some caution. For these reasons, different regional climate models have been developed and used to study both present and future Mediterranean climate systems within a Coordinated Regional Climate Downscaling Experiment (CORDEX) protocol ensuring that model simulations are carried out under similar conditions. In the framework of the CORDEX program, regional climate model simulations dedicated to the Mediterranean area belong to the Med-CORDEX initiative [1]. One of the objectives of this initiative is to explicitly represent the intense air-sea interactions that characterize the Mediterranean region, by developing ocean-atmosphere coupled models aimed at improving the performance of local information at climatological scales and provide reliable future projections.

Here we developed an improved version of the regional Earth system model ENEA-REG [2] specifically designed to downscale the models of the Coupled Model Intercomparison Project (CMIP6) over the Mediterranean basin.

2. Model description

The ENEA-REG [2] is a regional ESM comprising multiple modeling components, namely the atmosphere, ocean, land, and river routing, designed for high-resolution climate studies and applications. The data exchange, regridding, and interpolation among model components are facilitated by the utilization of the RegESM coupler [3]. RegESM is based on the Earth System Modeling Framework (ESMF) library, specifically version 7.1, and the NUOPC (National Unified Operational Prediction Capability) layer to establish interconnections, synchronization, and horizontal grid interpolation among the various model components.

ENEA-REG is based on the Weather Research and Forecasting (WRF version 4.2.2) to simulate the atmosphere dynamic, the Massachusetts Institute of Technology General Circulation Model (MITgcm version z67) to represent the ocean state and circulation, while the Hydrological Discharge (HD version 1.0.2) model is used to simulate freshwater fluxes over the land surface and to provide a river discharge to the ocean model. Compared to the first version of the ENEA-REG [2], here we use an updated WRF version that employs hybrid vertical levels instead of sigma-p vertical coordinates and the microphysics is simulated with a double moment scheme. The main improvement in the ocean model is represented by the introduction of the full non-linear free-surface formulation. The ocean boundary conditions are consistently changed with the inclusion of monthly sea level fields. In addition, temperature and salinity profiles at the boundary are also prescribed as monthly means rather than climatological values. Nile and Black Sea are prescribed as climatological monthly means, while the initial condition for the starting month (August) has been derived from the hindcast simulation performed using the previous version of the ocean model, after computing the monthly climatological averages for the temperature and salinity fields.

As in the original version, the atmospheric and the ocean model exchange sea surface temperature (SST), surface pressure, wind components, freshwater (evaporation – precipitation) and heat fluxes. Unlike the previous version, here the net heat flux is computed from net longwave, net shortwave, latent heat, and sensible heat fluxes, while we provide the shortwave radiation as a separate term able to penetrate the ocean. Furthermore, the hydrological model uses surface and sub-surface runoff, provided by WRF, to compute the river discharge and exchanges this field with the ocean component to close the water cycle. Table 1 summarizes the fields exchanged from the different model components. The coupling time step between the ocean and the atmosphere is set to 3-hours, while the coupling with the hydrological model is set to 1-day.

The model domain covers the Med-CORDEX region, as shown in Figure 1. The horizontal resolution of the atmospheric and ocean components is 12 km and $1/12^\circ$ (approximately 10 km) respectively, while the river routing model is implemented on a regular grid of 0.5° .

In this study we have performed a hindcast simulation initialized and forced by the ERA5 and ORAS5 reanalysis for the atmospheric and ocean components, respectively. In addition, an historical simulation using CMIP6 data has been downscaled; in particular we have selected the CMIP6 MPI-ESM1-2-HR as driving model; it is characterized by the following configuration: T127 (0.93° or ~ 103 km) for the atmosphere and TP04 (0.4° or ~ 44 km) for the ocean. Both the present-climate experiments cover the period 1st August 1980-31st December 2014.

Field	From	To	Notes
Sea surface temperature	MITgcm	WRF	Temperature at first ocean model level
Zonal wind	WRF	MITgcm	-
Meridional wind	WRF	MITgcm	-
Freshwater flux	WRF	MITgcm	Given as evaporation minus precipitation
Solar heat flux	WRF	MITgcm	Downward shortwave radiation considered as penetrative component of the air-sea heat flux

Non-solar heat flux	WRF	MITgcm	Non-penetrative component of the air-sea heat flux computed from longwave radiation, sensible and latent heat fluxes
Atmospheric surface pressure	WRF	MITgcm	-
Surface runoff	WRF	HD	From the NOAH-MP land model
Subsurface runoff	WRF	HD	From the NOAH-MP land model
Discharge at the river mouth	HD	MITgcm	Remapped and spread over the MITgcm gridpoints

Table 1. List of the variables exchanged through the RegESM coupler between the different model components. The coupling time step between the ocean and the atmosphere is set to 3-hours, while the coupling with the hydrological model is set to 1-day.

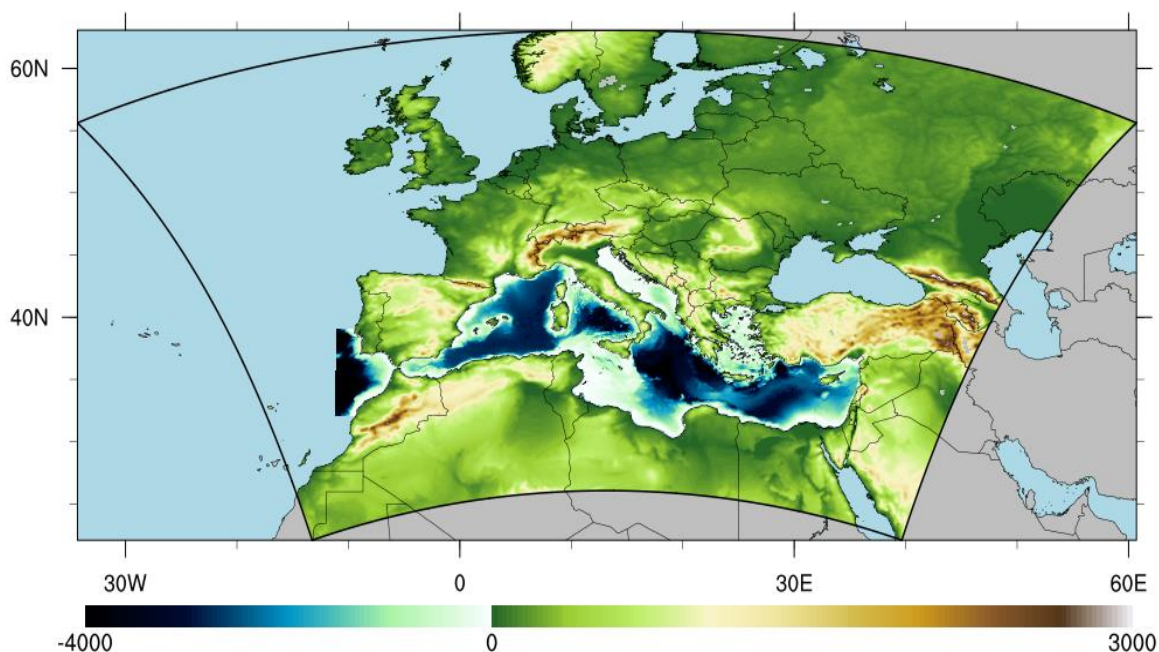


Figure 1. Domain used for the ENEA-REG simulations; the area defined by the black solid line represents the computational domain of the atmospheric model, with green shading highlighting the topography. The ocean domain is defined by the blue shading, used to represent bathymetry.

3. Results

In this section we present the validation of the ocean component of ENEA-REG; in particular, we show its capability of reproducing relevant fields, such as sea surface temperature (SST) and salinity, of the Mediterranean basin.

Considering the SST, we compare mean seasonal climatologies from the hindcast and historical ENEA-REG experiments with satellite-based observations; this latter is a daily, satellite retrieval reconstruction of SST, with a spatial resolution of 0.05° that is available through the portal of the Copernicus Marine Service (CMEMS; <https://marine.copernicus.eu/access-data>).

Figure 2 highlights a similar spatial distribution of the SST bias between the hindcast and the historical simulations, although this latter is systematically colder than the hindcast. Besides, both for the hindcast and for the historical run, the bias is positive during winter and negative in summer, implying a reduction in the amplitude of the seasonal cycle of the downscaling experiments with respect to the observations. On the other

side, the driving global ESM exhibits a less uniform pattern, with areas showing cold and warm biases during all the seasons; this is likely due to the insufficient representation of small-scale features which promotes large local differences with respect to satellite data.

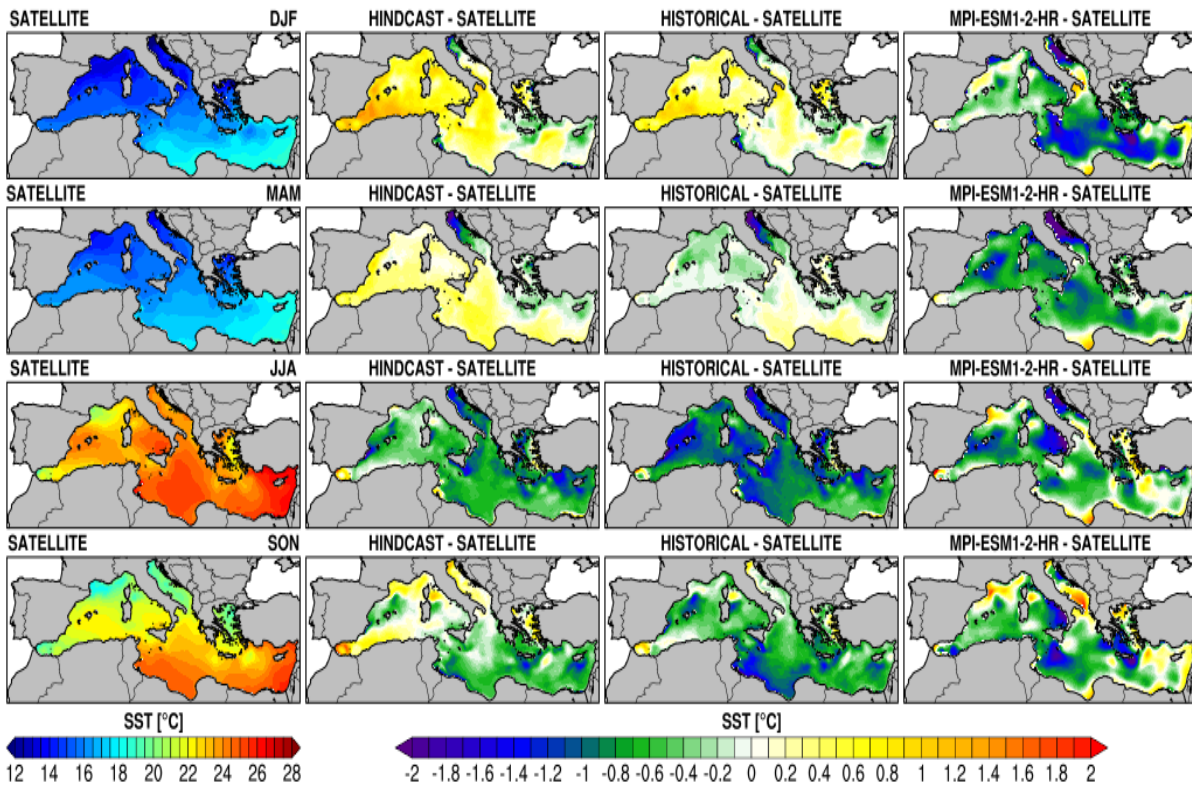


Figure 2. Comparison of seasonal sea surface temperature from satellite data, the ENEA-REG hindcast and historical experiments and the MPI-ESM1-2-HR model. Seasonal averages are computed in the temporal period 1982–2014.

Considering the sea surface salinity, results highlight a remarkable ability of the ocean model to realistically represent the spatial and temporal variability of the salinity in the Mediterranean sea; conversely, the driving CMIP6 model systematically underestimates the salinity with a bias larger than 1 g/kg.

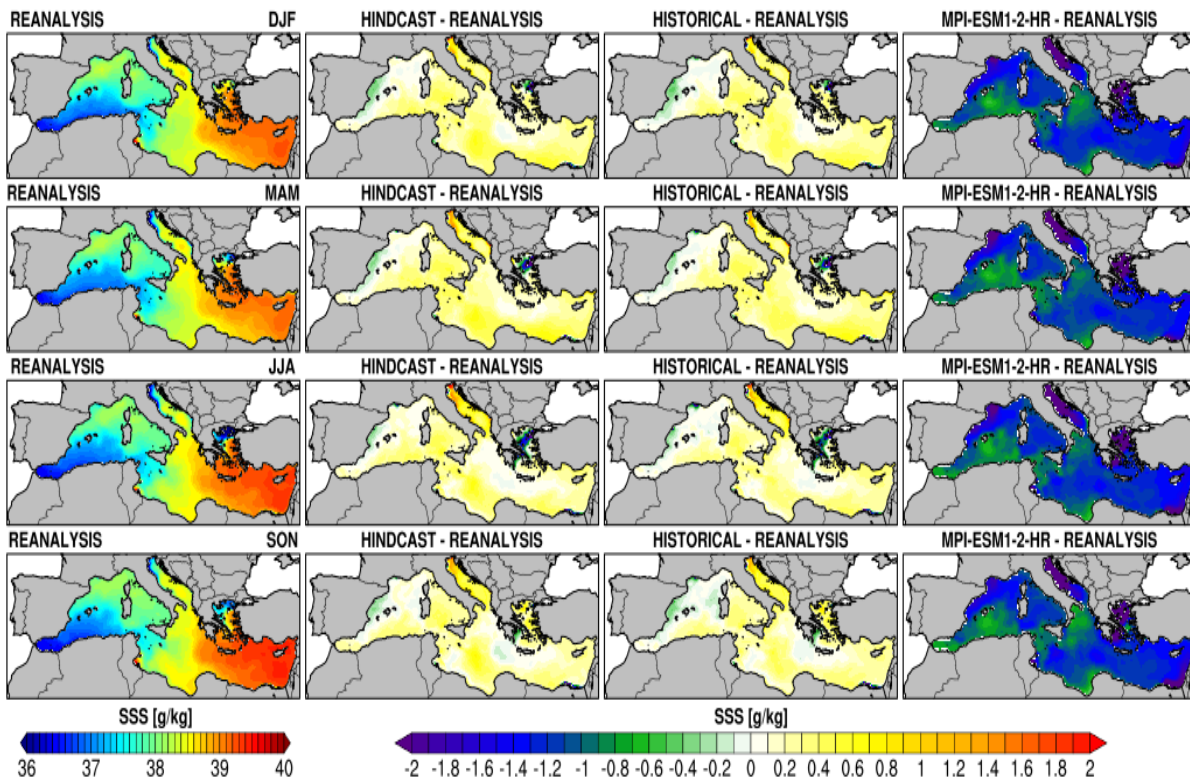


Figure 3. Comparison of seasonal sea surface salinity from satellite data, the ENEA-REG hindcast and historical experiments and the MPI-ESM1-2-HR model. Seasonal averages are computed in the temporal period 1982–2014.

4. Conclusions

We presented an improved version of a regional ESM [4] designed to represent the present and future climate variability over the Euro-Mediterranean basin, a well-known hot-spot region for climate change. The new version of the model goes in the direction of adhering to the Phase3 Med-CORDEX protocol. In particular, we have adopted the mandatory resolutions of the new protocol, for both atmosphere and ocean. We believe our results can contribute to the ensemble of climate projections over the Euro-Mediterranean region.

Acknowledgments

This study was carried out within:

ICSC Italian Research Center on High-Performance Computing, Big Data and Quantum Computing and received funding from the European Union Next-GenerationEU (National Recovery and Resilience Plan – NRRP, Mission 4, Component 2, Investment 1.4 – D.D: 3138 16/12/2021, CN00000013)

RETURN Extended Partnership and received funding from the European Union Next-GenerationEU (National Recovery and Resilience Plan – NRRP, Mission 4, Component 2, Investment 1.3 – D.D. 1243 2/8/2022, PE0000005)

CoCliCo (Coastal Climate Core Service) research project which received funding from the European Union’s Horizon 2020 Research and Innovation Programme under Grant agreement No. 101003598.

CAREHeat (deteCtion and threAts of maRinE Heat waves) project, funded by the European Space Agency (ESA, grant agreement no. 4000137121/21/I-DT)

References

- [1] P. Ruti, S. Somot, F. Giorgi, C. Dubois, E. Flaounas, A. Obermann, A. Dell'Aquila, G. Pisacane, A. Harzallah, E. Lombardi (2016). MED-CORDEX initiative for Mediterranean climate studies. *Bulletin of the American Meteorological Society* 97 (7):1187-1208
- [2] A. Anav, A. Carillo, M. Palma, M.V. Struglia, U. Turuncoglu, G. Sannino (2021). The ENEA-REG system (v1. 0), a multi-component regional Earth system model: sensitivity to different atmospheric components over the Med-CORDEX (Coordinated Regional Climate Downscaling Experiment) region. *Geoscientific Model Development* 14 (7):4159-4185
- [3] U. Turuncoglu U (2019) Toward modular in situ visualization in Earth system models: the regional modeling system RegESM 1.1. *Geoscientific Model Development* 12 (1):233-259
- [4] A. Anav et al. (2023) Dynamical downscaling of CMIP6 scenarios with ENEA-REG: an impact-oriented application for the Med-CORDEX region. *Climate dynamics*, under review

FROM MOSCAB TO MILCHAM TO MEASURE ATMOSPHERIC NEUTRONS: THE MODELLING OF THE NEW ANSWER FUNCTION USING FLUKA AND PHITS CODES ON CRESCO

Nunzio Burgio¹, Alfonso Santagata¹
¹ENEA, FSN-FIS-RNR, C.R. Casaccia, Rome, Italy

ABSTRACT. The MILCHAM (Metastable Ionizing Liquid CHAMber) initiative inherits the hardware of the MOSCAB (Materia OScura Camera A Bolle) detector to exploit its capability to detect high-energy neutrons, such as the one originating at the top of our atmosphere in the interaction with GCR (Galactic Cosmic Rays). This paper mainly focuses on the computational effort to define the detector answer function using extensive Monte Carlo modelling with FLUKA and PHITS nuclear particle transport codes implemented on CRESCO.

1. Introduction

In a precedent CRESCO report [1], we underline the role of the neutron/ion transport simulation implemented using MCNP [2] and SPECTRA-PKA [3] on the CRESCO computational facility in the calibration procedure of the MOSCAB geyser detector. A geyser chamber detects every nuclear interaction between particles and the nuclei of a suitable metastable liquid that causes ion recoils at kinetic energies higher than an intrinsic energy threshold. The MOSCAB [4-5] detector was initially designed to reveal WIMPS (Weakly Interactive Massive Particles) through a spin-dependent interaction with fluorine nuclei in a C₃F₈ (one type of freon) molecule into a supercooled (metastable) liquid state by rigorous control of the thermodynamic parameters of the chamber. After the interaction, the fluorine ion recoils away, leaving its molecule and depositing its kinetic energy in the surrounding liquid, causing a local vaporization germ that grows in a macroscopic bubble that can be detected by a visualization system [6]. Similarly, neutrons promote ion recoils within the active freon volume via elastic scattering, generating detectable vapour bubbles as postulated for WIMPS. Thus, using weak-intensity neutron sources, we proceeded to the detector calibration. After the detector calibration, realizing that the device could also reveal neutrons [7], we monitored the neutron background in the Hall C of the Gran Sasso National Laboratory (LNGS), obtaining neutron fluxes and energy spectra comparable to those reported in previously published measurements [8]. At the beginning of 2022, we moved the detector into the surface laboratory of LNGS, on the side of the Gran Sasso Mountain (1860 mt to sea level), to test its detection capability for atmospheric neutrons. Since the energy spectrum of atmospheric neutrons spans several orders of magnitude above the energy range of the LNGS background neutron spectra, we need to remodel the detector answer function (in particular, the first three stages see [1]) to consider the probability of interaction of neutrons having kinetic energy up to hundreds of GeV. Consequently, it is necessary to substitute MCNP and SPECTRA-PKA with high-energy transport codes in modelling the detection stages. To fulfil this purpose, we used the FLUKA code [9-11] to simulate the secondary particle shower caused by the GCR penetration from the Earth's atmospheric boundaries up to sea level, collecting the local neutron sources at the altitude and geomagnetic position of LNGS. Subsequently, such a neutron source is used in the PHITS [12] code to evaluate the energy spectra of the ion's recoils and their transport within the active freon volume of the geyser detector. Due to the demanding computing requested, implementing the two codes on the CRESCO facilities is mandatory. The results of the preliminary simulations show that all the requested transport features and reaction channels are correctly simulated, promising an improvement of the detector answer function toward the requested high-energy regime.

2. FLUKA and PHITS on CRESCO

As discussed in [13], we compiled the FLUKA package version 4.2.2 using gfortran 9 in the devtoolset-9 environment on CRESCO4 servers. To execute the simulations, we implement a bash script that was invoking the stream editor awk, prepares N replicas of the input file, each having a different seed for the FLUKA's RNG, and saves it in a dedicated subdirectory, along with the auxiliary files. Finally, the script submits the batch jobs on LSF. At the end of the calculation, another set of bash scripts collected the N individual results, using some auxiliary codes of the FLUKA package, and computed each estimated quantity's overall mean and standard deviation. The PHITS code allows the linking with both MPI and OpenMP libraries. Version 3.26A

of the PHITS executable was built on CRESCO4 servers using the Intel Fortran compiler version 17.0.4 and the Intel MPI libraries, and a bash script was implemented for submitting the jobs with the Load Sharing Facility (LSF).

3. FLUKA atmospheric model

The FLUKA's GCR tools model the interaction with the geomagnetic field simulating then the penetration of the ions in the atmosphere from an injection point at 71 km above the Earth's mean radius (6378.14 km) down to the planet's surface, also considering the coupling of GCR with the geomagnetic field. The template layout used to model cosmic ray showers in the Earth's atmosphere includes the whole planet simplified as a sphere of the average Earth's radius, with the atmosphere composed of 100 spherical layers from the Earth's surface up 70 km from the sea level.

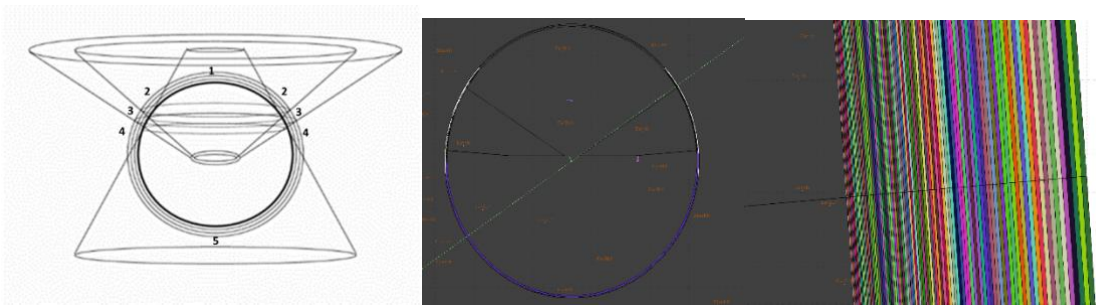


Fig.1: Schematic view of the Earth's atmospheric model (left), a cross-section of the FLUKA model (centre) and a magnification (left) of the one hundred atmospheric layers at different densities and composition.

According to Fig.1, the three cones divide the model regions into five sectors. Sector 3 is between the two coaxial cones and defines the regions of interest to estimate the progressive penetration of the GCRs and their secondaries into the Earth's atmosphere near the location of interest. Sectors 2 and 4 define the atmospheric shells between one of the two coaxial cones and the cone in the opposite direction. These additional regions are needed to consider the primary and secondary particles that reach the region of interest in Sector 3 from side trajectories originating from those regions. Consequently, the spherical crown regions of Sectors 1 and 5 have a negligible probability of generating particles with trajectories that could reach Sector 3. Thus, the users marked them as "without importance", and FLUKA terminates each kind of particle when entering to avoid wasting computational time following useless trajectories. Being the LNGS surface laboratory located at 42.25°N and 13.7°E at 1860 km of altitude from the sea level (Vertical geomagnetic cut off 6. GV), we specialized the model to collect the generated atmospheric neutron flux at an altitude of 1921 mt (s.l.) resolving it in terms of kinetic energy distribution and angular distribution.

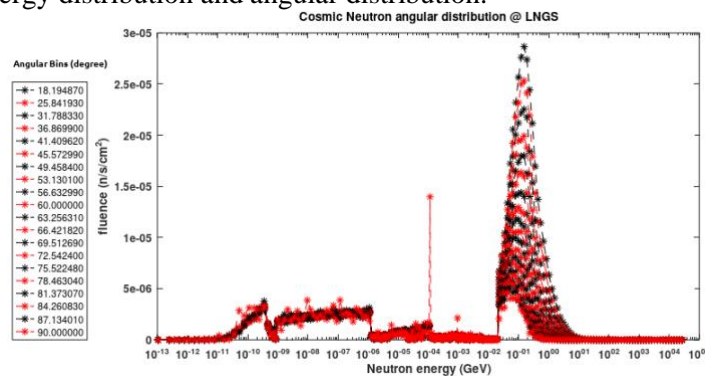


Fig.2: Energy neutron spectra crossing the 1921 m shell boundary directed toward LNGS location.

Fig. 2 reports the resulting fluxes that will be used to define to source neutron for the PHITS simulations. Figure 2 subdivides the energy spectra into several angular intervals that will be used to reconstruct the whole neutron sources in PHITS. The third column of **Table 1** resumes the resources used on CRESCO4 Casaccia to run the FLUKA simulation.

4. PHITS modelling of the MOSCAB detector

The second step of the simulation, consisting of evaluating the energy distributions of the recoil nuclei generated in the neutron reactions, was fulfilled with the PHITS code. The MOSCAB detector was implemented in the PHITS input by adding a concrete floor of 1 m thickness and the neutron source provided by FLUKA in the first step simulation. The concrete floor was added to the model to consider the number of neutrons that could reach the sensitive volume of the MOSCAB detector after scatterings in it. The neutron energy-angle distribution collected by FLUKA at the altitude of 1921 m, which means 61 m above the detector, was implemented at a lower distance, 10 m, for having statistically significant data for exploring the possibility of using PHITS in this problem.

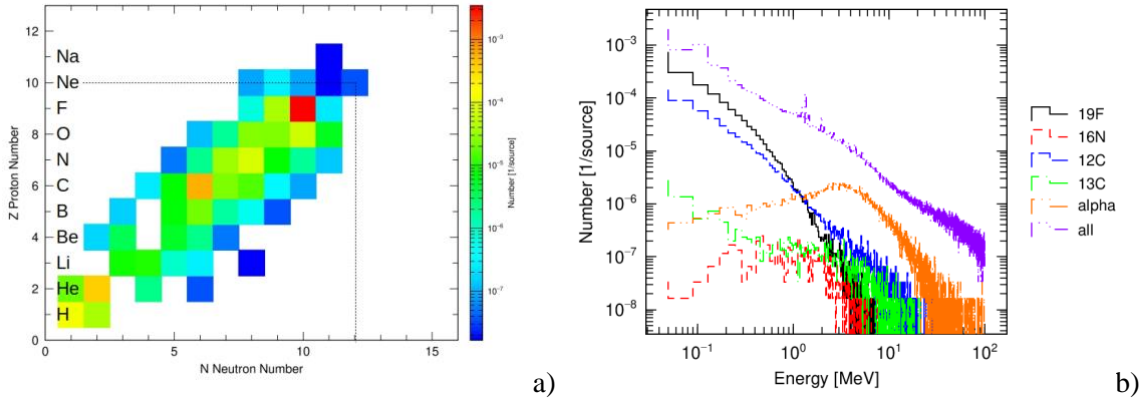


Fig. 3: Plots automatically produced by PHITS: (a) generated recoils. The colour and the vertical colour bar on the figure's right represent the yield intensity. (b) energy distributions in a log-log scale of some recoils.

Therefore, the consideration that we can do on the PHITS's results is limited to qualitative aspects of recoils yields and energy distributions. The results concerning the recoil yields show a wide variety of isotopes produced (see Figure 3a). Furthermore, the generation of recoils like ^{22}Na and ^{22}Ne , which cannot be ascribed to neutron reactions, are the results of reactions between alpha particles and ^{19}F , as verified by requesting PHITS the complete particle's phase-space file. These results confirm PHITS's capability to transport the secondary particles and evaluate their reactions when simulating the complete track structure of each neutron. The recoils energy distribution, with the user-defined energy intervals, can be provided by PHITS for only some selected isotopes and chosen based on the recoils yields distribution. Figure 3b reports the energy distribution of the most frequent ion recoils: ^{19}F , ^{16}N , ^{12}C , ^{13}C and α together, the sum of the energy distributions of all recoils.

The resources used by the PHITS executable on the CRESCO 4 server for producing the results of Fig. 3 are summarized in the second columns of **Table 1**.

Table 1: Resources used for PHITS simulation on CRESCO

Resource list	PHITS	FLUKA
Total number of source particles	2000000000	83200000
Number of CPU	160+1 (master)	416
CPU time	80282 s (22.3 h)	40700 s (11.3 h)
CPU time for particle	6.4 ms/particle	0.235 s/particle
Average Memory	216 MB	680 MB

5. Conclusions

- FLUKA, due to its validated capability to simulate the full GCR's atmospheric particles shower, also considers the ion's interaction with the geomagnetic field and is the best tool to estimate the atmospheric neutron distribution in the phase space. Furthermore, the new FLUKA version can simulate a very accurate neutron transport thanks to the adoption of the point-wise neutron cross-section.

- Potentially, PHITS could perform the full GCR's shower in the atmosphere, but implementing the geomagnetic field is demanding in terms of development time. However, the main PHITS advantage on FLUKA is the possibility of straightforwardly estimating the ion's recoil energy distribution. In addition, PHITS could easily transport the recoiling ions up to very low energy, considering their energy deposition in matter via a track-structure algorithm, allowing a detailed energy balance with the surrounding liquid. Future work will address this promising feature to obtain a more accurate detector answer function.
- Implementing both codes on the CRESCO facility was paramount to maintaining the simulation time and the accuracy of the results at sustainable levels.

References

- [1] N. Burgio, A. Santagata, CRESCO Report 2020 pag. 112, ISBN: 978-88-8286-429-3
- [2] C.J. Werner Editor, MCNP6 User's Manual, October 2017, LA-UR-17-29981.
- [3] M.R. Gilbert, J.Ch. Sublet, Journal of Nuclear Materials 504 (2018) 101-108.
- [4] R. Bertone et al., Nucl. Inst. Meth. A744 (2014) 61-68.
- [5] N. Burgio, A. Santagata et al., Eur. Phys. J. C (2017) 77:752
- [6] F. Seitz, Phys. Fluids 1, (1958) 2.
- [7] N. Burgio, A. Santagata et al., Eur. Phys. J. C (2021) 81:1028.
- [8] N. Burgio, A. Santagata et al. *Eur. Phys. J. C* 83, 354 (2023).
- [9] The Fluka CERN TEAM, Frontiers in Physics 9, 788253 (2022). <https://fluka.cern>
- [10] G. Battistoni, A. Ferrari, T. Montaruli, P.R. Sala, Astroparticle Physics, Volume 19, Issue 2, 2003, Pages 269-290, ISSN 0927-6505, [https://doi.org/10.1016/S0927-6505\(02\)00246-3](https://doi.org/10.1016/S0927-6505(02)00246-3)
- [11] C. Cipriani, Master Thesis – Facoltà di Ingegneria Civile ed Industriale- Roma1 AA 2019/2020
- [12] T. Sato, Y. Iwamoto, S. Hashimoto, T. Ogawa, T. Furuta, S. Abe, T. Kai, P.E. Tsai, N. Matsuda, H. Iwase, N. Shigyo, L. Sihver and K. Niita, Features of Particle and Heavy Ion Transport Code System PHITS Version 3.02, J. Nucl. Sci. Technol. 55, 684-690 (2018). <https://www.tandfonline.com/doi/full/10.1080/00223131.2017.1419890>
- [13] N. Burgio, A. Santagata, CRESCO Report 2021 pag. 43 ISBN: 978-88-8286-440-8

CRITICAL REVIEW OF RESULTS ON THE HEAT CAPACITY AND MELTING TEMPERATURE OF PuO_2

Rolando Calabrese

ENEA, Safety and Sustainability of Nuclear Energy Division, I-40129, Bologna, Italy⁹

ABSTRACT. A new generation of fast breeder reactors (FBRs) is under development with the objective of making nuclear energy more sustainable. Reactors developed for demonstrating the feasibility of most promising innovative systems are loaded with UO_2 - PuO_2 mixed oxide fuel (MOX) to make license procedures easier and less prone to unexpected delays. Plutonium content foreseen in MOX fuel spans up to 30 mol%. High plutonium content and irradiation conditions characterised by high temperatures and burn-ups could have a significant impact on MOX thermophysical properties. Sound knowledge of these topics is mandatory and research efforts in this direction have been undertaken at national and International level. In this frame, heat capacity is relevant for evaluation of thermal conductivity and performance under transient conditions. A lack of experimental measurements on PuO_2 at high temperatures makes drawing ultimate conclusions complex. This paper resumes main results we have obtained on PuO_2 heat capacity by means of MD calculations conducted in the temperature domain ranging from 2000 K up to the melting temperature. A critical review in the light of results published recently in the open literature has been carried out to identify areas of interest for future work.

1. Introduction

Next generation FBRs aim at improving nuclear energy sustainability by overcoming, among others, shortages in uranium resources. Prototypes and demonstrators of most promising innovative reactors' designs will require the use of MOX fuel with concentrations of plutonium dioxide up to 30 mol% [1]. If, on the one hand, the heat capacity of UO_2 has been deeply studied, on the other hand, toxicity, high radiation level, and behaviour at high temperature are all factors that make measurements of PuO_2 thermophysical properties complex [2]. Several authors have discussed the heat capacity of PuO_2 and correlations are recommended in the literature [3-6]. A lack of experimental measurements above 2370 K has raised questions on the behaviour of PuO_2 heat capacity in the temperature domain extending from 2400 K up to the melting temperature. Research community has pointed out the formation of oxygen Frenkel pairs (OFPs) as a dominant phenomenon for plutonium dioxide excess heat capacity at high temperatures [6-7]. We have developed an interatomic potential showing a formation energy of OFP that has been improved in comparison with the indications of potential in [8] and in better agreement with the values found in the open literature [9]. This paper presents a critical review of results obtained with a refined version of the potential presented in [9]. Focus of the review is on the Bredig transition and melting temperature of plutonium dioxide. MD calculations have been carried out by means of LAMMPS (v. 2019) [10]. Code runs have been carried out on the CRESCO6 cluster [11]. This machine supports the MPI message-passing library giving the opportunity to take advantage of the built-in parallel structure of the code. LAMMPS uses spatial-decomposition techniques to partition the simulation domain into small sub-domains of equal computational cost, one of which is assigned to each processor.

2. Interatomic potential

We have developed a Born-Mayer-Huggins pair potential (BMH) [9] that is consistent with measurements on the thermal expansion of PuO_2 and characterised by a formation energy of OFP lower than values derived with the potential published in [8]. The analytical expression of BMH potential partially ionic is presented in Eq. 1. Each term of Eq. 1 accounts for different types of interactions between ions: the first one for long-range Coulombic; the second and the third for short-range interactions due to Pauli's repulsion principle and van der Waals forces. Values of electronic charges z_i and z_j determine the degree of ionicity of atomic bonds; r_{ij} stands for the distance between ion i and ion j . A Morse potential accounts for the covalent bond between anion

⁹ Corresponding author. E-mail: rolando.calabrese@enea.it

and cation; see Eq. 2. In this equation r_{ij}^* is the covalent bond length. D_{ij} and β_{ij} determine the depth and shape of potential.

$$U_{ij}(r_{ij}) = \frac{z_i z_j e^2}{4\pi\epsilon_0 r_{ij}} + A_{ij} \exp\left(-\frac{r_{ij}}{\rho_{ij}}\right) - \frac{C_{ij}}{r_{ij}^6} \quad (1)$$

$$U_{ij}(r_{ij}) = D_{ij} \{ \exp[-2\beta_{ij}(r_{ij} - r_{ij}^*)] - 2 \exp[-\beta_{ij}(r_{ij} - r_{ij}^*)] \} \quad (2)$$

Effective charges of plutonium and oxygen are set to +2.02 and -1.01 with ionicity close to 50%. Coefficients applied in calculations are presented in Tab. 1. More details concerning MD calculations and model used for heat capacity are found in [9,12].

Table 1: Coefficients of the interatomic potential.

Pair (BMH)	A_{ij} (eV)	ρ_{ij} (Å)	C_{ij} (eV·Å ⁶)
O-O	334895.0	0.178	140.0
Pu-Pu	490000.0	0.250	0.0
Pu-O	4580.0	0.252	0.0
Pair (Morse)	D_{ij} (eV)	β_{ij} (Å ⁻¹)	r_{ij}^* (Å)
Pu-O	0.30	2.	2.37

3. Results on heat capacity of PuO₂

Heat capacity at constant pressure and at constant volume have been evaluated with MD calculations in the NPT ensemble and NVT ensemble, respectively. The heat capacity at constant pressure has been calculated by means of the correlation presented in Eq. 3. In this equation H is the enthalpy in J/mol and T is the temperature in K.

$$c_p = \left(\frac{\partial(H-H_0)}{\partial T} \right)_p \quad (3)$$

The heat capacity at constant volume has been calculated through the derivative of the total energy. Results of heat capacity at constant pressure (c_p) and constant volume (c_{ph}) are shown in Fig. 1. Curves recommended for UO₂ and PuO₂ are included for comparison [6]. Results of calculations are rather consistent up to 2300 K, thereafter our potential predicts a more pronounced increase of heat capacity as a consequence of a lower formation energy of OFP; see Fig. 1.a and Fig. 1.b [9,12]. Nevertheless, the deviation from recommended values remains significant especially from 2000 K up to 2400 K where our model does not predict any noticeable increase. This result could support the hypothesis that clustering and coupling of OFP defects play a relevant role for excess heat capacity. The onset of excess heat capacity is rather consistent with the Bredig transition that for actinide oxides should occur around 85% of the melting temperature ($T_{\text{melt}} = 2840$ K for PuO₂).

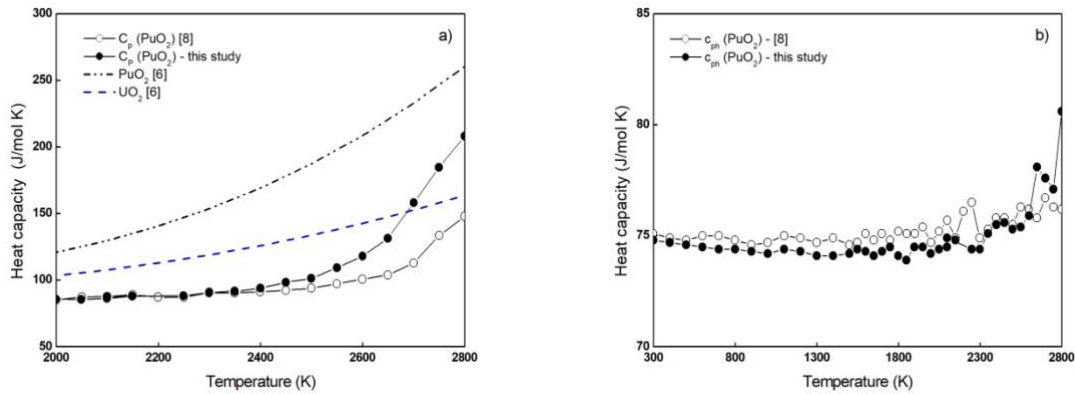


Fig.1: Specific heat at constant pressure: comparison with recommended curves a); specific heat at constant volume b).

4. Critical review of results

Most recent results of MD calculations on actinide oxides heat capacity are based on the use of Cooper-Rushton-Grimes (CRG) potential [13]. This potential considers a many-body EAM term which is added to Buckingham- and Morse-type pair interaction potentials. The use of a many-body additional term makes CRG capable of reproducing the Cauchy's violation observed in actinide oxides with fluorite type structure ($C_{12} \neq C_{44}$) [14]. This potential has been applied for the development of new correlations of heat capacity that have been introduced in fuel performance codes [15]. MD calculations showed a peak of heat capacity occurring before melting (Bredig transition) around 84% of the melting temperature that is 2800 K for PuO_2 . Authors computed for UO_2 a peak of heat capacity more pronounced than seen in recent experimental results, nevertheless, their prediction lies within the uncertainty bands of measurements [15]. The Bredig transition could be interpreted as a consequence of the formation of oxygen Frenkel pair defects or as a pre-melting transition of anion sub-lattice that at high temperatures can be considered like a liquid phase [14]. For MOX fuel, the presence of a peak of heat capacity around 2600 K has been confirmed with position of peak shifting towards lower temperatures with increasing plutonium content [14]. Authors state that position of the peak depends on the O/M ratio as well [14]. Disorder of oxygen sub-lattice starts from T_T (Tammann temperature) and increases up to T_λ (Bredig temperature) [16]. T_T and T_λ occur around 2/3 and 0.80 of melting temperature, respectively. This behaviour characterises actinide oxides as type II superionic material. These materials show a second order thermodynamic transition occurring at T_λ . Authors concluded their analysis stating that anion sub-lattice upon transition behaves alike glass-forming liquids [16]. Occurrence of a Bredig transition in MOX fuel has been suggested by MD simulations with CRG but this indication has not been confirmed in the predictions of a model based on OFP defects [7] nor in experimental data [17]. Deviations of OFP formation energy occurring at high temperatures could cause a shift of T_λ up to melting.

Our model, that does not account for a many-body contribution, predicts a monotonic increase up to the melting temperature instead of a well-defined peak of heat capacity at T_λ . Moreover, occurrence of T_T has not been noted. These results highlight the need for a term accounting for clustering of defects that plays a relevant role in excess heat capacity [7,14,17]. Our calculations are therefore in agreement with most recommended curves that in general do not consider the presence of T_λ . However, in view of a common modelling of actinide oxides most recent correlations tend to account for this transition as presented in [15]. Excess heat capacity predicted at melting by our potential is rather consistent with the peak shown at T_λ for PuO_2 [14]. Moreover, deviations of CRG results approaching melting are significant after the peak [14]. Therefore, some similarities can be noted between the results obtained at these two transitions. The difficulties encountered to identify a clear distinction between pre-melting and melting temperature was pointed out in [12]. Predictions of melting temperature by using CRG have been determined through a phase coexistence method [18]. With this regard, recent measurements performed on MOX fuel with plutonium concentration of 65% and 70% support the hypothesis that the melting temperature of plutonium dioxide is around 3040 K confirming that the assumption of ideal solid solution is not valid for MOX fuel at high plutonium concentrations [19]. Both potentials are, therefore, not updated as they predict a melting temperature of about 2800 K. The CRG potential identifies a non-ideal behaviour of MOX fuel, however, at a lower extent than observed in CALPHAD calculations [18].

5. Future work

In conclusion we can identify some critical issues concerning our potential that are worth being considered in future work:

- higher melting temperature of plutonium dioxide and refinement of potential coefficients;
- analysis of anion sub-lattice through oxygen diffusion and pair distribution function for a more detailed consideration of results beyond T_λ ;
- use of phase coexistence and moving interface methods to determine predictions of melting temperature in agreement with what has been done by the CRG developers.

References

- [1] A.K. Sengupta, K.B. Khan, J. Panakkal, H.S. Kamath, S. Banerjee, Evaluation of high plutonia (44% PuO₂) MOX as a fuel for fast breeder test reactor, *Journal of Nuclear Materials* **385**, pp. 173-177, (2009).
- [2] H. Balboa, L. Van Brutzel, A. Chartier, Y. Le Bouar, Assessment of empirical potential for MOX nuclear fuels and thermomechanical properties, *Journal of Nuclear Materials* **495**, pp. 67- 77, (2017).
- [3] J.K. Fink, Enthalpy and Heat Capacity of the Actinide Oxides, *International Journal of Thermophysics* **3**(2), pp. 165-200. (1982).
- [4] J.-M. Bonnerot, Propriétés Thermiques des Oxydes Mixtes d'Uranium et de Plutonium, Ph.D. thesis, CEA-R-5450, (1988).
- [5] J.H. Harding, D.G. Martin, P.E. Potter, Thermophysical and thermochemical properties of fast reactor materials, EUR 12402 EN, Commission of the European Communities, Luxembourg, (1989).
- [6] R.J.M. Konings, O. Beneš, A. Kovács, D. Manara, D. Sedmidubsky, L. Gorokhov, V.S. Iorish, V. Yungman, E. Shenyavskaya, E. Osima, The Thermodynamic Properties of the f-Elements and their Compounds. Part 2. The Lanthanide and Actinide Oxides, *Journal of Physical and Chemical Reference Data* **43**, p. 013101, (2014).
- [7] R.J.M. Konings, O. Beneš, The heat capacity of NpO₂ at high temperatures: The effect of oxygen Frenkel pair formation, *Journal of Physics and Chemistry of Solids* **74**(5), pp. 653-655, (2013).
- [8] T. Uchida, T. Sunaoshi, K. Konashi, M. Kato, Thermal expansion of PuO₂, *Journal of Nuclear Materials* **452**, pp. 281-284, (2014).
- [9] R. Calabrese, The Heat Capacity of PuO₂ at High Temperature: Molecular Dynamics Calculations, *ASME Journal of Nuclear Engineering and Radiation Science* **8**(4), p. 041603 (7 pages), (2022).
- [10] S. Plimpton, Fast Parallel Algorithms for Short-Range Molecular Dynamics, *Journal of Computational Physics* **117**, pp. 1-19, (1995).
- [11] High Performance Computing on CRESCO infrastructure: research activities and results 2021, Italian National Agency for New Technologies Energy and Sustainable Economic Development, Rome, (2022).
- [12] R. Calabrese, Heat Capacity of PuO₂ at High Temperature: a Comparison of Interatomic Potentials, International Conference Nuclear Energy for New Europe, Portorož, Slovenia, September 12–15, paper 605, (2022).
- [13] M.W.D. Cooper, M.J.D. Rushton, R.W. Grimes, A many-body potential approach to modelling the thermomechanical properties of actinide oxides, *Journal of Physics: Condensed Matter* **26**(10), p. 105401, (2014).
- [14] C. Takoukam-Takoundjou, E. Bourasseau, V. Lachet, Study of thermodynamic properties of U_{1-y}Pu_yO₂ MOX fuel using classical molecular Monte Carlo simulations, *Journal of Nuclear Materials* **534**, p. 152125, (2020).
- [15] D. Bathellier, M. Lainet, M. Freyss, P. Olsson, E. Bourasseau, A new heat capacity law for UO₂, PuO₂ and (U,Pu)O₂ derived from molecular dynamics simulations and useable in fuel performance codes, *Journal of Nuclear Materials* **549**, p. 152877, (2021).
- [16] H. Zhang, X. Wang, A. Chremos, J.F. Douglas, Superionic UO₂: A Model Anharmonic Crystalline Material.
- [17] S.O. Vălu, O. Beneš, D. Manara, R.J.M. Konings, M.W.D. Cooper, R.W. Grimes, C. Guéneau, The high-temperature heat capacity of the (Th,U)O₂ and (U,Pu)O₂ solid solutions, *Journal of Nuclear Materials* **484**, pp. 1-6, (2017).
- [18] C.O.T. Galvin, P.A. Burr, M.W.D. Cooper, P.C.M. Fossati, R.W. Grimes, Using molecular dynamics to predict the solidus and liquidus of mixed oxides (Th,U)O₂, (Th,Pu)O₂, and (Pu,U)O₂, *Journal of Nuclear Materials* **534**, p. 152127, (2020).
- [19] M.-M. Desagulier, MOX: melting temperature, PuMMA Workshop on Fuel Properties, Bologna, Italy, 15-16 June, (2023).

LES OF A H₂/Air CYCLONIC COMBUSTOR UNDER MILD REGIME

Donato Cecere^{1*}, Simone Carpenella¹, Eugenio Giacomazzi¹, Ilaria Quaranta²

¹ENEA, DTE-PCU-IPSE, S.P. 081, Via Anguillarese 301, 00123, Rome, Italy

² Department of Aeronautical Engineering, Roma Tre University, Via della Vasca Navale 79, 00146, Rome, Italy

ABSTRACT. MILD combustion is one of the promising techniques to reduce pollutant emissions, such as NO_x, in combustion processes. It is also a promising technique to burn hydrogen: the highly diluted conditions mitigate its reactivity and its calorific power. The cyclonic flow configuration adopted in this work may represent a proper way to enhance the mixing process while allowing for residence times long enough to achieve complete oxidation of diluted and preheated mixtures. In this work, Large Eddy Simulation (LES) of a Hydrogen/Air cyclonic burner operating in the MILD combustion regime at atmospheric pressure is performed using ENEA's in-house code, HeaRT. Accurate molecular transport properties and a reduced chemical mechanism are considered. Radiative and wall heat exchange effects are also modelled. Results show that temperature is quite uniform along the whole burner with an average value of 1350 K, lower than that typically measured in standard hydrogen combustion. This condition leads to a very low NO_x emissions, the thermal path being the main NO formation mechanism. The NO_x values obtained at the burner outlet are lower than 30 ppm, confirming the possibility of burning hydrogen under MILD combustion conditions.

1. Introduction

The scientific community interest is focused on the identification of new technologies that would allow more efficient energy production systems, in terms of energy production and of pollutants abatement. As a matter of fact, despite some innovative combustion technologies [1], the simultaneous attainment of a high combustion efficiency and of an acceptably low pollutant emission is very difficult due to increasingly more stringent regulations on pollutant emission limits. Among them, Mild combustion is based on the concept of hot exhaust gas recirculation, and consequently preheating and dilution of reactants. In fact, while the heat from the exhaust gases causes an increase in the reactants' temperature, the exhaust gases dilute the mixture, reducing the oxygen concentration and maintaining a low temperature in the combustion region [2]. In this combustion process, the inlet temperature of the reactant mixture is higher than the mixture self-ignition temperature whereas the maximum allowable temperature increase with respect to inlet temperature during combustion is lower than the self-ignition temperature [3]. Because of these conditions and of the presence of inert species concentration in the comburent flow, which is much larger than in the air condition, the characteristic times of chemical kinetics and turbulent mixing are comparable and the process is characterized by: a distributed reaction zone, relatively uniform temperatures, high radiative heat transfer, no visible flame, low noise, tendency to dampen fluctuations and instabilities, negligible soot formation, very low NO_x and CO emissions and flexibility with respect to fuel. A particular application of Mild combustion is in processes that employ hydrogen as fuel. In fact, Mild operative conditions allow mitigating the hydrogen characteristicssuch as its high laminar

*Corresponding author. E-mail: donato.cecere@enea.it.

flame speed, high adiabatic flame temperature, and heating value, high reactivity, which make conventional burners unsuited [4]. To realize Mild combustion operating conditions, configurations with high momentum injection of the reactants are adopted: the flue gas recirculation reduces the oxygen concentration in the flame zone, due to a fast mixing between the oxidizer and the combustion products flows, and increases the temperature of the fresh reactants realizing mixtures under ignition conditions distributed throughout the burner volume. An effective method to create the recirculation zone involves the use of a cyclonic configuration which allows long residence time inside the combustor, large and multi-reaction zones, high turbulence levels generated from the high shear between oxidant and fuel streams, as well as large toroidal recirculation zone. In this work a Large Eddy Simulation (LES) of a cyclonic burner operating in the Mild combustion regime at atmospheric pressure is performed. Accurate molecular transport properties were taken into account and a detailed kinetic mechanism [5] for hydrogen-air combustion, consisting of 18 transported species and 77 elementary reactions and radiative and wall heat exchange effects are also modeled.

The test case defined for this study consists of a prismatic $20 \times 20 \times 5$ cm³ burner (in the x-y-z direction respectively) at atmospheric pressure. The geometry is the same as that of the experimental device already analyzed in [6]. Two anti-symmetric couple of jets and the gas exit positioned at the central part of the burner top induce the cyclonic flow-field within the combustor chamber. Each couple of jets is composed of two cylindrical ducts, the oxidizer with an internal diameter of 0.8 cm, the fuel with 0.15 cm. The oxidizer flows are preheated to the inlet temperature of 550 K and injected at 28.9 m/s, while the fuel is 300 K with a velocity of 207 m/s. The nominal equivalence ratio is set to the stoichiometric value. The walls are set at 1253 K as in the experimental test. The oxidant injectors are located at 2 cm from the lateral walls, whereas the fuel injectors are at 4.5 cm. The domain is discretized through $330 \times 111 \times 250$ points in the x, y and z directions respectively. Appropriate refinement of the grid is performed in the regions with higher gradients: the minimum grid width is located near the injection zones with $\Delta x = 85 \mu\text{m}$, $\Delta y = 130 \mu\text{m}$ and $\Delta z = 350 \mu\text{m}$. The temperature and NO concentration are sampled with a frequency of 50 kHz on the yz-plane at $x = 8$ cm. Their average values are computed with 1000 samples at the moment, but new and more accurate statistics will be added.

The simulation was performed by means of the in-house parallel code HeART [7] and ENEA's super-computing facility CRESCO [8] (Computational Center for Complex Systems) requiring 3000 CPU hours on 3900 processors. The solution was advanced at a constant time step of 5.9 ns, with a CFL (Courant–Friedrichs–Lewy) set to 0.11, in order to ensure the stability of the numerical methods.

2. Results and discussion

The main operational characteristics of cyclonic combustion burner were investigated through temperature and exhaust gas emission numerical predictions. MILD Combustion regime was achieved with reduced combustion peak temperatures due to the H₂O recirculation. Figure 1a reports the predicted average temperature and the average NO concentration profiles along the air jet axis. The temperature profile is quite uniform from 10 cm downstream of the air injector, with an average value of 1250 K, lower than that typically measured in standard hydrogen combustion. This condition leads to very low NO emissions, the thermal path being the main NO formation mechanism. The maximum dry basis NO concentration is lower than 10 ppm and it's located 15 cm downstream of the inlet holes, but better statistics are necessary for a more accurate prediction. Figure 1b shows the instantaneous temperature field on a slice at $y = 0.025$ m. While the walls are set at the experimental temperature of 1253 K, it has a quite uniform field inside the volume, with an average value of about 1350 K. In addition, the isosurface at 1800 K shows how higher temperature values are confined in small regions of the combustion chamber, whereas the isosurface at 550 K highlights the air jet expansion and where the reactions begin to take place. The injection system coupled with the position of the exit and due to its lower pressure

allows for the establishment of a toroidal flow field (cyclonic motion) within the chamber. MILD combustion is therefore attained in the combustor due to the strong recirculation process of burned gases toward fresh reactants induced by this toroidal flow field. Figure 2 shows the average momentum field and the streamlines on a slice at $y=0.025\text{m}$. A trapped vortex takes place in the burner as well as two eddies near the corners in front of the jets, due to the presence of the walls. The high hydrogen momentum leads to a sharp change in the flow direction and because of its cross-flow injection, the H_2 jet is curved towards the near air jet; the longer potential core and suction effect of the air jet enhances the hydrogen jet bending. Moreover, where the two jets meet, a reacting shear layer develops exhibiting a non-premixed combustion with high-temperature hot pockets.

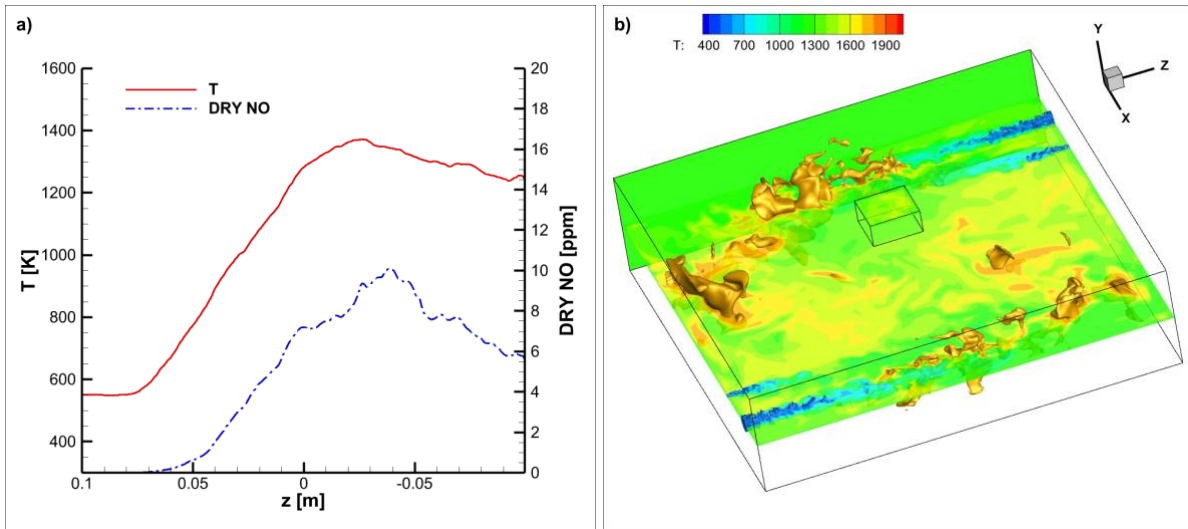


Fig. 1: a) Predicted average temperature (solid line) and average dry basis NO concentration (dashedline) along the air jet. b) Temperature instantaneous contour on a slice at $y=2.5$ cm and a temperature isosurface at 1800 K.

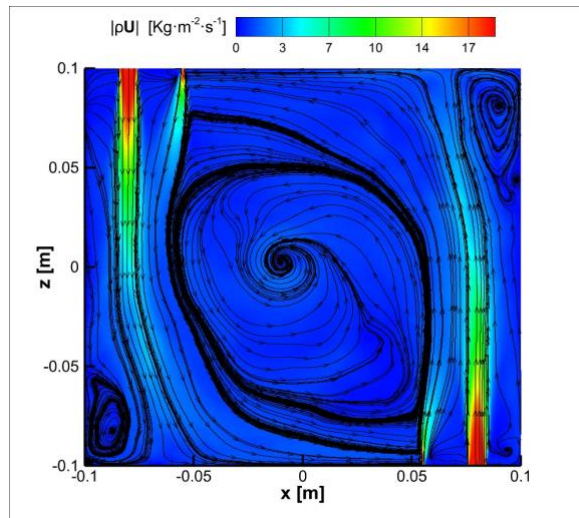


Fig. 2: 2D average momentum field and streamtraces on a slice at $y=2.5$ cm.

The trend of temperature obtained with LES is similar to the experimental one, as shown in Fig. 3, and at the reactor center it is consistent with the experimental results, but the error is not negligible at the

air jet inlet. This could be mainly attributed to the presence of thermocouples (25% of jet diameter) that perturb the fluid dynamics in the air jet and to the inlet air turbulent boundary conditions.

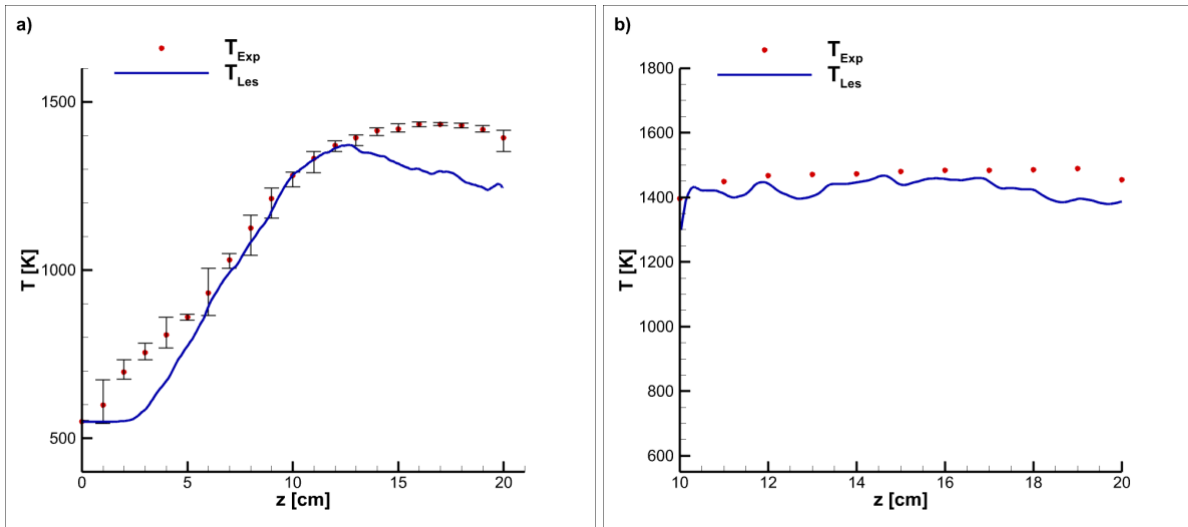


Fig. 3: a) LES (line) and Experimental (dot) average temperature profile along z-axis in the middleplane (xz) at air jet center (x=0.08 m). b) LES (line) and Experimental (dot) average temperature profile along z-axis in the middleplane (xz) at x=0 m.

Acknowledgements

The computing resources and the related technical support used for this work have been provided by CRESCO/ENEAGRID High Performance Computing infrastructure and its staff [8]. CRESCO/ENEAGRID High Performance Computing infrastructure is funded by ENEA, the Italian National Agency for New Technologies, Energy and Sustainable Economic Development and by Italian and European research programmes (see <http://www.cresco.enea.it/english>).

References

- [1] G. Sorrentino, P. Sabia, P. Bozza, R. Ragucci and M. de Joannon, “Impact of external operating parameters on the performance of a cyclonic burner with high level of internal recirculation under MILD combustion conditions”, *Energy* 137, 1167-1174 (2017).
- [2] Cecere D., Giacomazzi E., Picchia F. R., Arcidiacono N., “LES of H₂ Air MILD Combustion”, In Proceedings of the 31st Meeting of the Italian Section of the Combustion Institute (2008).
- [3] Cavaliere A., de Joannon M., “Mild Combustion”, *Progress in Energy and Combustion Science*, 30: 329-366 (2004).
- [4] Galletti C., Parente A., Derudi M., Rota R., Tognotti L., “Numerical and experimental analysis of NO emissions from a lab-scale burner fed with hydrogen-enriched fuels and operating in MILD combustion”, *International Journal of Hydrogen Energy*, 34: 8339-8351 (2009).
- [5] Bowman C.T., Hanson R.K., Davidson D.F., Gardiner W.C., Lissianski Jr., V., Smith G.P., Golden D.M., Frenklach M., Goldenberg M., http://www.me.berkeley.edu/gri_mech
- [6] Ceriello G., Sorrentino G., Cavaliere A., Sabia P., de Joannon M., Ragucci R., “The role of dilution level and canonical configuration in the modeling of MILD combustion systems with internal recirculation”, *Fuel*, 264: 116840 (2020).
- [7] D. Cecere, E. Giacomazzi, N.M. Arcidiacono, F.R. Picchia, et al., “Direct numerical simulation of turbulent lean premixed CH₄/H₂-Air slot flame”, *Combustion and Flame* 165, 384-401 (2016).
- [8] Iannone, F. and et al., “CRESCO ENEA HPC clusters: a working example of a multifabric GPFS Spectrum Scale layout”, *Proc. Int. Conf. on High Performance Computing and Simulation*, 1051-1052 (2019).

EVALUATION OF MCNPX CORRECTION FACTORS FOR PRE-CHARACTERIZATION ANALYSES OF MATERIALS FROM THE DECOMMISSIONING OF THE FRASCATI TOKAMAK UPGRADE FUSION FACILITY

Nadia Cherubini¹, Giada Gandolfo^{2*}, Luigi Lepore², Giuseppe Augusto Marzo²

¹ENEA, FSN-FISS, Nuclear Fission Technology, Facilities and Material Division

²ENEA, FSN-FISS-CRGR, Nuclear Material Characterization Laboratory and Nuclear Waste Management
ENEA Casaccia Research Center Via Anguillarese, 301, 00123 Roma, RM, Italy

ABSTRACT. Frascati Tokamak Upgrade (FTU) is a compact, high-magnetic-field tokamak, Deuterium-Deuterium fusion neutrons facility, built following the Frascati Tokamak experiment at ENEA Frascati Research Center, Rome. FTU construction was authorized in 1986, and operation begun in 1993. FTU officially ended its experimental activity in late 2019. With the end of operations, ENEA requested the formal closure of the radiological practice to competent Authorities (according to the Legislative Decree 230/95, retired in 2020). The Ministry of Ecological Transition provided authorizations to proceed with the FTU decommissioning on April 2021, with Technical Requirements to be respected (according to the Legislative Decree 101/20 currently in force).

According to the Radiological Characterization Plan, a radiological pre-characterisation of materials generated by the FTU decommissioning through non-destructive analyses and destructive analyses has been carried out, to identify and quantify radionuclides coming from neutron activation processes. Non-destructive analyses made large use of in-situ gamma spectrometry with transportable High Purity Germanium detector, and characterization actions took advantages of high parallel computing with Monte Carlo simulation to a proper efficiency calibration of complex measurements setup when the usual calibration by spectrometry software suite may not fit the specific case.

1. FTU operational history and evaluation of neutron activation levels

The decommissioning process for the FTU plant begun with the reconstruction of the operational history, the evaluation of neutron activation phenomena, and the determination of the radiological risks, if present. Only neutron activation processes have been considered significant as a source of radioactivity, without any possibility of components contamination. The analysis of the FTU logbook has shown that the effective average neutron flux and the total neutron fluence during the operational phase have been some orders of magnitude less than the design values.

Based on historical data and semi-empirical analysis founded on calculations (i.e., FISPACT simulations), a theoretical quantification of relevant radionuclides produced by neutron activation has been performed for the components located inside the tokamak cryostat, considering the effective total fluence and the energy spectrum of emitted neutrons characteristic of deuterium-deuterium fusion reactions. Activity concentrations <0.01 Bq/g for all the characteristic radionuclides resulted from this evaluation. The comparison of these results with the Clearance Levels (CL) pursuant to Table I-1B of Legislative Decree 101/20 suggested that free release could be suitable for most of the materials occurring in the FTU Plant, without constraints or limitations for the final destination or subsequent recycling or reuse. Anyway, prior to the free release of any material, the absence of significant activation radionuclides has to be demonstrated with specific radiological characterization actions.

The 'Radiological pre-characterization Plan' is the fundamental preliminary step to propose to the Italian Nuclear Regulatory Authority (ISIN) all technologies and methods expected to be utilized for activity determination of radionuclides in samples analysed. Radiological pre-characterization of materials coming from decommissioning of FTU involved non-destructive and destructive analyses. The former aimed to the

* Corresponding author. E-mail: giada.gandolfo@enea.it.

identification and quantification of gamma emitters coming from neutron activation processes (^{54}Mn , ^{58}Co , ^{60}Co , $^{110\text{m}}\text{Ag}$) by means of in situ gamma spectrometry; the latter were focused on quantification of the activated products with no significant gamma emission (e.g., beta emitters) via Liquid Scintillation Counting (LSC). For each one of the homogeneous groups previously defined, a measurement campaign was designed and carried out.

2. The Radiological Pre-Characterization Plan

The radiological pre-characterization plan aimed to define the type and quantity of radionuclides present in the plant, to enable planning and design of operational phases of dismantling, i.e. removal of components and structures, radiological characterization, management of waste and materials to be cleared and recycled/reused. From calculations, only the structures contained inside the cryostat could have a radiological relevance about neutron activation, so that the materials dismantled by FTU were grouped into two macro-categories:

- group a): materials subjected to neutron flux (inside the cryostat) and potentially activated;
- group b): materials not subjected to neutron flux or subjected to neutron flux of intensity negligible for activation purposes (outside the cryostat) and presumably not activated.

Components and materials belonging to group a) were divided in homogeneous groups on the basis of elemental composition and location, Figure 1. According to this grouping, materials available for measurements in pre-characterization phase were, for example:

- Titanium-Zirconium-Molybdenum (TZM) alloy facing tiles of the limiters. The limiter is the cylindrical band on the inner surface of the vacuum chamber which the plasma faces to and gives off excess of heat. Its purpose was to preserve the integrity of the liner of the vacuum chamber;
- support racks in AISI 316L steel on which the TZM cladding tiles of the toroidal and poloidal limiters were mounted;
- Copper components placed inside the ports of the vacuum chamber;
- ferrous metal components of similar composition to the vacuum chamber including tubular structures, flanges, gates and larger diagnostics (currently non-removable).

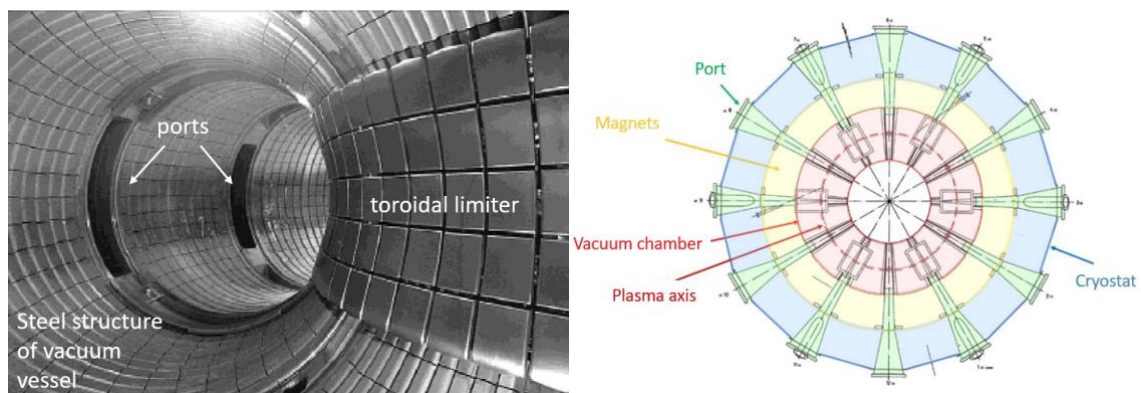


Fig.1: Left: internal view of the plasma chamber. Right: FTU horizontal plan: the plasma chamber (red), electromagnets (yellow), cryostat (light blue), port windows (green).

According to the technical request by ISIN, to reuse or recycle a material coming from FTU plant, the measured concentration or radionuclides activity (both per unit surface and mass) must be less than the CL, and each measurement must reach a Minimum Detectable activity Concentration (MDC) equal to or less than 30% of the corresponding CL.

Radiological pre-characterization of materials coming from decommissioning of FTU involved NDA (Non-Destructive Analysis) almost, to the identification and quantification of gamma emitters coming from neutron activation processes (^{54}Mn , ^{60}Co , ^{58}Co , $^{110\text{m}}\text{Ag}$) by means of in-situ gamma spectrometry. More than 100 distinct items belonging to the different homogeneous groups have been characterized using a transportable detection system equipped with Germanium detector, ISOCS System (In-Situ Object Counting System). The efficiency calibration is determined using the ISOCS software based on the MCNP (Monte Carlo N-Particle Transport Code) calculation code during the execution of the measurement of each sample. To perform the calibration, the code requires a detailed description of the measurement geometry and the type of materials present throughout the graphical interface 'Geometry Composer', equipped with various pre-set geometry models, i.e. "templates". The most suitable "template" to represent the setup of each measurement is completed

by the user, specifying the geometric parameters (distances and thicknesses), the materials and the density for each material involved in the measurement. Templates available by the ‘Geometry Composer’ code are suitable for real experimental setup in most cases, usually. When complex objects and particular geometry of components are not fitting the “template” completely, the user can take advantages of correction factors to be calculated by specialized codes, in this case MCNPX (Monte Carlo N-Particle eXtended) ver. 2.5.0 [1]. By means of the Monte Carlo simulation, in the virtual world reconstruction all possible paths travelled by the radiation in the model can be studied, by means of random samplings from all the probability density functions ruling physical phenomena. Very complex geometries can be built, and very accurate results can be produced if all the elements important to the transport of the analysed radiation are described into the model; moreover, an adequate computational power should be available for running a statistically significant number of histories.

3. Simulation strategy

If the analysed object is made of several parts with different materials having different neutron cross sections, with different densities and geometries, the induced activity could be in principle not uniformly distributed. To minimize the errors related to the efficiency evaluation caused by the non-uniformity of activity distribution, a preliminary scanning by a portable dose-rate meter is performed and if a region with a higher activity level is identified, the HPGe gamma spectrometry is carried out placing the object with the higher activity region in front of the detector. This choice ensures a conservative overestimation of the quantified activity.

Considering the opportunity to perform measurements on standard boxes containing homogeneous materials (an example of box containing metallic materials coming from FTU is shown in Fig. 2a), a set of MCNPX simulations has been carried out to identify a range of positions for a potential hot spot that would be certainly recognized.

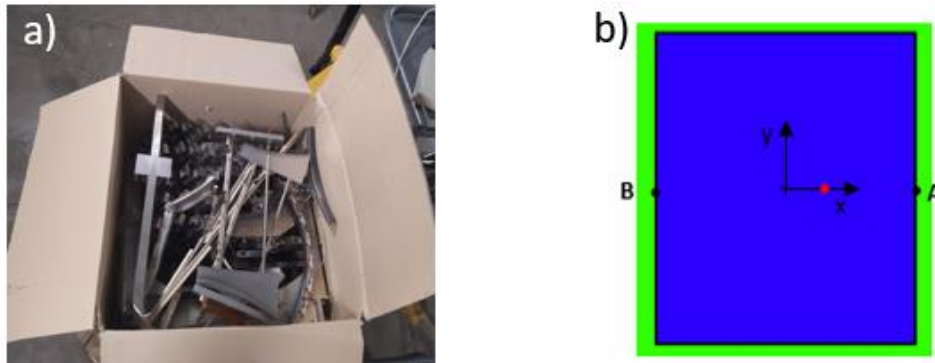


Fig.2: a) real box containing metallic materials coming from FTU, b) simulated box (blue) for dose rate evaluation in A and B positions due to point source along X axis (red point)

For a certain material of the matrix, a point source per investigated radionuclide has been separately simulated in different positions along the box axes (red point in Fig. 2b) and the dose rate has been evaluated in the corresponding projections on the external surfaces investigable through the HPGe detector (A and B points Fig. 2b). The goal of simulations was to evaluate the minimum distance of the source from the box centre allowing the hot spot identification through the portable dose-rate meter. As a very conservative hypothesis, the minimum distance has been defined as the corresponding one to a ratio between the dose rates at A and B equal to 10. Since the box has different length and width, the set of simulations has been performed placing the source along both axes. The ratio between dose rates at A and B as function of the hotspot position for ^{60}Co in a metallic matrix is reported as an example in Fig. 3.

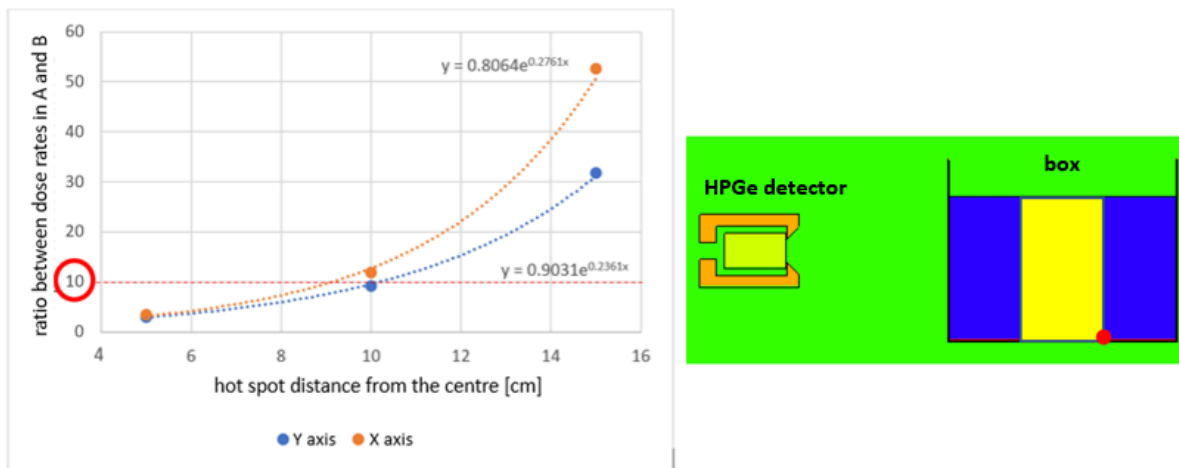


Fig.3: Left: simulation results for a ^{60}Co hot spot in a metallic matrix. Right: region of non-detectability of hotspots through portable dose-rate meter (yellow region)

A fitting procedure using an exponential function has been performed on the simulation results at different source positions to evaluate the hot spot position, corresponding to a ratio between dose rates at A and B equal to 10. The minimum distance of the source from the box centre allowing the hot spot identification through the portable dose-rate meter has been evaluated for both axes and the region of non-detectability has been defined (yellow region in Fig. 3).

In the worst case considered the hot spot would be placed in the farther position (respect to the HPGe detector) within the region of non-detectability (red point in Fig. 3). In this case the hot spot would not be identified in the preliminary scanning with the portable dose-rate meter and the gamma spectrometry would be performed with the hypothesis of homogeneous activity distribution resulting in an underestimation of the actual activity. To avoid underestimation, corrective factors for each investigated radionuclide and matrix have been evaluated through MCNPX simulations. The corrective factor has been defined as the maximum ratio between the actual activity from a hot spot within the non-detectability region and the calculated activity from ISOCS software with homogeneous activity distribution hypothesis.

This approach has been used just for small components that could be placed inside boxes. Since many components coming from the dismantling of FTU had dimensions incompatible with such a geometry, a case-by-case approach has been studied and applied.

Within the MCNPX code, some particular very complex objects analysed during the FTU Radiological Pre-Characterization have been reconstructed in order to get corrective factors to be applied to efficiency calibration provided by the ISOCS suite 'Geometry Composer' software, in order to get more accurate (and conservative in some cases) evaluation of the radionuclides activity.



Fig.5: Example of complex objects analysed during the FTU Radiological Pre-Characterization Plan. Left: instrument for reflectometry. Right: diagnostics (heavy steel components).

Simulations have exploited the usage of multi-processing on CRESCO High Parallel Computing Resources extensively. The computing resources and the related technical support used for this work have been provided by CRESCO/ENEAGRID High Performance Computing infrastructure and its staff [2]. CRESCO/ENEAGRID High Performance Computing infrastructure is funded by ENEA, the Italian National

Agency for New Technologies, Energy and Sustainable Economic Development and by Italian and European research programmes, see <http://www.cresco.enea.it/english> for information.

4. Characterization results and conclusions

Concerning non-destructive analyses performed during the FTU decommissioning pre-characterization campaign, and within more than one hundred items analysed, only few samples, such as some support racks for TZM tiles of toroidal and poloidal limiters, have been found affected by detectable neutron activation phenomena. Even in those cases, levels of radioactivity determined are similar to background and below the authorized CL.

Also, regarding beta emitters (^{55}Fe , ^{59}Ni , and ^{63}Ni), the analysis of some samples of AISI316L steel from chips obtained from one of the supports of FTU toroidal limiter have shown activity concentration of each radionuclide searched for less than CL values.

Radiological pre-characterization results demonstrated that materials present in the FTU Plant can be cleared to unconditional released as expected from historical data and semi-empirical analysis, without any constraints for the final destination or limitations for subsequent recycling or reuse.

References

- [1] J. F. Briesmeister, Ed., “MCNP: A General Monte Carlo N-Particle Transport Code,” 2000.
- [2] F. Iannone et al., “CRESCO ENEA HPC clusters: a working example of a multifabric GPFS Spectrum Scale layout,” in 2019 International Conference on High Performance Computing Simulation (HPCS), 2019, pp. 1051–1052.

STRUCTURAL, ELECTRONIC AND VIBRATIONAL PROPERTIES OF B₂₄N₂₄ NANOCAPSULES: NOVEL ANODES FOR MAGNESIUM BATTERIES

Domenico Corona^{1*}, Francesco Buonocore², Massimo Celino² and Olivia Pulci¹

¹*Department of Physics, University of Rome Tor Vergata, and INFN, 00133 Rome, Italy.*

²*Energy Technologies and Renewable Sources (TERIN), Italian National Agency for New Technologies, Energy and Sustainable Economic Development (ENEA), Casaccia Research Centre, 00123 Rome, Italy.*

ABSTRACT. In this manuscript, we present an *ab initio* study of B₂₄N₂₄ nanocapsules and of the effect of encapsulation of homonuclear diatomic halogens (Cl₂, Br₂, I₂) and chalcogens (S₂, Se₂) in the interaction of the B₂₄N₂₄ nanocapsules with the Mg²⁺ cation. To predict whether these BN nanostructures could be suitable negative electrodes for magnesium-ion batteries, the structural, electronic, and vibrational properties, as well as the interaction energy and the cell voltage, have been calculated in the density functional theory framework for each system highlighting differences and similarities. The encapsulation of halogen and chalcogen diatomic molecules increases the cell voltage with an effect enhanced down the group, reaching a remarkable cell voltage of 3.61 V for iodine-encapsulated anodes. The results shown here have been entirely obtained by calculations on CRESCO/ENEAGRID HPC infrastructure.

1. Introduction

The field of energy storage and conversion has experienced significant advancements in the last decades, this is merely driven by the growing demand for efficient and sustainable energy solutions. Rechargeable batteries have become the backbone of portable electronics and electric vehicles, enabling us to store and utilize energy conveniently. Lithium-ion batteries (LIBs) have dominated this landscape due to their high energy density and long lifecycle. However, as we strive for further innovation, researchers have turned their attention to alternative materials that could potentially outperform lithium-based systems [1]. A very promising candidate gaining considerable attention is magnesium. Magnesium is the eighth most abundant element in the Earth's crust and possesses unique properties that make it an attractive alternative to lithium in rechargeable batteries technology. While lithium ions remain the primary choice, the limitations associated with Li supply chain, cost, and safety concerns have prompted the exploration of alternative battery chemistries. The replacement of lithium with magnesium presents several potential advantages. First and foremost: the abundance of magnesium in comparison to that of lithium. This plenitude translates to lower costs and reduced reliance on limited lithium resources, contributing to a more sustainable energy landscape. Additionally, magnesium-ion batteries (MIBs) could offer increased energy density and improved safety characteristics [2]. One of the significant challenges in utilizing magnesium as an active ion lies in finding suitable electrode materials and electrolytes that can efficiently store and release magnesium ions during charging and discharging cycles. The overcome of these challenges requires multidisciplinary efforts to develop novel electrode architectures and electrolyte formulations tailored for magnesium-based systems. Despite the technical hurdles, significant progresses have been made in recent years towards the development of magnesium batteries; in fact, researchers have explored various strategies such as new electrode and electrolyte materials design, and cell architectures to enhance their performance and stability. The successful adoption of this technology could revolutionize the energy storage landscape, offering higher energy density, improved safety, and reduced environmental impact [3]. However, further research and development are necessary to overcome the remaining challenges and bring magnesium-ion batteries to commercialization. In recent years, the synergy between materials science, computational methods, and high-performance computing has opened exciting opportunities for accelerating the discovery of novel electrode materials [4]. HPC infrastructures provide the

computational power required to perform large-scale simulations and tackle complex materials design challenges. By leveraging HPC capabilities, researchers can employ sophisticated quantum mechanical calculations (e.g., density functional theory (DFT) calculations) and molecular dynamics simulations, to investigate the properties of thousands of potential electrode materials [5]. This computational approach not only accelerates the research and development process but also significantly reduces the costs associated with experimental synthesis and testing; enabling researchers to narrow down the vast materials space, guiding experimental efforts towards the most promising candidates, thus accelerating the overall materials discovery timeline. Among all possible materials, boron nitride (BN) has emerged as a promising electrode material with unique characteristics that hold great potential for advancing energy storage technologies; since it exhibits high thermal conductivity, chemical stability (makes it suitable for use in corrosive environments), and its insulating (ideal for a better control of charge transport within the energy storage system, reducing self-discharge) and its excellent mechanical properties (which further contribute to its suitability for energy storage applications) [6]. BN nanomaterials can be synthesized in various forms, including nanosheets, nanotubes, nanocages, etc., each offering distinct advantages for specific applications; moreover, BN nanomaterials exhibit a large surface area-to-volume ratio, providing ample active sites for ion intercalation and storage. This feature is particularly advantageous for battery applications, as it facilitates rapid ion diffusion and enhances the capacity and cyclability of the electrodes [7]. BN nanomaterials have shown promise as electrode materials for various rechargeable batteries, including lithium-ion batteries, sodium-ion batteries, and even emerging technologies such as magnesium-ion batteries. To fully realize the potential of boron nitride nanomaterials as electrode materials, researchers are actively exploring advanced synthesis techniques and tailoring their structural and surface properties; this includes engineering their morphology and their surface properties to optimize their electrochemical performance and compatibility with different electrolyte systems.

2. Methods

The results presented, obtained from *ab initio* calculations in the DFT framework, have been performed using the DMO13 package from Materials Studio with GGA-PBE XC functional and Grimme's DFT-D dispersion correction to take into account van der Waals interaction. The chosen basis set was DNP (double numerical plus polarization) where each basis function has been restricted to a global cut-off radius of 4.5 Å. The systems properties have been investigated with geometrically optimized structures.

3. Results

3.1. Encapsulation of B₂₄N₂₄ nanocapsules

The B₂₄N₂₄ nanocapsules [8] are constructed by arranging 24 boron atoms and 24 nitrogen atoms in a specific pattern, resulting in a hollow cage-like structure. Their atomic arrangement is highly symmetrical and stable, allowing them to retain their shape and structural integrity which is essential for their potential applications in various fields, including catalysis, and energy storage. Additionally, the hollow structure of B₂₄N₂₄ nanocapsules, provides an excellent environment for encapsulating other molecules or nanoparticles; this feature opens the possibility for encapsulating B₂₄N₂₄ with homonuclear diatomic molecules visible in Figure 1.

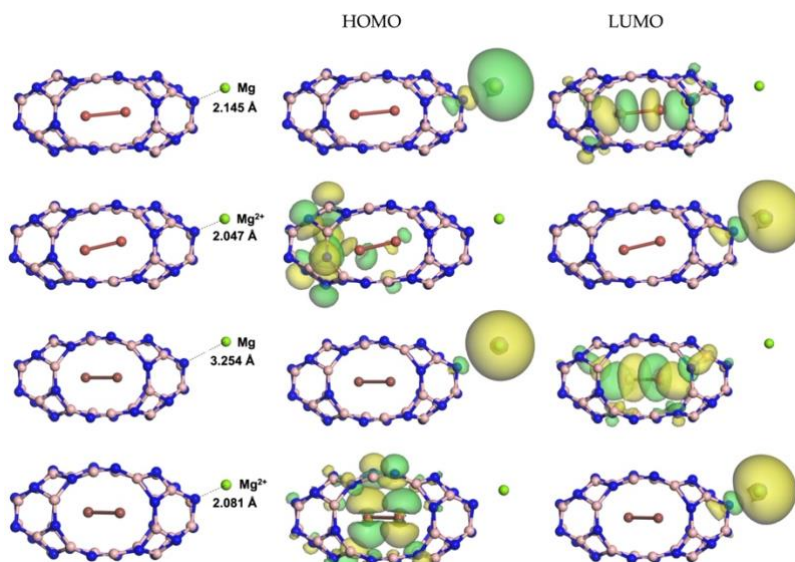


Fig.1: Geometrically optimized structures and molecular orbitals plots for (from top to bottom): $\text{Br}_2/\text{B}_{24}\text{N}_{24}/\text{Mg}^{0/2+}$ and $\text{I}_2/\text{B}_{24}\text{N}_{24}/\text{Mg}^{0/2+}$. Distances are in Å.

3.2. Electronic and vibrational properties of the endonanocapsules

To assess their potentiality as negative electrodes, the vibrational and electronic properties (e.g., formation energy, the interaction energy, and the cell voltage) have been calculated for each system. Interpreting the Raman spectra for these nanostructures provides valuable information about their structural characteristics, including bond strengths, flexibility, and confinement effects due to the finite size of the structure. Furthermore, the presence of encapsulated molecules onto the nanocapsules leads to changes in the Raman spectra as visible in Figure 2, indicating interactions between the pristine encapsulant and the molecule. By studying these spectral changes, it is possible to gain insights into the working mechanisms when these systems are used for energy storage applications.

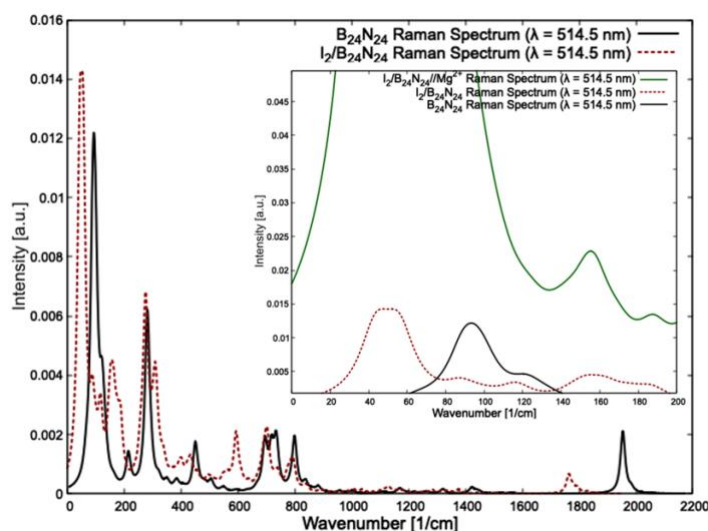


Fig.2: Raman Spectra of $\text{B}_{24}\text{N}_{24}$, $\text{I}_2/\text{B}_{24}\text{N}_{24}$ and $\text{I}_2/\text{B}_{24}\text{N}_{24}/\text{Mg}^{0/2+}$ at wavelength $\lambda = 514.5$ nm.

The transfer of electrons from the diatomic molecule to the nanocapsule surface enhances the interaction of Mg^{2+} with the capsule itself. Notable values of cell voltage have been obtained increasing the atomic number down the halogen and chalcogen group (due to an increase in the negative charge pumpable to the surface). A remarkable cell voltage has been obtained with the encapsulation of molecular iodine, reaching a value of 3.61 V as shown in Figure 3.

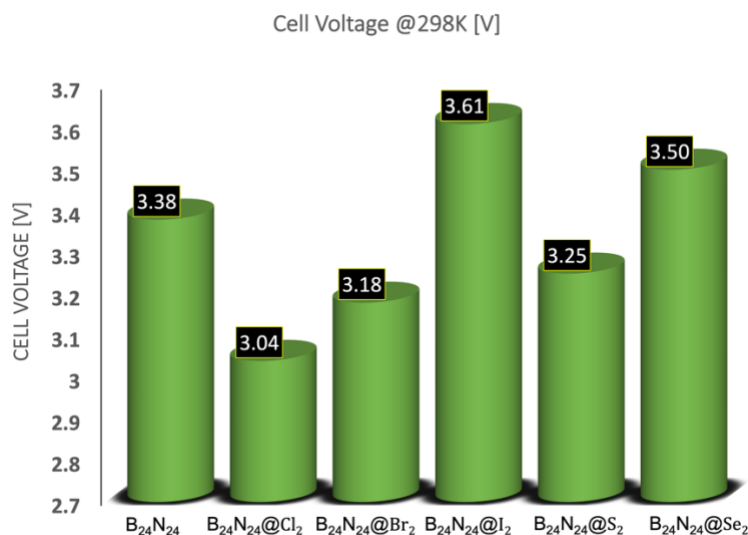


Fig.3: Voltage trends at 298.15 K and 1 atm for the studied nanostructures.

References

- [1] R. C. Massé, et al. Beyond Li-ion: electrode materials for sodium-and magnesium-ion batteries. *Science China Materials*, 58, 715-766, (2015).
- [2] C. You, et al. Advances in rechargeable Mg batteries. *Journal of Materials Chemistry A*, 8(48), 25601-25625, (2020).
- [3] R. Shah, et al. Magnesium-ion batteries for electric vehicles: Current trends and future perspectives. *Advances in Mechanical Engineering*, 13(3), 16878140211003398, (2021).
- [4] C. Kuang, et al. A review of electrode for rechargeable magnesium ion batteries. *Journal of Nanoscience and Nanotechnology*, 19(1), 12-25, (2019).
- [5] Y. S. Meng, et al. First principles computational materials design for energy storage materials in lithium ion batteries. *Energy & Environmental Science*, 2(6), 589-609, (2009).
- [6] D. Golberg, et al. Boron nitride nanotubes and nanosheets. *ACS nano*, 4(6), 2979-2993, (2010).
- [7] R. W. Murray. Nanoelectrochemistry: metal nanoparticles, nanoelectrodes, and nanopores. *Chemical reviews*, 108(7), 2688-2720, (2008).
- [8] H. S. Wu, et al. New boron nitride $B_{24}N_{24}$ nanotube. *The Journal of Physical Chemistry A*, 107(34), 6609-6612, (2003).

PRELIMINARY CFD INVESTIGATION OF A TURBULENT FLOW IN A 19-PIN WIRE WRAPPED FUEL BUNDLE

Roberto Da Vià^{10*}, Daniele Panico², Francesco Lodi¹, Giacomo Grasso¹

¹ENEA FSN-SICNUC-PSSN, C.R. "E. Clementel", via Martiri di monte sole 4, 40129 Bologna, Italy

² newcleo Srl, via Giuseppe Galliano 27, 10129, Turin, Italy

ABSTRACT. A preliminary hydraulic study by Computational Fluid Dynamics (CFD) has been performed to investigate the pressure losses that occur in turbulent liquid metal flow inside a 19-pin wire wrapped fuel bundle geometry. To overcome some of the issues of the mesh generation step, an in-house meshing algorithm has been developed on purpose. A fork of the open-source CFD code OpenFOAM, developed at ENEA within the PSSN laboratory, has been used to perform the simulations on the ENEA CRESCO6 High Performing Computing system.

1. Introduction

In the context of Liquid Metal Fast Reactors, hexagonal fuel assemblies have been historically chosen as the standard method for arranging the fuel pins through the reactor core, using a triangular lattice. This disposition strategy allows to enhance the heat transfer due to the tight pitch of the triangular lattice. To prevent the contact between adjacent fuel pins, potentially caused by vibrations or deformations that occur during the fuel pin lifetime, spacer means are used. Two different strategies have been exploited over the years: the adoption of spacer grids or of wire wrapped fuel pins. At the cost of an increased pressure loss, the wrapping wire strategy allows to enhance the uniformity of the temperature field thanks to the strong secondary flow that is induced by the presence of the wires.

Detailed Computational Fluid Dynamics simulations of turbulent flows in wire wrapped fuel bundles are used to predict pressure losses and heat transfer performances. From a modelling point of view, the discretization of wire wrapped fuel bundles is quite complex, due to the involved wide range of physical dimensions: the extent of the wire axial pitch is of the order of tens of centimeters, the narrow gaps between wires and adjacent fuel pins are of the order of fractions of millimeters. To properly catch all the geometry features, it is difficult to find a tradeoff between the amount of mesh cells and the quality of the computed mesh.

In the present report, we show some preliminary results obtained from simulations of isothermal turbulent flows of molten lead in 19 pin wire-wrapped fuel bundle geometries.

2. The software

The numerical simulations have been performed using the open-source CFD code OpenFOAM [1]. To overcome the mesh generation difficulty, an in-house meshing algorithm has been developed, namely *hexaBundleMesher*. With this tool, block structured meshes of predominantly hexahedral elements are generated with a small computational effort. The algorithm exploits the possibility of subdividing the fuel bundle geometry into blocks of fluid volumes, each one surrounding a single pin. This set of blocks can be further divided into a set of elementary blocks that allow to build the whole geometry once they are spanned through the core. A sketch of this partition into elementary blocks is shown in Figure 1, where a 19-pin and a 61-pin fuel bundle meshes are shown. Fuel pin blocks having the same color belong to the same elementary block. In this way it is quite simple to generate numerical grids of fuel bundles with a large amount of fuel pins, even with small computational resources. Each fuel pin domain is stored as the local domain of a decomposed mesh for parallel execution; the mesh of the whole domain is then computed by gathering all the fuel pin domains with the *reconstructParMesh* utility of OpenFOAM. *hexaBundleMesher* is currently hosted on a private repository of the ENEA FSN-SICNUC-PSSN gitlab website.

¹⁰ * Corresponding author. E-mail: roberto.davia@enea.it

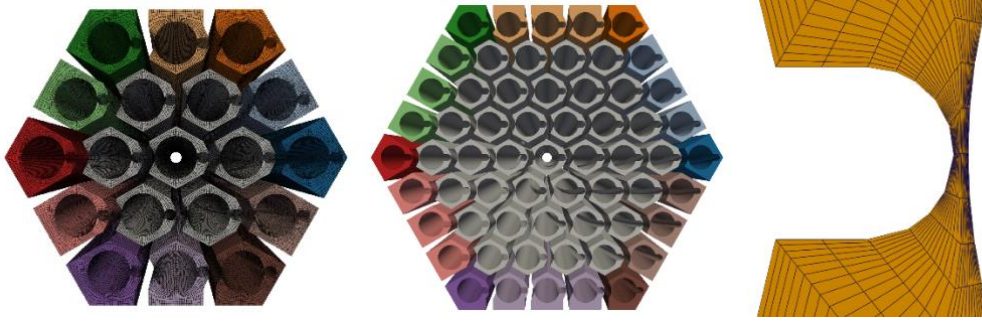


Fig. 1: Elementary fuel pin blocks for a 19 (left) and for a 61 (centre) wire wrapped fuel pin bundle. On the right, a close-up view of the approximated pin-wire contact with the “D” wire shape.

3. The geometrical and computational model

The considered fuel bundle consists of 19 wire wrapped fuel pins with the same characteristic geometrical dimensions of the SuperPhénix fuel pins [2], that is, pin diameter (8.5 mm), wire diameter (3.1 mm), tolerance gap (0.1 mm) and wire axial pitch (180 mm). A periodic flow is simulated over a single axial pitch of the wrapping wire. This is accomplished by using the cyclic boundary conditions provided by OpenFOAM. A target volume averaged velocity, leading to a Reynolds number value of approximately 20000, is setup using the *meanVelocityForce* utility of OpenFOAM. On all the wall boundaries (wrapper sides and fuel pins), no slip, zero gradient and wall function boundary conditions are used for the velocity, pressure, and turbulence variables, respectively. The used turbulence model is the k- ω SST. Three different mesh sizes have been considered, to perform a grid convergence analysis of the obtained results, in terms of the computed pressure losses, using the Grid Convergence Index method [3]. The meshes have been labelled as L0, L1 and L2 and the details of mesh cells and average mesh refinement are reported in Table 1. Due to a current constraint set by the mesh quality, the pin-wire contact has been approximated: instead of the real case single point contact, a “D” wire shape has been used, as shown in Figure 1.

Table 1: Mesh sizes and average refinement for each refinement level

Refinement level	L0	L1	L2
Number of cells	14 x 10 ⁶	53 x 10 ⁶	146 x 10 ⁶
Normalized average refinement (per space direction)	1	1.547	2.161

4. Results

The results of the refinement analysis are reported in terms of the computed friction factor f , defined as

$$f = \frac{\Delta p D_h}{0.5 L \rho U_b^2} \quad (1)$$

where D_h is the hydraulic diameter, L is the axial extent of the domain, ρ is the fluid density and U_b is the fluid bulk velocity on the assembly cross section. In order to have a reference value of the friction factor, simulations have also been performed with the subchannel code ANTEO+ [4] developed by ENEA. The obtained results are reported in Table 1, with a comparison between the values of f obtained with the three different meshes in OpenFOAM, the value obtained with ANTEO+ and the estimated value at grid convergence (for the CFD results) calculated using the GCI method. Although the results show a convergence towards the ANTEO+ computed value, the grid convergence analysis predicts a friction factor value much smaller than the one of ANTEO+. The grid convergence is not satisfactory, and the causes could be related to the mesh refinement, the mesh quality, and issues in the numerical convergence of each simulation. Moreover, the mesh could be also improved in the boundary layer thickness, as the obtained values of the non-dimensional wall distance y^+ would suggest: from Table 2 it can be seen that for cases L0 and L1 the maximum values of y^+ lies outside of both the viscous and logarithmic layers, leading to possible problems with the used boundary conditions.

Table 1: Comparison of obtained values of friction factor between OpenFOAM results, ANTEO+ and the estimated value at grid convergence using the GCI method

Case	L0	L1	L2	ANTEO+	GCI extrapolated
f	$3.59 \cdot 10^{-2}$	$3.33 \cdot 10^{-2}$	$3.16 \cdot 10^{-2}$	$3.09 \cdot 10^{-2}$	$2.00 \cdot 10^{-2}$

Table 2: Comparison of minimum, maximum and average y^+ values, obtained for the three levels of mesh refinement, on wrapper and pin boundaries

Case	Wrapper			Pin		
	L0	L1	L2	L0	L1	L2
min	0.2	0.08	0.04	0.28	0.17	0.1
max	19.6	13.8	7.8	11.4	8.9	4.4
average	7.6	5.2	2.6	4.9	3.4	1.8

A grid convergence analysis has also been performed on the computed values of the sub-channel mass flow rate distribution. The solutions, of each refinement level, have been sampled with cross section planes every 30 degrees of wrapping wire rotation. The mass flow rate has been computed on each plane for each sub-channel, and then averaged to get a single value for each sub-channel. As shown on the left of Figure 2, in this case the GCI analysis is satisfactory since the maximum GCI value, that is, a measure of the error of the finer mesh level with respect to the estimated value at grid convergence, is approximately 1.6%. On the same Figure the comparison of the OpenFOAM and of ANTEO+ sub-channel mass flow rate results is reported, showing a good agreement except for a systematic OpenFOAM mass flow rate overprediction in the corner sub-channels.

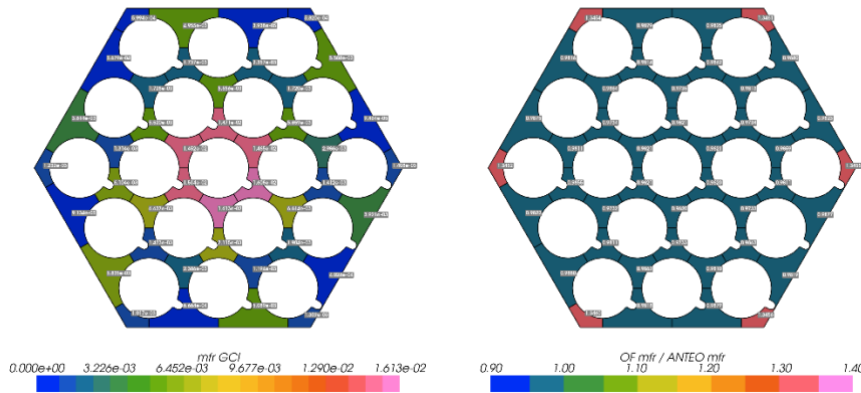


Fig. 2: Results of the grid convergence analysis for the sub-channel mass flow rate (left) and of the comparison between the OpenFOAM and the ANTEO+ sub-channel mass flow rate distributions.

5. Conclusions

A preliminary investigation of the pressure losses occurring in a 19-pin wire wrapped fuel assembly has been performed by means of CFD analyses using OpenFOAM. For this purpose, an in-house meshing algorithm, *hexaBundleMesher*, has been developed to facilitate the construction of the numerical grids needed to perform the CFD analyses. The length of the simulated geometry is equal to a single axial pitch of the wrapping wire. A periodic turbulent flow is then simulated by leveraging the cyclic boundary conditions available in OpenFOAM. Several meshes, with increasing refinement levels, have been used to perform a grid convergence analysis of the obtained friction factor values. In order to set a reference of the friction factor value, simulations have also been performed with the ANTEO+ subchannel code. Although with increasing mesh refinements the values of f seem to converge to the ANTEO+ code, the grid convergence analysis showed that the estimated value at grid convergence is much smaller than the one computed with ANTEO+. Many potential causes for this non optimal grid convergence analysis are related to the mesh, so further effort should be put to improve

hexaBundleMesher. A grid convergence analysis has also been performed on the computed values of subchannel mass flow rates, showing much better results with respect to the analysis for the friction factor.

References

- [1] Official OpenFOAM v9 GitHub repository: <https://github.com/OpenFOAM/OpenFOAM-9>
- [2] J. Guidez and G. Prele, *Superphenix Technical and Scientific Achievements*. Atlantis Press, 2017.
- [3] I. B. Celik, U. Ghia, P. J. Roache, C. J. F. H. Coleman and P. E. Raad. Procedure for Estimation and Reporting of Uncertainty Due to Discretization in CFD Applications. *J. Fluids Eng.* 130(7):078001 (2008)
- [4] F. Lodi, G. Grasso, D. Mattioli and M. Sumini. ANTEO+: A subchannel code for thermal-hydraulic analysis of liquid metal cooled systems. *Nucl. Eng. Des.* 301:128-152 (2016)

NANOCOMPARTMENTALIZATION STRUCTURES FROM BACTERIA'S LIPIDS

Antonio De Nicola^{1,*}

¹*Scuola Superiore Meridionale, Mathematical and physical sciences for advanced materials and technologies, Via Mezzocannone 4, 80138 Napoli, Italia*

ABSTRACT. The design of cellular functions in synthetic systems, inspired by the internal partitioning of the living cell, is a constantly growing research field. Several hierarchies of the internal compartments like liposomes and membranes are employed to control, transport, and release the chemistry of encapsulated species. Experimental characterization and the comprehension of glycolipids mesostructures is far from being fully addressed. In this work we combined approaches based on hybrid Particle-Field (hPF) Molecular Dynamics (MD) simulations and Small Angle X-Ray Scattering (SAXS) experiments to gain a molecular picture of the complex supramolecular structures of lipopolysaccharide (LPS) and Lipid A at low hydration level. The mutual support of data from simulations and experiments allowed the description of a complex Lipid A phase composed of liposomes of variable size and shape.

1. Introduction

The characterization of the supramolecular structure of bacterial lipids is a very complex matter, that makes its study a very challenging research area. The last two decades have witnessed a real bloom in the study of the structural and supramolecular properties of bacterial glycolipids since many of them are key actors of the bacterial interaction with eukaryotes and do elicit or suppress the host innate immunity. Despite this, the information on their behaviour when released by the microbe in biological fluids, such as blood, is scant, and this is reflected in a still limited knowledge of how these glycolipids are presented and recognized by their host receptor proteins.[1], [2] A key example is given by the lipopolysaccharide (LPS), which is the main constituent of the outer membrane of Gram-negative bacteria. LPS, with its glycolipid anchor to the membrane, i.e. the Lipid A, is known to interact with specific receptors of host innate immunity, including the receptor complex made up of Toll-Like Receptor 4/Myeloid Differentiation protein-2 (TLR4/MD-2) that is certainly the most studied. Upon this recognition event, a cascade of intracellular signalling events is activated, leading, in certain cases, to a dramatic inflammatory response with fatal outcomes for human health. Therefore, the mesoscopic characterization of such complex glycolipids is of primary importance to appreciate their behaviour in solution, and thus the early events of the binding to their receptors paving the way to the mechanisms allowing Lipid A extraction from a supramolecular architecture and then transportation and detection as a single glycolipid molecule.

On the other hand, several efforts are devoted to the implementation of cellular functions in synthetic systems through a so called bottom-up synthetic biology approach.[3], [4] Inspired by the internal partitioning of living cells, several multi-compartment systems using bottom-up assembly have been proposed. In particular, diverse hierarchies of the internal compartments have been explored by employing different types of interfaces including liposomes, protein capsules, emulsions and membranes.[5]–[7] The creation of compartments using different building blocks is paving the way towards new challenging applications such as highly functional systems able to regulate the chemistry of encapsulated reactant species.[5],[8]–[10] An exhaustive disentanglement of self-assembled structures, compartmentalization ability and its control, is pivotal towards the development of suitable building blocks for a bottom-up synthesis of living organisms.[3], [4]

In this study we report novel nano-compartmentalized superstructures obtained by self-assembly of lipids, named Lipid A, which are ubiquitous constituents of Gram-negative bacterial outer membranes. The first experimental studies on the phase behaviour of Lipid A date back to the nineties: Brandenburg and co-workers made several efforts in disentangling the phase diagram of Lipid A deriving from different sources and in different experimental conditions.[11] By employing pioneering SAXS experiments, they discovered that the phase diagram of Lipid A is particularly rich and characterized by the presence of lamellar and non-lamellar phases with different symmetries and arrangements. [11] The complexity of supramolecular self-assembled

structures together with the absence of available techniques strongly limited the formulation of more robust and conclusive hypotheses on the aggregate morphologies, such as the hypothesized presence, at low hydration level, of coexisting lamellar and non-lamellar phases. Thanks to the combination of hybrid Particle-Field (hPF) MD simulation technique[12], [13] and Small Angle X-Ray Scattering (SAXS,) we can describe for the first-time the molecular details of the morphology of Lipid A assemblies from *Escherichia coli* (*E. coli*) and *Pseudomonas aeruginosa* (*Pseudomonas*) in low hydration condition unveiling new, ordered and previously unrecognized nano-compartmentalized supermolecule structures.

2. Results and Discussion

The models of the Lipid A and water mixtures are based on the coarse-grained (CG) model of Lipid A specifically developed to reproduce reference atomistic results and able to correctly describe the self-assembly of lamellar and non-lamellar phases and structural properties of complex glycolipids.[14] MD simulations started from homogenous mixtures obtained by randomly placing all the species (Lipid-A, water, and counterions) in the simulation box. The self-assembly processes of the homogeneous mixtures were simulated until equilibrium structures were reached. The equilibrium condition was confirmed by the behaviour of the intermolecular particle-field potential, initially decreasing and then stably oscillating around constant value, and by the formation of stable structures. The morphologies at the equilibrium are quite similar for both lipids. In fact, an ordered honeycomb-like structure is found for *E. Coli* and *Pseudomonas*, as reported in Figure 1. Morphology time evolution shows a growing structure order as Lipid A molecules aggregate, leading to phase separation. During this time-interval, we observe the progressive confinement of water molecules in pockets giving rise to their reduction in number between two adjacent lipid layers (see the sequence of snapshots in Figure 1).

On similar systems, the experimental SAXS characterization has been done. An adequate amount of Lipid A from *E. Coli* and *Pseudomonas* has been isolated and purified; briefly, the LPS was exhaustively purified by an iterative chromatography and ultracentrifugation cycle and afterward, the Lipid A has been obtained by mild acid hydrolysis of the LPS. Then, SAXS profiles of both *E. Coli* and *Pseudomonas* Lipid A in poor hydration conditions (i.e., 35% w/w hydration) at room temperature were acquired. In Figure 2A the measured SAXS profiles for the two systems (circular points), are compared against those calculated by averaging from molecular configurations obtained from simulations (continuous lines). The SAXS comparison clearly unveils that *E. Coli* and *Pseudomonas* show similar patterns, in agreement with the similarity found in the morphologies obtained by MD simulations and suggesting that the modelled systems are representative of the experimental counterpart. In the limit of q range accessible from simulations, which is limited by the size of systems, the main features of computed SAXS profiles well reproduces the measured patterns (Figure 2B-D). This study shows, for the first time, how glycolipids derived from bacteria in some conditions can act as nanocompartments. The compartmentalized structures have been characterized by combining MD and SAXS studies. The proposed molecules and their self-assembled nanostructures have a strong potential as tools for synthetic biology for several reasons.

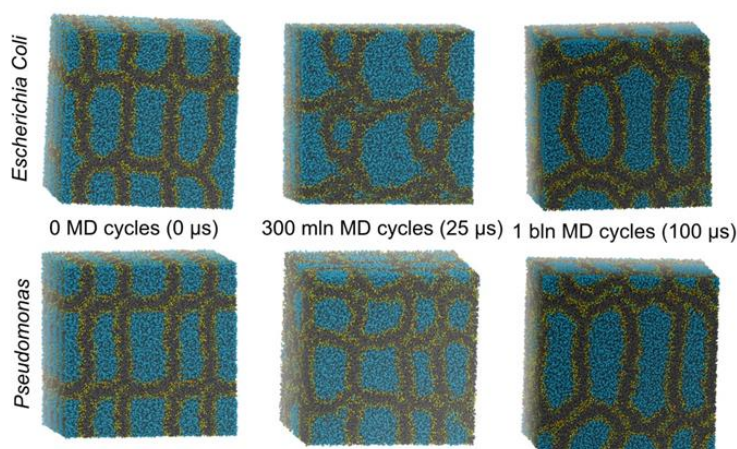


Fig.1: Snapshots sequence illustrating the formation of equilibrium structure for both lipids A from *Pseudomonas* and *E. coli*.

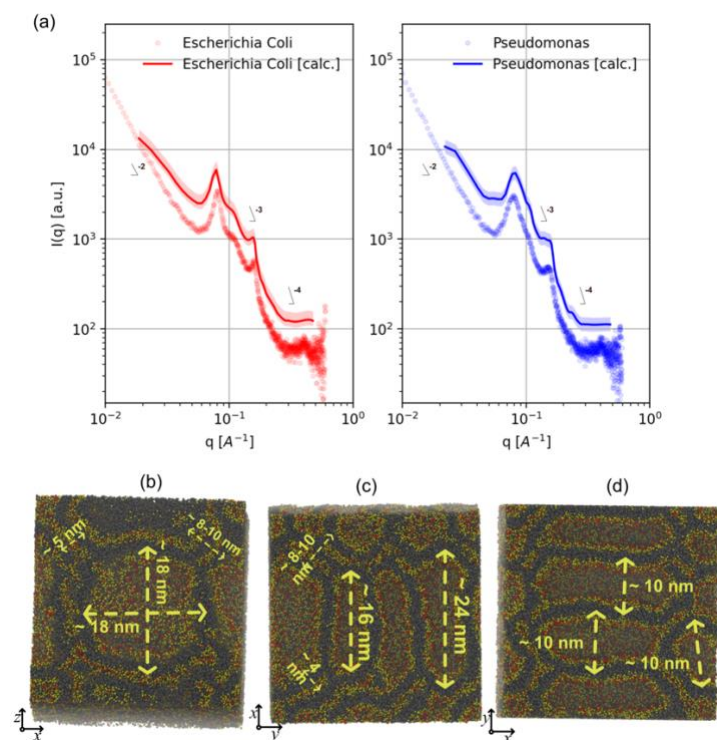


Fig. 2: (A) Log-log plot of experimental SAXS profiles obtained for *E. coli* (red circle) and *Pseudomonas* (blue circle) in the presence of 35% w/w hydration; SAXS profiles calculated from MD trajectories of *E. coli* (red line) and *Pseudomonas* (blue line) in the presence of 30% w/w hydration. The SAXS profile from simulations are computed by time averaging the last 2 μ s of the simulated trajectory of both Lipid-A assemblies. Representative snapshots of *E. coli* reported in three different orientations: (B) zx plane view, (C) yx plane view, (D) xy plane view. Water molecules are omitted for clarity. CG beads of Lipid A head are reported in yellow and red, instead, hydrophobic tails are reported in black.

Acknowledgments

I would like to offer special thanks to Prof. Antonio Molinaro and Prof. Alba Silipo of the University of Naples Federico II, for the purification of Lipid A and useful discussions regarding the whole project. I would also thank Prof. Debora Berti of the University of Florence, for the SAXS characterization and the scientific proficient discussions. Special thanks to Prof. Giuseppe Milano for all the support in the writing the manuscript, for all the discussions about theoretical treatment of the studied systems and for discussions to rationalize the results.

References

- [1] F. Di Lorenzo, K. A. Duda, R. Lanzetta, A. Silipo, C. De Castro, and A. Molinaro, "A Journey from Structure to Function of Bacterial Lipopolysaccharides," *Chem. Rev.*, vol. 122, no. 20, pp. 15767–15821, Oct. 2022, doi: 10.1021/acs.chemrev.0c01321.
- [2] C. Di Carluccio *et al.*, "Investigation of protein-ligand complexes by ligand-based NMR methods," *Carbohydrate Research*, vol. 503, p. 108313, May 2021, doi: 10.1016/j.carres.2021.108313.
- [3] M. Ryadnov, L. Brunsveld, and H. Suga, Eds., "Synthetic Biology," in *Synthetic Biology*, Cambridge: Royal Society of Chemistry, 2014, pp. P001–P005. doi: 10.1039/9781849737845-FP001.
- [4] M. Ryadnov, L. Brunsveld, and H. Suga, Eds., "Synthetic Biology," in *Synthetic Biology*, Cambridge: Royal Society of Chemistry, 2017, pp. P001–P004. doi: 10.1039/9781782622789-FP001.
- [5] H. R. Marsden and A. Kros, "Chapter 9. Functional frontiers: engineering biomimetic interfaces," in *Synthetic Biology*, M. Ryadnov, L. Brunsveld, and H. Suga, Eds., Cambridge: Royal Society of Chemistry, 2014, pp. 253–274. doi: 10.1039/9781849737845-00253.
- [6] D. E. Discher and F. Ahmed, "Polymersomes," *Annu. Rev. Biomed. Eng.*, vol. 8, no. 1, pp. 323–341, Aug. 2006, doi: 10.1146/annurev.bioeng.8.061505.095838.
- [7] J. U. Bowie, "Solving the membrane protein folding problem," *Nature*, vol. 438, no. 7068, pp. 581–589, Dec. 2005, doi: 10.1038/nature04395.

- [8] S. Okushima, T. Nisisako, T. Torii, and T. Higuchi, "Controlled Production of Monodisperse Double Emulsions by Two-Step Droplet Breakup in Microfluidic Devices," *Langmuir*, vol. 20, no. 23, pp. 9905–9908, Nov. 2004, doi: 10.1021/la0480336.
- [9] H. C. Shum, D. Lee, I. Yoon, T. Kodger, and D. A. Weitz, "Double Emulsion Templated Monodisperse Phospholipid Vesicles," *Langmuir*, vol. 24, no. 15, pp. 7651–7653, Aug. 2008, doi: 10.1021/la801833a.
- [10] J. A. Hanson, C. B. Chang, S. M. Graves, Z. Li, T. G. Mason, and T. J. Deming, "Nanoscale double emulsions stabilized by single-component block copolypeptides," *Nature*, vol. 455, no. 7209, pp. 85–88, Sep. 2008, doi: 10.1038/nature07197.
- [11] K. Brandenburg, U. Seydel, A. B. Schromm, H. Loppnow, M. H. J. Koch, and E. Th. Rietschel, "Conformation of lipid A, the endotoxic center of bacterial lipopolysaccharide," *Journal of Endotoxin Research*, vol. 3, no. 3, pp. 173–178, Jun. 1996, doi: 10.1177/096805199600300302.
- [12] G. Milano and T. Kawakatsu, "Hybrid particle-field molecular dynamics simulations for dense polymer systems," *The Journal of Chemical Physics*, vol. 130, no. 21, p. 214106, Jun. 2009, doi: 10.1063/1.3142103.
- [13] G. Milano and T. Kawakatsu, "Pressure calculation in hybrid particle-field simulations," *The Journal of Chemical Physics*, vol. 133, no. 21, p. 214102, Dec. 2010, doi: 10.1063/1.3506776.
- [14] A. De Nicola *et al.*, "Aggregation of Lipid A Variants: A Hybrid Particle-Field Model," *Biochimica et Biophysica Acta (BBA) - General Subjects*, p. 129570, Feb. 2020, doi: 10.1016/j.bbagen.2020.129570.

CFD-PBE FRAMEWORK FOR ASSESSING CLOSE CONTACT SARS-COV-2 TRANSMISSION

Valerio D'Alessandro^{1*}, Matteo Falone¹, Luca Giammichele¹ and Renato Ricci¹

¹*Università Politecnica delle Marche, Dipartimento di Ingegneria Industriale e Scienze Matematiche, Via Brecce Bianche 12, 60131, Ancona, Italy*

ABSTRACT. SARS-CoV-2 virus transmission is mainly attributed to airborne transport of small saliva droplets. Furthermore, non-volatile dry nuclei formation due to droplets evaporation could be a key element in evaluate the effectiveness of social distance adopted during pandemics. For this reason, in this work we present a multi-scale computational framework, developed for the evaluation of airborne saliva droplet transport in a close contact context.

1. Introduction

SARS-CoV-2 virus transmission has been largely attributed to droplets emitted during respiratory activities, both ordinary such as breathing and speaking and extraordinary (sneezing, coughing).

The disease spread mainly involves three possible routes of infection: the fomites, large droplets, and airborne transport of small saliva droplets, [1]. This latter was recognized as the dominant one, [2], and for this reason, a social distancing of 1-2 m (depending on the country), was imposed during the COVID-19 pandemic as protective measure. However, the effectiveness of such preventive action is still an open question, leading to research activities on the so-called “close contact”, in which the emitter and a possible receiver stands at the aforementioned social distancing, [3,4].

In this context, it is important to point out that droplets' evaporation produces non-volatile dry nuclei due to the crystallization process of the sodium chloride within the human saliva, [5]. This mechanism results in droplet nuclei that can stay airborne for a long period, playing a key role in the virus spreading, [6]. Hence, it is evident that a proper understanding of droplet nuclei formation process as well as a correct modelling of respiratory activities are needed for the evaluation of infection risk in a close contact context.

For this reason, this work aims to develop a multi-scale computational framework for the evaluation of airborne saliva droplet transport in a close contact context. The developed model relies on the well-established OpenFOAM library and couples the Population Balance Equation with the particle-source-in-cell (PSI-Cell) method.

2. Model description

The developed model adopts an Eulerian-Lagrangian approach, in which the coexisting phases are coupled through the particle-source-in-cell (PSI-Cell) method [7]. Compressible Reynolds Averaged Navier-Stokes equations was adopted to model the Eulerian phase, in which source terms in mass, momentum, energy, and chemical specie mass fraction equations ensure Lagrangian and Eulerian phases coupling, [8]. Furthermore, the Population Balance Equation (PBE) is adopted within the Lagrangian framework to model the sodium chloride crystallization kinetics and a coupling strategy between PSI-Cell and PBE allows to model micro-scale particles behaviour induced by meso-scale thermo-fluid dynamic phenomena, [6].

The unstructured, cell-centered finite volume approach available within OpenFOAM library was adopted to achieve the carrier phase governing equations solution.

A linear-upwind scheme was used for convective terms approximation, while standard central schemes for diffusive contributions are adopted. Furthermore, the Pressure-Implicit with Splitting Operators (PISO) procedure was employed for pressure-velocity coupling. Time integration technique relies on an implicit, three level, second-order scheme.

Lagrangian phase mass and momentum equations were solved using a backward Euler scheme for time-integration, whereas energy equation was solved analytically. An explicit Strong Stability Preserving Runge-Kutta (SSPRK) having 9 stages and 5-th order of accuracy was adopted for PBE time-integration to avoid blow-up of the computations.

* Corresponding author. E-mail: v.dalessandro@univpm.it

3. Test case

In the present work, a 3D computational domain having length and a width of 1.6 m, and a height $H = 3$ was considered. It represents part of a room in which two standing people are at a distance of 1m, as noticeable in Fig. 1. The susceptible subject was considered to be a mouth-breather. The subject at the domain left (Fig. 1) was considered as emitter through a cough event, so a sinusoidal approximation of breathing combined with a velocity peak is adopted to simulate a real-life condition. In particular, the sinusoidal velocity profile has amplitude of 1 m/s and a frequency of 0.2 Hz, while the coughing effect is modelled by means of a peak in velocity of 5 m/s, following Cortellessa et al. [3].

The initial total mass of saliva droplets laden into the domain during the cough event is 7.7 mg and the particles laden into the domain have initial diameters that follow the Rosin-Rammler distribution, calibrated as in [6]. Moreover, a completely diluted NaCl/water solution consisting in 1% of NaCl was adopted for the saliva chemical composition. The environmental parameter was considered the same of author's previous work, [8].

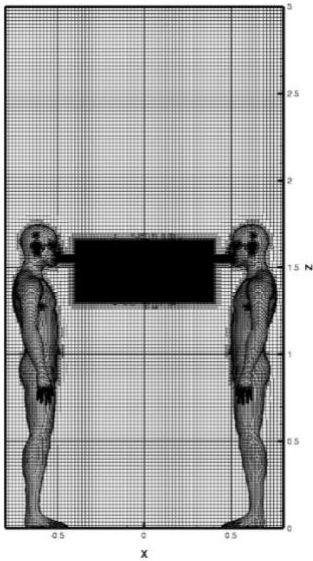


Fig. 1: Computational mesh.

The emitter and receiver mouths were modelled as circular surfaces with a diameter of 2 cm, the nostrils were modelled as circular surfaces with a diameter of 1.13 cm, and the eyes were modelled as ellipses with axes of 2.76 and 1.38 cm respectively, as schematized in Fig. 2.

A hexahedral-based unstructured computational grid realized employing the open source snappyHexMesh algorithm was adopted. It adopts a number of cells of approximately 2.5 million and a refinement in proximity of the emitter and receiver's mouth, in order to better capture the flow features in the breath/cough region, as depicted in Fig. 3.

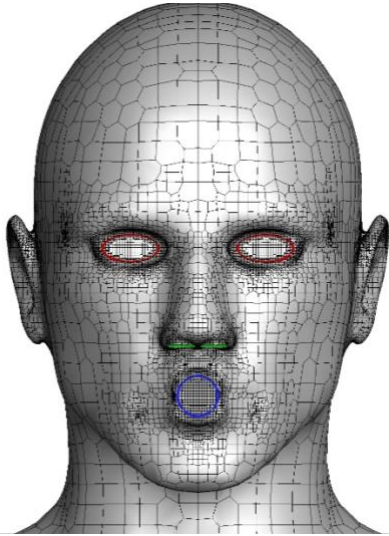


Fig. 2: Schematic of emitter/receiver mucosa.

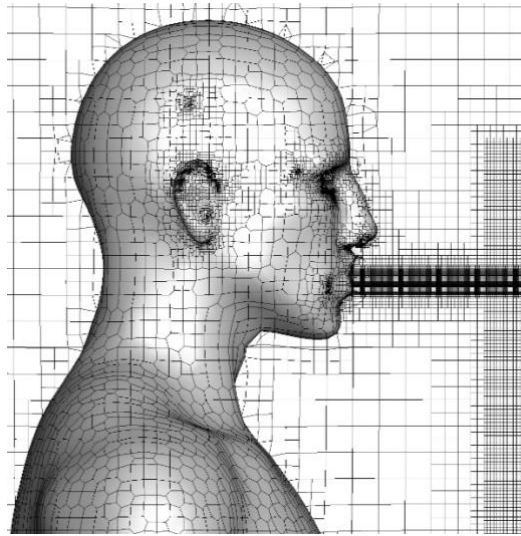


Fig. 3: Computational mesh: refinement in mucosa regions.

Preliminary tests highlights that most of the droplets produced during the cough event reach the receiver at an height of approximately 1 m or, in any case, sufficiently far from his mucosa (see Fig. 4). This confirms that the social distance adopted in Italy during COVID-19 pandemic can suffice to drastically reduce the infection risk.

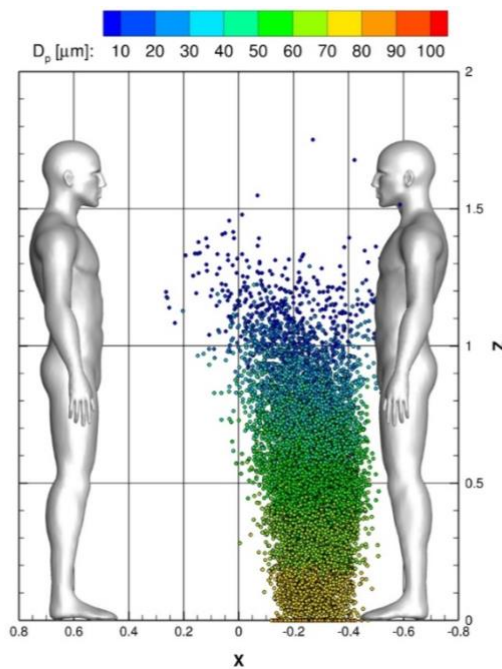


Fig. 4: Droplets evolution after 7s from the cough event (emitter on the left).

Nevertheless, it is important to point out that all the particles that remains at the height of receiver's mucosa consists in dry nuclei. This evidence confirms the importance in correctly model the NaCl crystallization process and leads to draw attention to how the environmental condition could drastically influence the SARS-CoV-2 spreading in a close contact context, due to droplet nuclei formation.

4. Conclusions

In this paper, we present a multi-scale computational framework developed for the evaluation of airborne saliva droplet transport in a close contact context. The developed model relies on the well-established OpenFOAM library and couples the Population Balance Equation with the particle-source-in-cell (PSI-Cell) method. It

admits evaluating the effectiveness of the commonly adopted social distancing during pandemics caused by virus airborne transport. Preliminary results confirms that 1 m can suffice to drastically reduce the infection risk. However, due to droplet nuclei formation that can stay airborne for a long period, the environmental conditions, such as Temperature and relative humidity, could drastically influence the virus spreading in a close contact context.

Acknowledgments

The authors want to acknowledge “Associazione Nazionale Big Data” that awarded this research work within COVID-19–Fast access to the HPC supercomputing facilities program. We acknowledge ENEA for awarding us access to CRESCO6 based at Portici.

References

- [1] Y. Li. Basic routes of transmission of respiratory pathogens—A new proposal for transmission categorization based on respiratory spray, inhalation, and touch. *Indoor Air* 2021, 31, 3-6.
- [2] R. Zhang, Y. Li, A. L. Zhang, Y. Wang, and M.J. Molina. Identifying airborne transmission as the dominant route for the spread of COVID-19. *Proceedings of the National Academy of Sciences of the*
- [3] G. Cortellessa, L. Stabile, F. Arpino, D.E. Faleiros, W. van den Bos, L. Morawska, G. Buonanno. Close proximity risk assessment for SARS-CoV-2 infection. *Sci. Total Environ.* 2021, 794, 148749.
- [4] Zhang N., Chen W., Chan P.-T., Yen H.-L., Tang J.W.-T., Li Y. Close contact behavior in indoor environment and transmission of respiratory infection. (2020) *Indoor Air*, 30 (4), pp. 645 - 661.
- [5] L. Liu, J. Wei, Y. Li, and A. Ooi. Evaporation and dispersion of respiratory droplets from coughing. *Indoor Air* 2017, 27, 179–190.
- [6] D’Alessandro V., Falone M., Giammichele L., Ricci R. A Multi-Scale Approach for Modelling Airborne Transport of Mucosalivary Fluid. (2022) *Applied Sciences (Switzerland)*, 12 (23).
- [7] C. T. Crowe, M. P. Sharma, and D. E. Stock. The particle-source-in cell (PSI-Cell) model for gas-droplet flows. *J. Fluids Eng.* 99, 325–332, (1977).
- [8] V. D’Alessandro, M. Falone, L. Giammichele, and R. Ricci. Eulerian–Lagrangian modeling of cough droplets irradiated by ultraviolet–C light in relation to SARS-CoV-2 transmission. *Phys. Fluids* 33, 031905, (2021).

A DFT INVESTIGATION OF LEAD-FREE PEROVSKITE FASIBR3 (CH(NH₂)₂SIBR3) USING GGA-PBESOL APPROXIMATION FOR PHOTOVOLTAIC APPLICATION

Youssef El Arfaoui^{1*}, Mohammed Khenfouch², Nabil Habiballah¹

¹*Theoretical Physics and High Energy Laboratory (LPTHE), Department of Physics, Faculty of Science, Ibn Zohr University, 8000 Agadir, Morocco*

²*Materials, Electrical Systems, Energy and Environment Laboratory (LMS3E), Materials and Energy Engineering group, Faculty of Applied Sciences, Department of Applied Physics, Ait Melloul, Ibn Zohr University, 86153 Agadir, Morocco*

Corresponding author:

E-mail address: youssef.elfarfaoui@edu.uiz.ac.ma

ABSTRACT. In this work, the density functional theory (DFT) and time-dependent density-functional theory (TDDFT) have been used to study the perovskite FASiBr₃ material for photovoltaic application. These methods implemented under the Quantum Espresso package using the infrastructure CRESCO HP super-computer. In fact, we investigate and discuss the structural and electronic properties of this new perovskite material using the calculation approximation GGA-PBESol. The band structure, the total and partial density of states (DOS and PDOS) of FASiBr₃ has been presented; it is found that this material exhibits semi-conductor behaviour, with a band gap energy value of 2.43eV. Moreover, the optical properties of the studied material have been elaborated and discussed.

1. Introduction

In the previous decade, Hybrid organic-inorganic perovskite solar cells (HOIPSC) made huge progress in efficiency from 3.8 % in 2009 to 25 % in 2020 [1]. Although the excellent efficiency of this material in photovoltaic application, there is severe issues concerning lead toxic effects of lead-based perovskites, in fact, Perovskite solar cells (PSCs) that contain hazardous metal are harmful to both the environment and human beings, for that it is recommended to develop perovskites do not include Pb element. In this work, we performed computational study of the structural and optoelectronic properties of the new Hybrid Organic-Inorganic Lead-free Perovskite FASiBr₃ for photovoltaic application, applying both approach: Density Functional Theory (DFT) and Time-dependent density-functional theory (TDDFT). Our findings showed that this perovskite material possessed direct band gap of 2.43eV, which is suitable for photovoltaic applications. Since this silicon-based perovskite have yet been fabricated, and still to be explored. Consequently, this study will shed some light on the silicon-based solar perovskite that is lead-free material for photovoltaic application.

2. Calculations Methods

In order to study the structural, electronic and optical properties of the new inorganic-organic perovskite FASiBr₃ materials, the calculations are performed using the first-principles density functional theory (DFT) and the time-dependent density functional theory (TDDFT) investigations executed in Quantum Espresso package [2]. In fact, the Perdew-Burke-Ernzerhof (GGA-PBESol) exchange-correlation functional with the ultra-soft pseudo-potentials was used for the electronic properties calculations [3,4]. For the optical properties we apply the norm conserving pseudo-potentials [5]. Also, in our calculations, the k-points [5×5×5] were used for the sampling of the first Brillouin zone.

3. Results and discussion

3.1. Structural properties of FASiBr₃

The crystal structures of the studies FASiBr₃ in these calculations were chosen to be the cubic structure with the *Pm3m* (no. 221) space group. the unit cell of this material contains five atoms as shown the geometry in fig.1, In fact, the FA, (formamidinium),CH(NH₂)₂ cation are positioned at the center of the unit cell and the Silicon (Si) atom is presented at the cubic corners, while the Br anion reside in the face-centered positions as shown in fig.1.

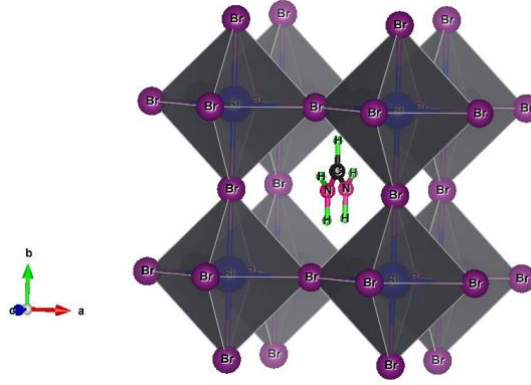


Fig.1: Illustration of the cubic FASiBr₃ perovskite structure using the Vesta package [6].

In fact, the Si atom occupies the corner positions having the "1a" Wyckoff position and (0, 0, 0) fractional coordinates under the crystallographic unit cell of this material. by "1b" Wyckoff location and (1/2, 1/2, 1/2) fractional coordinates, the FA, (formamidinium), CH(NH₂)₂ cation fills the body-centered unit cell positions, while the Br anion covers the side-centered of the unit cell locations through "3c" Wyckoff site and (0, 1/2, 1/2) fractional coordinates [7].

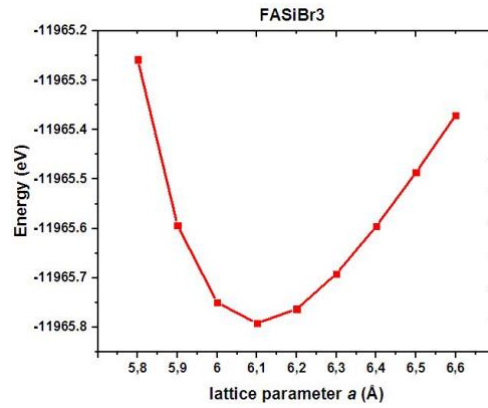


Fig.2: The calculated Total Energy E (eV) of the FASiBr₃ for various lattice parameter a (Å), applying the GGA-PBESol.

To inspect how the lattice parameter a (Å) affects the total energy of the FASiBr₃. We illustrate in fig.2 the variation of energy of FASiBr₃ with the lattice parameter. In fact, we provide in Fig.2 our findings While using the GGA-PBESol approximation, from this figure, It can be shown that the lattice parameter $a = 6.1$ Å corresponds to the lowest total energy for the GGA-PBESol approximation, which is the optimum value. Table.1. Summarize our findings of the lattice parameter a (Å) of the FASiBr₃ compared to other results.

Table 1: the current results compared with the previous work for the lattice parameter a (Å) of the FASiBr₃.

	Our result	[8]	Our result	[8]
Lattice parameter a (Å)	GGA-PBESol 6,1	6.07	Unit cell Volume V in (Å ³) 226,98	221

3.2. Electronic properties of FASiBr₃

To examine the electronic properties of the FASiBr₃ material when employing approximation GGA-PBESol, we study and discuss the electronic properties of the perovskite FASiBr₃ when applying this approximation. We present the band structures and the total and partial density of state for this approximation. In fact, we illustrate the calculated properties for the FASiBr₃, when the lattice parameter is $a=6.1$ Å, to investigate the band structure, DOS and PDOS. Indeed, Fig.3 (a) presents the band structure. From this figure, it's clear that this perovskite is a semi-conductor with band gap energy of 2.43eV. In addition, this figure demonstrates the direct band gap nature of this perovskite, located at R point, being similar to the conventional perovskites [9]. The theoretical studies of other researchers found the band gap values of this silicon based perovskite FASiBr₃: 1.11eV in Ref. [8], using DFT method when using GGA-PBE and the value of 1.92eV when applying the DFT-1/2 approach in the same reference.

Then, we illustrate in Fig.3 (b) the DOS and PDOS of FASiBr3, The band gap seen in fig.3 (a) is proven by this figure. Moreover, it is showed that the conduction band bottom CBB is created with combination of Si atom orbitals and Br atoms orbitals, while the valance band Top VBT is generated mainly with Br atoms orbitals.

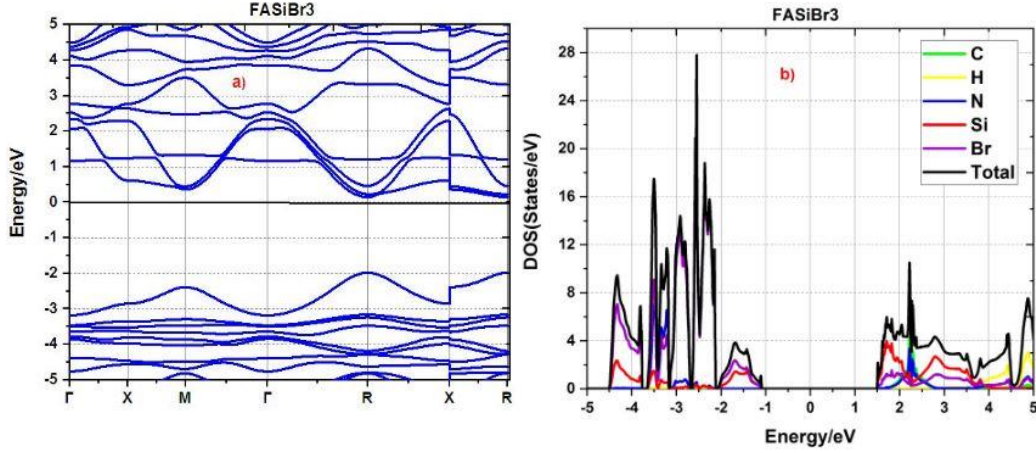


Fig.3: band structure in a), total and partial density of state in b) of the FASiBr3 perovskite applying the GGA-PBESol.

3.2.1. Optical Properties of FASiBr3

In this part, to further explore the optical properties, the time-dependent density functional theory TDDFT is utilized to illustrate the dielectric function of the examined material in terms the complicated dielectric function. In fact, the dielectric function in the excited state, are computed using the TDDFT approach. The complex dielectric function $\epsilon(\omega)$, which is a function of the amount of light absorbed by the material to characterize the system's response to an external electromagnetic field by using photon-electron interaction, was applied to analyse the optical properties of FASiBr3 material.

$$\epsilon(\omega) = \epsilon_1(\omega) + i\epsilon_2(\omega) \quad (1)$$

Here, $\epsilon_1(\omega)$ and $\epsilon_2(\omega)$ represents the real and imaginary elements, respectively. Which can be calculated by the Kramer–Kronig equation [10].

$$\epsilon_1(\omega) = 1 + \frac{2}{\pi} \int_0^{\infty} \frac{\epsilon_2(\omega')\omega' d\omega'}{\omega'^2 - \omega^2} \quad (2)$$

Where, the polarization of light as well as the incident photons dispersion in the material are indicated by the Re element $\epsilon_1(\omega)$ of the $\epsilon(\omega)$ function. While, the Im element $\epsilon_2(\omega)$ denotes the material's light absorption, the following equation provides this function:

$$\epsilon_2(\omega) = \frac{4\pi^2 e^2}{m^2 \omega^2} \sum_{i,j} |\langle i|M|j \rangle|^2 (f_i(1 - f_j)) \delta(E_f - E_i - \hbar\omega) d^3 k \quad (3)$$

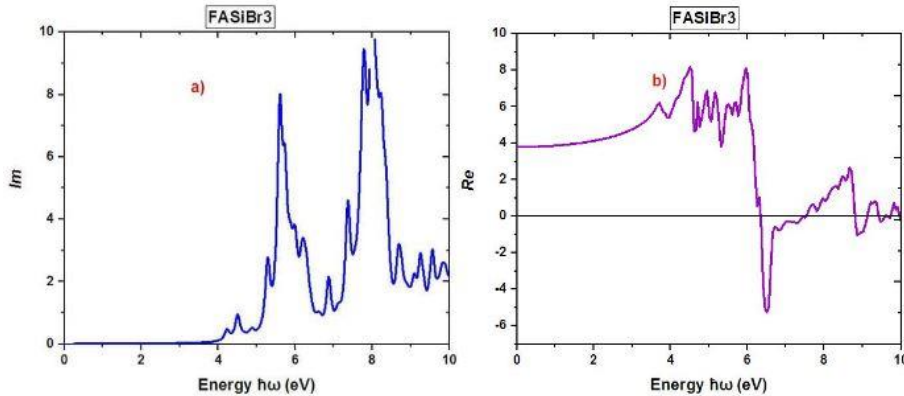


Fig.4: the calculated Im (a) and Re (b) elements of the dielectric function applying GGA-PBESol.

The optical characteristic of FASiBr3 were investigated by computing the Re and Im elements of $\epsilon(\omega)$ function employing the GGA-PBESol as a dependent of energy of incident photon and are presented in Fig.4 (a-b). This figures, display in a) the Im , $\epsilon_2(\omega)$ and in b) the Re , $\epsilon_1(\omega)$ plot of the FASiBr3 perovskite in the energy of photon from 0 to 10eV. In Im term, it is seen in fig.3 (a) the appearance of a main peaks in the Ultraviolet region 4-9 photon energy about 8eV, In addition, $\epsilon_2(\omega)$ ultimately has a positive value which indicated the semi-conductor behaviour of this perovskite material. On the other hand, For the real parts of this FASiBr3

perovskite, demonstrating that Value of $\epsilon_1(\omega)$ is low when incident photon energy was 0, until the incident photon energy attain the value around 2.5eV, This represents the optical band gap of FASiBr₃, In this region, electronic transition which occurs between the Valance band top and Conduction band bottom, after that point, It is found the appearance of several peaks in the energy range 4eV-6eV, It showed that the material under study demonstrates a significant absorption of electromagnetic radiation, when incident photon energy increases, it is observed that $\epsilon_1(\omega)$ also increases and reaches maximum value 8 at 6eV followed by a declining trend. Additionally, several findings of the real and imaginary elements of the dielectric function of others lead-free perovskites found quite analogous to our results, which verified the validity of the present research and supported these theoretical findings [11].

4. Conclusion

In this work, we have investigated the structural, electronic and optical properties of the new Silicon-based FASiBr₃ perovskite, applying the approaches: DFT and TDDFT. In fact, we executed the DFT approach using the Quantum Espresso code to analyze the structure, band structure and density of states (DOS, PDOS). The calculations have been performed using the GGA-PBESol approximation. It is demonstrated that this perovskite is a semi-conductor, the electronic band structure of this Pb-free perovskite shows that FASiBr₃ has a band gap of 2.43eV. Additionally, the optical properties of this material have been presented and discussed; the results of the optical dielectric function suggest that this FASiBr₃ material may be a cost-effective, ecologically alternative for toxic Pb-based perovskite for efficient solar cells.

Acknowledgments

The computing resources and the related technical support used for this work have been provided by CRESCO/ENEAGRID, the Italian National Agency for New Technologies and its staff. Most of the calculations have been carried on CRESCO/ENEAGRID High Performance Computing infrastructure and are part of the VIPERLAB project: FULLY CONNECTED VIRTUAL AND PHYSICAL PEROVSKITE PHOTOVOLTAICS LAB (proposal_VLAB-221-00041). We acknowledge the support of Dr. Simone Giusepponi and the ENEA-GRID team.

References

- [1] Best Research-Cell Efficiency Chart, (n.d.). <https://www.nrel.gov/pv/cell-efficiency.html>.
- [2] P. Giannozzi, S. Baroni, N. Bonini, M. Calandra, R. Car, C. Cavazzoni, D. Ceresoli, G.L. Chiarotti, M. Cococcioni, I. Dabo, A.D. Corso, S. de Gironcoli, S. Fabris, G. Fratesi, R. Gebauer, U. Gerstmann, C. Gougoussis, A. Kokalj, M. Lazzeri, L. Martin-Samos, N. Marzari, F. Mauri, R. Mazzarello, S. Paolini, A. Pasquarello, L. Paulatto, C. Sbraccia, S. Scandolo, G. Sclauzero, A.P. Seitsonen, A. Smogunov, P. Umari, R.M. Wentzcovitch, QUANTUM ESPRESSO: a modular and open-source software project for quantum simulations of materials, *J. Phys. Condens. Matter.* 21 (2009) 395502. <https://doi.org/10.1088/0953-8984/21/39/395502>.
- [3] J.P. Perdew, A. Ruzsinszky, G.I. Csonka, O.A. Vydrov, G.E. Scuseria, L.A. Constantin, X. Zhou, K. Burke, Restoring the density-gradient expansion for exchange in solids and surfaces, *Phys. Rev. Lett.* 100 (2008) 136406. <https://doi.org/10.1103/PhysRevLett.100.136406>.
- [4] D. Vanderbilt, Soft self-consistent pseudopotentials in a generalized eigenvalue formalism, *Phys. Rev. B.* 41 (1990) 7892–7895. <https://doi.org/10.1103/PhysRevB.41.7892>.
- [5] D.R. Hamann, M. Schlüter, C. Chiang, Norm-Conserving Pseudopotentials, *Phys. Rev. Lett.* 43 (1979) 1494–1497. <https://doi.org/10.1103/PhysRevLett.43.1494>.
- [6] K. Momma, F. Izumi, VESTA: a three-dimensional visualization system for electronic and structural analysis, *J. Appl. Crystallogr.* 41 (2008) 653–658. <https://doi.org/10.1107/S0021889808012016>.
- [7] M. Roknuzzaman, J.A. Alarco, H. Wang, A. Du, T. Tesfamichael, K. (Ken) Ostrikov, Ab initio atomistic insights into lead-free formamidinium based hybrid perovskites for photovoltaics and optoelectronics, *Comput. Mater. Sci.* 169 (2019) 109118. <https://doi.org/10.1016/j.commatsci.2019.109118>.

- [8] F. Valadares, I. Guilhon, L.K. Teles, M. Marques, Electronic Structure Panorama of Halide Perovskites: Approximated DFT-1/2 Quasiparticle and Relativistic Corrections, *J. Phys. Chem. C.* 124 (2020) 18390–18400. <https://doi.org/10.1021/acs.jpcc.0c03672>.
- [9] Monika, S. Pachori, R. Agrawal, B.L. Choudhary, A.S. Verma, An efficient and stable lead-free organic–inorganic tin iodide perovskite for photovoltaic device: Progress and challenges, *Energy Rep.* 8 (2022) 5753–5763. <https://doi.org/10.1016/j.egy.2022.03.183>.
- [10] D.C. Hutchings, M. Sheik-Bahae, D.J. Hagan, E.W. Van Stryland, Kramers-Krönig relations in nonlinear optics, *Opt. Quantum Electron.* 24 (1992) 1–30. <https://doi.org/10.1007/BF01234275>.
- [11] L. Peng, W. Xie, Theoretical and experimental investigations on the bulk photovoltaic effect in lead-free perovskites MASnI_3 and FASnI_3 , *RSC Adv.* 10 (2020) 14679–14688. <https://doi.org/10.1039/D0RA02584D>.

INTERPRETATION OF OUT-OF-CONTROL SIGNALS IN MULTIPLE STREAM PROCESS CONTROL CHARTS USING ARTIFICIAL NEURAL NETWORKS

Antonio Lepore*, Biagio Palumbo, Gianluca Sposito

Department of Industrial Engineering, University of Naples Federico II, Naples, Italy¹¹

ABSTRACT. A multiple stream process (MSP) is a process that generates multiple streams of output with quality variables and specifications that are identical across all streams. While several control charts for MSPs can indicate a change in the mean of the process, only a few can accurately identify the stream or group of streams responsible for the signal. In this report, we propose an artificial neural network (NN) that has been specifically trained to automatically interpret out-of-control signals in MSP control charts. Through an extensive Monte Carlo simulation, we demonstrate the superior performance of our proposed NN in correctly identifying the shifted streams.

1. Introduction

A multiple stream process (MSP) refers to a process that simultaneously generates multiple output streams at a given point in time. These streams have quality variables and specifications that are identical across all streams. MSPs are commonly encountered in many real-world processes, including pharmaceutical, chemical, service, and manufacturing industries. Traditional control charting schemes for MSPs are typically capable of identifying two types of out-of-control (OC) signals. The first type involves a mean shift in one or a few streams, while the second type refers to mean shifts occurring simultaneously in all streams. Differentiating between these two types of departures from the in-control (IC) state can provide valuable insights for diagnosis, as they may have distinct root causes. Despite the frequent application of MSPs in various industrial applications, the literature on the statistical process control (SPC) of such processes is not extensive. A detailed review of SPC for MSPs is provided by [1]. However, a limited number of authors have focused on the interesting problem of OC signal interpretation in MSP control charts. Signal interpretation refers to the identification of the stream or group of streams that contribute to the OC signal during the monitoring procedure. This task poses challenges for practitioners and remains an unresolved matter. To address this issue, a control chart can be designed for each stream to simultaneously detect multiple off-target streams. For instance, [2] proposed a two-step method that combines Hotelling's T^2 [3] and the Shewhart control chart proposed by [4] to identify and interpret signals in MSPs. However, their approach exhibits poor performance in accurately classifying shifted streams when the common stream variability is greater than the within-stream variability.

In recent times, the rapid development of computer technology and data acquisition systems has led numerous researchers from various scientific domains to rely on artificial neural networks (NNs) [5] for optimizing processes and resolving real-world problems. The broad and successful implementation of NNs has motivated researchers to explore their effective application in SPC [6-7].

In this report, we present a novel method for automatic and simultaneous signal interpretation in MSP control based on NNs. Section 2 introduces the definition of MSPs. Section 3 presents the proposed strategy for signal interpretation using NNs. Section 4 compares the performance of our proposed approach with the competing strategy proposed by [2,4] through an extensive Monte Carlo simulation.

2. Multiple stream process

[8] introduced a single factor linear model with two sources of variation to define the mathematical formulation of a MSP:

*Corresponding author. E-mail: antonio.lepore@unina.it

$$Y_{tjk} = \mu + A_t + e_{tjk} \quad t = 1, 2, \dots, T, \quad j = 1, 2, \dots, s \quad k = 1, 2, \dots, n, \quad (1)$$

where, μ represents the process mean, A_t represents the difference of the mean over all s streams and n observations at time t from μ , and e_{tjk} represents the deviation of the k th observation from the j th stream at time t from the mean over all the streams at time t . It is assumed that e_{tjk} is a normally distributed random variable with mean 0 and variance σ_e^2 . The variables e_{tjk} are assumed to be independent over t, j , and k . The variable A_t can be independent and normally distributed with zero mean and variance σ_A^2 , or it can exhibit some dynamical behaviour over time depending on the specific process. Throughout the report, the normality of A_t is assumed for simplicity. According to the MSP model described in Equation (1), Y_{tjk} can be decomposed into a process mean μ , a common stream component A_t representing the variation common to all the streams at time t , and an individual stream component e_{tjk} representing the variation between the streams at time t .

To address the OC signal interpretation problem mentioned in the introduction, [4] propose a control chart based on Y_{tjk} for each j may not accurately detect the shifted streams when $\sigma_A > \sigma_e$. Specifically, for each stream j , the sample mean $Y_{tj} = \sum_{k=1}^n Y_{tjk}$ at time t is plotted on the control chart. The lower control limit (LCL) and upper control limit (UCL) for the j th chart are calculated as follows:

$$\text{LCL} = \mu - L \frac{\sigma_Y}{\sqrt{n}}, \quad \text{UCL} = \mu + L \frac{\sigma_Y}{\sqrt{n}}, \text{ where } \sigma_Y = \sqrt{\sigma_A^2 + \sigma_e^2} \quad (2)$$

$\sigma_Y = \sqrt{\sigma_A^2 + \sigma_e^2}$ is the standard deviation of the quality variable Y_{tjk} . It is important to note that using independent univariate control charts can be misleading if not appropriately designed, and typically, the Bonferroni correction [3] is used to adjust for control limits (CLs) to counteract the problem of multiple hypothesis testing.

3. The proposed approach

In this section, we present an innovative approach based on NNs for the automatic identification of the streams that trigger the OC alarm. A multilayer perceptron (MLP) is used to solve a multi-label classification problem to recognize patterns in the data associated with OC streams. Each sample is monitored using a MSP control chart, and after detecting an OC state, the NN is employed to identify the streams that have deviated from the IC state. To formulate the problem as a multi-label classification problem, we define the label vector $\mathbf{y}^{(i)} = [y_1, y_2, \dots, y_l] \in R^l$ as a binary vector so that $y_j = 1$ indicates that the j th stream is shifted. Thus, the MLP is trained so that when a subset $p \subseteq \{1, \dots, s\}$ of streams deviate from the target, the corresponding components of the label vector is set to 1. For instance, in an MSP with $s = 2$ streams, there exist three possible OC scenarios: (1) the first stream is OC ($\mathbf{y} = [1, 0]$), (2) the second stream is OC ($\mathbf{y} = [0, 1]$), and (3) both the first and second streams are OC ($\mathbf{y} = [1, 1]$). To train the NN in identifying OC streams, we generate an appropriate dataset by simulating mean shifts in the streams while keeping the covariance matrix fixed. From all possible OC scenarios, where $p = 1, 2, \dots, s$ streams deviate from their IC state simultaneously, the quality variables Y_{tjk} from each of the p OC streams are simulated through a Monte Carlo simulation as normally distributed with a mean shift size of $\Delta\mu = K\sigma_e$, where $K = \{1, 2, 3, 4\}$ represents the shift magnitude relative to the standard deviation σ_e . The remaining $(s - p)$ streams are simulated as normally distributed with mean μ and variance $\sigma_A^2 + \sigma_e^2$ based on the MSP model (see Equation 1). For monitoring purposes and without loss of generality, we choose the R_t control chart [8] along with the \bar{X} chart [8]. Samples are generated with their corresponding label vectors until 10000 samples are detected as OC by at least one of the two control charts for each shift magnitude and OC scenario. Data are then normalized to have zero mean and unit variance and divided into two groups: a 70% training set and a 30% validation set for hyperparameter tuning optimization. The input layer of the NN consists of $s + 2$ neurons, representing the s sample means Y_{tj} at time t for each stream j , the range statistic R_t (difference between the largest and smallest Y_{tj}) at time t , and the overall mean Y_t at time t . The number of hidden layers and neurons is determined through design choices, aiming to maximize the accuracy in the classification of the shifted streams on the validation set. The output layer consists of s neurons, with each neuron using a sigmoid activation function to independently predict the

probability of the corresponding stream being OC. A value greater than 0.5 indicates that the stream has deviated from the target.

4. Simulation study

A simulation study is carried out to evaluate the performance of the proposed NN technique in identifying the OC streams in MSPs. Additionally, its performance is compared to that of the Shewhart control chart for each stream when a different number of streams p shift off target and under different mean shift size $\Delta\mu$ for a MSP with $s = 6$ streams and variances $\sigma_A = 4$ and $\sigma_e = 1$. We consider all possible scenarios in which a subset p of the streams deviates from the IC state. IC and OC streams are generated as described in Section 3. For each simulated OC scenario, 100000 samples are generated. To ensure a fair evaluation of signal interpretation performance, only those samples identified as OC by the R_t or \bar{X} control charts are processed by the two competing methods. The CLs for the two control charts are determined by simulating IC samples, based on Equation (1), in order to achieve an average run length (ARL_0) [3] of approximately 370.

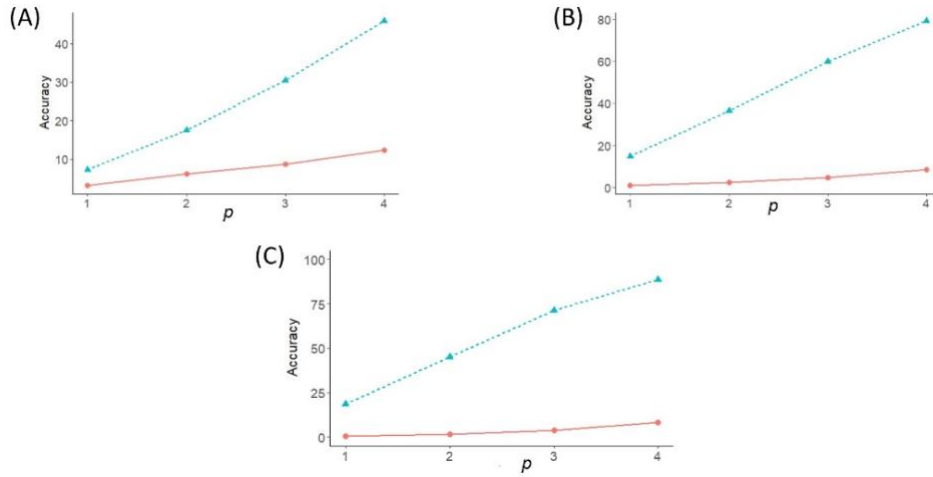


Fig. 1: Accuracy of the Shewhart control charts (red line) for each stream and the proposed NN (blue line) for different mean shift sizes (A) $\Delta\mu = 1\sigma_e$, (b) $\Delta\mu = 2\sigma_e$ and (c) $\Delta\mu = 3\sigma_e$ and for a MSP with $s = 6$, $n = 1$, $\sigma_A = 4$ and $\sigma_e = 1$, at different number $p = 1, 2, 3, 4$ of streams that shift off-target

To adequately train and design the MLP, 10000 samples are simulated for each OC scenario, along with the corresponding label vectors as discussed in Section 3.. A hyperparameters optimization using grid search is performed to explore different NN architectures and hyperparameters. A two-hidden-layer MLP with $s+2$ neurons in the input layer, hidden layers consisting of 20 and 10 neurons respectively, s neurons in the output layer, and rectified linear unit activation functions for the hidden layers, is shown to have a good performance. Figure 1 shows the accuracy of the Shewhart control charts for each stream and the proposed NN for different mean shift sizes (A) $\Delta\mu = 1\sigma_e$, (b) $\Delta\mu = 2\sigma_e$ and (c) $\Delta\mu = 3\sigma_e$ and for a MSP with $s = 6$, $n = 1$, $\sigma_A = 4$ and $\sigma_e = 1$, at different number $p = 1, 2, 3, 4$ of streams that shift off-target. We can see that our method outperforms the competing one in all simulated scenarios. In particular, the difference in their accuracy increases significantly when p increases at a given mean shift size and when mean shift size increase at a given p . The training of the MLP and all simulations are carried out on a single core of an Intel Xeon Platinum 8160 node of the ENEA CRESCO6 system (2.10GHz, 192 GB RAM, no GPU) [10].

5. Conclusion

A MLP is trained to identify the streams that have shifted from the normal state. This research represents the first attempt to tackle the interpretation of MSP control chart signals. Through a simulation study, the proposed NN-based method demonstrates superior performance compared to Shewhart control charts for each stream. The MLP achieves higher accuracy in correctly classifying the shifted streams, particularly when the variation between streams is greater than the variation within each individual stream.

References

- [1] E. K. Epprecht. Statistical control of multiple-stream processes: a literature review. *Frontiers in statistical quality control* **11**, pp. 49-64, (2015).
- [2] A. Ahmadi-Javid and M. Ebadi. A two-step method for monitoring normally distributed multi-stream processes in high dimensions. *Quality Engineering*, pp. **33**(1), 143-155, (2020).
- [3] D. C. Montgomery. Introduction to statistical quality control. John Wiley & Sons, (2020).
- [4] N. S. Meneces, S. A. Olivera, C. D. Saccone and J. Tessore. Statistical control of multiple-stream processes: a shewhart control chart for each stream. *Quality Engineering*, pp. **20**(2), pp. 185-194, (2008).
- [5] I. Goodfellow, Y. Bengio and A. Courville. Deep learning. MIT press, (2016).
- [6] F. Zorriassatine and J. D. T. Tannock. A review of neural networks for statistical process control. *Journal of intelligent manufacturing*, **9**, pp. 209-224, (1998).
- [7] S. Psarakis. The use of neural networks in statistical process control charts. *Quality and Reliability Engineering International*, **27**(5), pp. 641–650, (2011).
- [8] R. R. Mortell and G. C. Runger. Statistical process control of multiple stream processes. *Journal of Quality Technology*, **27**(1), pp. 1-12, (1995).
- [9] F. Iannone, F. Ambrosino, G. Bracco, M. De Rosa, A. Funel, G. Guarnieri, ... and P. Procacci. CRESCO ENEA HPC clusters: A working example of a multifabric GPFS Spectrum Scale layout. *In 2019 International Conference on High Performance Computing & Simulation (HPCS)*, pp. 1051-1052, (2019).

AN AUTOMATED WORKFLOW APPROACH FOR NUMERICAL SCREENING OF FUNCTIONALIZED SILICON SURFACES

Sara Marchio^{1*}, Francesco Buonocore¹, Simone Giusepponi¹, Barbara Ferrucci², Claudio Ronchetti¹ and Massimo Celino¹

¹ENEA, TERIN-ICT Division, CR Casaccia, Via Anguillarese 301, Roma, Italy

²ENEA, FSN-SICNUC Division, CR Bologna, Via Martiri di Monte Sole 4, Bologna, Italy

ABSTRACT. An automated ab initio calculation workflow has been devised and executed for systematically exploring many potential functional organic molecules along with their corresponding structural configurations for adsorption onto Si surfaces. The objective of this workflow is to assess the stability of various functional groups, enabling the identification of promising candidates for further investigation. The computational power of the ENEA's CRESCO cluster was harnessed to accurately simulate and explore numerous configurations using this workflow. The calculation results are automatically collected and recorded in the database installed on CRESCO.

1. Introduction

In recent years, numerical simulations aimed at the development of innovative materials have seen significant advancements, thanks in part to the increased performance of computational infrastructures. These simulations have opened doors for extensive material research and screening on a large scale. This capability allows for the identification of suitable candidates and desired physical parameters, warranting further examination through experimental means. However, one drawback in the intensive use of high-performance computing codes pertains to the management of a high volume of simulations on HPC infrastructures and the handling of vast amounts of data. Various tools have been developed to address these challenges, finding different applications in the fields of computational physics and chemistry. Of particular interest are studies focused on covalent functionalization by organic monolayers on Silicon surface that represent a versatile and powerful approach for tailoring the properties and functionalities of silicon-based materials and devices [1,2]. Indeed, high-coverage monolayers on silicon creates a passivating effect that prevents surface oxidation, which is a crucial step in the development of photovoltaic devices [3]. The functionalization of silicon with organic molecules has been shown to enhance semiconductor performance and offer applications in various fields, including biomolecule immobilization, electron transfer, and molecular catalysis [4-7].

Recent advancements in workflow management, coupled with the continuous increase in computing power, have made automated computational workflows possible. By utilizing this method, the default research workflow is automatically followed to investigate tens of thousands of molecules that can be employed to achieve the desired properties in the functionalized surface.

Here, we introduce a computational automated workflow integrated within the AiiDA framework [8], which has been implemented to systematically explore many potential functional molecules along with their corresponding structural configurations for adsorption onto a Si surface. This workflow takes the surface and functional molecules structures as inputs and generates multiple adhesion configurations corresponding to different binding orientations. The resulting dissociation energies are computed from DFT calculation outputs and stored in a database. This procedure facilitates a methodical assessment of the stability of various functional groups, enabling the identification of promising candidates for further investigation. Moreover, it serves as a guide in experimental efforts towards the realization of desired properties in devices and materials.

2. Workflow description

* Corresponding author. E-mail: sara.marchio@enea.it

The numerical workflow presented here has been tested in a preliminary study of a Silicon Si(111) surface grafted with a single organic molecule. The remaining dangling bonds of the surface are saturated with hydrogen atoms.

The steps of workflow [9] have been defined with particular attention to efficiently manage calculation resources, discard redundant configurations, and store the results in a structured manner for further analysis and retrieval. These can be summarized as follows (see Figure 1):

1. **Structure builder:**
 - a. The structures files of the organic molecule and the passivated H:Si(111) surface are fetched from cloud databases.
 - b. Two structural DFT relax calculations are performed both for isolated molecule and isolated H:Si(111) slab using Quantum Espresso (QE) package.
 - c. The outputs of relaxation calculations are parsed and n distinct structural input files with the molecule grafted onto the surface are generated. In each of the n structures, the molecule is grafted in different configurations, varying the ψ , θ , and γ angles as illustrated in the Figure 2a,b. The generated input files are stored in a dedicated folder.
2. **Symmetry equivalence check:** A check is performed on the structures. Any configuration found to exhibit symmetrical duplicate is discarded, preventing wastage of computational time and resources, and obtaining $m \leq n$ non symmetric configurations.
3. **Computing procedure:** For each of the m configurations of the functionalized surface, a structural relaxation calculation is carried out using Quantum ESPRESSO (QE).
4. **Adapter:** The output of each calculation is converted into JSON format.
5. **Store:** JSON are stored in a MongoDB collection.
6. **Property addition:** The collected data facilitates the analysis of properties (such as dissociation energy) for various systems, achieved by varying the functional groups and geometry. This data collection contributes to identify the most promising structures for further in-depth examination.

The workflow above described has been implemented using the AiiDA infrastructure, incorporating the PyMolDock Python script we have developed and the QE plugin code for carrying out DFT calculations.

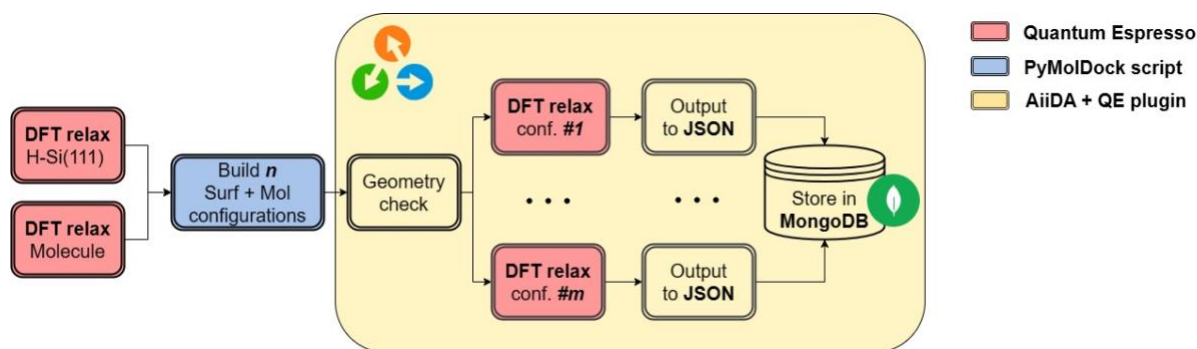


Fig.1: Schematic representation of the numerical workflow.

3. Computational methods

The structural optimization calculations within the automated workflow are performed using density functional theory (DFT) as implemented in the PWscf (Plane-Wave Self-Consistent Field) code from the Quantum Espresso package [10]. To account for Van der Waals interactions, the Wdv-df-cx functional [11] is employed. Electron-ion interactions are described by ultra-soft Vanderbilt pseudopotentials [12]. The Wdv-df-cx functional was used to consider Van der Walls interactions. Corrections for dipole interactions have been also implemented in the calculations. The kinetic energy cutoff has been set to 40 Ry for wavefunctions and to 320 Ry for charge density and potential. The k-point grid has been set 2x2x1. A Silicon slab of 15 Å has been used to model the (111) Si surface. The box dimension perpendicular to the slab is set $L_z = 50$ Å, creating a vacuum space to prevent interaction with adjacent images. The remaining dimensions are set to $L_x = L_y = 15$ Å.

Calculations were carried out exploiting two distinct levels of MPI parallelization, as made available by the Quantum Espresso Code. For each structural optimization calculation, 12 nodes, each equipped with 48 processors, were employed, resulting in a total of 576 processors.

The first level of parallelism involves partitioning into pools, each responsible for a subset of k-points. 4 pools were selected, with an allocation of 1 pool per k-point, thus assigning 3 nodes for each pool.

The second level of parallelization is PW parallelization. Within this scheme, the orbitals represented in the plane-wave (PW) basis set, along with charges and density in either reciprocal or real space, are distributed across multiple processors.

The code employs the 3D Fast Fourier Transform (FFT) to convert electronic wave functions between reciprocal and real space. To parallelize this process, the 3D real-space grid is partitioned into planes and distributed across multiple processors. Similarly, in reciprocal space, columns of G-vectors are allocated to processors to efficiently execute the FFT.

Parallelization of PWs demonstrates a good scaling, particularly when the number of processors in a pool divides evenly into the number of planes defined by the FFT mesh for charge density and wavefunction (respectively $nr3$ and $nr3s$). Here $nr3$ has been set at 576. Therefore, each pool has 144 cores, and 4 planes are assigned to each core.

4. Preliminary results: C₁₀H₁₁ alkenyl molecule

The automated workflow has been applied to graft the C₁₀H₁₁ alkenyl molecule, containing double covalent C=C bonds, onto the H:Si(111) surface. Multiple geometric input configurations are generated by automatic screening of the ψ , θ , and γ angles, represented in Figure 2a,b.

The AiiDA framework is used to implement the execution of the DFT relax calculations and to parse the optimized structures and the corresponding molecule/surface dissociation energies E_d , defined as

$$E_d = (E_m + E_s) - E_{sm} \quad (1).$$

In the Eq. 1 E_{sm} is the energy of the system with the molecule grafted onto the surface and E_m and E_s are the energy of isolated molecule and surface, respectively. The workflow allows to store the output structure's geometrical coordinates and the energy value of each structure in the MongoDB collection.

In Figure 2c, we report the values of E_d corresponding to different geometrical configurations, obtained by varying the γ angle, as an example of the capabilities of the infrastructure we implemented. Here, the ψ and θ angles are kept fixed to the value corresponding to the energy minima. The periodicity with respect to the gamma angle with period of 120°, as expected due to the symmetry of the bottom Si(111) surface, is quite evident. The screening of additional alkenyl molecules and of other class of molecules is in progress

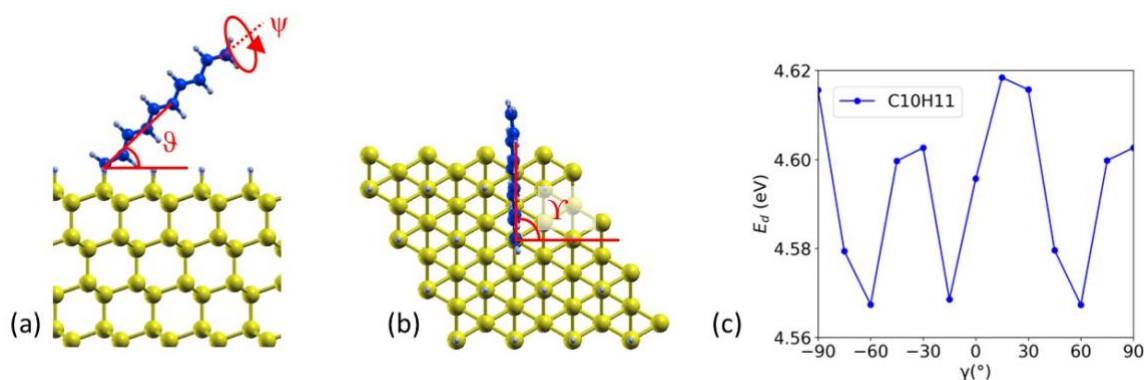


Fig.2: a) Side and b) top views of C₁₀H₁₁ alkenyl molecule grafted onto the hydrogenated Si(111) surface. The ψ , θ , and γ angles are shown therein. In c), the dissociation energy of the optimized configurations is shown by varying the γ angle, with the ψ and θ angles fixed to the value corresponding to the energy minima.

5. Conclusion

In conclusion, we introduced a computational automated workflow integrated within the AiiDA framework used to systematically explore many structural configurations of molecule docking onto a surface. This approach allows for a comprehensive understanding of physical properties and potential applications. We have demonstrated the capabilities of the workflow by employing it to the grafting of the C₁₀H₁₁ alkenyl molecule onto the H:Si(111) surface use case. The resulting dissociation energies and the optimized geometries are computed from DFT calculations and stored in the database. This procedure enables a systematic evaluation of the stability of different functional groups, allowing for the discovery of potential candidates for more in-depth exploration.

Code availability: The PyMolDock Python script has been released and it can be downloaded from <https://gitlab.brindisi.enea.it/francesco.buonocore/pymoldock.git>.

References

- [1] R.J. Hamers. Formation and characterization of organic monolayers on semiconductor surfaces. *Annual Review of Analytical Chemistry* 1, pp.707-736, (2008).
- [2] S.F. Bent. Organic functionalization of group IV semiconductor surfaces: principles, examples, applications, and prospects. *Surface science* 500.1-3, pp. 879-903, (2002).
- [3] Y. Li, S. Calder, O. Yaffe, D. Cahen, H. Haick, L. Kronik and H. Zuilhof. Hybrids of organic molecules and flat, oxide-free silicon: high-density monolayers, electronic properties, and functionalization. *Langmuir* 28.26, pp. 9920-9929, (2012).
- [4] W. Peng, S.M. Rupich, N. Shafiq, Y.N. Gartstein, A.V. Malko and Y.J. Chabal. Silicon surface modification and characterization for emergent photovoltaic applications based on energy transfer. *Chemical Reviews* 115.23, pp. 12764-12796, (2015).
- [5] F. Peng, Y. Su, Y. Zhong, C. Fan, S.T. Lee and Y. He. Silicon nanomaterials platform for bioimaging, biosensing, and cancer therapy. *Accounts of chemical research* 47.2, pp. 612-623, (2014).
- [6] Y. He, C. Fan and S.T. Lee. Silicon nanostructures for bioapplications. *Nano Today* 5.4, pp.282-295, (2010).
- [7] B. Fabre, Y. Li, L. Scheres, S.P. Pujari and H. Zuilhof. Light-Activated Electroactive Molecule-Based Memory Microcells Confined on a Silicon Surface. *Angewandte Chemie International Edition* 52.46, pp. 12024-12027, (2013).
- [8] G. Pizzi, A. Cepellotti, R. Sabatini, N. Marzari and B. Kozinsky. AiiDA: automated interactive infrastructure and database for computational science. *Computational Materials Science* 111, pp. 218-230, (2016).
- [9] C. Ronchetti, M. Puccini, S. Ferlito, S. Giusepponi, F. Palombi, F. Buonocore and M. Celino. Machine learning techniques for data analysis in materials science. *AEIT International Annual Conference 2022*, pp. 1-6, (2022).
- [10] P. Giannozzi, O. Andreussi, T. Brumme, O. Bunau, M.B. Nardelli, M. Calandra, R. Car, C. Cavazzoni, D. Ceresoli, M. Cococcioni and N. Colonna. Advanced capabilities for materials modelling with Quantum ESPRESSO. *Journal of physics: Condensed matter* 29.46, pp. 465901, (2017).
- [11] K. Berland and P. Hyldgaard. Exchange functional that tests the robustness of the plasmon description of the van der Waals density functional. *Physical Review B* 89.3, p.035412, (2014).
- [12] D. Vanderbilt. Soft Self-Consistent Pseudopotentials in a Generalized Eigenvalue Formalism. *Physical Review B* 41.11, pp. 7892-7895, (1990).

ARTIFICIAL INTELLIGENCE PROJECTS ON CRESCO PLATFORM

Angelo Mariano¹, Claudio Ronchetti², Serena D'Onofrio³ and Nicola Quercioli⁴

¹Energy Technologies and Renewable Sources Department, ICT Division, ENEA, Bari territorial office, Bari, Italy

²Energy Technologies and Renewable Sources Department, ICT Division, ENEA, Casaccia Research Center, Rome, Italy

³Energy Technologies and Renewable Sources Department, ICT Division, ENEA, Bologna Research Center, Bologna, Italy

⁴University of Bologna, DEI & WiLab-National Laboratory for Wireless Communications, CNIT, Italy

ABSTRACT. This paper focuses on the utilization of the CRESCO clusters for research projects in the field of artificial intelligence (AI). The CRESCO clusters, renowned for their computational power and advanced technologies, provide an ideal environment for conducting cutting-edge AI research and development. Researchers can leverage the cluster's high-performance computing capabilities and optimized software ecosystem to explore and innovate in AI. The integration of state-of-the-art AI frameworks, libraries, and tools within the Crescoware software stack further empowers researchers to leverage advanced deep learning and computer vision techniques in different domains.

1. Introduction

In the last decades, data-driven methods and Machine Learning and Artificial Intelligence algorithms become very attractive and they have been employed in several contexts. Deep Learning approaches are attractive because they are faster, and the algorithmic representation can be easier than normal code calculations: Deep Learning computations (based on Neural Networks) are dominated by linear algebra and can use very low numerical precision, which makes them very efficient on modern supercomputers. Also, they are easily portable to heterogeneous super-computing hardware as in the case of the CRESCO clusters through the Crescoware portal [1].

2. Fashion domain

The Artificial Intelligence projects related to the fashion domain are mainly focused on object detection and rebalancing based on dataset of fashion images. The first task is the construction of a tool able to recognize different bags in the images, that is an object recognition neural network based on Transformers architecture [3]. The second task regards the optimization of the rebalancing, that is the reorganization of fashion items in the different stores in order to follow the customer request and the market trends. To achieve such a task the technology used is a machine learning approach based on decisional trees. In particular, we implemented a gradient boosting framework using the library LightGBM. LightGBM is designed to be distributed and efficient with the following advantages: faster training speed and higher efficiency, lower memory usage, better accuracy, support of parallel, distributed, and GPU learning, capable of handling large-scale data.

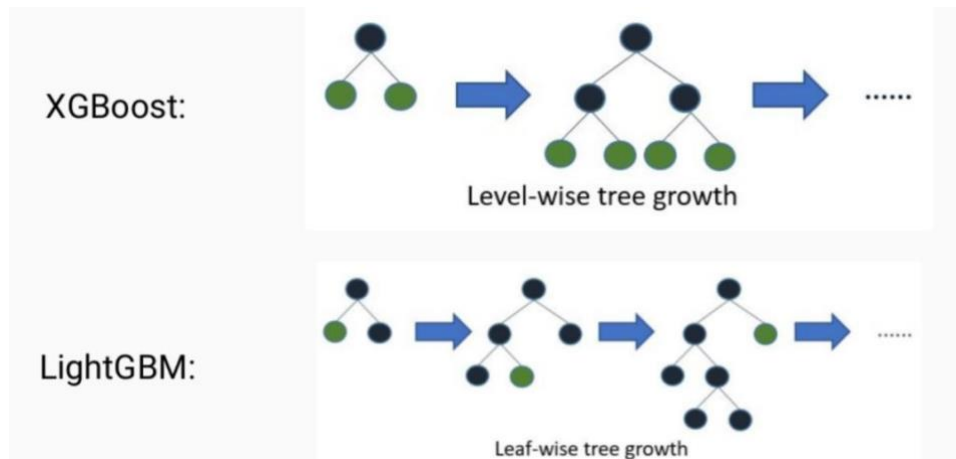


Fig. 1 Representation of the Gradient Boosting Decision Tree (GBDT) framework, focusing on LightGBM

We conducted an extensive scouting expedition into the realm of gradient boosting techniques and machine learning algorithms for the purpose of rebalancing items in the fashion domain. With a focus on improving inventory management, optimizing stock levels, and enhancing customer satisfaction, our exploration yielded fascinating insights and potential applications for the fashion industry.

The utilization of gradient boosting techniques in machine learning has proven to be an invaluable tool in addressing the challenges faced by fashion retailers in rebalancing their item inventory. By harnessing the power of these algorithms, retailers can intelligently predict customer demand, optimize stock levels, and dynamically adjust their inventory to meet the ever-changing preferences of fashion consumers. One of the key advantages of gradient boosting techniques is their ability to handle complex, non-linear relationships between various factors influencing item demand. This enables retailers to capture subtle trends, patterns, and seasonality, allowing for more accurate demand forecasting and proactive inventory management strategies. These algorithms can incorporate a wide range of input features, including historical sales data, customer preferences, product attributes, geographical factors, and even social media trends.

3. Historical ledgers

The objective of this project is to develop an AI-based pipeline for converting a collection of eighteenth-century ledgers into a digital format. The dataset comprises thousands of scanned historical documents from the seventeenth and eighteenth centuries, each containing handwritten information organized in a tabular structure. The primary aim is to transcribe the scanned ledgers into a digital format while preserving the original table structure. By leveraging artificial intelligence techniques, based on vision transformers and computer vision algorithms, the proposed pipeline aims to automate the process of extracting the handwritten information from the scanned ledgers. The system will employ advanced algorithms to accurately recognize and transcribe the text while retaining the tabular layout of the original documents. The successful implementation of this project will enable the efficient digitization of a large collection of historical ledgers, providing researchers and historians with a valuable resource for studying and analyzing historical data. Additionally, the development of the AI-based pipeline will contribute to the preservation and accessibility of valuable historical records, ensuring their availability for more sophisticated data analysis.



Fig. 2 Input source and desired output

The AI solution is based on three steps:

1. Automatic identification of words, numbers and symbols in the document.
2. Automatic transformation of handwritten text in digital text.
3. Construction of the table.

It is constructed using Machine Learning methods based on Transformers [2, 3] and currently is covering step 1 and 2. A demonstration has been shown to European Conference on Computer Vision (ECCV 2022) at Tel Aviv (see Ref. [4] for details).

4. Super-resolution

The application of the super-resolution technique in Artificial Intelligence, which involves the enhancement of low-resolution images to high-resolution images, can be employed in various domains. In this study, we have developed a tool utilizing this method on a dataset consisting of netCDF files that depict atmospheric data generated by the FORAIR-IT system running on the CRESCO cluster. Our objective is to employ Artificial Intelligence techniques to automatically transform the description of air pollutant concentrations within a 20×20 km² domain to a higher resolution representation within a 4×4 km² domain. By leveraging the capabilities of super-resolution, we aim to enhance the spatial resolution of the data, thereby enabling more precise analysis and insights in the domain of air pollution research.

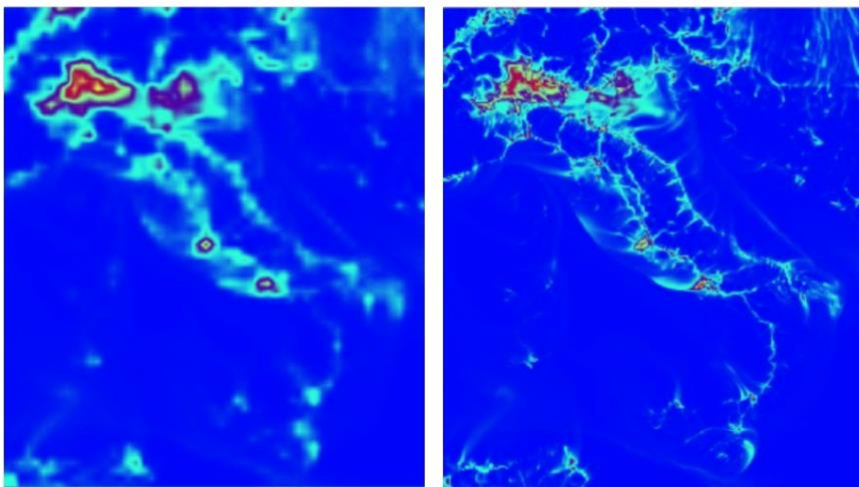


Fig. 3 Low and high resolution images used in the AI model

With the procedure of supervised learning, we trained and validated several neural networks, in particular a structure based on Transformers named SwinIR [5].

5. Software Heritage

The primary motivation for this project stems from the availability of a mirror of Software Heritage, the universal archive of software, within ENEA [6, 7]. This mirror represents the largest dataset accessible in ENEA and serves as an ideal foundation for the development of various Artificial Intelligence tools that heavily rely on software and code as input data. The project encompasses multiple goals, each with its own significance and potential impact. The first goal revolves around the development of a robust system capable of accurately classifying the files contained within the Software Heritage archive by detecting their corresponding license types. To accomplish this, prominent embedding techniques such as BERT [8] and Doc2Vec [9] are employed. These state-of-the-art methods leverage the power of deep learning to extract meaningful representations of textual data, enabling efficient and accurate license classification. By accurately identifying the license types associated with software files, this system facilitates compliance with licensing requirements, enhances software governance, and promotes transparency within the software development community. The second goal focuses on the creation of a new dataset derived from the Software Heritage mirror, utilizing the rich functionality of the Software Heritage API (Application Programming Interface). This new dataset plays a pivotal role in constructing the authors' graph, encompassing the entire software history. By analyzing the evolution of the software community through this graph, valuable insights can be gained, enabling social studies and a deeper understanding of the collaborative dynamics and trends within the software development ecosystem.

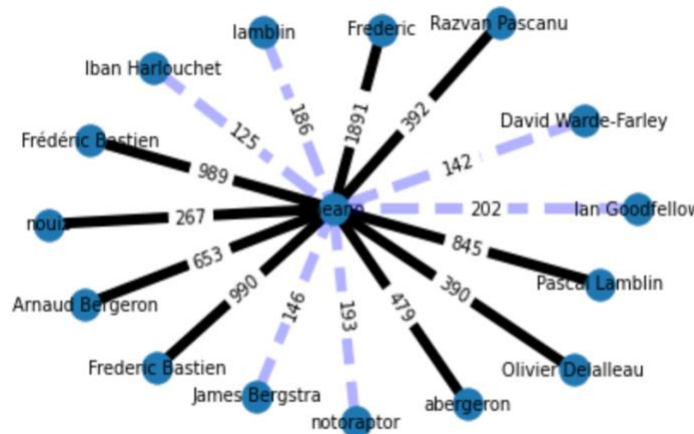


Fig. 4 Graph representation of the best 15 committers in Theano repository of GitHub

The authors' graph enables the exploration of relationships between developers, projects, and code contributions, facilitating the identification of influential individuals, collaboration patterns, and the evolution of software development practices over time. The successful execution of these goals necessitates the utilization of the CRESCO infrastructure, particularly the availability of GPUs (Graphics Processing Units). GPUs play a crucial role in training complex systems, such as the Transformer-based structures used in this project. These structures are characterized by their ability to model long-range dependencies and capture intricate relationships within the software data. By leveraging the computational power of GPUs, the training process can be accelerated, enabling the development of more sophisticated and accurate Artificial Intelligence tools for the analysis and understanding of the Software Heritage dataset.

6. Conclusions

This report aims to enhance ENEA's technology transfer capabilities in the field of artificial intelligence applied to different domains. We live in an algorithmic society, based on the analysis, through intelligent systems, of increasingly rich and detailed digital databases, which allow us to identify patterns of behaviour, profiles, habits. Data from modern digital devices and beyond can be

processed and interpreted through artificial intelligence-based tools to support the relevant scientific community.

References

- [1] Mariano, A., D'Amato, G., Formisano, G., Guarnieri, G., Santomauro, G., Migliori, S. (2022). Crescoware: A Container-Based Gateway for HPC and AI Applications in the ENEAGRID Infrastructure. In: *Arai, K. (eds) Intelligent Computing. SAI 2022. Lecture Notes in Networks and Systems*, vol 506. Springer, Cham.
- [2] Li, J., Xu, Y., Lv, T., Cui, L., Zhang, C., & Wei, F. (2022, October). Dit: Self-supervised pre-training for document image transformer. In *Proceedings of the 30th ACM International Conference on Multimedia* (pp. 3530-3539).
- [3] Carion, N., Massa, F., Synnaeve, G., Usunier, N., Kirillov, A., & Zagoruyko, S. (2020). End-to-end object detection with transformers. In *European conference on computer vision* (pp. 213-229). Springer, Cham
- [4] Ronchetti, C., et al (2022), <https://ict.enea.it/event/enea-a-eccv2022/> (Italian language)
- [5] Liang, J., Cao, J., Sun, G., Zhang, K., Van Gool, L., & Timofte, R. (2021). Swinir: Image restoration using swin transformer. In *Proceedings of the IEEE/CVF International Conference on Computer Vision* (pp. 1833-1844).
- [6] Pietri, A., Spinellis, D., & Zacchiroli, S. (2020, June). The software heritage graph dataset: Large-scale analysis of public software development history. In *Proceedings of the 17th International Conference on Mining Software Repositories* (pp. 1-5).
- [7] Di Cosmo, R., & Zacchiroli, S. (2017, September). Software heritage: Why and how to preserve software source code. In *iPRES 2017-14th International Conference on Digital Preservation* (pp. 1-10).
- [8] Devlin, J., Chang, M. W., Lee, K., & Toutanova, K. (2018). Bert: Pre-training of deep bidirectional transformers for language understanding. *arXiv preprint arXiv:1810.04805*.
- [9] Le, Q., & Mikolov, T. (2014, June). Distributed representations of sentences and documents. In *International conference on machine learning* (pp. 1188-1196). PMLR.

FAST-PETASE: A MOLECULAR DYNAMICS STUDY

Carla Orlando, Mario Prejanò,* Nino Russo and Tiziana Marino*

Dipartimento di Chimica e Tecnologie Chimiche, Laboratorio PROMOCS cubo 14C, Università della Calabria, I-87036 RENDE (CS), Italy.

ABSTRACT. FAST-PETase is an enzyme recently obtained by artificial intelligence and machine learning, with the ability to depolymerize polyethylene terephthalate (PET), a synthetic polymer employed in plastics and in clothing fibers. A model of four monomers was chosen to describe the PET substrate and all-atoms classical molecular dynamics simulations on apo- and substrate bound- FAST-PETase were carried out at 30°C and 50°C to perform a comparative investigation of the FAST-PETase in apoform and in the complex with substrate to gain insights on the binding step of the catalytic cycle. At 50 °C, the FAST-PETase suffers a pre-organization to bind the PET so that the interactions in the binding region favor conformation of the PET model more reactive improving the catalytic activity of the enzyme.

1. Introduction

Using enzymes that hydrolyze and recycle poly(ethylene terephthalate) (PET) represents an important challenge in biocatalysis devoted to find attractive eco-friendly solutions. Enzyme-based degradation of PET is an example of eco-friendly recycling strategy compared with other waste handling methods such as chemical and mechanical processes.

A recent study by means of machine learning techniques based on three-dimensional (3D) convolutional neural network (CNN), proposed stable mutations for the PETase enzyme, [1] and allowed to focus on one of these variants having improved hydrolytic activity, who was named FAST-PETase (FAST-: functional, active, stable, and tolerant, see **Figure 1**).

This engineered enzyme, having as template the ThermoPETase scaffold[2], contains five mutations compared to the wild-type form (Asn233Lys-Arg224Gln-Ser121Glu-Asp added by the prediction and Asp186His-Arg280Ala on the scaffold) presenting a wider working temperature range (30°C-60°C), with an optimal value at 50°C. Furthermore a superior catalytic activity compared to the wild-type enzyme and to the other already engineered forms was observed. [1] Although a lot of work is carried out on the PETase and other its variants [2-8], atomistic insights on the FAST-PETase working mechanism are lacking and the investigation of the early binding step is required to evidence the effects on the introduced mutations.

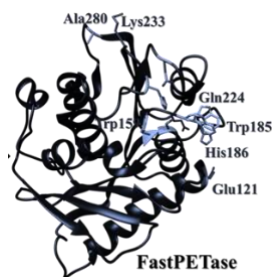
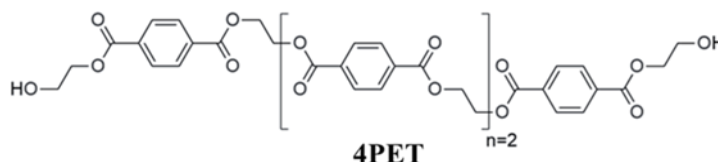


Fig. 1: FAST-PETase structure with the monitored residues during MD simulations.

A computational investigation applying Molecular Docking and Molecular Dynamics techniques on the engineered FAST-PETase of both the apoform and its corresponding complexed with a tetramer PET model as substrate was performed by a comparative analysis of *FAST-PETase*:4PET binary complex at 30°C and 50°C. In particular, we focused on the structural and dynamic properties of FAST-PETase enzyme, at 30°C and at the optimal working temperature of 50°C, [1] shedding light on protein-substrate and substrate-substrate interactions that may occur during the binding step of the catalytic mechanism and that we propose to be responsible of the improved FAST-PETase enzymatic activity.

2. Computational Methods

The X-ray structure (PDB code: 7SH6) [1] was used to obtain the FAST-PETase. All the simulations were carried out adopting the Gromacs package. [9] The ff99SB forcefield was selected to describe the protein. The polymer substrate was modeled considering four monomers (4PET, see Scheme 1), as already found in other *in silico* investigations. [5,10]



Scheme 1. The 4PET model used in our simulations.

The parameters for the 4PET (see Scheme 1) were calculated from HF/6-31G* optimizations using the Gaussian09 D.01 code. [11]

The protein systems were initially minimized and relaxed by applying harmonic positional constraints on all atoms ($50 \text{ kcal mol}^{-1} \text{ \AA}^2$) using 5000 steepest descent (SD) steps, followed by 5000 conjugate gradient (CG) steps, while in the second stage of minimization, the entire system was released unconstrained and then progressively heated to 30 °C and 50 °C for 20ns, using the Langevin thermostat in the NVT ensemble. For the phase productive of the MD simulations, 300 ns trajectory were collected, keeping the systems at 1 bar pressure in the NPT ensemble and selecting the Berendsen barostat with a time constant $\tau_p = 2.0$ ps. In all the simulations, the SHAKE algorithm, and Particle Mesh Ewald (PME) summation method were adopted, with an integration step of 2 fs and a cutoff radius of 10.0 Å, and the water molecules were treated with the TIP3P scheme. The same protocol was successfully applied in many previous investigations. [12-15] The conformational behavior of the alone 4PET in solution ($34 \times 30 \times 38 \text{ \AA}^3$ TIP3P water box) was also investigated, by considering different temperature values: 30 °C (303 K), 50 °C (323 K) and 150 °C (425 K). For each temperature considered, the final production was carried out for 150 ns. In brief, a total of 1.2 μs for apo FAST-PETase and its complexed form and 0.45 μs of MDs were performed for 4PET systems.

On all MD simulations the clustering analysis was applied in order to find the dominant conformation of the protein along the course of the simulations. In particular, the representative conformations were collected through RMSD-based geometric clustering, sampling similar structures during the MD simulations, selecting Gromos algorithm with a cut-off of 2.5 Å.

Molecular docking. Molecular docking was carried out using AutoDock version 4.2. [16] aiming to investigate possible binding modes and substrate interactions in the vicinity of the catalytic triad of the FAST-PETase protein (Ser160, His237, Asp206). The docking area was determined using AutoGrid. A size of $46 \times 46 \times 46 \text{ \AA}^3$ centering the grid on the $C\alpha$ of Ser160. The genetic algorithm (LGA) was used for the conformational search of the ligand. The final docked poses were grouped using an RMSD tolerance of 2 Å.

3. Results

3.1 MD simulations of FAST-PETase apoforn

For both performed simulations (30°C and 50°C), the trend of RMSD assumes values compatible with a good structural stability. The representative geometries generated by hierarchical clustering procedure showed similar conformational features of the system if compared to the X-ray structure in both cases. However, the analysis of RMSD calculated for backbone atoms of the FAST-PETase highlighted values oscillating in proximity of 1.2 Å and 1 Å, at 50 °C and at 30 °C, respectively in the region of the protein where the active site cleft is located and where the 4PET. As consequence of this, many grooves on the solvent accessible part are generated evidencing so, a pre-organization of the active site at 50°C takes place.

3.2 MD simulations of FAST-PETase-4PET

From the analysis of cMD simulations of the FAST-PETase-4PET complex at 50°C with respect to at 30°C is observed a more efficient orientation of aromatic amino acid residues such as Trp185 and Tyr87 implicated in the recognition of the substrate by anchoring the terephthalic rings of 4PET for the increased hydrophobic and π -stacked interactions.

Such protein-substrate interactions facilitate the W-shaped conformation of 4PET at 50 °C, which has a broadly extended shape of the substrate over the surface of the binding site of the protein. In contrast to the wrapped one, mainly encountered during the MD simulations at 30 °C, 4PET is closer to catalytically important residues, including the nucleophilic Ser160 and the oxyanion hole backbone of Met161, and can be therefore linked to the enhanced enzymatic activity observed at 50 °C. The W-shaped conformation better fits the cleft formed by the occurrence of salt-bridge between the mutated Lys233 and Asp204 and was further stabilized by the interaction with Arg90.

DFT calculations performed on the 4PET model alone on both wrapped and W- shapes further show the former one is a higher- and inaccessible energy conformation of 4PET in solution ($\Delta E \sim 12$ kcal/mol in favor of the wrapped-shape). Really, MD simulations of 4PET in solution, performed at 30 °C, 50 °C and 150 °C, contributes to better monitor when the W-shaped like conformation is more persistent. Outcomes propose that this kind of conformation for 4PET is mainly favored by the enzyme at 50 °C. (Figure 2)

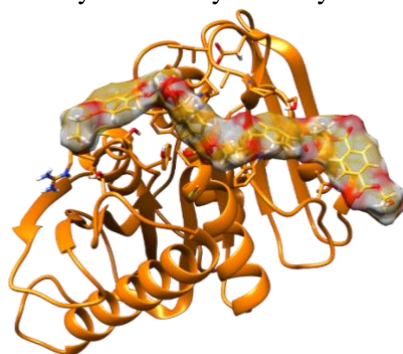


Fig. 2: The most frequent conformation assumed by 4PET inside the binding region of FAST-PETase during the MD simulation at 50°C.

From the MD simulations on the protein complexed to the PET model emerged that FAST-PETase environment at 50 °C improve the occurrence of catalysis via the destabilization of the substrate promoting its higher-energy conformations of the substrate not easily accessible in normal conditions. Results provide useful insights to rationalize the experimental outcomes. The average short distance of each 4PET monomer to the important FAST-PETase catalytic residues and mutated ones, from MD at both temperatures, can be related to the production of a greater number of monomers, at 50 °C.

Acknowledgments

"The computing resources and the related technical support used for this work have been provided by CRESCO/ENEAGRID High Performance Computing infrastructure and its staff [17]. CRESCO/ENEAGRID High Performance Computing infrastructure is funded by ENEA, the Italian National Agency for New Technologies, Energy and Sustainable Economic Development and by Italian and European research programmes, see <http://www.cresco.enea.it/english> for information".

References

1. H. Lu, D. J. Diaz, N. J. Czarnecki, C. Zhu, W. Kim, R. Shroff, D. J. Acosta, B. Alexander, H. O. Cole, Y. Zhang, N. A. Lynd, A. D. Ellington, H. S Alper. Machine learning-aided engineering of hydrolases for PET depolymerization. *Nature*, **604**, 662-667 (2022).
2. H. F. Son, I. J. Cho, S. Joo, H. Seo, H.-Y. Sagong, S.Y., Choi, S. Y. Lee, K.-J. Kim. Rational protein engineering of thermo-stable PETase from *Ideonella sakaiensis* for highly efficient PET degradation. *ACS Catal.* **9**, 3519-3526 (2019).
3. Y. Cui, Y. Chen, X. Liu, S. Dong, Y. Tian, Y. Qiao, R. Mitra, J. Han, C. Li, X. Han, W. Liu, Q. Chen, W. Wei, X. Wang, W. Du, S. Tang, H. Xiang, H. Liu, K. N. Houk, B: Wu. Computational redesign of a PETase for plastic biodegradation under ambient condition by the GRAPE strategy. *ACS Catal.* **11**, 1340-1350, (2021).

4. H. P. Austin, M. D. Allen, B. S. Donohohe, N. A. Rorrer, F. L. Kearns, R. L. Silveira, B. C. Pollard, G. Dominick, R. Duman, K. E. Omari, V. Mykhaylyk, A. Wagner, W. E. Michener, A. Amore, M. S. Skaf, M. F. Crowley, A. W. Thorne, C. W.; Johnson, H. L. Woodcock, J. E. McGeehan, G. T. Beckham. Characterization and engineering of a plastic-degrading aromatic polyestherase. *Proc. Natl Acad. Sci. USA*, **115**, E4350–E4357 (2018).
5. S. Joo, I. J. Cho, H. Seo, H. F. Son, H.-Y. Sagong, T. J. Shin, S. Y. Choi, S. Y. Lee, K.-J. Kim Structural insight into molecular mechanism of poly (ethylene terephthalate) degradation. *Nature Commun.*, **9**, 382, (2018).
6. C. Liu, C. Shi, S. Zhu, R. Wei, C.-C. Yin. Structural and functional characterization of polyethylene terephthalate hydrolase from *Ideonella sakaiensis*. *Biochem. Biophys. Res. Commun.*, **508**, 289-294 (2019).
7. B.-C. Knott, E. Erickson, M. D. Allen, J. E. Gado, R. Graham, F. L. Kearns, I. Pardo, E. Toèuzlu, J. J. Anderson, H. P. Austin, G. Dominik, C. W. Johnson, N. A. Rorrer, C. J. Szostkiewicz, V Copié, C. M. Payne, H. L. Woodcock, B. S. Donohoe, G. T. Beckham, J. E. McGeehan. Characterization and engineering of a two-enzyme system for plastics depolymerization. *Proc. Natl: Ac. Sci. USA* **117**, 25476-25485 (2020).
8. X. Han, W. Liu, J.-W. Huang, J. Ma, Y. Zheng, T.-P. Ko, L. Xu., Y.-S. Cheng, C.-C. Chen, R.-T. Guo. Structural insight into catalytic mechanism of PET hydrolase. *Nature Commun.* **8**, 2106, (2017).
9. M. J. Abraham, T. Murtola, R. Schulz, S. Páll, J. C. Smith, B. Hess, E. Lindahl. GROMACS: High performance molecular simulations through multi-level parallelism from laptops to supercomputers. *SoftwareX*, **1–2**, 19–25 (2015).
10. B. Guo, S. R. Vanga, X. Lopez-Lorenzo, P Saenz-Mendez, S. R. Ericsson, Y. Fang, X. Ye, K. Schrivier, E. Bäckström, A. Biundo, R. A. Zubarev, I. Furò, M. Hakkarainen, P.-O. Syren. Conformational Selection in Biocatalytic Plastic Degradation by PETase. *ACS Catal.*, **12**, 3397–3409 (2022).
11. Frisch, M.J.; Trucks, G.W.; Schlegel, H.B.; Scuseria, G.E.; Robb, M.A.; Cheeseman, J.R.; Fox, D.J. Gaussian 09. Gaussian, Inc.: Wallingford, CT, USA, (2009).
12. A. Perez-Gonzalez, M. Prejanò, N. Russo, T. Marino, A. Galano. Capsaicin, a powerful •OH-inactivating ligand. *Antioxidants*, **9**, 1247, (2020).
13. M. Prejanò, F. E. Medina, M. J. Ramos, N. Russo, P. A. Fernandes, T. Marino. How the Destabilization of a Reaction Intermediate Affects Enzymatic Efficiency: The Case of Human Transketolase. *ACS Catal.*, **10**, 2872-2881 (2020).
14. M. Prejanò, I. Romeo, M. A. La Serra, N. Russo, T. Marino. Computational study reveals the role of water molecules in the inhibition mechanism of LAT1 by 1, 2, 3-dithiazoles. *J. Chem. Inf. Model.*, **61**, 5883-5892 (2021).
15. A. Parise, G. Ciardullo, M. Prejanò, A. de la Lande, T. Marino. On the Recognition of Natural Substrate CTP and Endogenous Inhibitor ddhCTP of SARS-CoV-2 RNA-Dependent RNA Polymerase: A Molecular Dynamics Study. *J. Chem. Inf. Model.*, **62**, 4916-4927 (2022).
16. G. M. Morris, R. Huey, W. Lindstrom, M. F. Sanner, R. K. Belew, D. S. Goodsell, A. J. Olson. Autodock4 and AutoDockTools4: automated docking with selective receptor flexibility. *J. Comput. Chem.*, **16**, 2785-2791 (2009).
17. F. Iannone et al., "CRESCO ENEA HPC clusters: a working example of a multifabric GPFS Spectrum Scale layout," 2019 International Conference on High Performance Computing & Simulation (HPCS), Dublin, Ireland, 2019, pp. 1051-1052, doi: 10.1109/HPCS48598.2019.9188135.

PRELIMINARY CFD INVESTIGATION OF BARE FUEL BUNDLE FOR LMFR APPLICATIONS

Daniele Panico^{12*}, Roberto Da Vià², Giacomo Grasso²

¹*newcleo Srl, via Giuseppe Galliano 27, 10129, Turin, Italy*

²*ENEA FSN-SICNUC-PSSN, C.R. "E. Clementel", via Martiri di monte sole 4, 40129 Bologna, Italy*

ABSTRACT. A preliminary hydraulic study by Computational Fluid Dynamics (CFD) has been performed to evaluate pressure losses in fuel pin bundles for Liquid Metal cooled Fast Reactor (LMFR) applications. Indeed, the aim of this work is the assessment of the feasibility to use periodic boundary conditions to reduce the computational domain and thus saving computational resources. For this reason, the study focuses on simplified geometry. i.e., the bare bundle, as the pin spacing is not modelled. The open-source CFD code OpenFOAM has been used on ENEA CRESCO6 High Performing Computing system.

1. Introduction

Liquid-metal-cooled fast reactors represent one of the most promising technologies, in the field of nuclear power plants, to fulfil the requirements of energy production in terms of sustainability, safety and with a reduced impact on the environment [1]. Fuel pin bundles of LMFRs usually consists of hexagonal shape assemblies where pins are arranged in a triangular lattice. Common solutions adopted to separate the pins and keep them in position is to use a wrapping wire or grids. However, both spacing introduce some difficulties when performing Computational Fluid Dynamics calculations, in particular when generating the computational mesh because of the presence of very narrow gaps and geometrical sharp angles. Both determine an increase in the number of cells of the mesh to reach a good discretization level. The aim of this work is the investigation of the periodic boundary conditions available in the open-source software OpenFOAM as an option to save computational resources. In fact, such boundary conditions are used to reproduce a fully developed flow and they can be exploited to reduce the domain extension (along the flow direction) while preserving a good quality mesh at a given cross section. The main scope of the document is the comparison of pressure drop results obtained when those boundary conditions are used versus standard inlet-outlet ones for a 19-pin bundle at given flow regime. For this reason, the geometry was simplified as no spacing is considered. Thus, the proposed case study is representative of flow regions far from grids where fully developed flow conditions are reached.

2. Software and procedure

As aforementioned, the CFD software used is OpenFOAM, in particular this study was performed with OpenFOAM v9 [2]. Taking advantage of the geometry, it is possible to mesh only a limited section of the bundle axial length (referred to as "axial step") and then extrude it to reproduce the entire domain. The meshing stage is accomplished with the following steps:

1. Tetrahedral mesh of one axial step using SALOME [3]
2. Conversion of the tetrahedral mesh into polyhedral one using the OpenFOAM built-in application, *polyDualMesh*.
3. Addition of boundary layers using *meshContractionFoam* (an application developed on purpose).
4. Extrusion of the obtained mesh, along the axial direction, with the *extrudeMesh* (a utility provided with OpenFOAM).

¹² * Corresponding author. E-mail: daniele.panico@newcleo.com

Steps from 1 to 3 are performed on local machine, then the last one is performed in addition to the simulation when submitting the job on CRESCO6. The application *meshContractionFoam* was developed as the periodic boundary conditions of OpenFOAM adopted for this study (named *cyclic* [4]) requires a perfect match of the surface mesh on which it is applied. Built-in applications of OpenFOAM (like *snappyHexMesh*) failed to respect such constraint, therefore the necessity for the implementation arose. Finally, *simpleFOAM* solver was used to compute the steady-state incompressible fluid flow solution.

3. The geometrical and computational model

The cases under analysis consist of a 19-pin bare bundle with liquid lead as fluid. The geometrical data are summarized in Table 1 while the cross section is depicted in Fig. 1. Four cases are simulated, the first one actually uses the cyclic boundary conditions, and the simulated length is equal to 180 mm. Other three cases were simulated, adopting uniform velocity at the inlet and fixed zero pressure at the outlet, each of them with a different simulated length. Table 2 summarizes the cases analysed.

Table 1: 19-pin bundle geometry

Parameter	Value [mm]
Pin diameter	8.5
Lattice pitch	11
Pin centre to wall distance	5.53

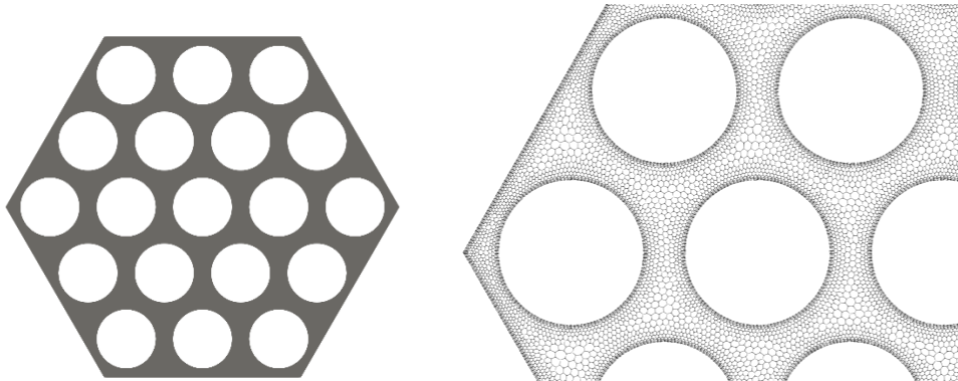
Table 2: Axial length of the analysed cases.

Case name	Axial length [mm]
cyclic	180
2H	360
3H	540
4H	720

All cases are steady state and incompressible with flow conditions corresponding to a Reynolds number of 18700 and a kinematic viscosity of $2.127e-7$ m²/s. The corresponding velocity is used as inlet value for cases 2H, 3H and 4H; as target velocity value for cyclic one. Turbulence is modelled with k-omega-SST model [5]. Boundary conditions on pins and wrapper walls are set as follows:

- Pressure: zero gradient
- Velocity: no-slip
- k-omega: wall functions

Finally, the (final polyhedral) mesh is shown in Fig. 1 while the numbers of cells for each case are given in Table 3.



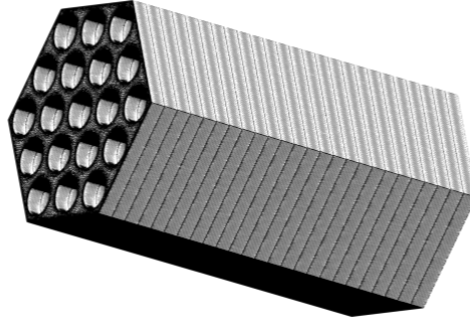


Fig.1: 19-pin fuel pin bundle cross section (left), detail of the computational mesh (right) and axial discretization for the cyclic case (bottom).

Table 3: Mesh characteristics for each case.

Parameter	cyclic	2H	3H	4H
Number of axial steps	25	50	75	100
Number of cells	743100	1486200	2229300	2972400

4. Results

Fig. 2 shows the pressure gradient results (divided by the lead density) as a function of the number of hydraulic diameters. The pressure gradient is directly available as an output of the solver for the cyclic case, while it was computed as the difference between the average pressure on two cross sections and the corresponding distance in axial direction for the other three cases. The selected cross sections are the ones corresponding to the last axial step before the boundary and the one placed 60 mm before in upstream direction. The entrance length, i.e., the axial length needed for the flow to fully develop, is usually expressed as a multiple of the hydraulic diameter [6]. Although, the expected entrance length is ~ 23 hydraulic diameters for the given Reynolds number, the boundary conditions still affect the pressure drop result. This is evident since by increasing the axial extent of the domain the result converges to the periodic boundary conditions one. Fig. 2 provides an indirect verification of the correct implementation of the cyclic boundary condition as well. Fig. 2 resumes also the computational cost of each case as the product between the execution time and the number of cores used to run the case. Finally, Table 4 provides the average y^+ values for all the cases over the pin and wrapper wall boundaries.

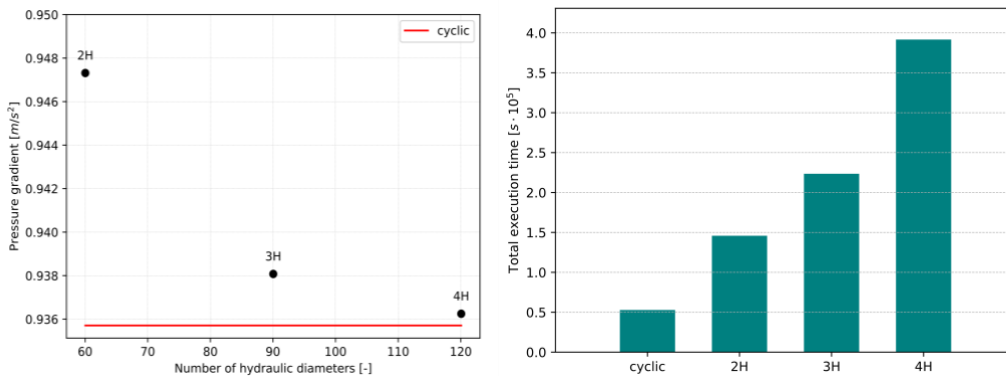


Fig.2: Pressure gradient results (left) and total execution time (right) for each case.

Table 4: Average y^+ values for each case over pin and wrapper wall boundaries.

Boundary	cyclic	2H	3H	4H
Pin wall(s)	3.26	3.25	3.25	3.25
Wrapper wall(s)	2.89	2.89	2.82	2.79

5. Conclusion

A preliminary CFD investigation has been performed to assess the possibility to use periodic boundary conditions to simulate heavy liquid metal flow in fuel pin bundles using the open-source software OpenFOAM. The results show that this setup has indeed notable advantages as it is able to correctly predict the fully developed pressure drop without being affected by boundary conditions together with a consistent reduction of resources both in terms of domain discretization and computational time. This simple benchmark suggests the application of such modelling approach also for more complex geometries like wire wrapped bundles.

References

- [1] R. Plunkienier and D. Ridikas. Modelling of HTRs with Monte Carlo: from a homogeneous to an exact heterogeneous core with micro particles. *Annals of Nuclear Energy* **30**, pp. 1573-1585, (2003).
- [2] Official OpenFOAM v9 github repository: <https://github.com/OpenFOAM/OpenFOAM-9>.
- [3] SALOME, The open-source platform for numerical simulation, <https://docs.salome-platform.org/latest/main/gui.html>.
- [4] OpenFOAM v9 boundary conditions' description: <https://doc.cfd.direct/openfoam/user-guide-v9/boundaries>.
- [5] F.R. Menter. Zonal Two Equation k- ω Trubulence Models for Aerodynamic Flows. AIAA 93-2906 (1993).
- [6] Munson, B.R. and Rothmayer, A.P. and Okiishi, T.H. Fundamentals of Fluid Mechanics, 7th Edition. Wiley (2012).

AB-INITIO STUDY OF VINYLENE CARBONATE REACTIVITY AT LITHIUM METAL INTERFACE

Michele Pavone^{1*}, Francesca Fasulo¹, Ana B. Muñoz-García², Arianna Massaro¹

¹University of Naples “Federico II”, Department of Chemical Sciences, Comp. Univ. Monte Sant’Angelo Via Cintia 21, 80126, Naples, Italy

²University of Naples “Federico II”, Department of Physics “Ettore Pancini”, Comp. Univ. Monte Sant’Angelo Via Cintia 21, 80126, Naples, Italy

ABSTRACT. We employed the Density Functional Embedding Theory (DFET) to dissect the tangled vinylene carbonate (VC) reactivity toward the formation of a stable and protective solid-electrolyte interphase (SEI) at Lithium metal anode interfaces. By exploring VC adsorption and dissociation paths, our DFET study reveals that the thermodynamically accessible mechanisms for VC ring-opening reductive reaction on Li(001) feature energy barriers of ~0.3 eV.

1. Introduction

The research carried out at the University of Naples “Federico II” has mainly targeted the vinylene carbonate (VC) reactivity at Lithium metal surfaces.¹ An efficient strategy to achieve durable and effective Lithium metal batteries is by engineering the solid-electrolyte interphase (SEI) with purposely designed molecules.² Some recent experiments proved that the vinylene carbonate (VC) promotes the formation of a stable and protective SEI between Li metal and the electrolyte.³⁻⁵ Notwithstanding the well-known SEI composition, it is difficult to control the VC reactivity, that involves dissociation and polymerization at the electrode surface. Different decomposition paths can be envisaged, involving an initial single-bond cleavage occurring either at the -O-C=C- vinyl ($C_V O_V$) or at -O-C=O carbonyl ($C_C O_V$) group.⁶⁻⁷ Therefore, to dissect these tangled processes, we studied the adsorption and dissociation of VC molecule on the most stable (001)-Li metal surface.⁸ We presented a new atomistic insights on VC-Lithium SEI formation via first-principles calculations by means of Density Functional Embedding Theory (DFET).⁹ Such approach is well suited to combine the best feasible approaches for molecular species (in our case, hybrid HSE06 functional for VC molecules and derivatives) and for Li metal electrode (semi-local PBE functional).

2. Methods and Computational details

Spin-polarized density functional theory (DFT) calculations were performed within periodic boundary conditions (PBC) by employing plane-wave (PW) basis sets as implemented in the Vienna Ab initio Simulation Package (VASP, ver. 5.4.1).¹⁰⁻¹³ We used the PBE-D3 functional^{14,15} and projector-augmented wave (PAW) potentials to describe core electrons. Pseudo-wave functions are expanded in a PW basis set with a kinetic energy of 600 eV, and 4x4x1 Monkhorst-Pack k-point mesh for sampling the Brillouin zone. The Kohn-Sham equations for clusters and environments were solved with a local DFET implementation within a modified ABINIT program.¹⁶ The DFET-HSE06-in-PBE energies are calculated as:

$$E = E_{Li-VC,PBC}^{PBE} - E_{Li-VC,cluster}^{PBE}[V_{emb}] + E_{Li-VC,cluster}^{HSE06}[V_{emb}] \quad (1)$$

where $E_{Li-VC,PBC}^{PBE}$ is the DFT-PBE energy of the system within PBC, while $E_{Li-VC,cluster}^{PBE}[V_{emb}]$ and $E_{Li-VC,cluster}^{HSE06}[V_{emb}]$ are the energies of the cluster system at, respectively, PBE and HSE06 level of theory, that are computed in a PBE-derived embedding potential, V_{emb} . We used the norm-conserving pseudopotential (NC) given by the fhi98PP program,¹⁷ and a kinetic energy cutoff of 1000 eV.

3. Results and Discussion

We addressed the adsorption of a single molecule on the Li(001) surface termination, as a first step for SEI formation at electrode/electrolyte interface. Adsorption energies in Figure 1 show that the most favorable configuration is given by the bidentate mode, $Li[OC_OV]$, followed by the two bridged states, $Li[OC]_{b,t}$ and $Li[OC]_{b,p}$, and then by the end-on ones, $Li[OC]_{e,t}$ and $Li[OC]_{e,p}$. This trend is explained by the extra stabilization

occurring in the two-bond configurations (bidentate and bridged states) compared to the single-bond ones (end-on coordinations).

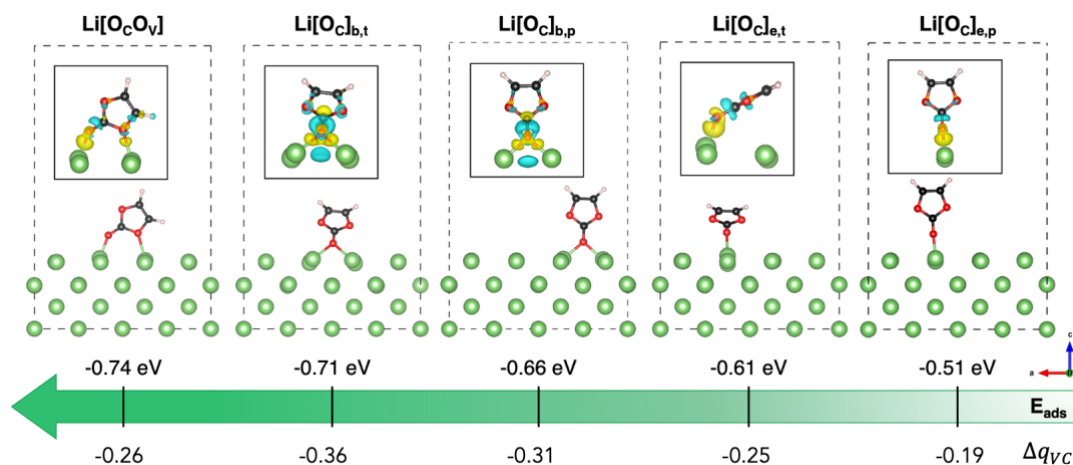


Fig. 1: VC-Li(001) adsorbed states in different configurations and corresponding adsorption energies ($E_{ads} = E_{VC-Li} - E_{Li} - E_{VC}$) at the PBE-D3 level of theory. Bader charge variation upon adsorption calculated on the whole VC molecule (Δq_{VC}). Insets: charge density difference plots ($\Delta\rho = \rho_{VC-Li} - \rho_{Li} - \rho_{VC}$ isosurface: $3 \text{ meV}/\text{\AA}^3$). Color code: Li (green), C (black), O (red), H (white); electron gain (yellow), electron loss (cyan).

Among these adsorption modes, the $\text{Li}[\text{OC}]_{b,t}$ could be considered as the most likely to initiate the reductive ring-opening reaction due to higher Bader charge variation on VC molecule (Δq_{VC}) and enhanced charge transfer (Fig. 1). Inspired by previous molecular studies,^{5,6} we considered the ring-opening along $\text{C}_C\text{-O}_V$ or $\text{C}_V\text{-O}_V$ bonds. Localized reduction occurs on the carbon sites of the two dissociated states, $\text{DISS}(\text{C}_C\text{O}_V)$ and $\text{DISS}(\text{C}_V\text{O}_V)$, respectively, and more accurate theoretical methods beyond DFT are required to achieve reliable and useful predictions of this highly correlated systems with localized electron density. To this end and to preserve a suitable description for the metal surface, we proposed the mechanistic study of ring-opening reactions by means of the DFET.⁹ We investigated the minimum-energy paths (MEPs) along the VC dissociation process by applying the CI-NEB method¹⁸ between the considered adsorbed state $\text{Li}[\text{OC}]_{b,t}$ (as initial state, *i.e.*, i00), and a given dissociated structure, $\text{DISS}(\text{C}_C\text{O}_V)$ and $\text{DISS}(\text{C}_V\text{O}_V)$, (final state, *i.e.*, i06). The energetics in Figure 2 clearly show that the DFET-HSE06-in-PBE method predicts an energy barrier of about 0.3 eV, associated to the formation of the high-energy i01 images along both MEPs, which is not detectable with semi-local DFT-PBE approaches. We quantified the structural reconstruction as the geometrical distortion on the carbonyl carbon atom from its original planar configuration: the further the $\text{O}_V\text{-O}_V\text{-C=O}$ dihedral angle from 180° value, the larger the rearrangement at the C_C atom. As shown in Figure 2, the dihedral angle decreases by 38° and 30° for i01- $\text{DISS}(\text{C}_C\text{O}_V)$ and i01- $\text{DISS}(\text{C}_V\text{O}_V)$, respectively, suggesting that the VC ring undergoes a structural reorganization from an approximately trigonal planar to a trigonal pyramidal geometry. The energy barriers predicted by the HSE06-in-PBE approach are therefore associated to the VC pyramidalization and formation of a radical anion. The minor extent of structural and electronic reorganization in i01- $\text{DISS}(\text{C}_V\text{O}_V)$ could account for the lower energy barrier and thus suggest a more accessible pathway leading to a more stable dissociated product. Moreover, our computed barrier heights are slightly lower than those reported by Wang *et al.*⁷ (~ 0.8 eV), owing to the presence of Li metal surface acting as electron donor and thus favoring the reductive reaction. In both cases, we found that the ring-opening reaction proceeds with further electron transfer from Li to VC, leading to two highly reactive products that can exert different activities towards SEI formation on Li metal surface.

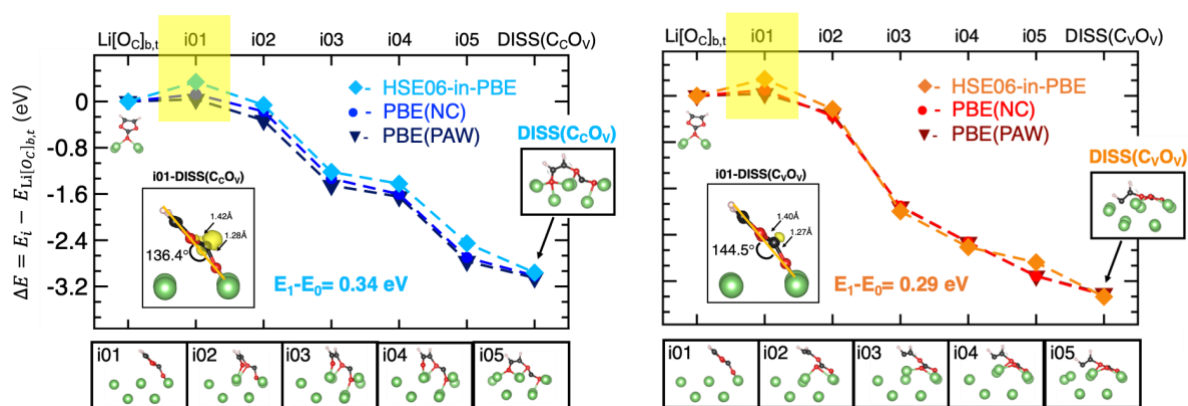


Fig. 2: Minimum energy paths (MEPs) for migration of VC molecule from its adsorbed to dissociated states, (left) DISS(CcOv) and (right) DISS(CvOv), computed via CI-NEB approach with corresponding energetics obtained at DFT-PBE(PAW) (dark-blue and burgundy lines), DFT-PBE(NC) (blue and red lines) and DFET-HSE06-in-PBE (light-blue and orange lines) levels of theory. Insets: CcOv/CvOv bond length and dihedral (Ov,Ov-C=O), spin density (isosurface 5×10^{-4} e-/bohr³).

4. Conclusions

Our theoretical study shows that an advanced DFET approach is necessary to properly describe the VC dissociation mechanisms and the related intermediates featuring localized charges. DFET represents an innovative computational tool capable of providing a reliable picture for electrocatalytic reactions occurring at heterogeneous interfaces. By elucidating the VC reductive mechanism on Li surface, we believe that this investigation can guide the rational design of SEI engineering towards safe, stable, and efficient Li metal anodes. These results are gathered in a paper that has been recently published on *Journal of Material Chemistry A*.¹ The computing resources and the related technical support used for this work have been provided by CRESCO/ENEAGRID High Performance Computing infrastructure and its staff; CRESCO/ ENEAGRID High Performance Computing infrastructure is funded by ENEA, the Italian National Agency for New Technologies, Energy and Sustainable Economic Development and by Italian and European research programmes. See: <http://www.cresco.enea.it/english> for information.¹⁹

References

- [1] F. Fasulo, A.B. Muñoz-García, A. Massaro, O. Crescenzi, C. Huang, M. Pavone, Vinylene carbonate reactivity at lithium metal surface: first-principles insights into the early steps of SEI formation. *J. Mater. Chem. A* 11, pp. 5660-5669 (2023).
- [2] A. Wang, S. Kadam, H. Li, S. Shi, Y. Qi, Review on modeling of the anode solid electrolyte interphase (SEI) for lithium-ion batteries. *npj Comput. Mater.* 4, 15 (2018).
- [3] G. Lingua, M. Falco, T. Stettner, C. Gerbaldi, A. Balducci. Enabling safe and stable Li metal batteries with protic ionic liquid electrolytes and high voltage cathodes. *J. Power Sources* 481, 228979 (2021)
- [4] Y. Qian, C. Schultz, P. Niehoff, T. Schwieters, S. Nowak, F. M. Schappacher, M. Winter. Investigations on the electrochemical decomposition of the electrolyte additive vinylene carbonate in Li metal half cells and lithium-ion full cells. *J. Power Sources* 332, pp. 60–71 (2016).
- [5] B. Zhang, M. Metzger, S. Solchenbach, M. Payne, S. Meini, H. A. Gasteiger, A. Garsuch, B. L. Lucht. Role of 1,3-Propane Sultone and Vinylene Carbonate in Solid Electrolyte Interface Formation and Gas Generation. *J. Phys. Chem. C* 119, pp. 11337–11348 (2015).
- [6] Y-K. Han, S. U. Lee. Density Functional Studies of Ring-Opening Reactions of Li⁺-(ethylene carbonate) and Li⁺-(vinylene carbonate) *Bull. Korean Chem. Soc.* 26, pp. 43–46 (2005).
- [7] Y. Wang, P. B. Balbuena. Theoretical Insights into the Reductive Decompositions of Propylene Carbonate and Vinylene Carbonate: Density Functional Theory Studies. *J. Phys. Chem. B* 106, pp. 4486–4495 (2002).
- [8] M. Ebadi, D. Brandell, C. M. Araujo. Electrolyte decomposition on Li-metal surfaces from first-principles theory. *J. Chem. Phys.* 145, 204701 (2016).
- [9] C. Huang, M. Pavone, E. A. Carter. Quantum mechanical embedding theory based on a unique embedding potential. *J. Chem. Phys.* 134, 154110 (2011).
- [10] G. Kresse, J. Hafner. Ab initio molecular dynamics for liquid metals. *Phys. Rev. B* 47, pp. 558–561 (1993).

- [11] G. Kresse, J. Furthmüller. Efficiency of ab-initio total energy calculations for metals and semiconductors using a plane-wave basis set. *Comput. Mater. Sci.* 6, pp. 15–50 (1996).
- [12] G. Kresse, J. Furthmüller. Efficient iterative schemes for ab initio total-energy calculations using a plane-wave basis set. *Phys. Rev. B* 54, pp. 11169–11186 (1996).
- [13] G. Kresse, J. Hafner. Ab initio molecular-dynamics simulation of the liquid-metal–amorphous-semiconductor transition in germanium. *Phys. Rev. B* 49, pp. 14251–14269 (1994).
- [14] J. P. Perdew, K. Burke, M. Ernzerhof. Generalized Gradient Approximation Made Simple. *Phys. Rev. Lett.* 78, pp. 1396–1396 (1997).
- [15] S. Grimme, J. Antony, S. Ehrlich, H. Krieg. A consistent and accurate ab initio parametrization of density functional dispersion correction (DFT-D) for the 94 elements H-Pu. *J. Chem. Phys.* 132, 154104 (2010).
- [16] C. Huang. Extending the density functional embedding theory to finite temperature and an efficient iterative method for solving for embedding potentials. *J. Chem. Phys.* 144, 124106 (2016).
- [17] M. Fuchs, M. Scheffler. *Comput. Phys. Commun.* 119, pp. 67–98 (1999).
- [18] G. Henkelman, B. P. Uberuaga, H. Jónsson. *J. Chem. Phys.* 113, pp. 9901–9904 (2000).
- [19] G. Ponti, F. Palombi, D. Abate, F. Ambrosino, G. Aprea, T. Bastianelli, F. Beone, R. Bertini, G. Bracco, M. Caporicci, B. Calosso, M. Chinnici, A. Colavincenzo, A. Cucurullo, P. Dangelo, M. De Rosa, P. De Michele, A. Funel, G. Furini, D. Giammattei, S. Giusepponi, R. Guadagni, G. Guarnieri, A. Italiano, S. Magagnino, A. Mariano, G. Mencuccini, C. Mercuri, S. Migliori, P. Ornelli, S. Pecoraro, A. Perozziello, S. Pierattini, S. Podda, F. Poggi, A. Quintiliani, A. Rocchi, C. Scio, F. Simoni, A. Vita The role of medium size facilities in the HPC ecosystem: the case of the new CRESCO4 cluster integrated in the ENEAGRID infrastructure, *Int. Conf. on High Perform. Comp. & Simul. (HPCS)* pp 1030-1033 (2014).

AB-INITIO STUDY OF THE CHARGE DYNAMICS AT THE SPIRO-MEOTAD/ LEAD HALIDE PEROVSKITES INTERFACE

Adriana Pecoraro^{1*}, Francesca Fasulo², Michele Pavone^{2,3} and Ana Belén Muñoz-García^{1,3}

¹ *Department of Physics “E. Pancini”, University of Naples Federico II, Napoli, Italy¹³*

² *Department of Chemical Sciences, University of Naples Federico II, Napoli, Italy*

³ *National Reference Center for Electrochemical Energy Storage (GISEL)-INSTM, via G. Giusti 9, 50121 Florence, Italy*

ABSTRACT. The long-term stability of perovskite solar cells (PSCs) is strongly affected by the interfaces between the perovskite and the hole transport material. We investigate such interfaces via first-principles calculations, unveiling how charge transfer times and mechanisms depend on the chemical composition and local environment.

1. Introduction

Hybrid organic-inorganic solar cells are a promising technology for solar-to-electric energy conversion [1]. Power conversion efficiencies (PCEs) up to 25% have been reached using mixed cationic/anionic perovskite compositions [2] such as the $\text{Cs}_{0.05}(\text{FA}_{0.83}\text{MA}_{0.17})_{0.95}\text{Pb}(\text{I}_{0.83}\text{Br}_{0.17})_3$ stoichiometry proposed by Saliba et. al., [3] which contains three cations, methylammonium (MA), formamidinium (FA) and Cs and two anions, I and Br. Such a triple lead halide perovskite (tri-LHP) composition is a modification of the archetypal methylammonium lead iodide (MAPI) and shows high efficiencies, improved stability and device reproducibility. [4],[5] Together with perovskite composition, another crucial aspect in PSCs is the proper choice of hole and electron charge transport materials (HTM and ETM, respectively) that have to swiftly conduct photogenerated charges to the electrodes. [6] The state-of-the-art HTM is the Spiro-MeOTAD. [7],[11] Here we employ the projection-operator diabaticization (POD) approach [12] as implemented in the cp2k software [13] to study the hole injection process at the tri-LHP/Spiro-MeOTAD and MAPI/Spiro-MeOTAD interfaces via DFT calculations. [14]

2. Results and Discussion

The bulk structure of both triLHP and MAPI used in this work has been built starting from the $\text{Cs}_8\text{FA}_{88}\text{MA}_{12}\text{Pb}_{103}\text{Cd}_5\text{I}_{269}\text{Br}_{55}$ supercell (108 f.u.) reported by Saidaminov,¹⁵ while SPIRO coordinates for have been taken from a previous work.⁸ LHP/Spiro-MeOTAD interface models consist of a Spiro-MeOTAD molecule lying the most stable (010) plane of each perovskite model. We account for surface termination by considering both AX (A=MA in MAPI or Cs,FA,MA in triLHP) and PbX_2 terminations (X=I in MAPI or I, Br in triLHP) so to investigate the specific interaction occurring at interfaces. The effect of Cs is studied by considering different compositions of the surface layer AX terminations in triLHP, i.e. exposing or not Cs atoms, labeled as CsFAMAX and FAMAX in the text, respectively. An additional CsFAMAX layer in which the interaction of Cs with the most active methoxy groups of Spiro-MeOTAD^{16,17} is maximized, has been considered and labeled CsFAMAX(O-Cs). We have also investigated two different PbX_2 -terminated surfaces, lacking or containing Cs atom in the subsurface layer, labeled as PbX_2 and $\text{PbX}_2(\text{Cs})$, respectively. Optimized structures for all these considered interfaces are shown in Figure 1.

¹³ Corresponding author. E-mail: adriana.pecoraro@unina.it.

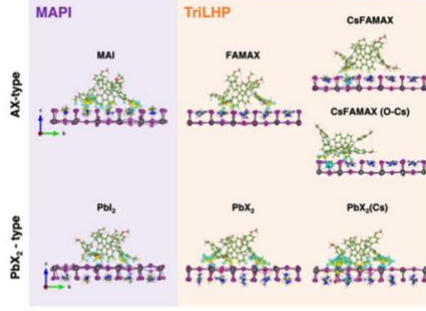


Fig. 1: Lateral views of the two outermost layers of each LHP are shown for the ease of viewing. Yellow and blue regions denote charge accumulation and depletions zones, respectively. Isosurface value = $0.001 e^-/\text{bohr}^3$. Color code: Cs(cyan), Br(magenta), I(violet), Pb(gray), C(green), H(light pink), N_{LHP} (blue), $N_{\text{Spiro-MeOTAD}}$ (light blue), O (red).

The prevalently electromagnetic binding of all the interfaces,¹⁴ is reflected by charge difference plots reported in Figure 1. Most of the charge reorganization at the interface occurs on the fluorene ring and the methoxy groups of Spiro-MeOTAD, which interact mostly with the A cation and with Pb atoms of AX and PbX_2 terminations, in agreement with other works.^{17,18} Such an analysis also points out the key role of the Cs atom in stabilizing the interaction with Spiro-MeOTAD. In the CsFAMAX (O-Cs) system, the increased charge density along the methoxy O-Cs bond and the O-Cs distance ($\sim 3.25 \text{ \AA}$), suggests the formation of a direct stabilizing interaction.¹⁹ In $\text{PbX}_2(\text{Cs})$ system a particularly pronounced electronic density rearrangement is observed that involves the whole interface. We calculated the donor-acceptor coupling matrix elements for transitions occurring between both HOMO and HOMO-1 molecular orbitals (MOs) of Spiro-MeOTAD and LHP's VBM since both CT are thermodynamically possible.¹⁴ Conceptually a hole transfer from the LHP's VBM and the SPIRO's HOMO/HOMO-1 is equivalent to the reverse electron injection. We also calculated the spectral function $\Gamma_d(E)$ that can provide an estimate of the CT timescale:

$$\Gamma_d(E) = 2\pi \sum_a |V_{ad}|^2 \delta(E - \varepsilon_a) \quad (1)$$

where V_{ad} is the electronic coupling matrix element between the diabatic donor d state and the acceptor a state of perovskite valence band, with energy ε_a . Coupling elements $|V_{ad}|$ and spectral functions Γ are depicted for all systems, together injection times, in Figure 2. The molecular orbital distribution is reported at the right of each plot.

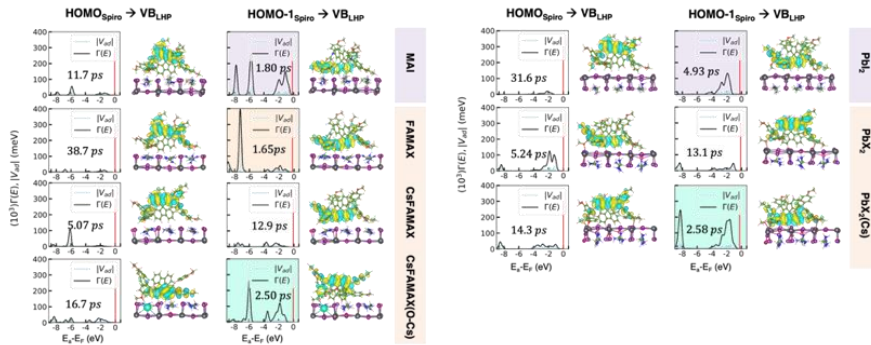


Fig. 2: Coupling matrix elements $|V_{ad}|$ between Spiro-MeOTAD HOMO and HOMO-1 donor states and LHPs VB acceptor states for AX-type and PbX_2 -type interfaces and spectral function $\Gamma(E)$ calculated according to equation 1. Spiro-MeOTAD donor state is represented by red vertical lines in $|V_{ad}|$ and $\Gamma(E)$ plots. In each plot are also reported the calculated injection times and the HOMO/HOMO-1 molecular orbital.

For most of the systems HOMO-1 is found to couple better than HOMO with the LHP VBM and almost all the models show the best couplings for MO pointing towards the surface. An apparent contradiction is observed for CsFAMAX, CsFAMAX(O-Cs) but a closer look at these MOs, depicted in Figure 3, can explain this finding. They comprise the most interacting methoxy group directly linked to the Cs-rich surface at 2.43 \AA

and 3.25 Å for CsFAMAX and CsFAMAX(O-Cs), respectively. Especially for the CsFAMAX(O-Cs)/HOMO-1 case, strong couplings involve Cs states suggest that Cs acts as direct hole transfer booster.

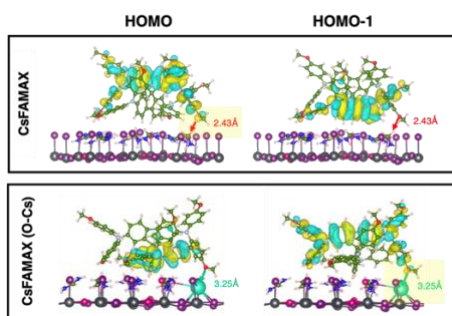


Fig. 3 HOMO and HOMO-1 MOs for two AX-type configurations, the CsFAMAX (top panel) and the CsFAMAX(O-Cs) (bottom panel).

Regarding times reported in figure 2, all obtained values are of the order of picosecond, in agreement with other experimental works.^{35,36,48} TriLHP presents the fastest injections, in particular for FAMAX/Spiro-MeOTAD(HOMO-1) (1.65 ps), CsFAMAX(O-Cs)/Spiro-MeOTAD(HOMO-1) (2.50 ps) and the PbX₂(Cs)/Spiro-MeOTAD(HOMO-1) (2.68 ps) interfaces. Regarding MAPI the MAI termination (1.80 ps) is more efficient than the PbI₂ one (4.93 ps).

3. Conclusions

In conclusion, our first-principles calculations address the interfaces of Spiro-MeOTAD HTM with the well-studied MAPI and with the triple cation LHP formulation, shading light on the chemical interactions leading to favorable binding of the hole transport molecule. These results show that triLHP is more efficient for CT than MAPI for which only the MAI termination (1.80 ps) is efficient. Moreover, we have found that Cs acts as additional CT booster both when it is directly linked to Spiro-MeOTAD, and when it is present in subsurface.

Acknowledgments

The computing resources and the related technical support used for this work have been provided by CRESCO/ENEAGRID High Performance Computing infrastructure and its staff; CRESCO/ ENEAGRID High Performance Computing infrastructure is funded by ENEA, the Italian National Agency for New Technologies, Energy and Sustainable Economic Development and by Italian and European research programmes. See: <http://www.cresco.enea.it/english> for information.²⁰

References

- [1] J. Y. Kim, J.-W. Lee, H. S. Jung, H. Shin and N.-G. Park, *Chem. Rev.*, 2020, **120**, 7867–7918.
- [2] H.-S. Kim, A. Hagfeldt and N.-G. Park, *Chem. Commun.*, 2019, **55**, 1192–1200.
- [3] M. Saliba, T. Matsui, J.-Y. Seo, K. Domanski, J.-P. Correa-Baena, M. K. Nazeeruddin, S. M. Zakeeruddin, W. Tress, A. Abate, A. Hagfeldt and M. Grätzel, *Energy Environ. Sci.*, 2016, **9**, 1989–1997.
- [4] P. Toloueinia, H. Khassaf, A. Shirazi Amin, Z. M. Tobin, S. P. Alpay and S. L. Suib, *ACS Appl. Energy Mater.*, 2020, **3**, 8240–8248.
- [5] M. M. Byranvand, C. Otero-Martínez, J. Ye, W. Zuo, L. Manna, M. Saliba, R. L. Z. Hoye and L. Polavarapu, *Advanced Optical Materials*, 2022, **10**, 2200423.
- [6] V. M. Le Corre, M. Stolterfoht, L. Perdigón Toro, M. Feuerstein, C. Wolff, L. Gil-Escrig, H. J. Bolink, D. Neher and L. J. A. Koster, *ACS Appl. Energy Mater.*, 2019, **2**, 6280–6287.
- [7] Z. Hawash, L. K. Ono and Y. Qi, *Advanced Materials Interfaces*, 2018, **5**, 1700623.
- [8] Y. Saygili, H.-S. Kim, B. Yang, J. Suo, A. B. Muñoz-García, M. Pavone and A. Hagfeldt, *ACS Energy Lett.*, 2020, **5**, 1271–1277.

- [9] J.-Y. Seo, S. Akin, M. Zalibera, M. A. R. Preciado, H.-S. Kim, S. M. Zakeeruddin, J. V. Milić and M. Grätzel, *Advanced Functional Materials*, 2021, **31**, 2102124.
- [10] X. Liu, B. Zheng, L. Shi, S. Zhou, J. Xu, Z. Liu, J. S. Yun, E. Choi, M. Zhang, Y. Lv, W.-H. Zhang, J. Huang, C. Li, K. Sun, J. Seidel, M. He, J. Peng, X. Hao and M. Green, *Nat. Photon.*, 2023, **17**, 96–105.
- [11] H. Zhang, Y. Shi, F. Yan, L. Wang, K. Wang, Y. Xing, Q. Dong and T. Ma, *Chem. Commun.*, 2014, **50**, 5020–5022.
- [12] I. Kondov, M. Čížek, C. Benesch, H. Wang and M. Thoss, *J. Phys. Chem. C*, 2007, **111**, 11970–11981.
- [13] Z. Futera and J. Blumberger, *J. Phys. Chem. C*, 2017, **121**, 19677–19689.
- [14] A. Pecoraro, F. Fasulo, M. Pavone and A. B. Muñoz-García, *Chem. Commun.*, 2023, **59**, 5055–5058.
- [15] M. I. Saidaminov, J. Kim, A. Jain, R. Quintero-Bermudez, H. Tan, G. Long, F. Tan, A. Johnston, Y. Zhao, O. Voznyy and E. H. Sargent, *Nat Energy*, 2018, **3**, 648–654.
- [16] Q. Wang, E. Mosconi, C. Wolff, J. Li, D. Neher, F. De Angelis, G. P. Suranna, R. Grisorio and A. Abate, *Advanced Energy Materials*, 2019, **9**, 1900990.
- [17] C. Coppola, A. Pecoraro, A. B. Muñoz-García, R. Infantino, A. Dessì, G. Reginato, R. Basosi, A. Sinicropi and M. Pavone, *Phys. Chem. Chem. Phys.*, 2022, **24**, 14993–15002.
- [18] A. Torres and L. G. C. Rego, *J. Phys. Chem. C*, 2014, **118**, 26947–26954.
- [19] A. Leclaire, *Journal of Solid State Chemistry*, 2008, **181**, 2338–2345.
- [20] G. Ponti, F. Palombi, D. Abate, F. Ambrosino, G. Aprea, T. Bastianelli, F. Beone, R. Bertini, G. Bracco, M. Caporicci, B. Calosso, M. Chinnici, A. Colavincenzo, A. Cucurullo, P. Dangelo, M. De Rosa, P. De Michele, A. Funel, G. Furini, D. Giammattei, S. Giusepponi, R. Guadagni, G. Guarnieri, A. Italiano, S. Magagnino, A. Mariano, G. Mencuccini, C. Mercuri, S. Migliori, P. Ornelli, S. Pecoraro, A. Perozziello, S. Pierattini, S. Podda, F. Poggi, A. Quintiliani, A. Rocchi, C. Sciò, F. Simoni and A. Vita, in *2014 International Conference on High Performance Computing & Simulation (HPCS)*, 2014, pp. 1030–1033.

RADIATION DAMAGE ANALYSIS OF THE LFR-AS-30 CORE

Roberto Pergreffi^{1,4}, Francesco Lodi¹, Giacomo Grasso¹, Alessia Di Francesco², Giorgia Mantovani²

¹ENEA – Italian National Agency for New Technologies, Energy and Sustainable Economic Development
Via Martiri di Monte Sole 4, 40129 Bologna - Italy

²newcleo srl
Via Galliano 27, 10129 Torino - Italy

ABSTRACT. As part of the analyses envisaged for the conceptual design of the core configuration of the LFR-AS-30, a small modular fast reactor cooled by lead and loaded with MOX fuel, the radiation damage analysis was performed on the structures exposed to the highest neutron irradiation such as fuel rod claddings of the hottest fuel assembly, amphora-shaped inner vessel and reactor vessel. The damage caused by neutron-only radiation was analysed in terms of Displacement Per Atom (DPA) using the NRT model. The results, calculated at beginning of life with the control rods inserted in the Middle of Cycle position and no modelling of the shutdown device, do not highlight any critical issues on the structures considered, the limits at the end of their lifetime being respected. All calculations were performed with the radiation transport code MCNP6.1 on CRESCO6.

1. Introduction

The LFR-AS-30 (Lead Fast Reactor – Amphora-Shaped – 30 MWe) is a small modular fast reactor cooled by molten lead designed to produce 30 MW of electric power by burning Uranium, Plutonium and Minor Actinides (MAs). This reactor was included in the agreement between *newcleo* srl and ENEA which entrusted ENEA as responsible for the conceptual design of the core.

The main requirements of the company for this reactor included the type of fuel (MOX), the thermal power (60 MW), the core inlet/outlet temperatures (370/440 °C), the hot spot cladding outer temperature (< 480 °C), the maximum radiation damages on fuel pin claddings and inner and reactor vessels (83 and 2 DPA, respectively), the limits on pressure drops in the core and in the primary circuit (0.4 and 0.7 bar, respectively), the number of fuel assemblies (37) and the control elements located outside the active region. An additional requirement included to take the opportunity to reassemble the existing fuel pins of the first fresh reload of the Superphénix-1 (SPX-1) reactor so as to exploit the reserves of fresh fuel still existing in France.

Based on these requirements, the design of the viable core configuration envisaged, as usual, the following analyses:

1. core neutronic analysis (in terms of reactivity evolution, mass balance, power distribution, flux distribution and reactivity coefficients);
2. fuel assembly thermal-hydraulic analysis (in terms of distributions of coolant and cladding wall temperatures);
3. fuel assembly thermo-mechanical analysis;
4. core thermo-mechanical analysis;
5. fuel performance analysis (in terms of fuel temperature and clad stresses and strains distributions);
6. radiation damage analysis.

In particular, the aim of the radiation damage analysis is to verify – by best estimate calculations – that the damage of the structures exposed to neutron irradiation respects the limit at the end of their design lifetime. The neutron radiation damage was assessed in terms of Displacement Per Atom (DPA) using the NRT model [1]. The calculations were carried out with the radiation transport code MCNP6.1 [2] on CRESCO6, the Linux cluster integrated in the ENEAGRID HPC infrastructure, over 40 nodes for a total of 1920 cores with a CPU time never exceeding 48,000 minutes. The main results of this analysis are summarized below.

2. Main results of the radiation damage analysis

The structures on which the radiation damage analysis was performed are:

¹⁴ Corresponding author. E-mail: roberto.pergreffi@enea.it.

- fuel rod claddings of the hottest FA;
- amphora shaped inner vessel (ASIV);
- reactor vessel (RV).

The fuel rod claddings are cylindrical tubes made of Z10 CNDT 15-15B, an austenitic stainless steel of class “15-15Ti”, sealed at both ends with plugs. For this analysis, they were discretized as follows:

- 1 axial region above the upper blanket,
- 1 axial region for the upper blanket,
- 5 equal volume axial regions for the active height (AH),
- 1 axial region for the lower blanket,
- 1 axial region below the lower blanket.

The final configuration exhibits six hottest FAs positioned in the third ring where the Plutonium enrichment is higher (in fact, to flatten the power distribution and increase the effectiveness of the control and shutdown systems located in the lead pool between the core and the ASIV, two different enrichments were used). Since possible power differences are only due to statistical reasons, the radiation damage analysis was performed on only one of them (see Fig. 2).

The inner vessel is an amphora shaped structure in AISI 316L used for both the core support and restraint safety functions. For this analysis, it was discretized as follows:

- 1 axial region for the cylindrical shell above the AH up to the upper limit of the system,
- 20 equal volume axial regions for the cylindrical shell corresponding to the AH,
- 1 axial region for the cylindrical shell below the AH up to the junction with the toro-spheric shell,
- 5 equal volume axial regions for the toro-spheric shell up to the cylindrical plate;
- 1 axial region for the lower part of the core interface.

The RV is a complex structure made of AISI 316. For this analysis only the lower region corresponding to the spherical shell is considered.

The discretization scheme of the three structures as modeled in MCNP6.1 is depicted in Fig. 2.

The neutron radiation damage rate in DPA/s was calculated using the NRT model. According to [3], the implementation of the NRT model in MCNP6.1 was done as follows:

- first, by applying a tally multiplier (FM) to a standard flux tally (type F4) in order to integrate over all energies the product between the energy-dependent flux and the damage-energy cross section;
- secondly, by multiplying the result obtained in the previous point by a normalization factor, being the FM-multiplied tally given in units of MeV-barn/cm² per source neutron;
- finally, by multiplying the normalized value by $\eta/2E_d$ where η is the efficiency correction factor (0.8) and E_d is the displacement threshold energy associated to Iron (assumed equal to 40 eV).

The damage-energy cross sections in MeV*b calculated by NJOY [4] and tabulated in neutron ACE files in MT=444 were used.

The calculations were performed considering 110 k-eigenvalue source iteration cycles, of which the first 10 skipped, with 1.0E+05 histories per cycle. As neutron and photon transport libraries, the ENDF/B-VIII.0 distribution [5] processed by LANL in ACE format and the MCPLIB84 [6] were chosen, respectively.

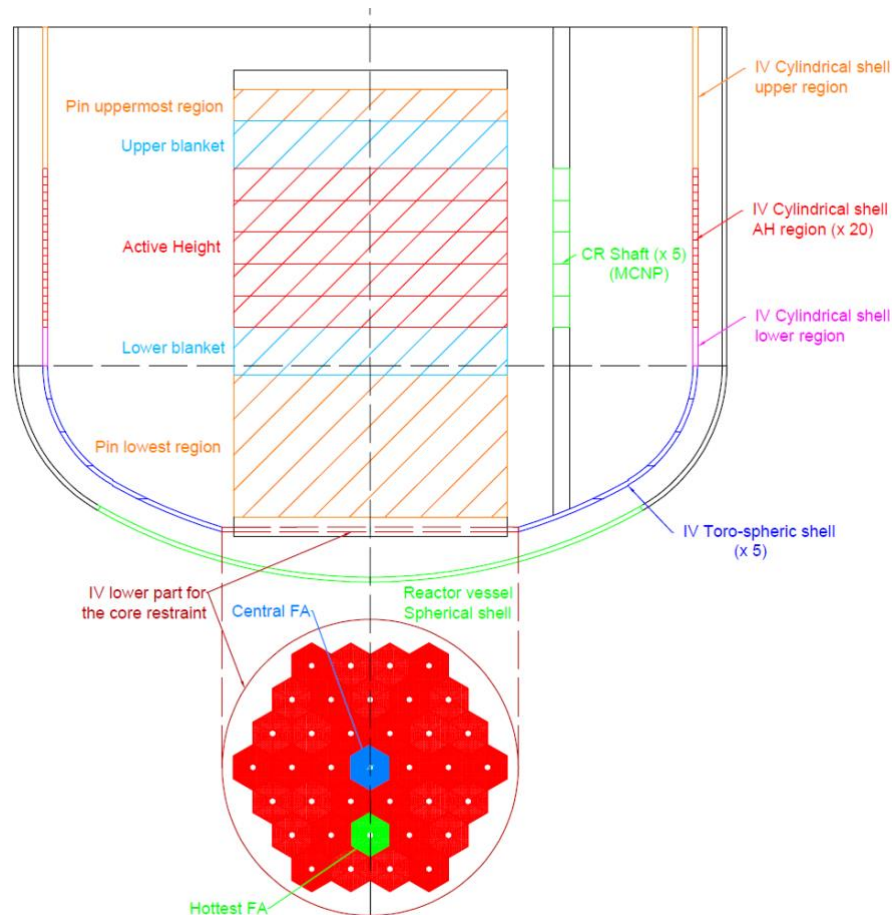


Fig. 2. Discretization scheme in MCNP6.

The main results of the radiation damage analysis in terms of DPA rate, DPA and minimum time to DPA critical threshold are summarized in Table 1 and 2. It should be noted that they refer to a core configuration at BoL with all CRs inserted in the Middle of Cycle (MoC) and no modelling of the shutdown devices. The neutron radiation damage in DPA was calculated by multiplying the max DPA rate at BoL by the corresponding irradiation time assuming constant irradiation conditions. The following values are used as reference irradiation times:

- 12 years (equal to the in-pile irradiation cycle) for the fuel rod claddings;
- 40 years (equal to the reactor lifetime) for the IV and RV.

The following is observed:

- the maximum DPA rate of the most radiated axial region of the most radiated cladding of the hottest FA is 6 DPA/y as shown in Table 1. This rate, after 12 years in the core, causes a damage of approximately 70 DPA, therefore lower than that assumed as the maximum radiation damage for the available fuel pins (83 DPA).
- the maximum DPA rate of the most radiated region of the IV is 8.3E-03 DPA/y as reported in Table 2. This rate, after 40 years, causes a maximum radiation damage of 3.31E-01 DPA. It follows that it would take more than 200 years to reach the corresponding critical threshold of 2 DPA.
- the maximum DPA rate of the spherical part of the RV shown in Table 2 is 1.99E-04 DPA/y i.e., significantly lower than that of the inner vessel. Consequently, even after 40 years, the radiation effects on this structure are completely negligible.

For each structure, the uncertainty value at 1 standard deviation associated with the DPA rate is provided. This value, expressed by relative error in percentage, was computed by propagating the statistical uncertainties of the MCNP outputs of the quantities from which the DPA rate was derived.

Table 1. Radiation damage on the most radiated axial region of the most radiated cladding of the hottest FA.

Structure	Max DPA rate [DPA/y]	Max DPA after 12 y [DPA]	Min time to 83 DPA [years]	Statist. uncertainty (1 σ) [%]
Fuel rod cladding	6	70.1	13.8	1.4

Table 2. Radiation damages on the most radiated region of the inner vessel and reactor vessel.

Structure	Max DPA rate [DPA/y]	Max DPA after 40 y [DPA]	Min time to 2 DPA [years]	Statist. uncertainty (1 σ) [%]
Inner vessel	8.3E-03	3.31E-01	242	1.3
Reactor vessel	1.99E-04	7.95E-03	> 10000	2.4

3. Conclusions and open items

This study addressed radiation damage analysis on some critical structures of the LFR-AS-30 core such as the claddings of the hottest fuel assembly, the inner vessel, and the reactor vessel. The damage caused by neutron-only radiation was assessed in terms of DPA according to the NRT model.

The results, calculated with the radiation transport code MCNP6.1 at beginning of life with the CRs inserted in the MoC position and no modelling of the shutdown rods, do not highlight any critical issues on the structures considered, being respected the limits at the end of their design lifetime. Thus, the feasibility of the LFR-AS-30 core in terms of neutron radiation damage can be considered preliminarily verified. At the same time, the following should be noted about the results obtained:

- these values were calculated using the flux at BoL. In general terms, this is a non-conservative assumption since the flux increases over time, but in this case, it must be considered that the change of the flux with time in radial and axial directions is not completely predictable due to the complexity of the core configuration with two enrichment zones. In any case, a fully conservative approach would require calculating the radiation damages in the worst case, that is, using the maximum flux values.
- these values were calculated by only considering the damage caused by neutrons, that is, neglecting other possible contributions such as those due to gammas and activated products (the most documented case refers to Ni-59, synthetic isotope produced by the transmutation of Ni-58, that can undergo (n, α) or (n,p) reactions [3]). Although these contributions are expected to be very small compared to that of neutrons, they should be included for highly accurate predictions of radiation damage.

References

- [1] M. J. Norgett, M. T. Robinson and I. M. Torrens. A proposed method of calculating displacement dose rates. Nucl. Eng. Des. 33(1):50-54 (1975). DOI: 10.1016/0029-5493(75)90035-7.
- [2] J.T. Goorley et al, Initial MCNP6 release overview – MCNP6 version 1.0, internal report LA-UR-13-22934, LANL, Los Alamos, 2013.
- [3] A. Mata Cruz. Radiation Damage Calculation Methodology. Technical report INL/RPT-22, Idaho National Laboratory, Idaho Falls, Idaho, March 2022.
- [4] R.E. Macfarlane, D.W. Muir, and F.M. Mann, Radiation Damage Calculations with NJOY. Journal of Nuclear Materials 122 & 123: 1041-1046 (1984).
- [5] D. A. Brown et al. ENDF/B-VIII.0: The 8th major release of the nuclear reaction data library with CIELO-project cross sections, new standards and thermal scattering data. Nucl. Data Sheets 148:1-142 (2018). DOI: 10.1016/j.nds.2018.02.001.
- [6] J. L. Conlin et al. Release of ENDF/B-VIII.0-based ACE data files. Technical report LA-UR-18-24034, LANL, Los Alamos, 2018.

MOLECULAR DYNAMICS SIMULATIONS OF ACID B-GLUCOSIDASE ENZYME: DYNAMICAL AND STRUCTURAL EFFECT OF A PARKINSON'S-ASSOCIATED MUTATION

Davide Pietrafesa¹, Alessia Casamassa³, Massimo Santoro², Claudia Consales², Jessica Diana Rosati³ and Caterina Arcangeli^{2*}

¹*Department of Biology, University of Rome Tor Vergata, Via della Ricerca Scientifica 1, 00133 Rome, Italy*

²*Laboratory of Health and Environment, Italian National Agency for New Technologies, Energy and Sustainable Economic Development (ENEA), Via Anguillarese, 301, 00123 Rome, Italy*

³*CSS Mendel, Viale Regina Margherita, 261, 00198 Rome, Italy*

ABSTRACT. The acid- β -glucosidase (GCase) is a hydrolase-functioning enzyme required for the proper degradation of glycosphingolipids. Mutations in the GBA1 gene may increase the risk of Parkinson's syndrome onset. To date it has not yet been clarified how the mutations may change the structural and functional features of the protein. As the GCase has been experimentally found in both monomeric and multimeric forms, mainly as a dimer, it has been hypothesized that dimerization is an important process for the protein activation and function. In this report, we present the results of classical molecular dynamics (MD) simulations of GCase's dimers, which were employed to study the effect of a specific mutation associated with Parkinson's syndrome. All the simulations were performed on CRESCO6 infrastructure using GROMACS 2019 package.

1. Introduction

The correlation between the risk of developing Parkinson's disease (PD) and mutations in the GBA1 gene, which encodes for GCase enzyme, has been known since the 1990s [1,2]. More than 490 mutations are known to be linked to Gaucher's disease, (GD). GD is a lysosomal storage disorder in which the GCase enzyme lacks its catalytic activity and cells accumulate the glycosphingolipids. The GCase is transported by the lysosomal integral membrane protein 2 (LIMP-2) from the endoplasmic reticulum (pH 7.0) to the lysosome (low pH), where it hydrolyzes glucosylceramide into ceramide and glucose with the assistance of the activator protein Saposin C.

Of the large number of GD-causing mutations in the GBA1 gene, only the N370S (mild) and L444P (severe) are associated to PD [3]. The E326K mutation predisposes patients to PD both in homozygous and heterozygous forms [4,5] but is known that it does not cause GD. This feature suggests that deficient lysosomal activity alone may not be the only contributor to the PD mechanism, which is multifactorial. Indeed, the E326K mutation causes a significant increase in insoluble α -Synuclein aggregates and lipid droplet formation, despite not significantly reducing enzymatic activity, according to recent *in vitro* experiments on human fibroblasts [6].

¹ Corresponding author. E-mail: caterina.arcangeli@enea.it

Although some attempts to establish possible interactions between mutations, protein structure, GD manifestation and enzymatic activity have been reported in the literature, it is still unclear how specific mutations affect the risk of PD.

One structural characteristic of the wild type GCase is that it is more stable and functional when it is in a dimeric form with the active site partially buried [6]. The GCase multimerization is unaffected by α -Synuclein binding to GCase, which has been hypothesized to take place in the lysosome at an acidic pH [8]. Some studies [9,10] suggest that dimerization may play a significant role in the activation of GCase.

In this study, we investigated, through classical MD simulations, the effects of the E326K mutation on the structure, function and stability of the GCase's dimers at two distinct pH to mimic the endoplasmatic reticulum and lysosome environment.

2. Computational Methods

A total of six complexes (two wild-type homodimers, two mutated homodimers, two heterodimers) were simulated at neutral and acidic pHs to mimic the endoplasmic reticulum and the lysosome environment. The 3D structures were obtained by selecting the A and B chains of the crystal (PDBID:3GXI) [11] and the mutation was introduced through the CHARMM-GUI platform [12]. The protonation states of titratable amino acids at both pHs were predicted with PROPKA 3.1 by means of the PlayMolecule tool [13]. All the MD simulations were performed by using Gromacs 2019 [14,15] with the GROMOS 53a6 united-atoms force field [16] in combination with TIP3P model [17]. Periodic boundary conditions were applied and after 5000 steps of steepest descent minimization [18] and 200 ps of equilibration, unrestrained MD were carried out in NPT ensemble for 200 ns. Table 1 summarizes some details of the simulations. Three replicas for each system were simulated, for a total time of simulation of 18 microseconds (μ s). The MD simulations were run on 10 nodes of the Cresco6 cluster; the total amount of the storage occupied by each simulation was 700 GB. Trajectories were visualized by means of VMD molecular visualization program [19], all the analyses were performed via Gromacs 2019 and VMD molecular visualization program.

Table 1: Equilibration Procedure.

a = simulation time (ps); b = timestep (fs); c = temperature (K); d = positionally constraint force ($\text{kJ/mol}^{-1}/\text{nm}^{-2}$); e = temperature coupling constant (ps) for solute (1) and solvent and ions (2); f = pressure bath coupling (ps)

	Time ^a	Δt^b	T ^c	Fc (10^3) ^d	τ_t^1	τ_t^2	τ_p^e
NVT	200	2	100	1000	0.1	0.1	-
NPT	200	2	310	1000	0.1	0.1	2.0

3. Results

The structural stability of the systems has been assessed by calculating the Root Means square deviations (RMSDs) on the carbon-alpha trace of the proteins as a function of the simulation time.

As shown in Fig.1, all complexes undergo an initial phase of increase in the RMSD curve, with values between 0.7 and 0.3 nm until they reach, at different times, a *plateau* in which the RMSD values oscillate around an average value. The reaching of the *plateau* is an index of convergence.

To support quantitatively the RMSDs, a principal component analysis (PCA) has been carried out to analyse the cosine's content (cc) of the projections of the first eigenvector (PC1); being the cc value an index of the sampling convergence [20]. For all the complexes a significant cc's value was obtained after approximately half the time of simulation, suggesting that a full convergence is achieved and that 1 μ s of simulation for each replica is sufficient to reach a conformational stability for all dimeric systems at both the pHs analyzed.

This result allows to identify the last 400 ns as the best interval to conduct further analysis.

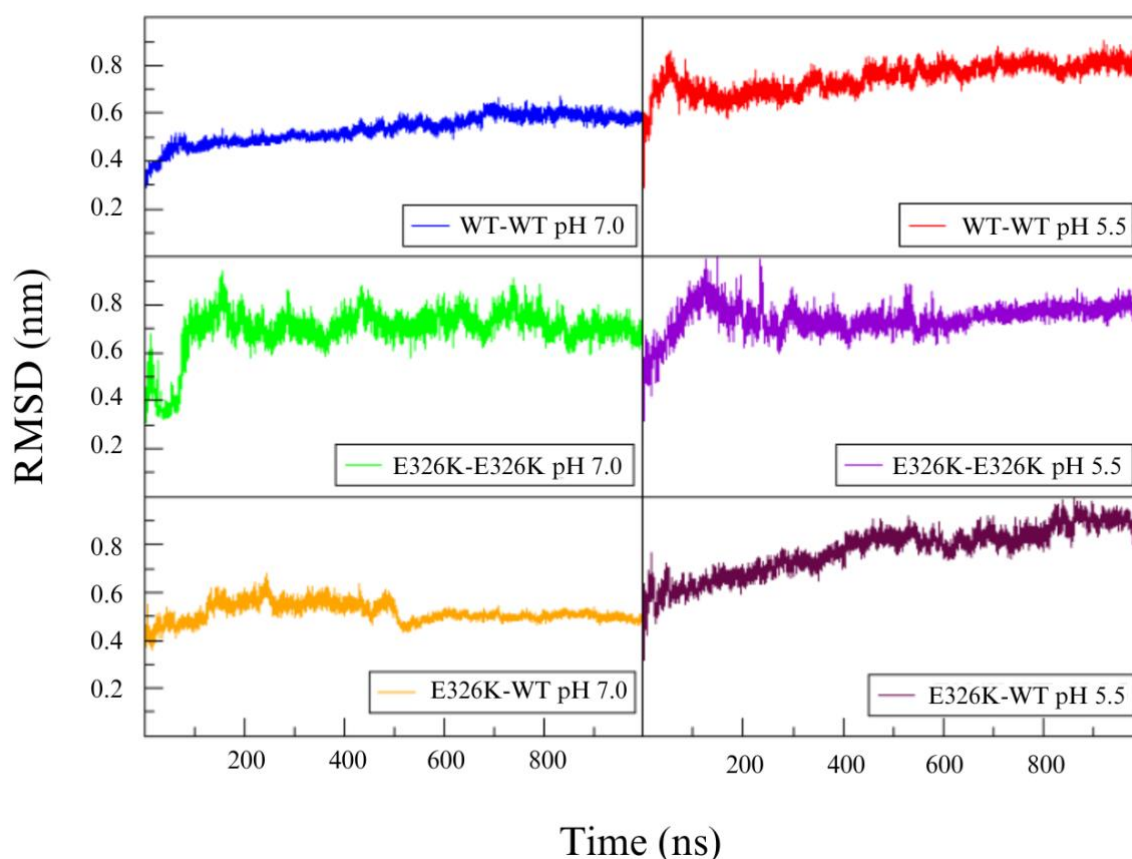


Fig.1: RMSD curves of the first replica of the complexes WT-WT pH 7.0 (blue), E326K-E326K pH 7.0 (green), E326K-WT pH 7.0 (orange), WT-WT pH 5.5 (red), E326K-E326K pH 5.5 (purple), E326K-WT pH 5.5 (purple)

In order to better understand the effect of the mutation on the catalytic active site, an analysis of intrachain interactions, such as hydrogen bonds and salt bridges, has been carried out. This analysis (not shown) has highlighted that the E326K mutation does not alter the activity of the catalytic dyad.

The possible role played by the E326K mutation on the dimerization was investigated through the analysis of the collective motions of the systems. The collective motions, i.e., the large-amplitude motions, were captured by the first eigenvectors (PC1) and shown in Fig. 2 and Fig. 3. Such analysis highlights a greater mobility in the mutated homodimers than in the wild-type homodimers, identifying the E326K-E326K at pH 5.5 (Fig. 3, right) as the complex with the largest-amplitude motions.

At neutral pH the monomers A and B of the mutated homodimer (Fig.2, right) show a departure movement, not visible in the wild-type homodimer (Fig. 2, left), in which low mobility is shown instead, even if it can be observed a large motion of the loop containing the E326 of the chain B.

At acidic pH the mutated homodimer (Fig.3, right) shows a motion in which chain A and B move closer to each other. Such movement is partially found also in the wild-type homodimer (Fig. 3, left). The loops of both chains of the E326K-E326K, containing the mutated residue K326, are extremely mobile.

Graphical representation of collective motions made by VMD showing the WT-WT (left) and E326K-E326K (right) systems at pH 7.0. The color bar show the amplitude of motions. For both, chain A is shown on the left, chain B on the right; in yellow is shown the residue E326, in orange the mutated residue K326. The arrow

shows the direction of motions

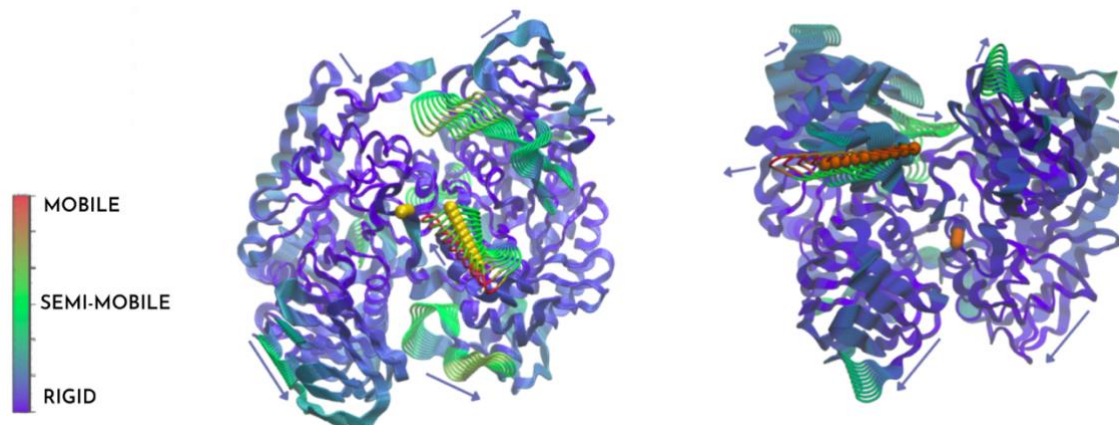


Fig.2: Graphical representation of collective motions made by VMD showing the WT-WT (left) and E326K-E326K (right) systems at pH 7.0. The color bar show the amplitude of motions. For both, chain A is shown on the left, chain B on the right; in yellow is shown the residue E326, in orange the mutated residue K326. The arrow shows the direction of motions

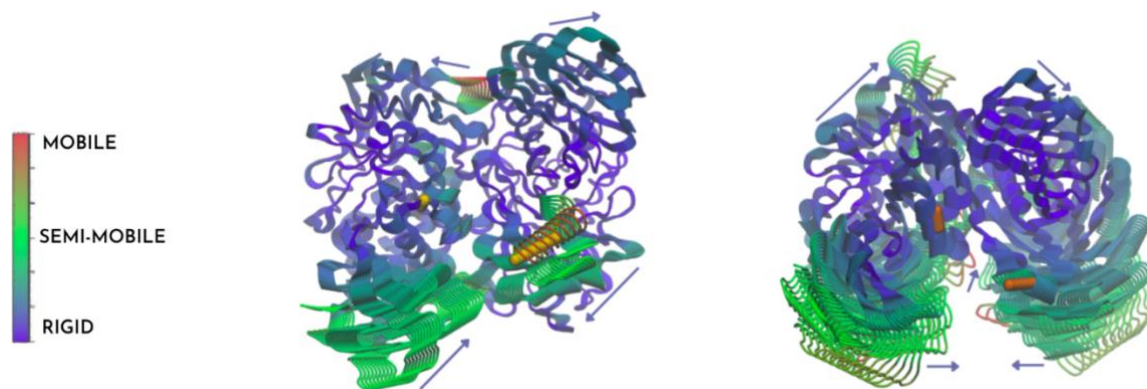


Fig.3: Graphical representation of collective motions made by VMD showing the WT-WT (left) and E326K-E326K (right) systems at pH 5.5. The colour color bar show the amplitude of motions. For both, chain A is shown on the left, chain B on the right; in yellow is shown the residue E326, in orange the mutated residue K326. The arrow shows the direction of motions

4. Discussion and Conclusions

The analyses of the trajectories show that the E326K does not significantly affect the structure of the catalytic dyad of the GCcase while it significantly affects the collective motions of the dimers.

The presence of the mutation leads to higher large-amplitude motions of the dimer. Indeed, the analysis of collective motions highlights the highest mobility of large portions of GCcase at pH 5.5, condition in which the enzyme should be active.

Some studies have hypothesized the importance of the dimerization, but still it is not known how this process influences the GCcase activation [9,10]. Based on these results, it can be suggested that the E326K could have a possible effect on the stabilization of the dimeric form of GCcase, reducing the strength of the interaction between monomers and decreasing the enzyme stability.

The results of the present study are part of an article in preparation [22].

Acknowledgments

The computing resources and the related technical support used for this work have been provided by CRESCO/ENEAGRID High performance Computing infrastructure and his staff [21]. CRESCO/ENEAGRID High performance Computing infrastructure is funded by ENEA, the Italian National Agency for New Technologies, Energy and Sustainable Economic Development and by Italian and

European research programmes, see <http://www.cresco.enea.it/english> for information. C.A. acknowledges Project ECS 0000024 Rome Technopole, - CUP B83C22002820006, National Recovery and Resilience Plan (NRRP), Mission 4, Component 2 Investment 1.5, funded from the European Union – NextGenerationEU for funding part of this activity.

References

- [1] O. Neudorfer, N. Giladi, D. Elstein, A. Abrahamov, T. Turezkite, E. Aghai, A. Reches, B. Bembi, A. Zimran. Occurrence of Parkinson's syndrome in type I Gaucher disease. *QJM* **89**, pp. 691-694, (1996).
- [2] N. Tayebi, J. Walker, B. Stubblefield, E. Orvisky, M.E. LaMarca, K. Wong, H. Rosenbaum, R. Schiffmann, B. Bembi, E. Sidransky. Gaucher disease with parkinsonian manifestation: does glucocerebrosidase deficiency contribute to a vulnerability to parkinsonism? *Mol Genet Metab* **79**, pp.104-109 (2003).
- [3] R. Duran, N.E. Mencacci, A.V. Angeli, M. Shoai, E. Deas, H. Houlden, A. Mehta, D. Hughes, T.M. Cox, P. Deegan, A.H. Schapira, A.J. Lees, P. Limousin, P.R. Jarman, K.P. Bhatia, N.W. Wood, J. Hardy, T. Foltynie. The glucocerebrosidase E326K variant predisposes to Parkinson's disease, but does not cause Gaucher's disease. *Mov Disord* **28**, pp. 232-236 (2013).
- [4] T. Behl, G. Kaur, O. Fratila, C. Buhas, C.T. Judea-Pusta, N. Negrut, C. Bustea, S. Bungau. Cross-talks among GBA mutations, glucocerebrosidase and α -Synuclein in GBA-associated Parkinson's disease and their targeted therapeutic approaches: a comprehensive review. *Transl Neurodegener* **10**, pp. 4 (2021)
- [5] M. Horowitz, M. Pasmanik-Chor, I. Ron, E.H. Kolodny. The enigma of the E326K mutation in acid β -glucocerebrosidase. *Molecular Genetics and Metabolism, Special Issue: Personalized Medicine* **104**, pp. 35–38 (2011).
- [6] L. Smith, S. Mullin, A.H.V. Schapira. Insights into the structural biology of Gaucher disease. *Experimental Neurology, Translating scientific advances into disease-modifying therapies for Parkinson's disease* **298**, pp. 180–190 (2017).
- [7] J. Zheng, L. Chen, O.S. Skinner, D. Ysselstein, J. Remis, P. Lansbury, R. Skerlj, M. Mrosek, U. Heunisch, S. Krapp, J. Charrow, M. Schwake, N.L. Kelleher, R.B. Silverman, D. Krainc. β -Glucocerebrosidase Modulators Promote Dimerization of β -Glucocerebrosidase and Reveal an Allosteric Binding Site. *J Am Chem Soc* **140**, pp. 5914–5924 (2018).
- [8] T.L. Yap, J.M. Gruschus, A. Velayati, W. Westbroek, E. Goldin, N. Moaven, E. Sidransky, J.C. Lee. Alpha-synuclein interacts with Glucocerebrosidase providing a molecular link between Parkinson and Gaucher diseases. *J Biol Chem* **286**, pp. 28080–28088 (2011).
- [9] J. Benz, A.C. Rufer, S. Huber, A. Ehler, M. Hug, A. Topp, W. Guba, E.C. Hofmann, R. Jagasia, R.M.R. Sarmiento. Novel β -Glucocerebrosidase Activators That Bind to a New Pocket at a Dimer Interface and Induce Dimerization. *Angewandte Chemie International Edition* **60**, pp. 5436–5442 (2021).
- [10] J.M. Gruschus, Z. Jiang, T.L. Yap, S.A. Hill, A. Grishaev, G. Piszczek, E. Sidransky, J.C. Lee. Dissociation of glucocerebrosidase dimer in solution by its co-factor, saposin C. *Biochemical and Biophysical Research Communications* **457**, pp. 561–566 (2015).
- [11] R.L. Lieberman, J.A. D'aquino, D. Ringe, G.A. Petsko. Effects of pH and iminosugar pharmacological chaperones on lysosomal glycosidase structure and stability. *Biochemistry* **48**, pp. 4816-27 (2009).
- [12] S. Jo, T. Kim, V.G. Iyer, W. Im. CHARMM-GUI: A web-based graphical user interface for CHARMM. *Journal of Computational Chemistry* **29**, pp.1859–1865 (2008).
- [13] G. Martínez-Rosell, T. Giorgino, G. De Fabritiis. PlayMolecule ProteinPrepare: A Web Application for Protein Preparation for Molecular Dynamics Simulations. *J Chem Inf Model* **57**, pp. 1511–1516 (2017).
- [14] D.V.D. Spoel, E. Lindahl, B. Hess, G. Groenhof, A.E. Mark, H.J.C. Berendsen. GROMACS: Fast, flexible, and free. *Journal of Computational Chemistry* **26**, pp. 1701–1718 (2005).
- [15] M.J. Abraham, T. Murtola, R. Schulz, S. Páll, J.C. Smith, B. Hess, E. Lindahl. GROMACS: High performance molecular simulations through multi-level parallelism from laptops to supercomputers. *SoftwareX* **1–2**, pp. 19–25 (2015).
- [16] C. Oostenbrink, A. Villa, A.E. Van Gunsteren. A biomolecular force field based on the free enthalpy of hydration and solvation: the GROMOS force-field parameter sets 53A5 and 53A6. *Journal of computational chemistry* **25.13**, pp. 1656-1676 (2004).
- [17] W.L. Jorgensen, J. Chandrasekhar, J.D. Madura, R.W. Impey, M.L. Klein. Comparison of simple potential functions for simulating liquid water. *J. Chem. Phys.* **79**, pp. 926–935 (1983).

- [18] S.S. Petrova, A.D. Solov'ev. The Origin of the Method of Steepest Descent. *Historia Mathematica* **24**, pp. 361–375 (1997).
- [19] W. Humphrey, A. Dalke, K. Schulten. VMD: visual molecular dynamics. *J Mol Graph* **14**, pp. 33–38, 27–28 (1996).
- [20] B. Hess, Convergence of sampling in protein simulations. *Phys. Rev. E* **65** (2002)
- [21] D. Pietrafesa, A. Casamassa, M. Santoro, C. Consales, J.D. Rosati, C. Arcangeli. Structural and functional effects of the Parkinson-associated E326K mutations: an in silico approach. 2023 in preparation
- [22] F. Iannone, F. Ambrosino, G. Bracco, M. De Rosa, A. Funel, G. Guarnieri, S. Migliori, F. Palombi, G. Ponti, G. Santomauro, P. Procacci. CRESCO ENEA HPC clusters: a working example of a multifabric *GPFS Spectrum Scale layout*, *Int. Conf. High Perform. Comput. Simulation, HPCS 2019*, pp. 1051–1052 (2019).

JOINT UNIFI-ENEA PARTICIPATION TO THE INTERNATIONAL SAMPL9 BLIND CHALLENGE FOR PREDICTING TOLUENE-WATER LOGP PARTITION COEFFICIENTS USING MASSIVELY PARALLEL NON EQUILIBRIUM ALCHEMICAL SIMULATIONS

Piero Procacci^{1*}, Guido Guarnieri²

¹University of Florence, Chemistry Dept. U. Schiff, Via della Lastruccia 3, 50019 Sesto Fiorentino, Italy

²ENEA, Portici Research Centre, DTE-ICT-HPC, P.le E. Fermi, 1, I-80055 Portici (NA) (Italy)

ABSTRACT. We present our blind predictions for the LogP_{tw} toluene-water partition coefficients in the context of the SAMPL9 international challenge by way of atomistic molecular dynamics with the GAFF2 non polarizable force field. The calculations were performed on the CRESCO6 cluster using a nonequilibrium alchemical approach relying on the fast growth of the initially decoupled solute. Canonical sampling of the associated end-state is efficiently obtained by performing a Hamiltonian Replica Exchange simulation of the gas-phase solute molecule, combined with equilibrium configurations of explicit solvent, followed by a swarm of fast recoupling trajectories. Our submission was the best-performing and most efficient MD-based approach among the eight MD-based blind submissions.

1. Background

The Statistical Assessment of the Modeling of Proteins and Ligands (SAMPL) is a well established international initiative[1] for advancing the computational techniques in drug design. New experimental data, such as host-guest dissociation free energies, hydration free energies, acid-base dissociation constants, or partition coefficients are undisclosed to participants until the prediction submission deadline, so that the true predictive power and computational efficiency of methods can be assessed. In the 9-th edition of the challenge, participants were required to predict the LogP_{tw} for a series of compounds with disparate flexibility or molecular weight and coarsely spanning a significant portion of the “drug-like” chemical space, including moieties such as carboxyl, carbonyl, sulfonic, oxydryl, amino, amide, halogen, phenyl, hetero-cyclic, alkyl (see Figure 1). Given that the drug-receptor binding affinity is implicitly driven by the difference of two solvation free energies, namely that of the drug when bound to the receptor and that of the drug in bulk solvent,[2], the reliable and efficient prediction of partition coefficients, strictly related to solute transfer free energy between the two solvents, is an essential requirement for applying approach to the challenging case of drug design. The LogP_{tw} is computed as

$$\text{LogP}_{\text{tw}} = \frac{-(\Delta G_t - \Delta G_w)}{RT \log(10)} \quad (1)$$

where ΔG_t and ΔG_w are the solvation free energies in toluene and water, respectively, R is the gas constant and T is the temperature. Our MD approach is based on the nonequilibrium fast-growth (NE-FG) of an initially decoupled solute. The solvation free energies are computed independently by first sampling the solute conformations *in the gas-phase* at constant temperature ($T=300$ K) using Hamiltonian Replica Exchange (HREM) and then launching in parallel a swarm (typically from few tens to few hundreds) of alchemical recoupling nonequilibrium (NE) in the NPT ensemble in standard conditions, originated from an end-state where the HREM-sampled gas-phase conformations are combined with equilibrated snapshots of the pure (explicit) solvent. In an *alchemical* MD trajectory, the solute-solvent interaction V_{SS} is progressively re-coupled at constant pressure and temperature by a time-dependent driven λ parameter, performing the work $W =$

¹ Corresponding author. E-mail: piero.procacci@unifi.it.

$\int_0^\tau (\partial V_{ss}(\lambda)/\partial \lambda) \dot{\lambda} d\lambda$ on the system, with τ being the duration of the NE transition. The solvation free energy is recovered by applying the Jarzynski[3] identity to the resulting work distributions:

$$\Delta G = -RT \log(\int P(W) e^{-\beta W} dW). \quad (2)$$

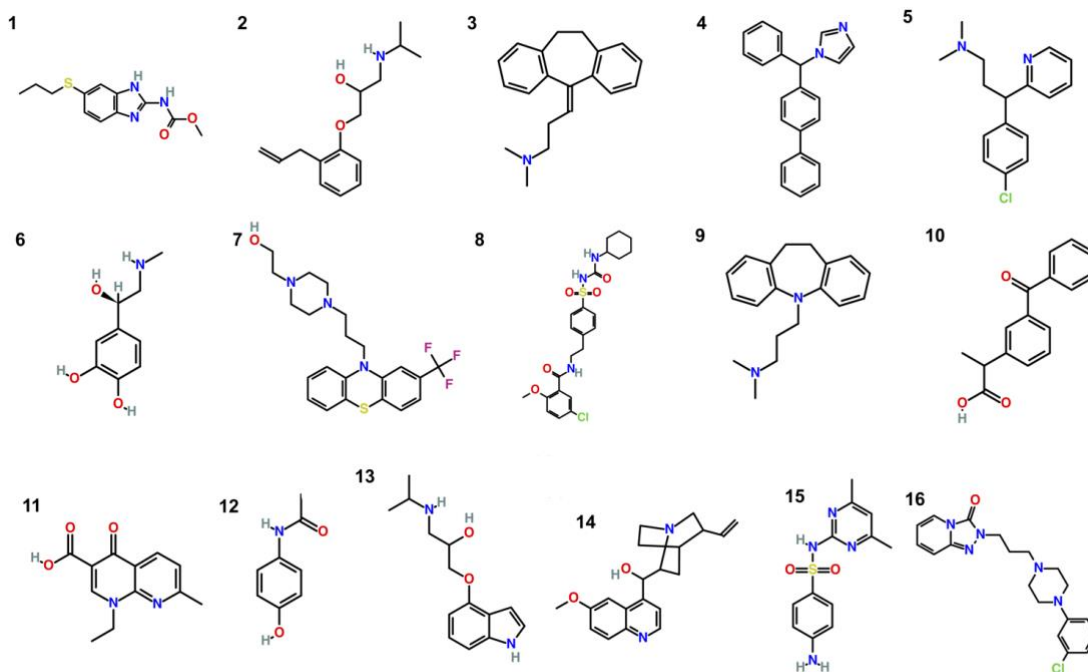


Fig. 1: Compounds for SAMPL9 blind challenge for toluene/water partition coefficients.

We used for the sixteen solute molecules of Figure 1 and the toluene solvent the well-established GAFF2 force field[4]. For water we used the OPC3 model.[4]

A hybrid OpenMP-MPI parallel job for a solute solvation free energy consisted of 96 concurrent non-communicating parallel alchemical trajectories with solute re-coupling time τ of 0.45 ns, each corresponding to an MPI process. A single trajectory was further parallelized using 6 OpenMP threads for a total 576 cores. A parallel job was completed on CRESCO6 in a wall-clock time of one or two hours depending on the solvent. The calculation of the sixteen LogP_{tw} partition coefficients required a total of 28000 core-hours (32 jobs). All calculations were done using the open-source program ORAC[5] (compiled with Intel19 and impi-intel19). The code is available for the public at the website <http://www1.chim.unit.it>. Documentation and user guide for ORAC can be found at the address <http://www1.chim.unifi.it/orac/MAN/>.

2. Results and Discussion

In the Figure 2 we report the correlation plot between NE-FG calculated and experimental LogP_{tw} .

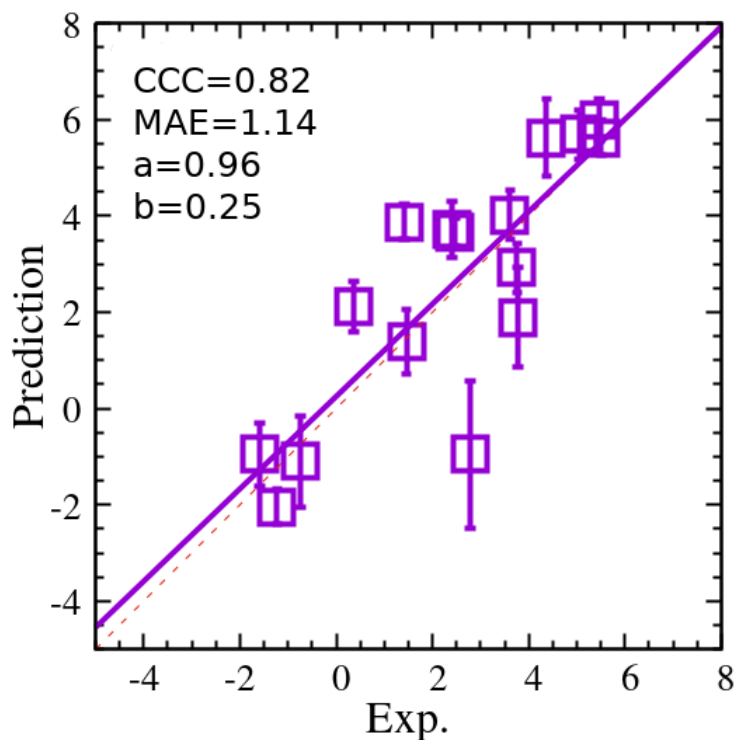


Fig 2: Correlation plot for the NE-FG submission. CCC: correlation concordance coefficient. MAE: mean absolute error. a: slope for the best line fit. b: intercept of the best line fit.

Correlation is assessed using the Lin concordance correlation coefficient, CCC. CCC ranges from -1 and 1 and cannot exceed the Pearson correlation coefficient R. CCC effectively measures the inter-rater reliability among two independent observable, x, y, combining the R metrics regarding ranking and the MAE outcome sensing the accuracy. The best fitting line is found to be nearly coincident with the optimal line $y=x$ with a Pearson correlation coefficient of $R=0.83$.

Subm.	method	FF	Charges	Ranked	t_{sim}/ns	CCC	MAE	R
VoltzLab	FEP/alchemy/EE	OpenFF-2.0	AM1-BCC	T	$\approx 3E4$	0.82	1.26	0.90
NE-FG	NE/alchemy	GAFF2	AM1-BCC	T	90	0.82	1.12	0.83
Beckstein-Iorga	FEP/alchemy	GAFF/TIP3P	AM1-BCC	F	≈ 250	0.75	1.50	0.79
Beckstein-Iorga	FEP/alchemy	OPLS/M24	mol2ff	T	≈ 250	0.73	1.72	0.88
Beckstein-Iorga	FEP/alchemy	OPLS/TIP4P	CM1A	F	≈ 250	0.72	1.88	0.91
Sprick	FEP/alchemy/HREM	GAFF/TIP3P	IpolQ-Mod	T	240	0.47	3.03	0.66
Oxford	E-S/MCC	GAFF2/TIP3P	AM1-BCC	T	1200	0.42	1.78	0.44
MD(Patel)	FEP/alchemy	CGenFF/TIP4P	cGenFF	F	216	0.21	2.63	0.25

Fig. 3: Comparative analysis of the MD-based blind predictions in the SAMPL0 $\text{Log}P_{tw}$ challenge

In Figure 3 we compare our submission with the other seven MD-based submissions. The importance of this assessment lies in the fact that, while knowledge-based (KB) empirical methodologies or QM-based techniques

generally perform better than MD-based approaches for LogP or pKa properties, when these methods are applied to the calculation of host-guest or drug-receptor binding affinities, their performances are significantly degraded.[1] QM and KB techniques are apparently unable to reliably cope with the solute inhomogeneous environment and related microsolvation phenomena. On the contrary, the reliability of the MD approaches is much less affected when passing from LogP predictions to drug-receptor or host-guest binding affinities calculations,[1]

Six of the MD-based predictions whose metrics is given in Figure 3 are done using the standard equilibrium alchemical free energy perturbation (FEP) method based on the so-called lambda stratification.[6] The “Oxford” submission on the end-state determination of the energy and entropy with the latter computed according to the so-called multiscale cell correlation. Our blind prediction is the only one produced using an NE alchemical approach. Full methodological details of each of the seven competitive submissions can be found at the SAMPL9 GitHub website.[7] Based on the MAE and CCC metrics our prediction *ranked first* in challenge. The computational cost (entry t_{sim}/ns in Figure 3) is measured in invested simulation time (in ns) on a per-solute basis, deduced from the information reported in the methodological sections of the submissions csv files, available in Ref. [7]. Such a measure is independent of the power of the MD engine and of the hardware configuration. NE-FG was by far the most efficient MD-based approach, with a computational cost of more than two order of magnitude smaller than that of the best performing method according to the R and CCC metrics (VotzLab). The latter used “lambda hopping” [8] to enhance the sampling with FEP simulation extending for as long as 1 μs . Full details of the performances of all the 20 blind predictions of the SAMPL9 LogP challenge are provided at the GitHub site <https://procacci.github.io/LogP-SAMPL9>.

The results obtained by the NE-FG in the challenge neatly show that nonequilibrium alchemical techniques are a reliable, cost-effective, inherently parallel alternative to the traditional equilibrium approaches based on free energy perturbation for the calculation of solvation free energies. The proposed NE method, when applied to drug-receptor dissociation free energies, has the potential to become an essential tool in high-level screening on HPC platforms for the elimination of false positive resulting from extensive docking or machine learning campaigns.

Acknowledgements

The computing resources and the related technical support used for this work have been provided by CRESCO/ENEAGRID High Performance Computing infrastructure and its staff. CRESCO/ENEAGRID High Performance Computing infrastructure is funded by ENEA, the Italian National Agency for New Technologies, Energy and Sustainable Economic Development and by Italian and European research programmes (see www.cresco.enea.it for information).

References

- [1] Amezcua, M.; El Khoury, L.; Mobley, D. Sampl7 host-guest challenge overview: assessing the reliability of polarizable and non-polarizable methods for binding free energy calculations. *J. Comput.-Aided Mol. Des.*, **35**, pp. 1–35 (2021). Muddana, H.S; Fenley, A.T.; Mobley, D.; Gilson, M.K. The sampl4 host-guest blind prediction challenge: an overview. *J. Comput Aided Mol. Des.*, **28**, pp. 305–317 (2014). Yin, J; Henriksen, N.; Slochow, D.; Shirts, M.; Chiu, M.W; Mobley, D.; Gilson, M.K. Overview of the sampl5 host-guest challenge: Are we doing better? *J. of Comput. Aided Mol. Des.*, **1**, pp. 1–19, 2016.
- [2] Procacci, P.; Chelli, R. Statistical Mechanics of Ligand-Receptor Noncovalent Association, Revisited: Binding Site and Standard State Volumes in Modern Alchemical Theories. *J. Chem. Theory Comput.*, **13**, pp1924–1933 (2017)
- [3] Jarzynski, C. Nonequilibrium equality for free energy differences. *Phys. Rev. Lett.*, **78**, 2690–2693 (1997).
- [4] Procacci, P. PrimaDORAC: A Free Web Interface for the Assignment of Partial Charges, Chemical Topology, and Bonded Parameters in Organic or Drug Molecules. *J. Chem. Inf. Model.* **57**, 1240–1245 (2017). Izadi, S.; Onufriev A.V. Accuracy limit of rigid 3-point water models. *J. Chem. Phys.*, **145**, pp. 074501 (2016).
- [5] Procacci, P. Hybrid MPI/OpenMP Implementation of the ORAC Molecular Dynamics Program for Generalized Ensemble and Fast Switching Alchemical Simulations. *J. Chem. Inf. Model.* **56**, 1117–1121 (2016).
- [6] Pohorille, A.; Jarzynski, C.; Chipot, C. Good Practices in Free-Energy Calculations. *J. Phys. Chem. B* **114**, pp. 10235–10253 (2010).
- [7] <https://github.com/samplchallenges/SAMPL9/tree/main/logP/Analysis/Submissions>.
- [8] Procacci, P. Does hamiltonian replica exchange via lambda-hopping enhance the sampling in alchemical free energy calculations? *Molecules*, **27**, pp. 4426-1-4426-12 (2022).

EVALUATION OF PHTHALOCYANINE AND HYPERICIN AS NOVEL ENTRY INHIBITORS AGAINST SARS-COV-2

Alice Romeo^{1*}, Federico Iacovelli¹ and Mattia Falconi¹

¹*Department of Biology, University of Rome Tor Vergata, Via della Ricerca Scientifica 1, 00133, Rome, Italy*¹⁶

ABSTRACT. A previous virtual screening procedure identified phthalocyanine and hypericin compounds as possible SARS-CoV-2 Spike entry inhibitors. Here, to explore the multi-target inhibitory potential of these molecules, atomistic and coarse-grained simulations of a complete model of the Spike embedded in a viral membrane have been performed, in the presence of metal-free phthalocyanines or hypericins, to describe their interaction with key protein regions and their insertion within the membrane. Experimentally, the pre-treatment of a pseudovirus exposing the Spike protein with these compounds resulted in an evident inhibition of its cell entry, confirming that these molecules should directly target the viral envelope surface. Therefore, computational and in vitro results support the role of hypericin and phthalocyanine as promising SARS-CoV-2 entry inhibitors.

1. Introduction

Although the World Health Organization (WHO) declared the end of the COVID-19 pandemic as a global health emergency, and vaccines highly reduced the risk of developing a severe disease, thousands of new weekly cases are still being reported by the WHO Coronavirus (COVID-19) Dashboard (<https://covid19.who.int/>). Thus, research of specific antiviral molecules is still fundamental considering the risk of reinfection in vaccinated people, the reduced protection for immunocompromised subjects and the limited worldwide availability of vaccines [1]. The SARS-CoV-2 Spike (S) glycoprotein regulates virus infection and disease outcome in the first stages of the disease [2]. Based on effective Respiratory Syncytial Virus (RSV) fusion inhibitors, we previously proposed that targeting an internal cavity of the prefusion S glycoprotein would block its transition to postfusion conformation and prevent virus entry [3]. The metal-free 31h-phthalocyanine and hypericin were identified from a virtual screening as the highest-affinity compounds for the S internal pocket [3]. Antiviral activity of both compounds or their derivatives against enveloped viruses was already known, and after the publication of our study a phthalocyanine-containing mouthwash was shown to reduce disease severity in COVID-19 patients, without side effects [4] and different studies showed that hypericin can inhibit SARS-CoV-2 without affecting cell viability [5–7]. Based on these evidence, it can be hypothesized that these compounds exert a concerted antiviral activity over the viral envelope, acting on multiple targets to interfere with virus attachment and fusion. Here, we evaluated this idea by performing Gaussian accelerated Molecular Dynamics (GaMD) simulations [8] of a complete S model embedded in a viral membrane [9], in the presence and absence of several phthalocyanine or hypericin molecules fluctuating in the solvent. To overcome the sampling limitations of these large atomistic systems, a Coarse-Grained (CG) model of a SARS-CoV-2 envelope portion was also modelled and simulated including only hypericin as an inhibitory molecule, resulting as the best interactor in the atomistic trajectories. Finally, the efficacy of phthalocyanine and hypericin in blocking SARS-CoV-2 fusion has been also experimentally verified in collaboration with Dr Giulia Cappelli (CNR) [10].

2. Computational methods

2.1 Gaussian accelerated MD simulations

A complete model of the SARS-CoV-2 S glycoprotein in prefusion conformation [9] was inserted in a bilayer mimicking the viral envelope using the CHARMM-GUI interface [11], parametrizing the system with the

¹⁶

Corresponding author. E-mail: falconi@uniroma2.it.

CHARMM36m force field [12]. Three models have been simulated: I) S protein without compounds (S-REF), II) S protein and phthalocyanine molecules (S-PHT), III) S protein and hypericin molecules (S-HYP). Compounds were randomly placed around the protein using the Packmol program [13]. Their structures were obtained from the PubChem database [14] and parameters were generated using the CGenFF program (<https://cgenff.umaryland.edu>) and the CHARMM general force field [15]. Each model was inserted in a rectangular box of TIP3P water molecules and neutralized with 0.15 M of NaCl. Structures were minimized in ten runs including 2000 steps each, decreasing constraints applied on all atoms from 20.0 to 0.0 kcal/mol. Minimized systems were thermalized in a canonical ensemble (NVT) using a 1.0 fs timestep, increasing the temperature from 0 to 310 K every 30.0 ps using Langevin dynamics and applying a constraint of 5.0 kcal/mol on protein and membrane atoms. Then, equilibration was performed in an anisotropic NPT (NPT-A) ensemble using the Nosè–Hoover Langevin piston method at a constant pressure of 1.0 atm, gradually releasing constraints applied on protein and membrane every 250 ps during a 2250 ps run. For the production dynamics, the timestep was increased to 2.0 fs and the systems were simulated for 10.0 ns using classical MD before starting 150 ns of dual-boost GaMD [8] (2.0 ns of classical MD preparation, 50.0 ns of GaMD equilibration, and 100 ns of GaMD production). Electrostatic interactions were calculated using the PME method and cut-off for non-bonded interactions was set to 12.0 Å. All simulations were performed using the NAMD 2.13 software [16] on 14 CPU nodes of the ENEA CRESCO6 HPC cluster. On the cluster, atomistic simulations required a total of 600 GB of storage each, after removing water molecules from the trajectories.

2.2 Coarse-grained MD simulations

A CG model of a SARS-CoV-2 envelope portion, including the S protein, a viral membrane and surrounding hypericin molecules, was built using the martinize2 (<https://github.com/marrink-lab/vermouth-martinize>) and Insane [17] tools, starting from the atomistic model of the protein. An elastic network was automatically generated for the protein based on the input structure. Hypericin was modelled and parametrized at CG resolution following the Martini 3 building-block approach, starting from its atomistic structure [10], and hypericin molecules were randomly placed around the protein using the insert-molecules tool of GROMACS [18]. The system was solvated using Martini 3 water beads and 0.15 M NaCl. Simulations were performed using the Martini 3 force field [19] and the GROMACS 2020 software [18] on 1 CPU node of the ENEA CRESCO6 HPC cluster. Details on the simulation protocol can be found in the paper [10]. A total of 14 simulation replicas of 10.0 μ s were performed for the S-hypericin system, randomizing initial hypericin positions, while 5 replicas of a reference system without hypericin were also simulated for 10.0 μ s each. CG simulations required a total of about 1 TB of storage after removing water molecules from the trajectories.

2.3 Trajectory analyses

All analyses were performed using the VMD 1.9.3 [20] or GROMACS 2020 [18] programs on 1 node of the ENEA CRESCO6 HPC cluster. Membrane thickness was evaluated using the VMD MEMBPLUGIN Tool [21] and 2D thickness maps were generated using an in-house Python script. The binding persistence of compounds with each S domain was calculated in VMD. Occupancy of CG hypericin molecules on the S protein was calculated using the VMD Volmap tool. S bending angles were calculated using an in-house Tcl script in VMD. Radial distribution functions (RDFs) and PCA analyses were performed using GROMACS, setting S C α atoms as reference set of positions.

3. Computational results

3.1 All-atom GaMD simulations of hypericin and phthalocyanine

During the simulations, one phthalocyanine and two hypericin molecules entered the viral membrane, localizing below the interface between the hydrophobic lipid tails and polar heads. Membrane thickness heatmaps generated over the production phase of the GaMD trajectory (50-150 ns) show distinct alterations in the thickness patterns between the three systems, particularly at the compounds' insertion regions, with both compounds inducing a decrease in bilayer thickness and a general re-organization of its pattern in the whole membrane (Fig. 1). This suggests these compounds could alter the structural organization of the viral envelope, decreasing the efficacy of viral-cell membrane fusion.

RDFs indicate that hypericin molecules remain closer to the protein, showing one density peak at 1.0 - 2.0 nm from its surface (data not shown) [10]. In accord, contact analysis showed that only six phthalocyanine molecules interact with S for more than 50% of the simulation time, while several hypericin molecules stably contact crucial S regions such as the NTDs, RBDs, HR1 domains and fusion peptides, and HR2 domains, with persistence ranging from 26 to 99%. Insertion of two hypericins into a pocket between the three RBDs suggests

that this compound may limit RBDs motions, consequently reducing S-ACE2 interactions, and its interaction with the other S functional domains could interfere with fusion peptides release and ultimately hinder S transition to postfusion conformation. PCA performed on S C α atoms in the three simulations allowed to isolate major fluctuations contributing to the protein dynamics, with the obtained cross-correlation matrices showing that phthalocyanine or hypericin induce a different dynamical behaviour in several protein regions compared to the reference (data not shown). For the S-HYP system, this effect is particularly evident in the regions highly contacted by this compound (NTDs and RBDs). On the other hand, S motions in the presence of the two compounds are similar in all main considered protein domains. In both cases altered motions in the protein CTD (data not shown) are observed, indicating that membrane thickness alterations induced by the compounds (Fig. 1) could have also influenced the dynamics of protein regions directly contacting the bilayer. Projection of the first eigenvector (accounting for about 46% of the total protein motion) over the simulation time indicates that the directions of the main motion characterizing the protein are very similar in the S-PHT and S-HYP systems, while they show an opposite trend in the S-REF (Fig. 2A). This suggests that compounds' diffusion around the protein could alter the major motions defining the protein structural dynamics and consequently also influence its native conformational behaviour on the virion surface.

3.2 Microseconds coarse-grained simulations of hypericin

To extend the sampling timescale, an equivalent S-membrane model was also simulated at CG resolution in the presence of hypericin. In these simulations, about 6 to 14 hypericin molecules inserted in the bilayer, confirming that hypericin is highly attracted to the membrane due to its amphipathic character. However, membrane thickness was not particularly altered by their presence, evaluating 41 Å on average in both simulated conditions. Interaction analysis and visual inspection of hypericin distribution over the S surface indicates that hypericin compounds mostly cluster around the protein NTDs, RBDs and HR1 domains (Fig. 2B), achieving binding locations similar to those observed in the atomistic simulation. This reproducibility strongly indicates that these regions possess specific clefts favouring the attachment of free hypericin molecules. Interestingly, the insertion of two to three hypericin molecules at the interface of the S internal cavity was also observed in four replicas (Fig. 2B), supporting the inhibition mechanism hypothesized in our previous paper [5]. Protein bending angles were also monitored in both conditions, but a similar trend has been obtained for the S protein in the reference and hypericin systems (data not shown) [10]. The lowest peak observed for the reference system was a curvature of 84°, while that of the hypericin-bound protein was 94°.

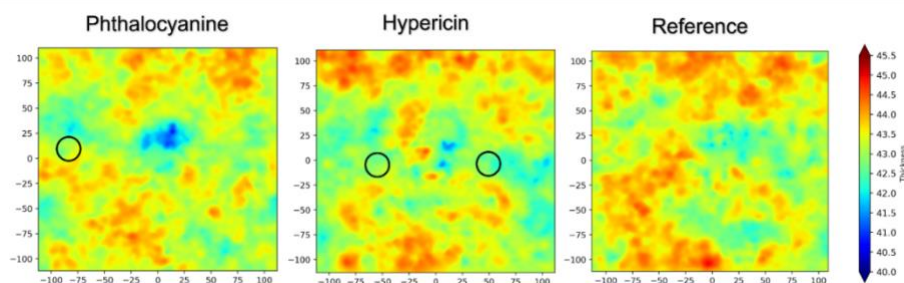


Fig.1: Membrane thickness heatmaps calculated for the viral membrane in the three atomistic systems. Black circles indicate compounds' insertion regions.

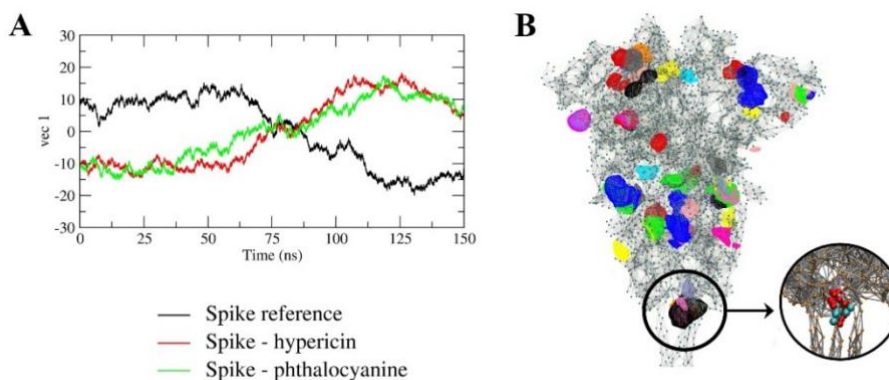


Fig.2: A) Projection of the three GaMD trajectories on the first eigenvectors calculated on S C α atoms. B) Binding locations of hypericin on the S protein, represented by surfaces colored according to the simulation replica. Hypericins

binding within the protein internal pocket are highlighted with a circle and one of the obtained binding configurations is magnified on the right. Protein elastic network is shown as grey wires and backbone beads as small spheres. Hypericin molecules in the pocket are shown as spheres coloured by bead type.

4. Discussion

This work evaluated hypericin and phthalocyanine as SARS-CoV-2 entry inhibitors, verifying their potential activity on a SARS-CoV-2 envelope model at both all-atom and CG resolution. Both methods highlighted the presence of several drugs' binding sites on the protein surface and their propensity to insert within the viral bilayer and modify its thickness profile. Hypericin shows a higher attraction than phthalocyanine towards the S protein, targeting different protein functional domains (the NTDs, RBDs, fusion peptides, HR1 and HR2). In CG simulations, even starting from different initial configurations, hypericin achieves similar binding sites on the S surface, overlapping those observed in the atomistic trajectory. Notably, several hypericin molecules also inserted at the protein internal cavity interface, suggesting this compound could bind to this internal region to prevent S transition to postfusion conformation, as we previously suggested [5]. Following computational results, antiviral assays were performed in collaboration with Dr Giulia Cappelli (CNR) using a SARS-CoV-2 pseudovirus expressing the S protein. Results indicated that virus pre-treatment with low hypericin or phthalocyanine concentrations (0.78 $\mu\text{g/ml}$ and 0.005 $\mu\text{g/ml}$) strongly inhibits its entry into cells, indicating their antiviral activity should involve the targeting of the viral envelope surface as suggested by computational data [10]. In conclusion, the obtained results support a further evaluation of phthalocyanine and hypericin as entry inhibitors against SARS-CoV-2 and, possibly, other viruses sharing a similar envelope composition.

Acknowledgments

This work was supported by the National Research Center for HPC, Big Data and Quantum Computing, within the CN1 spoke 6 "Multiscale Modelling and Engineering Applications".

References

- [1] A. Telenti, A. Arvin, L. Corey, D. Corti, M.S. Diamond, A. García-Sastre, R.F. Garry, E.C. Holmes, P.S. Pang, and H.W. Virgin. After the pandemic: perspectives on the future trajectory of COVID-19. *Nature* **596**, pp. 495–504, (2021).
- [2] T. Tang, M. Bidon, J.A. Jaimes, G.R. Whittaker, and S. Daniel. Coronavirus membrane fusion mechanism offers a potential target for antiviral development. *Antiviral Research* **178**, pp. 104792, (2020).
- [3] A. Romeo, F. Iacovelli, and M. Falconi. Targeting the SARS-CoV-2 spike glycoprotein prefusion conformation: virtual screening and molecular dynamics simulations applied to the identification of potential fusion inhibitors. *Virus Research* **286**, pp. 198068, (2020).
- [4] P.S. da Silva Santos, B. da Fonseca Orcina, R.R.G. Machado, F.V. Vilhena, L.M. da Costa Alves, M.S.R. Zangrando, R.C. de Oliveira, M.Q.S. Soares, A.N.C. Simão, E.C.I.N. Pietro, J.P.G. Kuroda, I.A. de Almeida Benjamim, D.B. Araujo, S.H. Toma, L. Flor, K. Araki, and E.L. Durigon. Beneficial effects of a mouthwash containing an antiviral phthalocyanine derivative on the length of hospital stay for COVID-19: randomised trial. *Scientific Reports* **11**, pp. 19937, (2021).
- [5] P. Delcanale, E. Uriati, M. Mariangeli, A. Mussini, A. Moreno, D. Lelli, L. Cavanna, P. Bianchini, A. Diaspro, S. Abbruzzetti, and C. Viappiani. The Interaction of Hypericin with SARS-CoV-2 Reveals a Multimodal Antiviral Activity. *ACS Applied Materials and Interfaces* **14**, pp. 14025–14032, (2022).
- [6] F.F. Mohamed, D. Anhlan, M. Schöfbänker, A. Schreiber, N. Classen, A. Hensel, G. Hempel, W. Scholz, J. Kühn, E.R. Hrincius, and S. Ludwig. Hypericum perforatum and Its Ingredients Hypericin and Pseudohypericin Demonstrate an Antiviral Activity against SARS-CoV-2. *Pharmaceuticals* **15**, (2022).
- [7] A. da R. Matos, B.C. Caetano, J.L. de Almeida Filho, J.S.C. de C. Martins, M.G.P. de Oliveira, T. das C. Sousa, M.A.P. Horta, M.M. Siqueira, and J.H. Fernandez. Identification of Hypericin as a Candidate Repurposed Therapeutic Agent for COVID-19 and Its Potential Anti-SARS-CoV-2 Activity. *Frontiers in Microbiology* **13**, pp. 1–11, (2022).
- [8] J. Wang, P.R. Arantes, A. Bhattarai, R. V. Hsu, S. Pawnikar, Y.M. Huang, G. Palermo, and Y. Miao. Gaussian accelerated molecular dynamics: Principles and applications. *WIREs Computational Molecular*

Science **11**, pp. 1–32, (2021).

[9] H. Woo, S.J. Park, Y.K. Choi, T. Park, M. Tanveer, Y. Cao, N.R. Kern, J. Lee, M.S. Yeom, T.I. Croll, C. Seok, and W. Im. Developing a Fully Glycosylated Full-Length SARS-CoV-2 Spike Protein Model in a Viral Membrane. *The Journal of Physical Chemistry. B* **124**, pp. 7128–7137, (2020).

[10] A. Romeo, G. Cappelli, F. Iacovelli, V. Colizzi, and M. Falconi. Computational and experimental validation of phthalocyanine and hypericin as effective SARS-CoV-2 fusion inhibitors. *Journal of Biomolecular Structure and Dynamics* **0**, pp. 1–15, (2023).

[11] S. Jo, T. Kim, V.G. Iyer, and W. Im. CHARMM-GUI: A web-based graphical user interface for CHARMM. *Journal of Computational Chemistry* **29**, pp. 1859–1865, (2008).

[12] J. Huang, S. Rauscher, G. Nawrocki, T. Ran, M. Feig, B.L. De Groot, H. Grubmüller, and A.D. MacKerell. CHARMM36m: An improved force field for folded and intrinsically disordered proteins. *Nature Methods* **14**, pp. 71–73, (2016).

[13] L. Martínez, R. Andrade, E.G. Birgin, and J.M. Martínez. PACKMOL: A package for building initial configurations for molecular dynamics simulations. *Journal of Computational Chemistry* **30**, pp. 2157–2164, (2009).

[14] S. Kim, J. Chen, T. Cheng, A. Gindulyte, J. He, S. He, Q. Li, B.A. Shoemaker, P.A. Thiessen, B. Yu, L. Zaslavsky, J. Zhang, and E.E. Bolton. PubChem in 2021: new data content and improved web interfaces. *Nucleic Acids Research* **49**, pp. D1388–D1395, (2021).

[15] K. Vanommeslaeghe, E. Hatcher, C. Acharya, S. Kundu, S. Zhong, J. Shim, E. Darian, O. Guvench, P. Lopes, I. Vorobyov, and A.D. Mackerell. CHARMM general force field: A force field for drug-like molecules compatible with the CHARMM all-atom additive biological force fields. *Journal of Computational Chemistry* **31**, pp. 671–690, (2010).

[16] J.C. Phillips, R. Braun, W. Wang, J. Gumbart, E. Tajkhorshid, E. Villa, C. Chipot, R.D. Skeel, L. Kalé, and K. Schulten. Scalable molecular dynamics with NAMD. *Journal of Computational Chemistry* **26**, pp. 1781–1802, (2005).

[17] T.A. Wassenaar, H.I. Ingólfsson, R.A. Böckmann, D.P. Tieleman, and S.J. Marrink. Computational lipidomics with insane: A versatile tool for generating custom membranes for molecular simulations. *Journal of Chemical Theory and Computation* **11**, pp. 2144–2155, (2015).

[18] M.J. Abraham, T. Murtola, R. Schulz, S. Páll, J.C. Smith, B. Hess, and E. Lindah. Gromacs: High performance molecular simulations through multi-level parallelism from laptops to supercomputers. *SoftwareX* **1–2**, pp. 19–25, (2015).

[19] P.C.T. Souza, R. Alessandri, J. Barnoud, S. Thallmair, I. Faustino, F. Grünewald, I. Patmanidis, H. Abdizadeh, B.M.H. Bruininks, T.A. Wassenaar, P.C. Kroon, J. Melcr, V. Nieto, V. Corradi, H.M. Khan, J. Domański, M. Javanainen, H. Martinez-Seara, N. Reuter, R.B. Best, I. Vattulainen, L. Monticelli, X. Periole, D.P. Tieleman, A.H. de Vries, and S.J. Marrink. Martini 3: a general purpose force field for coarse-grained molecular dynamics. *Nature Methods* **18**, pp. 382–388, (2021).

[20] W. Humphrey, A. Dalke, and K. Schulten. VMD: Visual molecular dynamics. *Journal of Molecular Graphics* **14**, pp. 33–38, (1996).

[21] R. Guixà-González, I. Rodríguez-Espigares, J.M. Ramírez-Anguita, P. Carrió-Gaspar, H. Martinez-Seara, T. Giorgino, and J. Selent. MEMBPLUGIN: Studying membrane complexity in VMD. *Bioinformatics* **30**, pp. 1478–1480, (2014).

MATERIALS SCIENCE USING MACHINE LEARNING

Claudio Ronchetti^{17*}, Marco Puccini¹, Sergio Ferlito², Simone Giusepponi¹, Filippo Palombi³,
Francesco Buonocore¹ and Massimo Celino¹

¹*Energy Technologies and Renewable Sources Department, ICT Division, ENEA,
Casaccia Research Center, Rome, Italy*

²*Energy Technologies and Renewable Sources Department, ICT Division, ENEA,
Portici Research Center, Portici, Italy*

³*Energy Technologies and Renewable Sources Department, ICT Division, ENEA,
Frascati Research Center, Frascati, Italy*

ABSTRACT. This paper shows an application of Graph Neural Networks (GNNs), a class of deep learning methods, used to predict physical properties and to obtain optimal cathode materials for batteries. Two GNNs are selected: Crystal Graph Convolutional Neural Networks (CGCNN) and the more recent Geometric-Information-Enhanced Crystal Graph Network (GeoCGNN). Both networks are trained on a selected open-source ab initio Density Functional Theory (DFT) dataset for solid-state materials to predict the formation energy and then calculate the redox potential. The results compare the run times between a data-driven and a physics-based model carried out on CRESCO infrastructure.

This approach allows us to detect the optimum faster than physics-based computational approaches.

1. Introduction

Science has been characterized by four paradigms: empirical models, formulation of physical/chemical laws, physics-based computational approaches, and data-driven techniques. This work is based on the exploitation of the fourth paradigm in order to speed up scientific discovery.

The current procedure applies the ab initio approach based on Density Functional Theory (DFT) calculations to obtain material properties using physics-based codes like Quantum Espresso [1, 2]. Generally, a DFT calculation requires a lot of execution time (hours) and hardware resources like High-Performance Computing (HPC). The combinatorial space of the materials is far too large to be evaluated directly via DFT calculations. In recent years, there has been rapid progress in the development of deep learning-based neural networks in order to predict the properties of materials. Such networks have produced accurate and rapid predictions. The molecule or crystalline material is represented as a graph where the atoms constitute the nodes, and their atomistic bonds correspond to the edge.

The use case is to calculate the material properties, such as formation energy and redox potential, on several structures that are variations of a starting structure to obtain the optimal material. The starting structure has been determined based on preliminary studies by materials scientists. This structure is NaMnO₂, and calculations are performed in a supercell made up of 48 atoms. This experiment is based on the doping of the starting structure by replacing Manganese with Titanium and Nickel, and on the calculation of the formation energy and redox potential for each structure. In this work, two networks were used, CGCNN [3] and the more recent Geometric-Information-Enhanced Crystal Graph Network (GeoCGNN) [4], to predict the formation energy as a material property.

2. Dataset

* Claudio Ronchetti. E-mail: claudio.ronchetti@enea.it

Machine learning in materials science is mostly concerned with supervised learning. The success of such methods depends mainly on the amount and quality of data that is available. Fortunately, this challenge has recently been met by worldwide crystallographic databases based on FAIR principles [5], such as Materials Project (MP) [6], the inorganic crystal structure database, and others (Materials genome initiative [7], the NOMAD archive [8], Materials Cloud [9], Inorganic Crystal Structure Database of National Institute of Standards and Technology [10]) containing information on numerous properties of known materials.

Our dataset consists of 126,162 structure-formation energy pairs from the February 2022 version of MP database, and it is available on Ref. [11]. This dataset was stored into Red Hat Ceph Storage (S3 bucket) [12], an open, scalable, simplified storage solution engineered for data analytics, Artificial Intelligence/Machine Learning (AI/ML), and emerging workloads. The dataset consists of Crystallographic Information File (CIF) and a descriptor (pre-processed) file for each structure, and it takes up **121.3 GB** of memory.

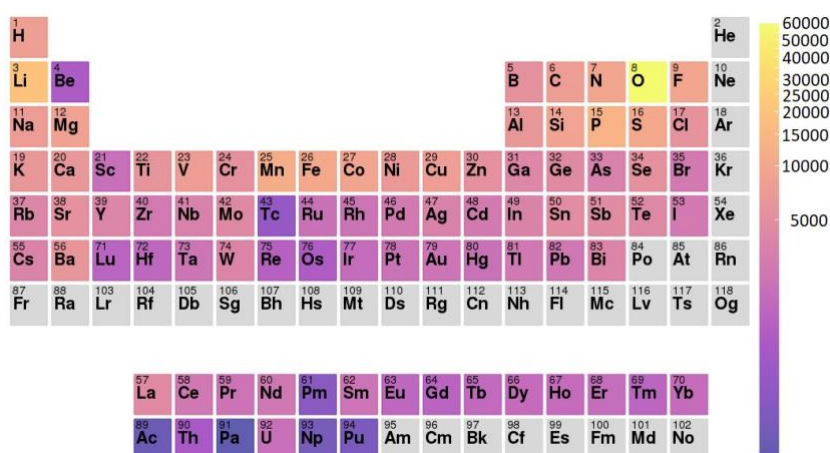


Fig. 3: Elements frequency in dataset on a logarithmic basis.

3. Developing environment

CGCNN and GeoCGNN have been implemented using *Pytorch* [13], a robust library that allows to perform neural networks (NN) on CPUs and GPUs of multiple and heterogeneous hardware architectures. It was necessary to modify both networks' codes, available on GitHub [14, 15], to access and manage the dataset. The developed code is available on ENEA's GitLab [16].

A container-based virtual environment was created to package up code and all its dependencies, so the application runs quickly and reliably from one computing environment to another. Singularity engine [17] was used to build container images and to run complex applications on HPC clusters in a simple, portable, and reproducible way. The building procedure was completed via CRESCOWARE [18], a container-based gateway for HPC/AI applications in the CRESCO/ENEAGRID infrastructure.

4. Computing results

The data-driven models were trained with the dataset described in the section *Dataset* to predict the formation energy. The data set is divided into three parts – training, validation, and test set respectively using 80%:10%:10% splits.

Each model was trained on the training set for 500 epochs, and the configuration and hyperparameters with the lowest validation error were selected. Finally, the test Mean Absolute Error (MAE) is calculated. The models were trained on a node equipped with a Nvidia Quadro RTX 6000 GPU available in the CRESCO/ENEAGRID infrastructure.

Once the best model was obtained, it was used to perform the inference on about 8000 structures randomly chosen in the combinatorial space.

The execution time to run the inference took about **60ms** for each structure using 48 CPUs on a node, which is not remotely comparable to the **3h** on average required to run the DFT calculations using 576 CPUs distributed on 12 nodes.

5. Conclusions

This work explained an application of deep learning neural networks in materials science, which allows to speed up materials discovery (see Ref. [21] for details).

The regression tasking models were trained on the formation energy to learn physical correlations in a highly heterogeneous DFT dataset.

The computing results show that GNNs reduce the time needed to predict the material properties by a factor of thousands compared to the original DFT calculations.

Primary future applications of GNNs are expected: it's planned to integrate physics-based and data-driven models together in scenarios where the trained GNN surrogate model can act as an initial guess for a further refined DFT calculation. In computational workflows using AiiDA [19, 20] infrastructure, this could substantially reduce the total simulation time without any change in the final accuracy. This could have an impact on energy consumption that should not be underestimated.

Acknowledgment

This work is part of the IEMAP (Italian Energy Materials Acceleration Platform) project supported by MiTE (Ministero per la Transizione Ecologica) under the international initiative Mission Innovation as described in Ref. [22].

References

- [1] P. Giannozzi *et al.* Advanced capabilities for materials modelling with Quantum ESPRESSO. *J. Phys. Condens. Matter* **29**, 465901, (2017).
- [2] www.quantum-espresso.org.
- [3] T. Xie and J. C. Grossman. Crystal graph convolutional neural networks for an accurate and interpretable prediction of material properties. *PRL* **120**(14), 145301, (2018).
- [4] J. Cheng, C. Zhang and L. Dong. A geometric-information-enhanced crystal graph network for predicting properties of materials. *Comm. Materials* **2**(1), pp. 1-11, (2021).
- [5] M. D. Wilkinson *et al.* The FAIR Guiding Principles for scientific data management and stewardship. *Scientific data* **3**(1), pp. 1-9, (2016).
- [6] A. Jain *et al.* Commentary: The Materials Project: A materials genome approach to accelerating materials innovation. *APL materials* **1**(1), 011002, (2013).
- [7] J. J. de Pablo *et al.* New frontiers for the materials genome initiative. *npj Computational Materials* **5**(1), pp. 1-23, (2019).
- [8] C. Draxl and M. Scheffler. NOMAD: The FAIR concept for big data-driven materials science. *Mrs Bulletin* **43**(9), pp. 676-682, (2018).
- [9] L. Talirz *et al.* Materials Cloud, a platform for open computational science. *Scientific data* **7**(1), pp. 1-12, (2020).
- [10] A. Belsky, M. Hellenbrandt, V. L. Karen and P. Luksch. New developments in the Inorganic Crystal Structure Database (ICSD): accessibility in support of materials research and design. *Acta Crystallographica Section B: Structural Science* **58**(3), pp. 364-369, (2002).
- [11] C. Ronchetti. *Materials Project Dataset* (February 2022) [Data set]. Zenodo. <https://doi.org/10.5281/zenodo.6811684>.
- [12] S. A. Weil, S. A. Brandt, E. L. Miller, D. D. Long and C. Maltzahn. Ceph: A scalable, high-performance distributed file system. *In Proceedings of the 7th symposium on Operating systems design and implementation* pp. 307-320, (2006, November).

- [13] A. Paszke *et al.* Pytorch: An imperative style, high-performance deep learning library. *Advances in neural information processing systems* 32, (2019).
- [14] T. Xie. "CGCNN", github.com. <https://github.com/txie-93/cgcn> (accessed Sep 15, 2022).
- [15] J. Cheng, C. Zhang, and L. Dong. "Geo-CGNN", github.com. <https://github.com/Tinystormjojo/geo-CGNN> (accessed Sep 15, 2022).
- [16] C. Ronchetti. "ai4mat", <https://gitlab.brindisi.enea.it/claudio.ronchetti/ai4mat> (accessed July 15, 2023)
- [17] Sylabs, "Singularity", sylabs.io. <https://sylabs.io/singularity/> (accessed Sep 15, 2022).
- [18] A. Mariano, G. D'Amato, G. Formisano, G. Guarnieri, G. Santomauro and S. Migliori. Crescoware: A Container-Based Gateway for HPC and AI Applications in the ENEAGRID Infrastructure. In *Science and Information Conference* pp. 196-206, (2022). Springer, Cham.
- [19] G. Pizzi, A. Cepellotti, R. Sabatini, N. Marzari and B. Kozinsky. AiiDA: automated interactive infrastructure and database for computational science. *Comp. Mat. Sci.* **111**, pp. 218-230, (2016).
- [20] S. P. Huber *et al.* AiiDA 1.0, a scalable computational infrastructure for automated reproducible workflows and data provenance. *Scientific data* **7**(1), pp. 1-18, (2020).
- [21] Ronchetti, Claudio, et al. "Machine learning techniques for data analysis in materials science." 2022 AEIT International Annual Conference (AEIT). IEEE, 2022.
- [22] A. Aspuru-Guzik and K. Persson. Materials Acceleration Platform: Accelerating Advanced Energy Materials Discovery by Integrating High-Throughput Methods and Artificial Intelligence. Mission Innovation, (2018).

ATOMISTIC SIMULATIONS OF QUANTUM DOTS

Gabriele Saleh¹, Juliette Zito¹ and Ivan Infante^{2,3,18}

¹ *Nanochemistry, Istituto Italiano di Tecnologia, Via Morego 30, 16163 Genova, Italy*

² *BCMaterials, Basque Center for Materials, Applications, and Nanostructures, UPV/EHU Science Park, Leioa 48940, Spain*

³ *Ikerbasque Basque Foundation for Science, Bilbao 48009, Spain*

ABSTRACT. Semiconductor nanocrystals play an increasingly important role in optoelectronic devices. The full understanding of the atomistic and electronic structures of these nanocrystals, and in particular of their surface, is a key step for the design of better performing materials. This work reports on quantum chemical simulations, performed on the Cresco4 and Cresco6 supercomputers, adopted to tackle this issue on two types of nanocrystals architectures: core-only and core-shell.

1. Introduction

Semiconductor nanocrystals (NCs), generally known as quantum dots (QDs) are generally defined as semiconductor materials which have one or more dimensions in the nanometer scale. This feature confers them with properties that differ fundamentally from their bulk counterpart and that can be tailored to obtain the desired properties [1], for example to tune the absorption and emission wavelengths. Core-only QDs, the simplest form of QDs, are crystallites of a single material passivated by an outer shell of organic ligands, whose role however goes beyond the mere stabilization of QD in solution: the ligands form an integral part of the QDs functionality (more on this in Sect. 2 of this document). Core-shell QDs, where a shell of a commensurate wide-bandgap semiconductor is grown around a core-only QD, is another established approach to passivate QD surfaces. In this contribution, we illustrate the computational work of our group on QDs. In particular, Section 2 and Section 3 report, respectively, on the density functional theory (DFT) simulations adopted to investigate the atomistic and electronic structure of core-only and core-shell QDs.

2. Core-only QDs

In this section, we illustrate the DFT simulations we carried out on core-only QDs. We studied two systems, in synergical collaboration with the experimental research groups in our institute who carried out the synthesis and characterization: BiSX (X=Cl, Br, I) and Bi-doped Cs₂Ag_{1-x-y}Na_xK_yInCl₆ NCs.

2.1. Rationalizing the mixed valence character and the optical properties of Bismuth Chalcogenide nanocrystals

Our experimental colleagues developed a new colloidal synthetic method to obtain bismuth chalcogenide nanocrystals [2] (Fig. 1a). In a subsequent study, we adopted DFT simulations to shed light on the structure of Bi₁₃S₁₈X₂ compounds (X=Br, I), which present some significant crystallographic disorder, and on their optical properties [3]. In particular, the simulations aimed at explaining why these materials display an unusually low band gap (0.80 eV). First, we explored the energetics of the possible configurations resulting from the crystallographic disordered structure. We concluded that the most stable structure features Bi dimers lying parallel to the *c* crystallographic axis. We then moved to the electronic structure analysis: band structure, density of states, and charge density. A peculiar chemical bonding scenario emerges: these dimers are Bi₂⁴⁺ entities, and they form as a consequence of Peierls distortion due to their subvalent character (Bi²⁺, i.e. Bi³⁺ ions with one additional *p* electron each). Importantly, the electronic state corresponding to these Bi-Bi bonds

¹⁸ Corresponding author. E-mail: ivan.infante@bcmaterials.net

create a state in the middle of the band gap (Fig. 1b-c), thus explaining the low-energy peak observed in the experimental absorption spectra.

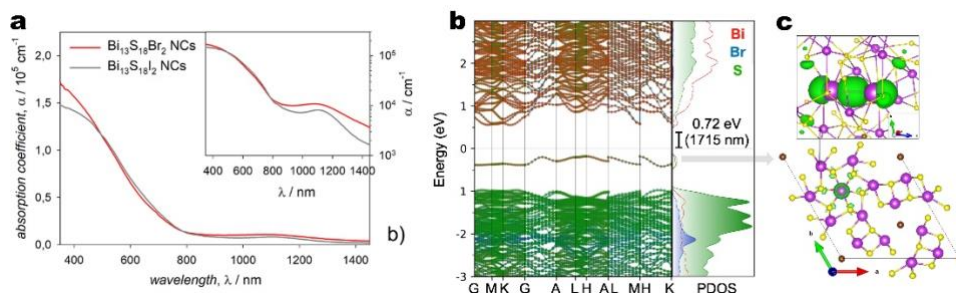


Fig.1: Optical and electronic properties of $\text{Bi}_{13}\text{S}_{18}\text{Br}_2$. a) experimental absorption spectrum. The insets show an enlargement of the low-energy peak. b) band structure and density of states of BiSBr calculated by DFT. c) charge density distribution (green isosurface) of the highest occupied band. Violet, Yellow, and brown sphere represent Bi, S, and Br atoms, respectively.

The simulations described in this paragraph were performed with the Vienna ab initio software package (VASP) [4] on cresco4 and cresco6 clusters. The Perdew-Burke-Ernzerhof (PBE) functional [Error! Bookmark not defined.] was adopted throughout and complemented with the Tkatchenko-Scheffler correction [5] to accurately reproduce dispersive forces. The plane wave energy cutoff was set to 500 eV for geometry optimizations and 400 eV for band structure calculations. The reciprocal space was sampled through a uniform, Γ -centered grid with $0.28/2\pi \text{ \AA}^{-1}$ point spacing. For all the studied systems, the cell parameters and atomic positions were optimized to the closest energy minimum.

2.2. Bi-doped $\text{Cs}_2\text{Ag}_{1-x-y}\text{Na}_x\text{K}_y\text{InCl}_6$ nanocrystals

In this work, our experimental colleagues identified the partial replacement of Na^+ with K^+ ions as an efficient tool to modulate the photoluminescence quantum yield (PLQY) of Bi-doped $\text{Cs}_2\text{Ag}_{1-x}\text{Na}_x\text{InCl}_6$ double perovskite (DP) NCs, which was increased up to the record value of $\sim 68\%$ with a K^+ content of 7%, and then systematically decreased upon further increasing of the K^+ content. To rationalize the effect of the K^+ substituent on the electronic and optical features of these complex DP systems, we performed a series of DFT calculations. First, we computed the band structures of Bi,Ag-doped $\text{Cs}_2\text{NaInCl}_6$ and $\text{Cs}_2\text{KInCl}_6$ $1 \times 1 \times 1$ unit cells, evidencing how in both systems the copresence of Bi^{3+} and Ag^+ cations is key to achieve an efficient PL emission, which was ascribed to a localized $\text{BiCl}_6 \rightarrow \text{AgCl}_6$ transition. Then, we computed the oscillator strength of the lowest $\text{BiCl}_6 \rightarrow \text{AgCl}_6$ electronic transition in more realistic Bi,Ag-doped $\text{Cs}_2\text{NaInCl}_6$ and $\text{Cs}_2\text{KInCl}_6$ $2 \times 2 \times 2$ supercells as well as the energetics of the ground state (singlet) and lowest excited state (triplet) upon systematic elongation of the Bi-Cl bond along the Bi-Cl-Ag, thus simulating the partial break of this bond upon photoexcitation (Figure 2a). Through such DFT analyses, we successfully ascribed the lower PLQY of the DP system with high K^+ content to: *i*) a lower oscillator strength for the $\text{BiCl}_6 \rightarrow \text{AgCl}_6$ transition; *ii*) local orthorhombic distortions occurring during the photoexcitation which can activate efficient non-radiative quenching channels. Finally, we computed the electronic structure of ~ 3.5 nm $\text{Cs}_2\text{Ag}_{0.60}\text{Na}_{0.40}\text{InCl}_6$ and $\text{Cs}_2\text{Ag}_{0.60}\text{K}_{0.40}\text{InCl}_6$ NC models upon systematic displacement of CsCl ion pairs to mimic the displacement of ionic ligand pairs from the NC surface, resulting in both systems in the emergence of deep Cl surface trap states above the valence band (Figure 2b). As a matter of fact, the improved PLQY at low K^+ content was attributed to an expansion in the lattice parameters (K^+ ions which are bigger than Na^+ ions) that enables to better accommodate surface ligands, hence to passivate a higher number of such surface states. Overall, the work revealed how an atomistic understanding of the parameters influencing carrier trapping/relaxation can be employed to boost the PLQY of double perovskites NCs.

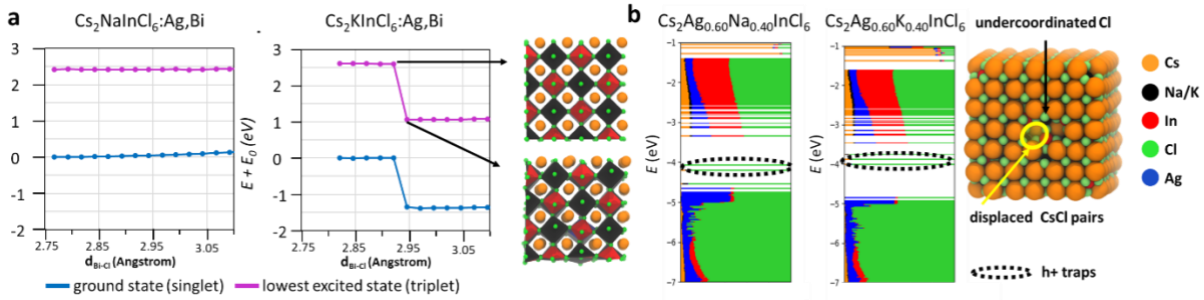


Fig.2: (a) Trend of the ground state and triplet state energies upon stretching of the Bi-Cl bond computed for $\text{Cs}_2\text{Na(K)InCl}_6$ bulk systems ($2 \times 2 \times 2$ supercells) doped with 1 Ag^+ and 1 Bi^{3+} ions. The (relaxed) ground state structures are taken as reference 0 energy values for both systems. For the K-based system, we observe a distortion from the cubic to the orthorhombic structure when the bond is stretched above a threshold length of 2.92 Å. (b) Electronic structure of ~ 3.5 nm cubic $\text{Cs}_2\text{Ag}_{0.60}\text{Na}_{0.40}\text{InCl}_6$ NC models. Each molecular orbital has been decomposed according to each atom type. In both systems, the removal of two CsCl ionic pairs from the surface leads to the insurgence of deep hole trap states.

Band structure calculations were performed using the VASP package on cresco6 cluster. The PBE functional [5] was adopted with further inclusion of the spin-orbit coupling term within the noncollinear approximation. The plane wave energy cutoff was set to 400 eV. A k mesh grid of $4 \times 4 \times 4$ was employed for the Brillouin zone integration. For both systems, the cell parameters and atomic positions were relaxed until the forces were smaller than 0.001 hartree/Å. Further bulk calculations were performed at the Γ point of $2 \times 2 \times 2$ supercells using the cp2k software [6] on cresco6. The PBE exchange-correlation functional was adopted.[7] All core electrons were included in the pseudopotential, while the valence electrons were described with a double- ζ basis set plus polarization functions (DZVP) and with plane waves having an energy cutoff of 400 Ry. For both systems, the cell parameters and atomic positions were optimized to the closest energy minimum. Transition dipole moments for the lowest energy transition were evaluated using the Fermi's golden rule. Structural relaxation and analysis of the electronic structure of the explicit NC models was carried out at the DFT/PBE/DZVP level of theory using the cp2k software [8] on cresco6. Here, all calculations were performed in vacuum.

3. Core-shell QDs

In this section, we illustrate the DFT simulations we carried out on core-shell QDs. In particular, relying on the synergical collaboration with the experimental research groups in our institute who carried out the synthesis and characterization, we studied InAs@ZnSe core-shell QDs.

Core-shell QDs are nanocrystals in which a shell of a semiconductor material is grown on a nanocrystal made of a different semiconductor. In our case, ZnSe is grown on InAs, with the band gap of the former being significantly larger than that of the former. These types of core-shell QDs are generally known as type I QDs, and the presence of the shell generally improves the PLQY, a key property for optoelectronic applications. Indeed, we experimentally observed that the growth of ZnSe on InAs boosts the PLQY from 2% to over 60% [9, 10] (Fig. 3a). To understand the mechanisms responsible for this PLQY improvement, and in general to reveal the atomistic and electronic structure of the InAs@ZnSe QDs, quantum chemical simulations are to be performed. Indeed, this type of information is generally not available experimentally, especially for nanocrystals due to their small dimension. However, the task of studying these systems with quantum chemistry is represented by the fact that the exact composition of the QDs is not known, only the elemental ratios can be qualitatively measured. This issue is discussed in detail in Sect. S7 of the Supporting Information of ref. **Error! Bookmark not defined.** To overcome this limitation, we devised a non-conventional approach that allowed us to build a reliable atomistic model for the InAs@ZnSe QDs, focusing on the one with 2 monolayers (2ML) of ZnSe. We adopted a trial-and-error in which we performed a large number of DFT simulations in which the structural details (such as the QD surface shape), the composition, and the elements distribution were varied until we obtained a model that displayed an electronic structure compatible with the observed optical properties and that had sizes and elemental ratios that qualitatively match the experimental measurements. The final model is displayed in Fig. 3b. An important result uncovered by our atomistic modelling is the presence of an intermediate layer between the core and the shell formed by In, Zn, Se, and

cation vacancies. Moreover, our DFT simulations granted access to the electronic structure of the QDs (Fig. 1c), thus allowing to rationalize their optical properties.

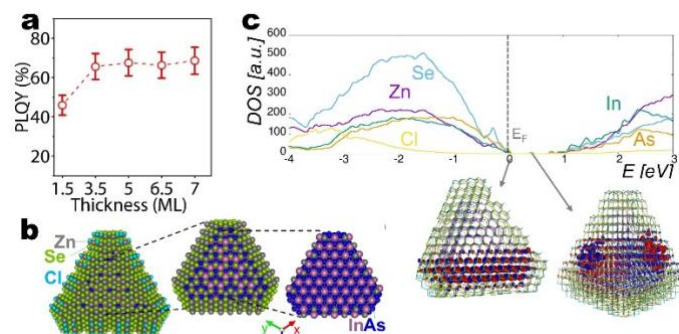


Fig.3: Optical, structural, and electronic properties of InAs@ZnSe quantum dots. a) experimentally measured PLQY for various ZnSe thicknesses. For comparison, the PLQY of InAs (no ZnSe shell) is < 5% [Error! Bookmark not defined.]. b) atomistic structure of InAs@ZnSe quantum dots with 2 shell monolayers ($\text{In}_{462}\text{As}_{373}@Zn_{722}\text{Se}_{798}\text{Cl}_{115}$) as determined by DFT simulations. We report the whole core@shell NC (left), the core and the In-Zn-Se interlayer (middle) and the core (right). c) density of states with atomic orbital projection. Two representative molecular orbitals are shown as red/blue isosurfaces.

The simulations were performed with the cp2k software [11] on cresco6, generally adopting 1052 cpu's for geometry optimization and 526 cpu's for properties evaluation. The PBE exchange-correlation functional was adopted.[12] All core electrons were included in the pseudopotential, while the valence electrons were described with the DZVP basis set included in the cp2k package and with plane waves having an energy cutoff of 320 Ry and 400 Ry for geometry optimization and electronic structure calculation, respectively.

Note that these simulations were performed across the period August 2022- April 2023, hence they will be reported in the 2023 report as well.

References

- [1] El-Sayed, M. A. (2004). Small is different: shape-, size-, and composition-dependent properties of some colloidal semiconductor nanocrystals. *Accounts of chemical research*, 37(5), 326-333.
- [2] Quarta, D., Toso, S., Giannuzzi, R., Caliendo, R., Moliterni, A., Saleh, G., ... & Giansante, C. (2022). Colloidal Bismuth Chalcogenide Nanocrystals. *Angewandte Chemie International Edition*, 61(22), e202201747.
- [3] Quarta, D., Toso, S., Saleh, G., Caliendo, R., Moliterni, A., Griesi, A., ... & Giansante, C. (2023). Mixed Valence of Bismuth in Hexagonal Chalcogenide Nanocrystals. *Chemistry of Materials*.
- [4] Kresse, G., & Furthmüller, J. (1996). Efficiency of ab-initio total energy calculations for metals and semiconductors using a plane-wave basis set. *Computational materials science*, 6(1), 15-50.
- [5] Tkatchenko, A., & Scheffler, M. (2009). Accurate molecular van der Waals interactions from ground-state electron density and free-atom reference data. *Physical review letters*, 102(7), 073005.
- [6] VandeVondele, J., & Hutter, J. (2003). An efficient orbital transformation method for electronic structure calculations. *The Journal of chemical physics*, 118(10), 4365-4369.
- [7] Perdew, J. P., Burke, K., & Ernzerhof, M. (1996). Generalized gradient approximation made simple. *Physical review letters*, 77(18), 3865.
- [8] VandeVondele, J., & Hutter, J. (2003). An efficient orbital transformation method for electronic structure calculations. *The Journal of chemical physics*, 118(10), 4365-4369.
- [9] Zhu, D., Bellato, F., Bahmani Jalali, H., Di Stasio, F., Prato, M., Ivanov, Y. P., ... & Manna, L. (2022). ZnCl₂ Mediated Synthesis of InAs Nanocrystals with Aminoarsine. *Journal of the American Chemical Society*, 144(23), 10515-10523.
- [10] Zhu, D., Jalali, H. B., Saleh, G., Stasio, F. D., Prato, M., Polykarpou, N., ... & Manna, L. (2023). Boosting the Photoluminescence Efficiency of InAs Nanocrystals Synthesized with Aminoarsine via a ZnSe Thick-shell Overgrowth. *Advanced Materials*, 2303621..
- [11] VandeVondele, J., & Hutter, J. (2003). An efficient orbital transformation method for electronic structure calculations. *The Journal of chemical physics*, 118(10), 4365-4369.
- [12] Perdew, J. P., Burke, K., & Ernzerhof, M. (1996). Generalized gradient approximation made simple. *Physical review letters*, 77(18), 3865.

MCNP ANALYSES FOR THE nIORT® TREATMENT OF SOLID CANCERS BY A COMPACT NEUTRON GENERATOR

Massimo Sarotto^{1*}, Maurizio Martellini²

¹ ENEA FSN-SICNUC-PSSN, C.R. Saluggia, Strada per Crescentino 41 – 13040 Saluggia (VC)¹⁹

² UNINSUBRIA, Via Ravasi 2 – 21100 Varese. TheranostiCentre S.r.l. scientific director

ABSTRACT. This report briefly summarizes the last findings of the collaborative research study between ENEA and TheranostiCentre S.r.l. started in 2019. While the first prototype of a Compact Neutron Generator (CNG) for materials irradiation is under testing in the ENEA Brasimone (BO, Italy) laboratories, a new CNG design - to be used in a hospital operating room for the neutron irradiation of the solid cancer's tumour bed by means of the Intra-Operative Radiotherapy (IORT) technique, the so-called neutron-IORT (nIORT®) - is currently under development. Accurate Monte Carlo simulations with the MCNP code, modelling the CNG and the typical IORT applicator to be inserted in the surgical cavity, forecast very promising irradiation performances for potential nIORT® treatments in different regimes: from 10 up to 75 Gy (RBE), that can be administered in a single session of about 4 to 30 minutes. Besides the dose peak in the centre of the tumour bed, the almost isotropic neutrons emission allows to irradiate the tissues surrounding the tumour bed – usually filled by potential quiescent cancer cells – reducing the chances of local recurrences. The rapid dose decrease in tissues depth (in few centimetres) spares the neighbouring organs at risk from harmful radiations.

1. Introduction

The Intra-Operative Radiotherapy (IORT) is a treatment technique which associates radiotherapy with surgery, that foresees the administration of a dose of radiation directly on the tumour surgical cavity, by irradiating the tissues that cannot be dealt by surgical resection after having removed the primary neoplastic mass. The direct visualization and the possibility to space out normal tissues allows to maximize the dose to the tumour while minimizing the dose to normal tissues. Conventionally, IORT is performed by low-energy (~50 keV) X-rays or by high-energy (~1 MeV) electrons: besides some significant advantages with respect to the External Beam Radiation Therapy (EBTR), these standard techniques still present some limitations: e.g., tumour beds with significant topographic irregularities remain a therapeutic challenge with existing IORT technologies employing a focused beam most reliable for flat tissue surfaces. This limitation could be overcome using fast neutrons as ionizing radiation (IR) particles and adopting the so-called neutron-IORT (nIORT®) technique [1], invented by the TheranostiCentre S.r.l. company (TC, Italy) and further developed in collaboration with the Berkion Technology LLC company (BT, USA) and ENEA [2]. Indeed, in comparison with the conventional IORT and EBTR techniques with a focused irradiation beam, the main rationale for the nIORT® therapy is the diffuse spatial dose distribution of the neutrons in the tissues. The almost spherically symmetric neutrons IR on the tumour bed has the advantages to be less sensitive to the margins of the surgical cavity and to the possible intra-tumour heterogeneity of the solid tumour cells.

¹⁹

Corresponding author. E-mail: massimo.sarotto@enea.it

The research studies on nIORT® are currently ongoing with the experimental tests of the first prototype of a Compact Neutron Generator (CNG) designed, developed and built by TC, BT and ENEA [3]. The irradiation performances of the CNG – producing neutrons of 2.45 MeV energy through the deuterium-deuterium (DD) fusion reaction – are going to be measured in a new equipped laboratory at the ENEA Brasimone (BO, Italy) research centre [4]. Fig. 1 shows the conceptual design of the CNG – enclosed in a cylindrical column made of High-Density Polyethylene (HDPE) in which the D+ ions are accelerated against a Ti target where fusion reactions occur – and the instrumentation adopted for the first experimental tests. The DD-CNG is self-shielded, lightweight (~120 kg, making possible its remote handling by a robotic arm) and can supply a neutron flux $\sim 10^8 \text{ cm}^{-2} \text{ s}^{-1}$ at its irradiation window.

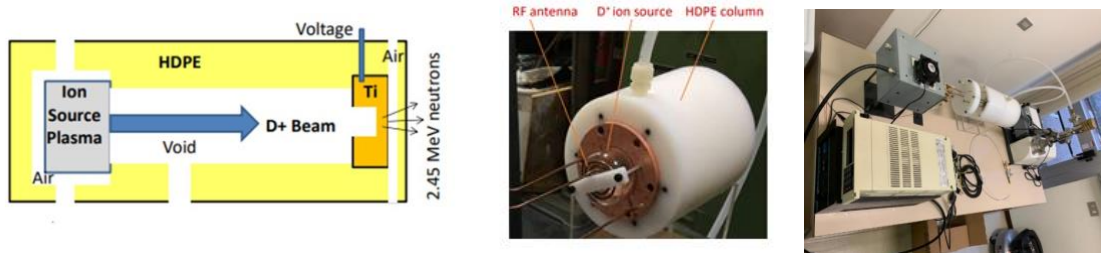


Fig.1: CNG for materials irradiation: conceptual design (left), accelerator column (centre) and equipment for the first experimental tests (right).

In parallel with the experimental characterization of the first CNG prototype (see Fig. 1), a new DD-CNG design is currently under development. As shown in the illustrative sketch in the left frame of Fig. 2, the new design envisages an applicator pipe to be adopted in IORT treatments, instead of the irradiation window used for materials characterization measurements. The IORT applicator (or adaptor) via hard-docking can be inserted close to – or in contact with – the tumour bed inside the surgical cavity. The potential performances of this configuration – suitable to be installed in an operating room dedicated to nIORT® treatments – were evaluated by foreseeing the CNG equipped by an IORT applicator (almost transparent to neutrons) having a 6 cm diameter and about 2 cm length. Differently from the Boron Neutron Capture Therapy (BNCT) exploiting thermal and epithermal neutrons to induce (n, α) reactions in boron carriers injected into patients, the fast neutrons (2.45 MeV) interact directly and efficiently with the hydrogen nuclei, producing recoil protons that ionize tissues.

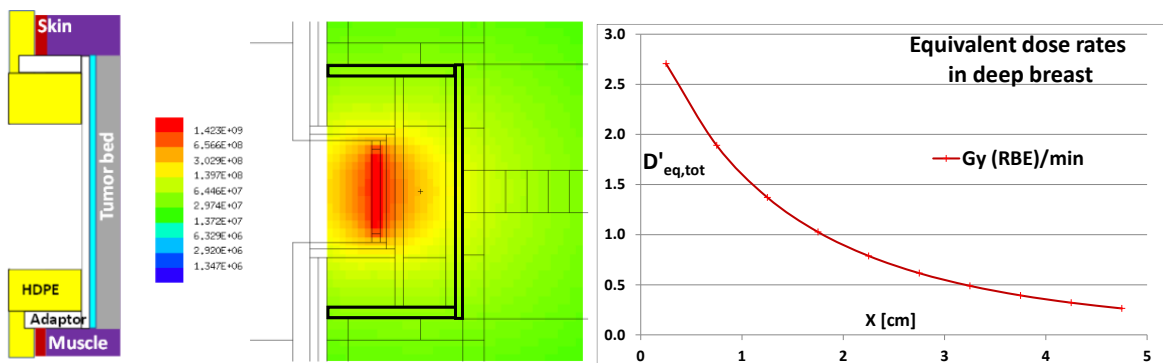


Fig.2: Illustrative sketch of the IORT applicator/adaptor with surrounding tissues in the surgical cavity (left), 2D neutron flux spatial distribution near the IORT applicator of 6 cm diameter (marked by a thicker black line; centre) and equivalent dose rate profile in tissues depth (right).

2. MCNP dose analyses for nIORT® treatments

Accurate Monte Carlo simulations were carried out by means of the Monte Carlo N-Particle (MCNP) ver. 6.1 code [5] coupled with the most up-to-date ENDF/B-VIII.0 nuclear data [6]. The MCNP analyses have shown that the nIORT® delivers on the tumour bed a fast-neutron IR with a high linear energy transfer (LET: $\sim 40 \text{ keV}/\mu\text{m}$ as average) and a relative biological effectiveness (RBE) of about 16 [7], significantly higher than the RBE unitary values for X-rays and electrons, thus resulting very efficient in producing DNA double strand breaks (DSBs) of the cancer cells. The MCNP simulations were not restricted to neutrons (*i.e.*, the primary ones from the Ti target and the secondary ones coming from the scattering with the CNG walls and into the

biological tissues), but they also include photons: i.e., gammas created by neutrons interaction with matter. The physical dose rates (Gy/min) into the biological tissues due to neutrons ($D'_{f,n}$) and gammas ($D'_{f,\gamma}$) were calculated with MCNP by simulating the nIORT® treatment of the breast cancer [8]. The total equivalent dose rate values ($D'_{eq,tot}$ in Gy (RBE)/min) in breast and surrounding muscle and skin tissues of the surgical cavity were obtained by:

$$D'_{eq,tot} = D'_{eq,\gamma} + \int w_n(E)D'_{f,n}(E)dE \quad [\text{Gy (RBE)/min}] \quad (1)$$

where:

- “ $w_n(E)$ ” is the radiation weighting factor for neutrons ($\cong 16$ at 2.45 MeV);
- the radiation weighting factor for photons is one (i.e., $D'_{eq,\gamma} \equiv D'_{f,\gamma}$);
- the photon flux level in the superficial tissues of the tumour bed is about 20 times lower than the neutron one. Because of the higher flux ($\cong 20x$), LET ($\cong 5x$) and RBE ($\cong 16x$), the neutrons contribution to the total dose rate results three order of magnitude higher than the photons one.

The central frame of Fig. 2 shows the 2D neutron flux spatial distribution obtained by MCNP near the IORT applicator (6 cm diameter) and in the surrounding surgical cavity. Besides the flux (and dose) peak at the tumour bed’s centre, the almost isotropic neutrons emission allows to irradiate its surrounding tissues – usually filled by potential quiescent cancer cells – thus reducing the chances of local recurrences by improving the local control of the tumour. The right frame of Fig. 2 shows the total equivalent dose rate profiles vs depth in breast and muscle tissues (with 0.5 cm steps): while the overwhelming part of the dose is released at tissues surface, going in depth the dose level decreases strongly in few centimetres by sparing the neighbouring organs at risk from harmful radiations.

Table 1 reports the dose rate levels delivered in the surface tissues of the surgical cavity, calculated with MCNP for the nIORT® treatment of the breast cancer. As a Monte Carlo code, MCNP is affected by the statistical noise of the results due to its stochastic nature. For easiness, the results uncertainty is not indicated: their relative standard deviation is however lower than ~1%. The dose rates were evaluated in all the 0.5 cm thick tissue cells surrounding the IORT applicator, that represent the highest dose administered in the tumour bed and in the surrounding muscle and skin (healthy) tissues of the surgical cavity. For the tumour bed, the peak, middle and minimum values were calculated and reported. For the muscle and skin tissues on the lateral side of the applicator, only the maximum dose rate values are reported. These two “healthy” tissues receive almost the same dose rate level (0.65 Gy(RBE)/min), that is about 4 times lower than the one administered at the centre of the tumour bed.

Table 2 reports the CNG irradiation performances for different dose regimes adopted in the standard IORT protocols foreseeing clinical end-points ranging from 10 up to 75 Gy (RBE). The Boost and Radical IORT regimes [9] were examined by assuming, respectively, 10 and 20 Gy (RBE) for the peak and average dose targets in the tumour bed: it results evident that the Treatment Time (TT) is limited to about 4÷9 minutes, depending on the endpoint chosen (10÷20 Gy (RBE)). By envisaging 20 Gy (RBE) as average dose target in the tumour bed, the peak dose delivered in its centre reaches up to 24.5 Gy (RBE): actually, this case could be also classified as belonging to the so-called Ultra-Radical IORT regime. Thanks to the high neutron flux and dose rates supplied by the CNG, even higher dose targets could be administered in a limited TT, as sometimes it could be required in the most severe cases of pancreatic ductal adenocarcinoma (PDAC) cancer and the glioblastoma multiforme (GBM) brain tumour. As reported in the last two rows in Table 2, the 50÷75 Gy (RBE) dose target range could be administered by a single irradiation spot of about 19÷28 min only. It can be noticed that in the BNCT field the 12.6 Gy (RBE) limit is usually assumed as peak dose for the healthy tissues [10]: with the 6 cm diameter IORT applicator, this limit results exceeded in the “healthy” muscle and skin tissues on its lateral surface when the peak dose in the centre of the tumour bed exceeds 50 Gy(RBE)/min.

Table 1: Total equivalent dose rate values in the biological tissues of the surgical cavity (MCNP results for the treatment of the breast cancer with a 6 cm diameter IORT applicator).

Total dose Rate	Peak in Tumour bed	Average in Tumour bed	Minimum in Tumour bed	Peak in “healthy” Muscle	Peak in “healthy” Skin
Gy (RBE)/min	2.70	2.20	1.15	0.66	0.65

Table 2: CNG irradiation performances for nIORT® treatments in Boost (10 Gy(RBE)), Radical (20 Gy (RBE)) and Ultra-Radical (> 20 Gy (RBE)) regimes (with a 6 cm diameter IORT applicator).

DoseTarget [Gy (RBE)]	TT [min]	Peak in Tumour	Average in Tumour	Minimum in Tumour	Peak in Muscle	Peak in Skin
10 as Peak	3.7	10.0	8.2	4.3	2.4	2.4
10 as Ave	4.6	12.3	10.0	5.2	3.0	2.9
20 as Peak	7.4	20.0	16.3	8.5	4.9	4.8
20 as Ave	9.1	24.5	20.0	10.5	6.0	5.9
50 as Peak	18.5	50.0	40.7	21.3	12.2	12.0
75 as Peak	27.8	75.0	61.1	31.9	18.3	18.1

3. Conclusions

The potential advantages of n-IORT® treatments – to be administered to oncological patients with different solid cancer pathologies – will be further investigated through the CNG design optimization in the view of its possible utilization in a dedicated operating room. The potential benefits will have to be successively verified by *in vitro* and *in vivo* preclinical tests, sufficiently comprehensive to identify strengths and weaknesses of the nIORT® treatment, especially versus the traditional IORT techniques.

Acknowledgments

The authors acknowledge the expert assistance and collaboration of the TC (Dr. Ing. G. Gherardi and L. Falzone), BT (Dr. Ing. K. Leung) and ENEA (Drs. Ing. A. Rizzo and G. Ottaviano) colleagues.

References

- [1] nIORT® deposit 302019000045726 (3rd July 2019).
- [2] Collaboration agreement ENEA-Theranosti Centre Srl, ENEA/2019/25134/FSN-ING (2019).
- [3] M. Martellini et al., Multi Purpose Compact Apparatus for the Generation of a high-flux of neutrons, particularly for Intraoperative Radiotherapy, *Int. Patent PCT/IT2021/000032* (2021).
- [4] LINCER project, funded by Emilia Romagna with “Legge Regionale 27/12/2018 N.25”, DGR N. 545/2019 – *CUP I74I19000360003* (2019-2021).
- [5] B. Pelowitz et al., “MCNP6 USER’S MANUAL”, *Report LA-CP-13-00634 Rev. 0* (2013).
- [6] ENDF/B-VIII.0 evaluated nuclear data library, <https://www.nndc.bnl.gov/endl/> (2018).
- [7] Annals of the ICRP, *ICRP n. 103, Vol. 37*, ISSN 0146-6453, ISBN 978-0-7020-3048-2 (2007).
- [8] M. Sarotto and M. Martellini, “MCNP analyses of the 100 kV D-ion-based compact neutron source: irradiation performances for nIORT® treatments with different irradiation window diameters”, *Technical Report ENEA SICNUC-P000-045* (2022).
- [9] S. Hashemi, “Comparison of IORT (Radical and Boost Dose) and EBRT in Terms of Disease-Free Survival and Overall Survival according to Demographic, Pathologic, and Biological Factors in Patients with Breast Cancer”, *Int. J. of Surgical Oncology, Article ID 2476527* (2021).
- [10] International Atomic Energy Agency, “Current status of neutron capture therapy”, *IAEA TECDOC-1223* (2001).

MAGNETOHYDRODYNAMIC MODELLING OF LIQUID METAL WATER-COOLED BREEDING BLANKETS FOR NUCLEAR FUSION APPLICATIONS

Alessandro Tassone* and Simone Siriano

¹*Dep. of Astronautical, Electrical and Energy Engineering (DIAEE) - Nuclear Engineering Research Group, Sapienza University of Rome, Corso Vittorio Emanuele II, 244, Roma, 00186, Italy*

*Corresponding author: alessandro.tassone@uniroma1.it

ABSTRACT. In this contribution, the magnetohydrodynamic analyses performed to characterize the flow in water-cooled liquid metal breeding blankets are reported. Two cases are considered, both featuring a large number of internal cylindrical obstacles: fully developed forced convection vertical flow with obstacles aligned with the main flow direction and horizontal natural convection with uneven volumetric heating and transverse cooling pipes.

1. Introduction

The Breeding Blanket (BB) is a critical component of a fusion reactor which has the fundamental tasks of breed the tritium required for the reactor operations and of extract the thermal power generated by the fusion reactions. The most promising concepts involve the use of a Liquid Metal (LM) as working fluid, the lead-lithium eutectic alloy (PbLi), due to its excellent thermal properties and the possibility to double the coolant role as tritium breeder. In the framework of the development of the European fusion reactor industrial demonstrator DEMO [1], one LM blanket concept is currently under development as a “driver” blanket for early deployment: the Water-Cooled Lead Lithium (WCLL) [2].

A challenging engineering issues in the BB design is the necessity to account for the interaction between the electrically conductive LM and the magnetic field employed to confine the plasma in the vacuum chamber, that leads to the magnetohydrodynamics (MHD) effects. Modifications in the flow features are observed even for moderate intensity of the magnetic field due to generation of Lorentz forces. MHD effects that need to be considered for the BB design include, but are not limited to, pressure drop increase by several order of magnitude compared with hydrodynamic losses, altered velocity distribution, and degraded heat transfer [3]. In this contribution, we present the analyses performed in 2022 to advance the characterization of MHD phenomena in LM water-cooled BB designs and, in particular, the important case of MHD flow around immersed obstacles, i.e. the component cooling pipes. First, the isothermal flow in presence of a large number of cooling pipes aligned with the streamwise direction is discussed. Second, the magneto-thermo-fluid dynamic problem of a layer of fluid unevenly heated by a volumetric heat source and cooled by a large number of cooling pipes aligned with the magnetic field is considered. All calculations have been performed using ANSYS CFX 2021R1 on the CRESCO6 cluster.

2. MHD isothermal flow with many stream-wise obstacles

The baseline WCLL configuration, shown in the top half of Fig. 4, is characterized by a modular approach in which the LM is circulated through a large number of elementary cells at a very low velocity (0.2 mm/s). One of the main risks associated with the current concept is the conspicuous number of welds necessary to realize its cooling system which is composed by several hundred thousands horizontal pipes. To overcome this issue, a variant concept called WCLL-double bundle (WCLL-db) has been proposed, shown in the bottom half of Fig. 4, which minimizes the amount of cooling pipes (here vertical) and changes the LM flow path to a bottom-to-top once-through.

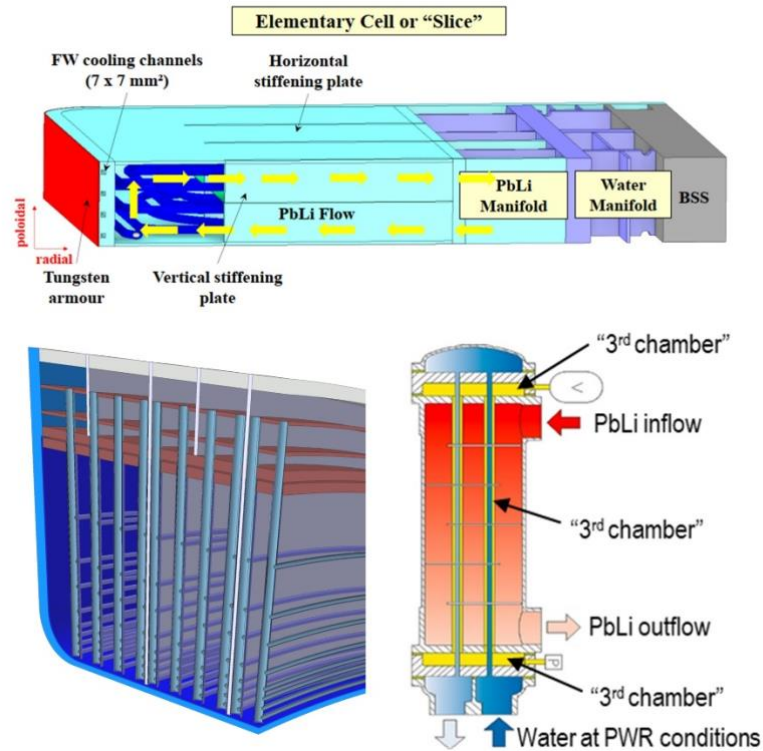


Fig. 4 – WCLL baseline (top) and alternative configuration (bottom, WCLL-db)

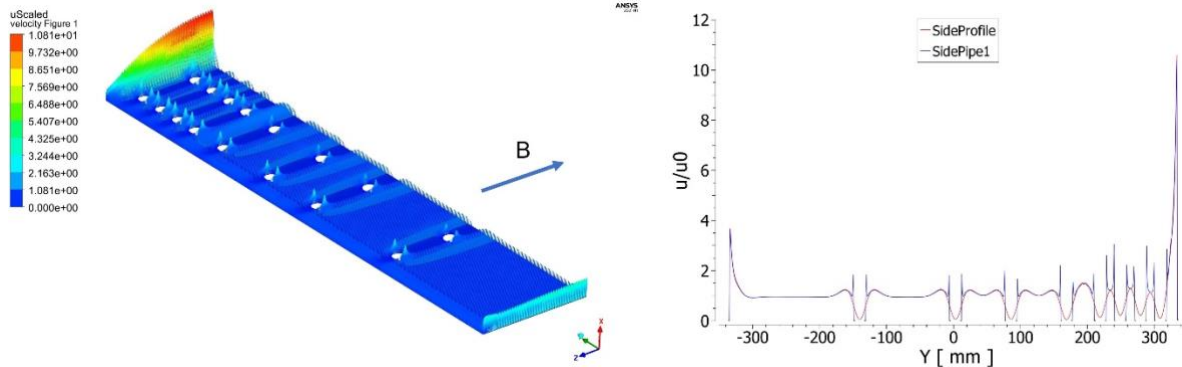


Figure 5 – Normalized velocity distribution (left) for $Ha = 1.2 \times 10^4$ and $Re = 1.5 \times 10^3$ and velocity profiles (right) passing through the center of the pipes (blue line) and along the symmetry surface (red line)

The purpose of this activity was to characterize the fully developed MHD isothermal flow in the proposed WCLL-db layout. The equatorial region as been taken as a reference for this analysis. Only an abridged discussion is reported here, a more comprehensive review is presented in Ref. [4].

The elementary WCLL-db channel is a rectangular duct elongated in the direction perpendicular to the magnetic field ($B = 3.5 \text{ T } \hat{z}$) and bounded by steel walls of uneven thickness: two stiffening plates, 6-mm thick, a chamber wall, 5 mm-thick, and a back plate, 30-mm thick. These last two walls are parallel to the magnetic field direction, whereas the first two are perpendicular. Thirty-two cooling pipes, external diameter 16 mm and 1-mm thick wall, are used to extract the thermal power which is unevenly deposited in the LM, warranting a clustering of the heat sinks closer to the chamber wall. Due to the symmetry of the problem, only half of the cross-section is simulated. A fluid mean velocity, $u_0 = 1.5 \text{ mm/s}$, is imposed at the inlet, whereas an outflow boundary condition is imposed at the outlet.

Figure 5 shows the velocity distribution. The electrically conductive walls cause the promotion of velocity jets close to those parallel to the magnetic field. These jets are affected by the uneven wall thickness since electrical currents induced in the LM tend to close through them: the thinner chamber wall will have a lower equivalent conductance and, as a result, nearby currents will tend to be less intense, causing a lower braking Lorentz force. Away from the walls, the velocity field is characterized by a uniform low velocity, slug-like flow, also called core flow. Cooling pipes offer additional paths for current closure and cause the definition of distinct

core regions separated by internal layers. These develop tangential to pipes (where small velocity overshoots can be observed) and propagate as free shear layers along magnetic field lines. Flow in the region enclosed by nearby pipes is strongly dampened.

The effect of the cooling pipes on the pressure drop is found to be rather limited despite the significant modification of the flow distribution. A pressure penalty of 8% is found for the nominal magnetic field intensity compared with analytical relations developed for fully developed flow in channels devoid of any obstacles [4].

In future work, the effect of buoyancy in the vertical channel is going to be investigated.

3. Magnetoconvection in a horizontal cell cooled by transverse pipes

Dedicated CFD analyses have been conducted to characterize the magnetoconvective regime in the baseline WCLL equatorial elementary cell considering an idealized pipe layout (straight toroidal tubes), in lieu of the more complex one presented in Fig. 4. Compared to previous studies [5][6], the present model aimed to investigate the effect of a skewed magnetic field (a 18° degree angle on the horizontal surface has been considered), more accurate FW thermal boundary conditions, and higher magnetic field intensity (≈ 4 T, $Ha = 9159$). A more detailed discussion of the results presented here can be found in Ref [7].

In this configuration, the thermal load is provided by an intense ($q''_{Max} \approx 15$ MW/m²) and spatially varying volumetric heating caused by the neutron flux incoming from the plasma: the maximum is located closer to the interface with the plasma and q''' exponentially decays away from it. To model the radiative heat loss from the plasma, a surface thermal load $q''=0.32$ MW/m² has been imposed on the external face of the tungsten layer (2 mm thick). Buoyancy is providing the main momentum source for the fluid and it is modelled with the Boussinesq approximation. A weak forced convection flow, mean velocity equal to 0.2 mm/s, is imposed at the inlet, but the flow is expected to be dominated by natural convection phenomena.

Heat removal in the first wall, the component directly facing the plasma and underneath the protective tungsten layer, has been simulated considering an imposed convective boundary condition on the surface of the four-square colling channels rather than on the whole FW surface, which would otherwise unduly magnify the available heat sink. LM is refrigerated by 11 cooling pipes, arranged in 4 ranks, which are assumed to be transverse to the main flow and aligned with the magnetic field. A convective boundary condition is imposed on their internal surface, similar to the case of the FW channel.

Fig. 6 shows the velocity and temperature distribution at $Ha = 9159$. In broad agreement with the previous studies [5][6], the flow is suppressed by the intense magnetic field and observed in a laminar-like state with several convective cells formed between ranks of adjacent pipes. No temperature fluctuations have been identified after a 100-300s of transient and heat transfer is dominated by diffusive processes with pipe Nusselt numbers ranging from 1.1 to 1.2. The inclined magnetic field disrupt large-scale convection cells, for instance observed in Ref [6], and promotes instead a more granular flow structure, as shown in Fig. 6.

This phenomenological change appears to have only a minor impact on the heat transfer regime, which remains consistent with that from Ref. [5]. The more accurate boundary condition for the heat sink in the FW estimates a maximum temperature of 740 K in the LM. This is an increase in the predicted maximum temperature of about 90 K with respect the ones computed in [5], suggesting a narrower safety margin with EUROFER limit temperature compared with previous calculations.

Future work will focus on the modelling of the flow features in more complex tube layout including, for instance, curved pipes partially aligned with the direction of decreasing volumetric heating and helically pipes placed close to the hotspot in order to improve heat transfer performances.

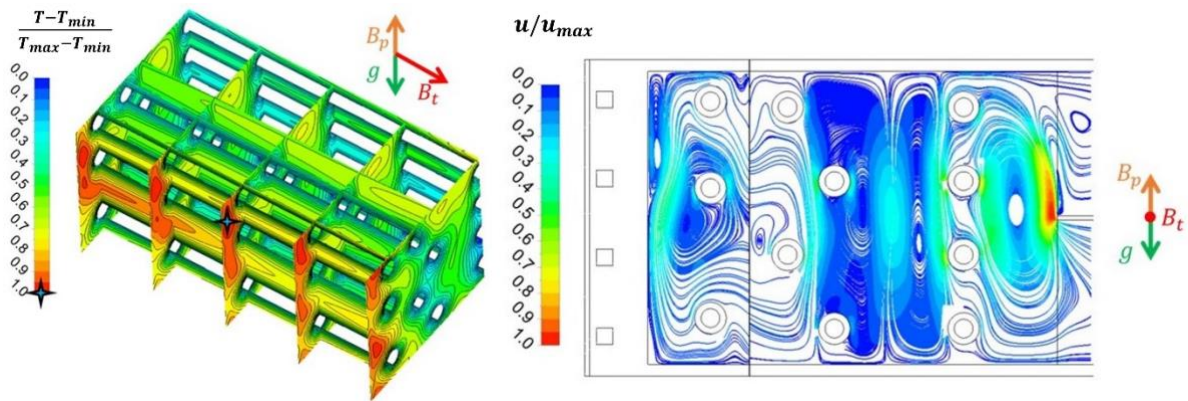


Fig. 6 – Normalized temperature distribution (maximum value is marked by a star) and velocity streamlines in the baseline WCLL elementary cell

Acknowledgments

This work has been carried out within the framework of the EUROfusion Consortium, funded by the European Union via the Euratom Research and Training Programme (Grant Agreement No 101052200 — EUROfusion). Views and opinions expressed are however those of the author(s) only and do not necessarily reflect those of the European Union or the European Commission. Neither the European Union nor the European Commission can be held responsible for them.

References

- [1] L. V. Boccaccini *et al.*, “Status of maturation of critical technologies and systems design: Breeding blanket,” *Fusion Eng. Des.*, vol. 179, p. 113116, Jun. 2022, doi: 10.1016/j.fusengdes.2022.113116.
- [2] P. Arena *et al.*, “The demo water-cooled lead–lithium breeding blanket: Design status at the end of the pre-conceptual design phase,” *Appl. Sci.*, vol. 11, no. 24, p. 11592, Dec. 2021, doi: 10.3390/app112411592.
- [3] U. Müller and L. Bühler, *Magnetofluidynamics in Channels and Containers*. Berlin, Heidelberg: Springer Berlin Heidelberg, 2001.
- [4] DES-FS.BB.S-T002-D001 MHD analyses on WCLL-db, [2PNL4D v1.0](#)
- [5] Y. Yan, A. Ying & M. Abdou (2020). Numerical study of magneto-convection flows in a complex prototypical liquid-metal fusion blanket geometry. *Fusion Engineering and Design*, 159, 111688
- [6] F. R. Ugorri, I. Fernández-Berceruelo & D. Rapisarda (2021). Magneto-Convective Analyses of the PbLi Flow for the EU-WCLL Fusion Breeding Blanket. *Energies*, 14, 6192
- [7] BB-S.02.03-T001-D008: WCLL BB design activities - 2022 ENEA contribution, [2QSA7X v1.0](#)

COMPUTER SIMULATIONS OF POLYMER MODELS OF CHROMOSOME FOLDING ARE TESTED AGAINST SINGLE-CELL MICROSCOPY DATA IN HUMAN CELLS

Francesca Vercellone¹, Andrea Esposito², Simona Bianco², Andrea Maria Chiariello², Andrea Fontana², Florinda Di Pierno², and Mattia Conte^{2*}

¹*DIETI, Università di Napoli Federico II, Biennio Ingegneria, Via Claudio 21, 80125, and INFN Napoli, Complesso Universitario di Monte Sant'Angelo, 80126, Naples, Italy*

²*Dipartimento di Fisica, Università di Napoli Federico II, and INFN Napoli, Complesso Universitario di Monte Sant'Angelo, 80126, Naples, Italy*

**Corresponding author. Email: mattia.conte@na.infn.it*

ABSTRACT. Recent advances in molecular biology have provided innovative technologies to probe the complex spatial organization of chromosomes within the cell nucleus. That pushed the development of quantitative models from math and physics to shed lights on the underlying folding mechanisms. Here, we review two models of polymer physics, investigated by massive numerical simulations, that reflect two distinct scenarios of DNA folding: loop-extrusion and chromatin phase separation. The single-molecule conformations predicted by those models are shown to be statistically consistent with single-cell microscopy data of key genomic regions in human cells, highlighting how the combination of polymer physics models, experimental data and computer simulations can be crucial in understanding genome structure and function.

1. Introduction

A key challenge of modern biology is understanding the molecular mechanisms that shape the three-dimensional (3D) conformation of chromosomes in the cell nucleus. Chromosomes have indeed a multi-layered self-organized structure that involve, e.g., the formation of DNA loops [1] and Topological Associated Domains (TADs) [2],[3] at the megabase scale, and their hierarchical folding at the nuclear scale [4]. Those complex structures have been shown to be crucial in many functional activities, such as the regulation of gene transcription [5]–[8]. These findings have been achieved via innovative, powerful technologies of DNA contact detection such as Hi-C [9], GAM [10] and SPRITE [11], and other important techniques, such as super-resolution multiplexed FISH [12]. However, despite those major advances, the molecular mechanisms that produce such a complex 3D architecture of the genome are not yet understood. To this aim, quantitative models based on math and physics have been proposed and tested by computer simulations [13]–[18].

Here, we review a recent work [19] in which two main classes of models of chromosome folding, i.e. loop-extrusion (LE) and polymer phase separation, are tested against recent super-resolution multiplexed FISH single-molecule data in human cells [12]. LE model postulates that the physical proximity between distant genomic sites is established through the action of molecular motors that bind DNA and extrude loops [20]–[24] This process is an active, out-of-equilibrium mechanism that requires cell energy, such as ATP, consumption. Experiments suggest that specific protein complexes, like Cohesin, can be part of the motor complex, while CTCF sites may serve as anchor points [24], [25]. Numerical studies have shown that those models can explain the formation of loops and TADs as observed, for instance, in population-averaged (e.g. Hi-C) contact maps [20]. On the other hand, phase separation models are based on a different scenario whereby the interactions between distal genomic sites are mediated by diffusing molecules, such as transcription factors, or by direct (e.g., homotypic histone-histone) interactions [19], [26]–[29]. A representative example of this class of models is the Strings and Binders Switch (SBS) model [29]–[35], which represents chromatin as a self-avoiding chain of beads with specific binding sites for diffusing cognate binders. The SBS model has been

shown to explain independent experiments of chromosome structure, such as Hi-C, SPRITE, GAM [36], and also single-cell super-resolution microscopy [26].

In the next sections, following [19], we (i) describe the molecular ingredients of LE and SBS models and their Molecular Dynamics (MD) implementation; (ii) then we compare their structural predictions against real microscopy data of genomic loci in human cells, showing how do they perform relative to each other in capturing folding at the single-molecule level.

2. DNA loop-extrusion and polymer phase-separation as mechanisms of chromatin contact formation

To understand how well different mechanisms of chromosome folding, such as LE and SBS, explain chromatin structure in single molecules, we first describe here their main ingredients.

In both models, chromatin is represented as a polymer chain composed of monomer beads with a finite diameter. All interaction potentials for the models are taken from classical studies of polymer physics simulations [37]. Specifically, consecutive beads are connected via FENE springs with standard parameters [37] and their overlap is avoided via a short-range sterically repulsive interaction, implemented via a Weeks-Chandler-Anderson (WCA) repulsive potential [37].

In the LE model [21], the loop-extruding motors are modelled as additional harmonic springs attached to the polymer chain, which actively extrude loops by translocating along the polymer backbone (Fig. 1a). Their number is fixed, they cannot cross each other, and their translocation stops when they encounter another motor or anchor points with opposite orientation, or they stochastically detach from the chain. To simulate the extrusion process, at every 500 MD time iterations steps the simulation is updated by moving the spring from the bead pair (i, j) to $(i-1, j+1)$. A standard way to determine positions and orientations of the anchor sites is by using a standard motif finding analysis (using the FIMO tool [38]) based on the peaks of available CTCF [39] ChIP-seq data, e.g., from ENCODE [40], for the genomic regions of interest.

In the SBS model [26], a chromatin region is represented as a Self-Avoiding Walk (SAW) chain along which there are different types of specific binding sites (represented by different colours) for their corresponding molecular binders (Fig. 1b). The binders are diffusing Brownian particles, and they can bridge their cognate sites on the polymer via specific attractive interactions, thus driving, in a thermodynamics process, a phase-separation of the chain in distinct globules. Indeed, as the number of binders or their energy affinity grows above a given threshold, the model undergoes a thermodynamics phase transition from a coil, i.e., open randomly folded, to a phase separated globule state, in which the specific interactions between cognate sites guide the self-assembly of the chain into spatially segregated globules. As stated by polymer physics [41], the equilibrium conformations of the model fall in those two main folding classes that correspond to the system emergent, and universal, thermodynamics phases [42]. The genomic locations of the binding sites of the SBS model are inferred by a machine learning procedure based on the PRISMR method [27], [28], [43], [44], which takes as input only bulk Hi-C data with no prior knowledge of chromatin factors or chemical histone modification.

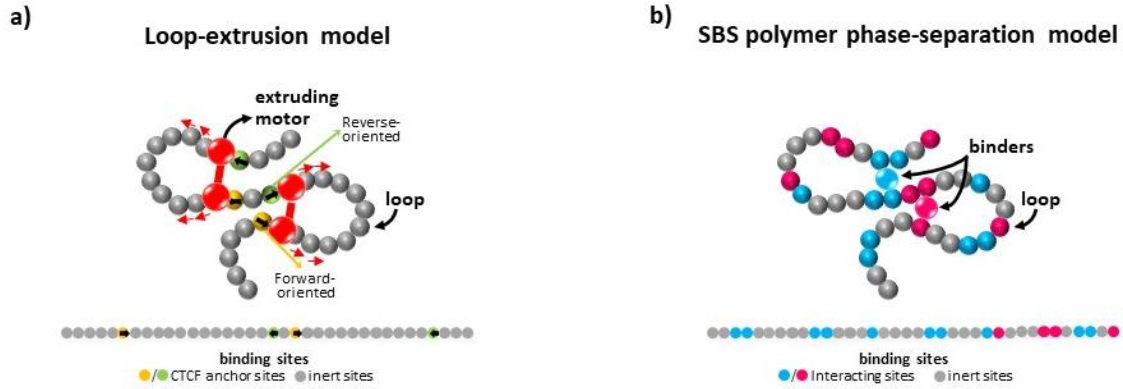


Fig.1: a) LE model: active motors (in red) extrude loops until encountering anchor sites (yellow and green) with opposite orientation. **b)** SBS model: homotypic polymer sites (visually represented by using the same color, blue or violet in the figure) interact through specific cognate molecular binders that drive the folding of the chain in a thermodynamics phase-transition-like process.

In both LE and SBS models, the dynamics of each bead is subject to the Langevin equation, numerically integrated via the Velocity-Verlet algorithm by using the MD LAMMPS [45] and HOOMD software [46]. The polymer system is confined within a cubic simulation box with periodic boundary conditions. The initial states of the MD simulations are independent SAW conformations, prepared as described in [47]. To reach the steady state, polymer conformations thermalize up to 10^8 MD time iteration steps, when stationarity is fully reached [26], [47]. To get a statistically significant set of conformations, an ensemble of 10^3 single-molecule conformations is recorded in the steady state [19]. Such a huge computational effort can be achieved thanks to high-performance computing (HPC) resources, such as ENEA-CRESCO [48], which were crucial, e.g., for the simulations analyzed in [26], [19].

In the next section, we discuss the LE and SBS models of a 2Mb long genomic locus in human fibroblasts IMR90 cells, where single-cell super-resolution microscopy data [12] at 30 kb resolution are available.

3. Polymer models based on loop extrusion and phase separation quantitatively capture single-cell chromatin conformations

In this section we validate the LE and SBS models against single-cell super-resolution microscopy data [12] for a 2Mb wide genomic region, specifically chr21: 28-30 Mb in the IMR90 human cell line. In [19] it has been shown that those models well capture the complex patterns of DNA contacts at the cell-population averaged level. Here we discuss how well they recapitulate the 3D conformations of the studied genomic region in single DNA molecules [19].

To assess the statistical significance of the ensemble of 3D structures predicted by the models, the authors in [19] employed a computational method based on the root-mean-square deviation (RMSD) criterion [26], [49]. This method allows to compare experimental and model-derived conformations by aligning them through rotational transformations and minimizing the RMSD of their particle positions. This can be achieved, e.g., by using efficient Python packages, such as “MD Analysis”, which uses the fast quaternion-based characteristic polynomial (QCP) algorithm [26],[19]. By performing an all-against-all structural comparison, where each microscopy 3D structure is associated, for each type of model, to its best-matching conformation based on the least RMSD, the authors could establish the level of agreement between experiments and models [26],[19]. To ensure a fair comparison, a z-score was applied to both sets of coordinates.

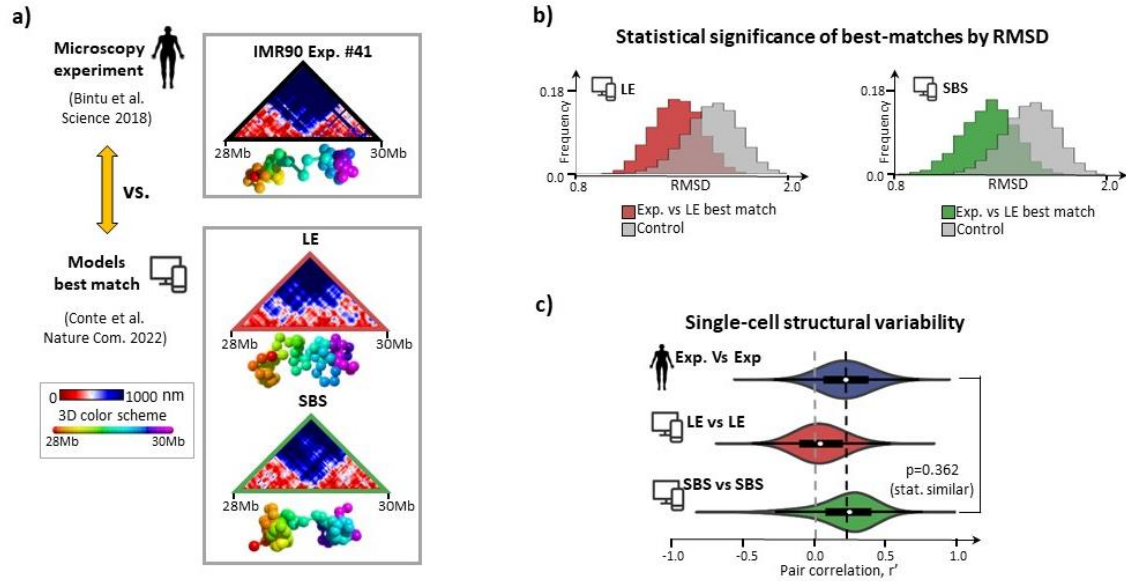


Fig.2: a) Microscopy single-cell chromatin structures of the IMR90 locus [12] (top) and their corresponding best-matching single-molecule conformations for each type (LE and SBS) of model (down). The best-match is determined by using the minimum RMSD criterion [26], [49]. An example of those 3D best matches, along with their corresponding distance maps, is reported. **b)** The RMSD distribution of the best-matching pairs between experimental and model structures, for both polymer models, significantly differs from a control distribution consisting of random pairs of experimental structures (two-sided Mann-Whitney test p-value < 0.001). **c)** The variability of microscopy single-molecule structures is measured by comparing the distribution of r' correlations between pairs of distance matrices with the variability of in-silico structures. The r' distribution of the SBS model is statistically indistinguishable from the experimental distribution (two-sided Mann-Whitney test p-value = 0.362). The boxplots display the median, interquartile ranges, and whiskers within 1.5 times the interquartile range. $n=1000$ independent single-molecule conformations for each model.

(Adapted from [19])

In Fig. 2a we report, for a given exemplificative microscopy single molecule, its best-matching conformations from the different models identified by the RMSD method [19]. The example shows that both LE and SBS consistently recapitulate the main TAD-like structures observed in the single-cell imaged distance map. To establish the statistical significance of the RMSD analysis, the authors in [19] compared the distribution of RMSD values for the experiment-model best matches with a control distribution where RMSD values are calculated for random pairs of imaged conformations. For each model type, they found that the distribution of best matches was statistically distinguishable from the control (Fig. 2b, two-sided Mann-Whitney test p-value < 0.001).

The all-against-all RMSD analysis allowed to examine how well the polymer models represent the ensemble of single-cell imaged 3D structures of the studied chromatin loci. The results indicated that both loop-extrusion and phase-separation models significantly represent these structures, providing a non-trivial representation of chromatin molecules within individual cells.

Next, following [26],[19], the structural variability of single-molecule conformations [12] can be assessed by computing the distribution of genomic distance corrected Pearson, r' , correlations between pairs of single-molecule imaged and model distance matrices (Fig. 2c). The experiment-experiment r' distribution exhibited a broad range and a non-zero average value (average $r'=0.23$, variance= 0.18), indicating a significant variability among the structures [12], [26]. The corresponding r' distributions of the models had similar shapes and variances but returned different average values. LE exhibited a lower average r' value close to 0 ($r'=0.06$, gray dotted line in Fig. 2c), suggesting a lower degree of similarity between its single-molecule structures compared to the imaged chromatin conformations. In contrast, the SBS model closely matched the experimental r' distribution, with an average $r'=0.23$ (black dotted line in Fig. 2c), equal to the experiment value, indicating a significant level of similarity. Statistical analyses confirmed that the r' distribution of the

SBS model was statistically indistinguishable from the experimental distribution (two-sided Mann–Whitney test p -value=0.362), while LE showed significant differences ($p < 0.001$).

In conclusion, those comprehensive analyses revealed that both loop-extrusion and phase-separation models accurately represent chromatin structures at the single-molecule level, albeit the latter better explain the microscopy-observed variability of single-cell conformations. These findings contribute to our understanding of chromatin organization and provide insights into the fundamental molecular processes that shape genomic architecture at the single-molecule level.

Conclusions

To understand the complex 3D structure of the human genome, two main physical processes have been investigated, i.e., loop-extrusion (LE) [20]–[24] and phase-separation (SBS) [29]–[35]. However, their role in explaining single DNA molecules is still elusive. To this aim, we reviewed here the key findings discussed in [26],[19], where LE and SBS models have been tested against super-resolution microscopy data [12] for a specific, real chromosome region in human fibroblast cells. The major result is that both processes effectively describe single-cell chromatin conformations, albeit, interestingly, phase-separation better reflects the globular structure and variability of human loci as observed in real single-molecule microscopy. That sheds light on the physical mechanisms underlying single-molecule chromosome 3D structure, which is crucial in controlling biological activities such as the gene regulation.

Overall, those studies demonstrate the potential of combining experimental (e.g., microscopy) data with quantitative physics models to understand genome structure and regulation. Due to the highly demanding weight of computer (e.g., molecular dynamics) simulations, their successful implementation heavily relies on leveraging HPC resources [48]. These are essential for the efficient running of high-complexity simulations and serve as a crucial tool in advancing research in this field.

References

- [1] S. S. P. Rao *et al.*, “A 3D map of the human genome at kilobase resolution reveals principles of chromatin looping,” *Cell*, vol. 159, no. 7, 2014, doi: 10.1016/j.cell.2014.11.021.
- [2] J. R. Dixon *et al.*, “Topological domains in mammalian genomes identified by analysis of chromatin interactions,” *Nature*, vol. 485, no. 7398, 2012, doi: 10.1038/nature11082.
- [3] E. P. Nora *et al.*, “Spatial partitioning of the regulatory landscape of the X-inactivation centre,” *Nature*, vol. 485, no. 7398, 2012, doi: 10.1038/nature11049.
- [4] J. Fraser *et al.*, “Hierarchical folding and reorganization of chromosomes are linked to transcriptional changes in cellular differentiation,” *Mol Syst Biol*, vol. 11, no. 852, 2015.
- [5] I. Salamon *et al.*, “Divergent Transcription of the Nkx2-5 Locus Generates Two Enhancer RNAs with Opposing Functions,” *iScience*, vol. 23, no. 9, 2020, doi: 10.1016/j.isci.2020.101539.
- [6] A. Esposito *et al.*, “Higher-order Chromosome Structures Investigated by Polymer Physics in Cellular Morphogenesis and Differentiation,” *Journal of Molecular Biology*, vol. 432, no. 3, 2020. doi: 10.1016/j.jmb.2019.12.017.
- [7] C. A. Brackley *et al.*, “Predicting the three-dimensional folding of cis-regulatory regions in mammalian genomes using bioinformatic data and polymer models,” *Genome Biol*, vol. 17, 2016, doi: 10.1186/s13059-016-0909-0.
- [8] A. M. Chiariello *et al.*, “A Dynamic Folded Hairpin Conformation Is Associated with α -Globin Activation in Erythroid Cells,” *Cell Rep*, vol. 30, no. 7, 2020, doi: 10.1016/j.celrep.2020.01.044.

- [9] E. Lieberman-Aiden *et al.*, “Comprehensive mapping of long-range interactions reveals folding principles of the human genome,” *Science (1979)*, vol. 326, no. 5950, 2009, doi: 10.1126/science.1181369.
- [10] R. A. Beagrie *et al.*, “Complex multi-enhancer contacts captured by genome architecture mapping,” *Nature*, vol. 543, no. 7646, 2017, doi: 10.1038/nature21411.
- [11] S. A. Quinodoz *et al.*, “Higher-Order Inter-chromosomal Hubs Shape 3D Genome Organization in the Nucleus,” *Cell*, vol. 174, no. 3, 2018, doi: 10.1016/j.cell.2018.05.024.
- [12] B. Bintu *et al.*, “Super-resolution chromatin tracing reveals domains and cooperative interactions in single cells,” *Science (1979)*, vol. 362, no. 6413, 2018, doi: 10.1126/science.aau1783.
- [13] L. Fiorillo *et al.*, “Analysis of Genome Architecture Mapping Data with a Machine Learning and Polymer-Physics-Based Tool,” in *Lecture Notes in Computer Science (including subseries Lecture Notes in Artificial Intelligence and Lecture Notes in Bioinformatics)*, 2021. doi: 10.1007/978-3-030-71593-9_25.
- [14] A. Esposito *et al.*, “Polymer models are a versatile tool to study chromatin 3d organization,” *Biochemical Society Transactions*, vol. 49, no. 4. 2021. doi: 10.1042/BST20201004.
- [15] L. Fiorillo *et al.*, “Inference of chromosome 3D structures from GAM data by a physics computational approach,” *Methods*, vol. 181–182, 2020, doi: 10.1016/j.ymeth.2019.09.018.
- [16] L. Fiorillo *et al.*, “A modern challenge of polymer physics: Novel ways to study, interpret, and reconstruct chromatin structure,” *Wiley Interdisciplinary Reviews: Computational Molecular Science*, vol. 10, no. 4. 2020. doi: 10.1002/wcms.1454.
- [17] S. Bianco *et al.*, “Modeling Single-Molecule Conformations of the HoxD Region in Mouse Embryonic Stem and Cortical Neuronal Cells,” *Cell Rep*, vol. 28, no. 6, 2019, doi: 10.1016/j.celrep.2019.07.013.
- [18] A. Esposito *et al.*, “The Physics of DNA Folding: Polymer Models and Phase-Separation,” *Polymers*, vol. 14, no. 9. 2022. doi: 10.3390/polym14091918.
- [19] M. Conte *et al.*, “Loop-extrusion and polymer phase-separation can co-exist at the single-molecule level to shape chromatin folding,” *Nat Commun*, vol. 13, no. 1, 2022, doi: 10.1038/s41467-022-31856-6.
- [20] A. L. Sanborn *et al.*, “Chromatin extrusion explains key features of loop and domain formation in wild-type and engineered genomes,” *Proc Natl Acad Sci U S A*, vol. 112, no. 47, 2015, doi: 10.1073/pnas.1518552112.
- [21] G. Fudenberg, M. Imakaev, C. Lu, A. Goloborodko, N. Abdennur, and L. A. Mirny, “Formation of Chromosomal Domains by Loop Extrusion,” *Cell Rep*, vol. 15, no. 9, 2016, doi: 10.1016/j.celrep.2016.04.085.
- [22] C. A. Brackley *et al.*, “Nonequilibrium Chromosome Looping via Molecular Slip Links,” *Phys Rev Lett*, vol. 119, no. 13, 2017, doi: 10.1103/PhysRevLett.119.138101.
- [23] D. Racko, F. Benedetti, J. Dorier, and A. Stasiak, “Transcription-induced supercoiling as the driving force of chromatin loop extrusion during formation of TADs in interphase chromosomes,” *Nucleic Acids Res*, vol. 46, no. 4, 2018, doi: 10.1093/nar/gkx1123.
- [24] E. J. Banigan and L. A. Mirny, “Loop extrusion: theory meets single-molecule experiments,” *Current Opinion in Cell Biology*, vol. 64. 2020. doi: 10.1016/j.ceb.2020.04.011.

- [25] H. Huang *et al.*, “CTCF mediates dosage- and sequence-context-dependent transcriptional insulation by forming local chromatin domains,” *Nat Genet*, vol. 53, no. 7, pp. 1064–1074, Jul. 2021, doi: 10.1038/s41588-021-00863-6.
- [26] M. Conte, L. Fiorillo, S. Bianco, A. M. Chiariello, A. Esposito, and M. Nicodemi, “Polymer physics indicates chromatin folding variability across single-cells results from state degeneracy in phase separation,” *Nat Commun*, vol. 11, no. 1, Dec. 2020, doi: 10.1038/s41467-020-17141-4.
- [27] S. Bianco *et al.*, “Polymer physics predicts the effects of structural variants on chromatin architecture,” *Nat Genet*, vol. 50, no. 5, 2018, doi: 10.1038/s41588-018-0098-8.
- [28] A. Esposito *et al.*, “Polymer physics reveals a combinatorial code linking 3D chromatin architecture to 1D chromatin states,” *Cell Rep*, vol. 38, no. 13, 2022, doi: 10.1016/j.celrep.2022.110601.
- [29] M. Barbieri *et al.*, “Complexity of chromatin folding is captured by the strings and binders switch model,” *Proc Natl Acad Sci U S A*, vol. 109, no. 40, 2012, doi: 10.1073/pnas.1204799109.
- [30] M. Nicodemi and A. Prisco, “Thermodynamic pathways to genome spatial organization in the cell nucleus,” *Biophys J*, vol. 96, no. 6, 2009, doi: 10.1016/j.bpj.2008.12.3919.
- [31] M. Conte *et al.*, “A Polymer Physics Model to Dissect Genome Organization in Healthy and Pathological Phenotypes,” in *Methods in Molecular Biology*, 2022. doi: 10.1007/978-1-0716-1390-0_16.
- [32] M. Conte *et al.*, “Efficient computational implementation of polymer physics models to explore chromatin structure,” *International Journal of Parallel, Emergent and Distributed Systems*, vol. 37, no. 1, 2022, doi: 10.1080/17445760.2019.1643020.
- [33] A. M. Chiariello *et al.*, “Physical mechanisms of chromatin spatial organization,” *FEBS Journal*, vol. 289, no. 5, 2022. doi: 10.1111/febs.15762.
- [34] M. Conte, A. Esposito, F. Vercellone, A. Abraham, and S. Bianco, “Unveiling the Machinery behind Chromosome Folding by Polymer Physics Modeling,” *International Journal of Molecular Sciences*, vol. 24, no. 4, 2023. doi: 10.3390/ijms24043660.
- [35] M. Conte *et al.*, “Polymer Models of Chromatin Imaging Data in Single Cells,” *Algorithms*, vol. 15, no. 9, 2022. doi: 10.3390/a15090330.
- [36] L. Fiorillo *et al.*, “Comparison of the Hi-C, GAM and SPRITE methods using polymer models of chromatin,” *Nat Methods*, vol. 18, no. 5, pp. 482–490, May 2021, doi: 10.1038/s41592-021-01135-1.
- [37] K. Kremer and G. S. Grest, “Dynamics of entangled linear polymer melts: A molecular-dynamics simulation,” *J Chem Phys*, vol. 92, no. 8, 1990, doi: 10.1063/1.458541.
- [38] C. E. Grant, T. L. Bailey, and W. S. Noble, “FIMO: Scanning for occurrences of a given motif,” *Bioinformatics*, vol. 27, no. 7, 2011, doi: 10.1093/bioinformatics/btr064.
- [39] N. Kubo *et al.*, “Promoter-proximal CTCF binding promotes distal enhancer-dependent gene activation,” *Nat Struct Mol Biol*, vol. 28, no. 2, pp. 152–161, Feb. 2021, doi: 10.1038/s41594-020-00539-5.
- [40] I. Dunham *et al.*, “An integrated encyclopedia of DNA elements in the human genome,” *Nature*, vol. 489, no. 7414, 2012, doi: 10.1038/nature11247.
- [41] P. G. De Gennes, “Scaling concepts in polymer physics. Cornell university press.,” *Ithaca N.Y.*, 1979.

- [42] M. Conte *et al.*, “Dynamic and equilibrium properties of finite-size polymer models of chromosome folding,” *Phys Rev E*, vol. 104, no. 5, 2021, doi: 10.1103/PhysRevE.104.054402.
- [43] M. Conte *et al.*, “Hybrid Machine Learning and Polymer Physics Approach to Investigate 3D Chromatin Structure,” in *Lecture Notes in Computer Science (including subseries Lecture Notes in Artificial Intelligence and Lecture Notes in Bioinformatics)*, 2020. doi: 10.1007/978-3-030-48340-1_44.
- [44] S. Bianco *et al.*, “Computational approaches from polymer physics to investigate chromatin folding,” *Current Opinion in Cell Biology*, vol. 64. 2020. doi: 10.1016/j.ceb.2020.01.002.
- [45] A. P. Thompson *et al.*, “LAMMPS - a flexible simulation tool for particle-based materials modeling at the atomic, meso, and continuum scales,” *Comput Phys Commun*, vol. 271, 2022, doi: 10.1016/j.cpc.2021.108171.
- [46] J. A. Anderson, J. Glaser, and S. C. Glotzer, “HOOMD-blue: A Python package for high-performance molecular dynamics and hard particle Monte Carlo simulations,” *Comput Mater Sci*, vol. 173, 2020, doi: 10.1016/j.commatsci.2019.109363.
- [47] A. M. Chiariello, C. Annunziatella, S. Bianco, A. Esposito, and M. Nicodemi, “Polymer physics of chromosome large-scale 3D organisation,” *Sci Rep*, vol. 6, 2016, doi: 10.1038/srep29775.
- [48] F. Iannone *et al.*, “CRESCO ENEA HPC clusters: A working example of a multifabric GPFS Spectrum Scale layout,” in *2019 International Conference on High Performance Computing and Simulation, HPCS 2019*, 2019. doi: 10.1109/HPCS48598.2019.9188135.
- [49] T. J. Stevens *et al.*, “3D structures of individual mammalian genomes studied by single-cell Hi-C,” *Nature*, vol. 544, no. 7648, 2017, doi: 10.1038/nature21429.

THRUST COMPUTATION USING EXPERIMENTAL OPTICAL AND MORPHOLOGICAL PROPERTIES OF SOLAR PHOTON SAILS

Danilo Zola^{1*}, Salvatore Scaglione¹, Rocco C. Pellegrini², Enrico Cavallini², Christian Circi³

¹ENEA, Department of Energy Technologies and Renewable Sources,
Casaccia Research Center, via Anguillarese 301, 00123 Rome, Italy.

²Italian Space Agency (ASI), via del Politecnico snc 00133 Rome, Italy

³Department of Astronautical Electrical Engineering, Sapienza University of Rome,
via Salaria 851-881, 00138 Rome, Italy.

ABSTRACT. Numerical calculations for determining the thrust generated by solar radiation pressure on a sail are carried out using optical models that also consider the sail surface morphology. Additionally, these calculations rely on experimental optical properties and the topography of the sail samples. The algorithms were implemented using the script language of GNU Octave. Given the large number of points that need to be computed in order to estimate the momentum of the solar photon sail at different angles of incidence, parallelization of the algorithm is necessary. This parallelization is implemented both the cores of a single node and multiple nodes of the cluster in straightforward way. This approach enables the utilization of values for radiation pressure, more realistic, which can then be employed in the design of spacecraft trajectories and maneuvers propelled by solar photon sails.

1. Basic introduction to solar sail thrust.

Our investigation aims to calculate the thrust of solar photon sails (SPS) as a function of angle of incidence of sunlight. The input data are experimental optical properties and statistical parameters of the surface of small SPS prototypes made partially in ENEA laboratories.

SPS thrust is given by $\vec{f} = -\vec{D}_T S \cos \theta_i$ where \vec{D}_T represents the change in the total momentum of the photons per unit time and surface area; S is the sail surface and θ_i is the incidence angle of the sunlight [1]. In the following the vector \vec{D} with its various declination is referred to as the *photon momentum*. Despite the photon having zero mass, it has a momentum whose magnitude is $h\lambda$, where h is the Plank constant and λ is the wavelength. Solar photons, incident on the sail, have an intensity I that depends on λ and the distance (d) between the SPS and the Sun. The solar spectral irradiance $I(\lambda, d)$ is measured in $W/(m^2 nm)$. The total power per unit area of solar photons at distance d (called total solar irradiance TSI (d)) is obtained by integrating the solar irradiance over the entire solar spectrum.

Under the assumption that all solar photons travel in parallel, the momentum per unit time and surface area is D_0 which has therefore the dimensions of a pressure. At a distance of one Astronomical Unit (1 A. U) outside Earth's atmosphere $D_0 = 4.55699 \mu Pa$. A SPS distance 1 U.A. will always be considered in the following. The change in photons momentum is due to the reflection of the sail surface:

$$\vec{D}_T = \vec{D}_r - \vec{D}_i \quad (1)$$

where $\vec{D}_i = D_0(\sin \theta_i, 0, -\cos \theta_i)$ is the momentum of the incident photons and $\vec{D}_r = \vec{D}_{rs} + \vec{D}_{rd}$ is the momentum of both specularly (\vec{D}_{rs}) and diffusively reflected photons (\vec{D}_{rd}). The contribution from photons emitted by the sail is not taken into account in Eq.1, as the sail emits photons isotropically from both its front and back faces resulting in a null momentum change for the emitted photons from the two faces. Additionally, photons absorbed by the sail do not contribute to \vec{D}_T and no photons are transmitted.

The values of \vec{D}_{rs} and \vec{D}_{rd} are estimated by computing the spectral optical quantities, namely the spectral reflectance $R_s(\lambda, \theta_i)$, and the bidirectional reflective distribution function $BRDF(\lambda, \theta_i, \varphi_s, \theta_s, \cdot)$. Essentially $R_s(\lambda, \theta_i)$ represents the fraction of incident photons with wavelength λ that are specularly reflected by the SPS within a unit of time. Similarly, the BRDF provides the fraction of scattered photons within a unit of time and

solid angle, in the direction defined by the in-plane and azimuth angles (φ_s, θ_s) . To obtain \vec{D}_{rs} one must integrate R_s over the sun spectral irradiance $I(\lambda)$:

$$\vec{D}_{rs}(\theta_i) = \left(\frac{1}{c} \int_{\lambda_{min}}^{\lambda_{max}} I(\lambda) R_s(\lambda, \theta_i) d\lambda \right) \vec{d}_i \quad (2)$$

where $\vec{d}_i = (\sin \theta_i, 0, \cos \theta_i)$ represent the unit vector of the momentum. Moreover \vec{D}_{rd} is calculated integrating on $I(\lambda)$ and the entire hemisphere above the SPS [2]:

$$\vec{D}_{rd} = \frac{1}{c} \int_{\lambda_{min}}^{\lambda_{max}} I(\lambda) d\lambda \int_{\Omega_s} \cos \theta_s \text{BRDF}(\lambda, \theta_i, \theta_s, \varphi_s) \vec{d}_s d\Omega_s \quad (3)$$

where $d\Omega_s = \sin \theta_s d\theta_s d\varphi_s$, and $\vec{d}_s = (\sin \theta_s \cos \varphi_s, \sin \theta_s \sin \varphi_s, \cos \theta_s)$ identifies the momentum direction of each scattered photon at (φ_s, θ_s) angles. As shown in Fig. 1 the impinging photons are scattered in the different direction covering the shaded yellow region. \vec{D}_{rd} is the resultant of the momentum vectors of the photons scattered in the hemisphere.

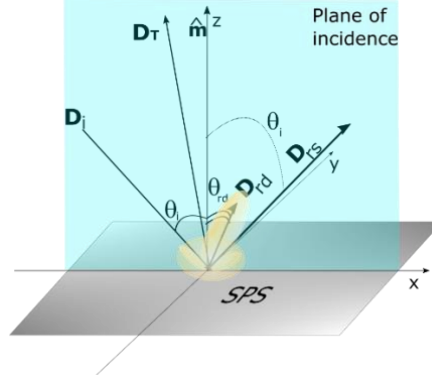


Fig.1: Illustration of the different momentum vectors in a solar photon sail.

Incident light is partially scattered due to surface roughness which can be quantitatively expressed by two statistical parameters: z , representing the mean square roughness and ℓ , the correlation length [3]. The amount of light scattered by the sail relies on the ratio between λ , z and ℓ . To simplify, when $\lambda \gg z$ then the surface has low scattering causing photons to be nearly all reflected specularly. Conversely, when $\lambda \ll z$, photons are predominantly scattered. For these reasons, BRDF also depends on λ , z , ℓ .

The optical properties depend on light polarization (referred as p a s polarization) as the angle of incidence changes. The incoming sunlight is unpolarized i.e it is a superimposition of both polarizations. However, the reflected light is partially polarized due to the different behaviour of p and s components. The polarization factor on the reflectance of SPS is accounted by knowing the spectral refraction $n(\lambda)$ and extinction $k(\lambda)$ indexes of the sail reflecting layer. Ultimately the BRDF as function of θ_i also depends on n and k .

To estimate R_s of the sail, the law of energy conservation in optics is used:

$$R_s(\lambda, \theta_i) + R_d(\lambda, \theta_i) + T(\lambda, \theta_i) + A(\lambda, \theta_i) = 1 \quad (4)$$

where R_d , A and T basically represent the fraction of scattered, absorbed, and transmitted photons respectively for a given wavelength λ and angle of incidence θ_i . SPS are fully opaque, and T is negligible. R_s results by subtracting from the incoming photons what is neither absorbed nor diffused. The spectral quantities A and R_d depend on the surface morphology of the SPS, and they must be calculated by means of scattering models as explained in Ref. [4,5]. These same models also allow the calculation of the BRDF.

To compute these optical quantities, certain experimental parameters must be known. These include the surface roughness parameters z and ℓ of the sail, as well as the spectral optical functions n and k of the reflecting layer. Measurement of these parameters involves optical and profilometric characterizations performed on samples of sail.

2. Outline of algorithms

The code for computing D_T is implemented using the GNU Octave script language [6]. On CRESCO, the root installation is GNU Octave version 5.1. However, to ensure access to the latest functions and libraries such as OpenBlas and SuiteSparse, a local user compilation of GNU Octave from source, along with its dependent libraries, has been performed. Currently, the most recent version available on the CRESCO user account is the 6.4. Additionally, to leverage the computational power of the 48 cores on each CRESCO6 node, the "parallel" package [7] of GNU Octave has also been compiled and loaded.

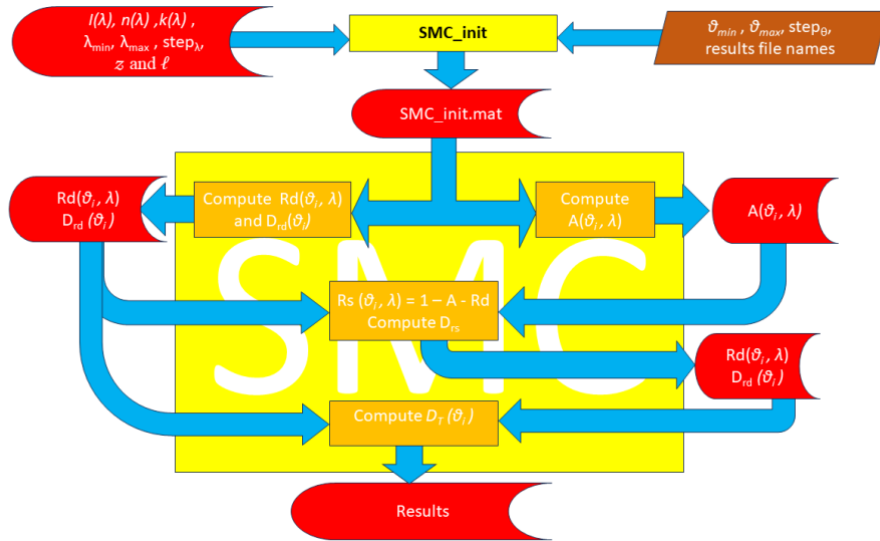


Fig.2: Block diagram of the SMC algorithms

The computation code, referred to as "Sail Momentum Computation" (SMC), is structured according to the block diagram depicted in Figure 2. It comprises a main script that generates a data file containing the three components of sail momentum D_T as a function of the angle of incidence, with a specified step size. Upon startup, the script loads the "SMC_init.mat" file, which stores all the variables name and their values used in the script and the experimental data necessary for the calculations. The generation of this ".mat" file is facilitated by a separate script called SMC_init, which can be executed on a PC desktop as well. The resulting "SMC_init.mat" file is then transferred to the user partition on CRESCO using the SSH protocol.

SMC_init relies on a graphical user interface (GUI) environment created using Octave UI functions. I/O dialogs requires the loading of two files: the first file contains the solar irradiance spectra $I(\lambda)$, while the second file contains the experimental spectral indices $n(\lambda)$ and $k(\lambda)$ of the reflecting layer, covering the wavelength range from 200 nm to 20000 nm with the same wavelength step size (typically 1 nm) for both files. This spectral range ensures accurate results. Additionally, input parameters such as z and ℓ , the angle range ($\theta_{min} \div \theta_{max}$), and the step size for θ_i are also required. Running SMC, the subroutines SMC_A, SMC_Drd are executed in parallel. SMC_A computes the spectral absorption $A(\lambda, \theta_i)$ tacking into account the sail surface roughness. SMC_Drd subroutine computes the spectral diffuse reflection $Rd(\lambda, \theta_i)$ and the three components of $D_{rd}(\theta_i)$. Both subroutines use functions which parallelize the execution for different λ on the 48 cores of CRESCO6 node. The quantities computed and the name of the corresponding variables are saved on two different mat files. By using A and Rd , the $Rs(\lambda, \theta_i) = 1 - A - Rd$ is determined and the $D_{rs}(\theta_i)$ components are thus computed by the subroutine SMC_Drs. Finally, $D_T(\theta_i)$ is simply given by $D_i(\theta_i) - [D_{rs}(\theta_i) + D_{rd}(\theta_i)]$.

The parallelization of the computation is implemented using the "parallel" package of Octave, allowing for simultaneous calculations on $(19800/\lambda\text{-step})$ wavelength values. This approach enables the computation of 48 different wavelengths per shot.

To parallelize the computation for different values of θ_i , where the total number of values is determined by $(\theta_{max} - \theta_{min}) / \theta_{step}$, multiple replicas of the same code are executed using the LSF command "bsub." Each replica is indexed with a specific θ_i value. The resulting DT values from each SMC replica are saved in the same file specified in the "SMC_init.mat" file.

If queued processes are interrupted, it is possible to resume the execution by running the SMC code specifically for the missing angle values, without the need to rerun the entire script from the beginning.

The use of the CRESCO6 computing cluster allows for a reduction in the computation time of DT by a factor of 30 to 60, taking into account the waiting time in the queue. The code is implemented using an interpreted scripting language, making it evident that the program would be slower if it were written in C. Additionally, the script can be further improved by optimizing the parallelization across multiple nodes.

Currently, the code assumes that the surface of the Solar Photon Sail (SPS) is flat. Future developments of the code aim to compute D_T in cases where the sail exhibits wrinkles or is not perfectly flat. In such scenarios, it will be necessary to divide the sail into a grid of more or less dense cells. Each cell will have its own orientation with respect to the sun and its level of roughness. The current algorithm needs to be repeated for each cell in

the grid. The final value of D_T will be determined by the resultant vector of the momentum from each cell in the grid.

Acknowledgments

This work is supported by the Italian Space Agency (ASI) under the project “Research and Development on Solar Photonic Propulsion” CUP F84I19001070005 , which is a cooperative research agreement with the involvement of Agenzia Spaziale Italiana (ASI), Consiglio Nazionale delle Ricerche (CNR), Dipartimento di Ingegneria Astronautica, Elettrica ed Energetica (DIAEE), Dipartimento Ingegneria Chimica Materiali Ambiente (DICMA), Agenzia Nazionale per le Nuove Tecnologie, l'Energia e lo Sviluppo Economico Sostenibile (ENEA), Istituto Nazionale di AstroFisica (INAF), Micro Wave, RINA, Università di Pisa (UniPi), and Università di Roma Tor Vergata (UniRoma2).

References

- [1] G. Vulpetti, “Fast Solar Sailing, Space Technology “ (Springer Netherlands, 2013), Vol. 30.
- [2] Giovanni Vulpetti. “Applying vector scattering theory to solar-photon sail thrust modelling”. In Malcolm Macdonald, editor, *Advances in Solar Sailing*, Springer Praxis Books, pages 489–508. Springer Berlin Heidelberg, (2014).
- [3] J. C. Stover, *Optical Scattering: Measurement and Analysis*, 3rd ed. (SPIE, 2012), vol. PM224.
- [4] D. Zola, C. Circi, G. Vulpetti, and S. Scaglione. Photon momentum change of quasi-smooth solar sails. *J. Opt. Soc. Am. A*, 35(8):1261–1271, (2018).
- [5] D. Zola and S. Scaglione “Computation of Solar Sail Thrust by Using Light Scattering Models” in “High performance computing on CRESCO infrastructure: Rsearch activity and results 2019” pag. 122-125, (2020) ISBN: 978-88-8286-403-3
- [6] John W. Eaton, David Bateman, Søren Hauberg, Rik Wehbring
“GNU Octave version 5.1.0 manual: a high-level interactive language for numerical computations”
URL: <https://www.gnu.org/software/octave/doc/v5.1.0/>

HYBRID COVE-EDGED GRAPHENE NANORIBBONS FOR ATOMISTIC PROTEIN SEQUENCING

Giuseppe Zollo^{1*}, Tommaso Civitarese¹

¹Università di Roma “La Sapienza”, Dipartimento di scienze di Base e Applicate per l’Ingegneria Via A. Scarpa 14–16, 00161 Rome, Italy^{[1][SEP]}

ABSTRACT. Recently synthesized metallic cove-edged graphene nanoribbons are considered as 1D electrodes for ideal atomistic resolved recognition of amino-acids. Using the non-equilibrium Green function scheme based on the Spin Density Functional Theory, we propose a nanogap device where the transversal tunneling current flowing across is collected during the translocation of a model Gly homo-peptide. We show that the signal calculated from the metallic spin states is characterized by double peak per residue in analogy with the results obtained with 1D graphene nanoribbons template electrodes. The presented results pave the way for experimentally feasible atomistic resolved tunneling current recognition using metallic edge engineered graphene electrodes obtained by bottom-up fabrication strategies.

1. Introduction

Sequencing the primary structure of proteins and peptides is crucial to evidence mutations or post-translational modifications that affect the protein 3D conformation and can result in wrong behaviour in the human cells and hence human illnesses. This task require new sequencing methods and devices because the present ones are time and cost consuming and with low resolution. One of the proposed alternative methods rely on the measurement of the transversal tunneling current flowing between two nano-electrodes during the protein translocation across a nanogap [1] and has the advantage that the signal measured (and the AAs recognition) comes directly from the quantum mechanical nature of the chemical and physical properties of the piece of molecule occupying the nanogap at a given time [2-4]. However, the control of the translocation dynamics is still an open question. Recently we have shown that an ideal device conceived as an array of sub-nanometer gaps in graphene nanoribbons (GNR) was able to sense single peptide bonds (PB) [5–8] 2D electrodes and graphene has been considered as a natural choice for that. with atomistic resolution with clear specific features from the atoms involved. However, the electrodes employed were considered in their metastable metallic phase, not the ground state one, as a paradigmatic template of metallic or half-metallic 1D graphene-based electrodes. Indeed, while it is known that the electronic ground state of such ribbons is a semi-conducting ferromagnetic state [9,10], the spin polarized ground state might undergo a transition to semi-metal when properly treated with electric fields. Therefore in this letter we focus on a newly conceived edge engineered cove edged metallic GNRs showing that if they are employed as electrodes, the main features of the previous finding obtained with template metallic nano-ribbons still hold.

2. Computational models and theory

The ideal device and the system employed is schematically drawn in Figure 1. Here the two electrodes are two semi-infinite hydrogenated zig-zag antisymmetric-even cove- edged GNR with 8 zig-zag carbon rows (8CEZGNR)- The central device region contains pieces of the cove-edged ZGNR that are connected to two pieces of zig-zag GNR with 6 carbon rows (6ZGNR).

The gap between the two pieces of ZGNRs is $dG = 5\text{\AA}$ consistently to the previous literature [5,7,8] and the Gly homo-peptide translocates in between.

The initial stage is the peptide translocation across the gap simulated by non-equilibrium steered classical molecular dynamics (SMD) [11] in water to collect the translocation configurations that will be further processed as detailed in the following. In this stage the system contained a total number of atoms $N = 27322$ that includes the device the peptide and the water at ambient conditions. Before the SMD the system is equilibrated at $T = 300$ K, $P = 1$ atm by classical MD. Then a constant velocity SMD is applied.

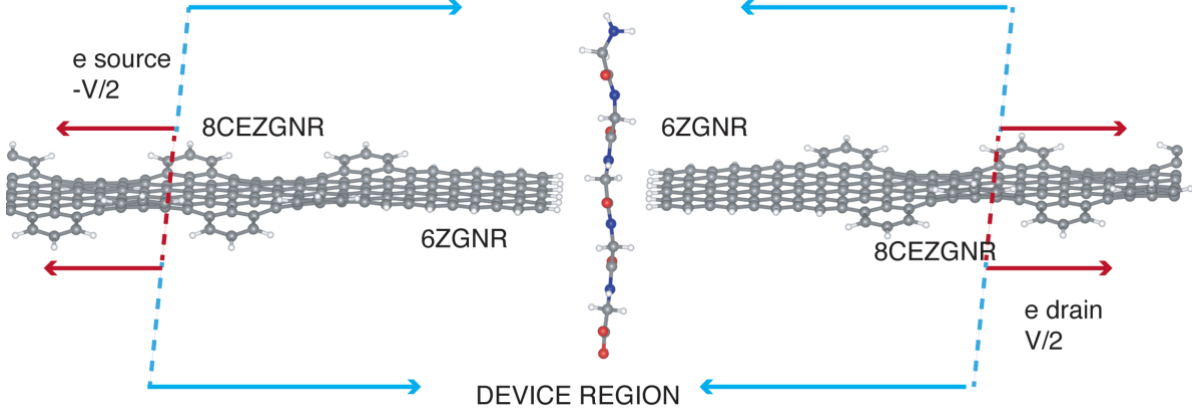


Fig.1: Nanodevice for protein sequencing. The electrodes are metallic 8CEGNRs while the central device contains one unit cell of 8CEZGNR and six unit cells of 6ZGNR. The device contains also the translocating peptide in the middle of the gap.

During the SMD we collect some configurations to sample the peptide backbone during the translocation. More precisely we have considered the following groups: the carboxyl CO and the amino NH groups (that are bonded together in the peptide bond), the side chain (SC) and the middle-bond configurations between these three groups, namely CBSN_i (CBSC_i), Center of the Bond between the carbon bonded to the Side chain and the Nitrogen (the C_α atom) of the *i*th residue, and PB_{ij} (center of the peptide bond between the *i*th and the *j*th residues), with *i*(*j*)=1-5 indicating the amino acid in the peptide central subsequence in order of translocation. The quantum transport calculations have been carried out in dry ambient since the presence of water does not affect the transport properties of the ZGNR nanogap [5, 7, 12]

The selected configurations have been further relaxed at $T = 0$ K, in the context of spin-polarized Local Density Approximation density functional theory (LSDA-DFT) using the SIESTA package [13] with a large threshold for the atomic forces, that was set to 0.1 eV/Å to conserve the thermal disorder of the SMD configurations. After the relaxation, we have calculated the transmission function and the tunneling current according to the DFT-NEGF scheme [14] as implemented in the TRANSIESTA code [15] although being a ground state theory and not a steady-state one, DFT-NEGF is the most popular approach for steady-state transport in nanostructures and has been successfully applied in many cases with results similar to the ones obtained from formally correct steady-state methods. The spin resolved transmission function is:

$$T(\varepsilon) = Tr[G(\varepsilon)\Gamma_L(\varepsilon)G^\dagger(\varepsilon)\Gamma_R(\varepsilon)] \quad (1)$$

where $G_\sigma(\varepsilon) = \lim_{\eta \rightarrow 0^+} (\varepsilon_\sigma + i\eta - H_\sigma)^{-1}$ is the Green's function of the system and $\Gamma^\sigma(\varepsilon) = i[\Sigma^\sigma(\varepsilon) - \Sigma^{\dagger\sigma}(\varepsilon)]$ is the left(right) spin resolved coupling function and $\Sigma_{L(R)}$ is the left (right) electrode self-energy for the σ spin. The related tunneling current is obtained through the Landauer-Büttiker formula for an external bias voltage $V = 1$ V applied along the *z* direction

$$I(V) = \frac{2e}{h} \int_{-\infty}^{+\infty} T(\varepsilon) [f(\varepsilon - \mu_L) - f(\varepsilon - \mu_R)] d\varepsilon \quad (2).$$

3. Results and discussion

We First analyse the behavior of the 8CEZGNR electrodes. Their structure is reported in Figure 2(a),(b) where the alternate up/down edge bending is evidenced. In the spin resolved band structure reported in Figure 2(c) we evidence that the cove-edged ribbon is nearly metallic (the two spins have identical band structures), the π

and π^* orbitals being nearly degenerate at the Γ point of the 8CEZGNR Brillouin zone (BZ) where we have measured a gap of $E_g \approx 3.5\text{meV}$ (d). This is the result graphene BZ folding that superimpose the graphene K point onto the 8CEZGNR Γ point. Such a negligible gap is easily overcome at 300 K that is the electronic temperature employed here.

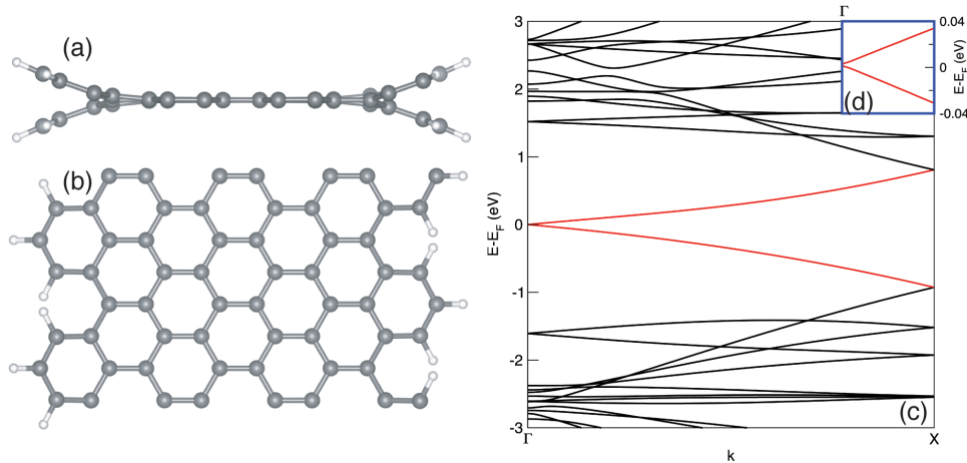


Fig. 2: Antisymmetric-even cove-edged GNR with 8 zig-zag carbon rows (8CEZGNR): side (a) and top (b) views. Spin resolved band structure of the 8CEZGNR (c). The nearly metallic behaviour can be appreciated from the magnified band structure at the Γ point (d).

The nearly degenerate orbitals at the Γ point are reported in Figure 3 for the two spin states: the valence band spin states have pseudo- π characters with higher densities at the opposite edges similarly to the "conduction band" pseudo π^* spin states but with opposite distribution of the up and down spins.

As mentioned, the device region also contains two pieces of 6ZGNR that is semi-conducting for both spins with a band gap of $E_g \approx 0.35\text{ eV}$. The antiferromagnetic spin polarized ground state of narrow ZGNRs has been demonstrated to be stable up to RT for ZGNRs produced by nanolithography from graphene sheets.

Of course the transmission function of the 8CEZGNR+6ZGNR nano-gap is nearly zero in the $[-0.5\text{ V} : 0.5\text{ V}]$ range for a bias of 1 V between the electrodes (not shown), the sub-nanometer gap being sufficiently wide to avoid any meaningful tunneling of the electrons when the gap is empty: indeed we have measured a dark current of the order of the fA, five orders of magnitude lower than the signal. The properties of this structure, however, evidence interesting features at equilibrium (no bias applied). The spin polarized model of the 6ZGNR-8CEZGNR junction barrier between the semiconducting 6ZGNR and the nearly metallic semi-infinite 8CEZGNR should predict a Schottky barrier based on the respective band structures.

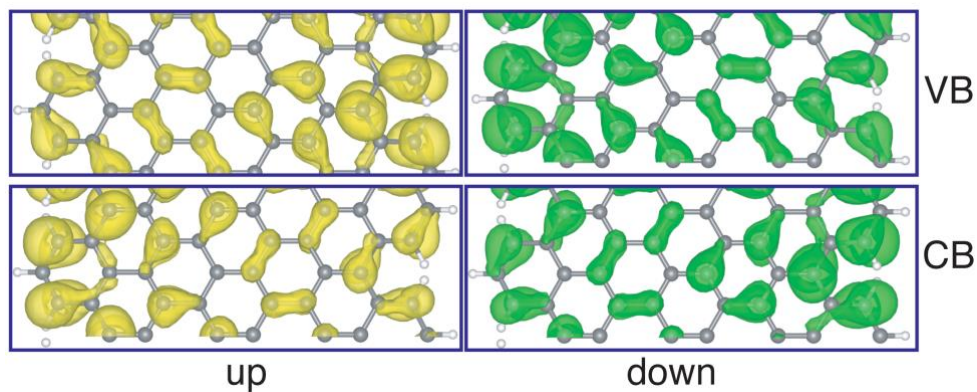


Fig. 3: Spin resolved orbitals of the lower and higher nearly degenerate states at the Γ point of the 8CEZGNR band structure in Figure 2.

Of course the transmission function of the 8CEZGNR+6ZGNR nano-gap is nearly zero in the $[-0.5\text{ V} : 0.5\text{ V}]$ range for a bias of 1 V between the electrodes (not shown), the sub-nanometer gap being sufficiently wide to avoid any meaningful tunneling of the electrons when the gap is empty: indeed we have measured a dark

current of the order of the fA, five orders of magnitude lower than the signal. The properties of this structure, however, evidence interesting features at equilibrium (no bias applied). The spin polarized model of the 6ZGNR-8CEZGNR junction barrier between the semiconducting 6ZGNR and the nearly metallic semi-infinite 8CEZGNR should predict a Shottky barrier on the basis of the respective band structures.

We consider now the tunneling current flowing across the gap during the translocation of a Gly homo-peptide that is reported in Figure 4 for the central part of the peptide.

In all the cases examined at various translocation configurations and spin state, we have found just one transmission channel. The signal collected is characterized by a structured peak feature per residue, basically the same behavior found when using template metallic 2-ZGNR narrow electrodes in an unpolarized regime [5,6] indeed each residue is characterized by a double peak around each Gly peptide bond with maxima in correspondence of the center of the $PB_{i,j}$ ($i = 2, 3; j = 3, 4$) peptide bonds and around the NH_i ($i = 2,3$) configurations with the NH groups lying in the GNR plane and is in the middle of the gap. The signal shape of the current tunneling signal is quite similar to the one obtained previously using template metallic 2-ZGNR electrodes [5,7] even though the signal intensity is approximately one order of magnitude lower. The reason of this lower tunneling current is strictly related to the lower Density of States (DoS) in the $[-0.5, 0.5]$ energy range for the cove-edged electrode than the metastable unpolarized metallic narrow zigzag GNR employed previously.

The calculated signal intensity, however, is still well above the detection sensitivity limits of the currently available picoammeters and could be easily detected with standard instruments.

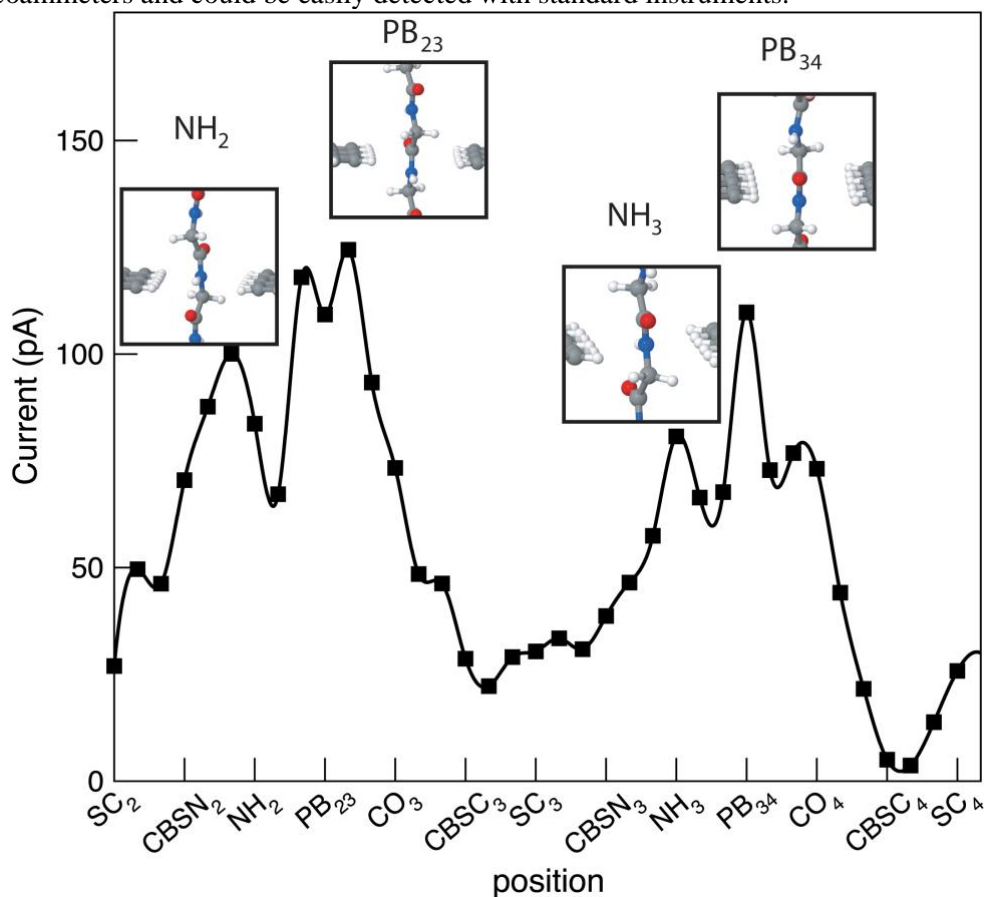


Fig. 4: Tunneling current calculated during the translocation of Gly homo-peptides across the nanogap. In the insets are reported the configurations where the tunneling signal is peaked.

4. Conclusions

1D electrodes made of asymmetric-even cove edged nanoribbons can be experimentally manufactured using current bottom-up fabrication nanotechnology. Using the DFT-NEGF method in the elastic regime we have calculated the tunneling current flowing across a nanogap in such electrodes for a Gly model peptide taken as reference. We have shown that the signal obtained in this new sequencer is characterized by a structured double

peak per residue where the major contributions come from the tunneling across the Gly CH₂ groups that include the C α group and the H side chain, with a minor contribution from the peptide bond groups. The signal level calculated is lower than the one obtained using the template metallic zig-zag GNR electrodes but, nevertheless, still well within the measurable range of currently available picoammeters. Therefore, realistic GNR based devices can be definitely employed as peptide sequencer because recent bottom-up strategies have allowed the synthesis of cove-edged zig-zag graphene nanoribbons as narrow as the ones here considered. Of course, the signal level depends on the gap size and therefore the atomistic control of this parameter is critical. The present results pave the way toward the fabrication of realistic GNR metallic electrodes and devices for atomistic resolved recognition of the amino acids in peptides and proteins.

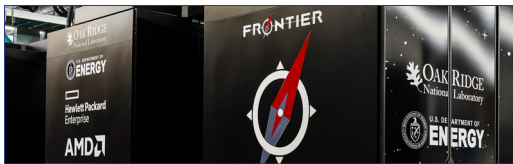
Acknowledgments

Part of the computing resources and the related technical support have been provided also by CRESCO/ENEAGRID High Performance Computing infrastructure and its staff [16]. CRESCO/ENEAGRID High Performance Computing infrastructure is funded by ENEA, the Italian National Agency for New Technologies, Energy and Sustainable Economic Development and by Italian and European research programmes, see <http://www.cresco.enea.it/english> for information.

References

- [1] Zwolak, M.; Di Ventra, M. Electronic Signature of DNA Nucleotides via Transverse Transport. *Nano Letters* 2005, 5, 421–424.
- [2] Ohshiro, T.; Tsutsui, M.; Yokota, K.; Furuhashi, M.; Taniguchi, M.; Kawai, T. Detection of post-translational modifications in single peptides using electron tunneling currents. *Nat. Nanotechnol.* 2014, 9, 835–840.
- [3] Di Ventra, M.; Taniguchi, M. Decoding DNA, RNA and peptides with quantum tunnelling. *Nat. Nanotechnol.* 2016, 11, 117–126.
- [4] Heerema, S. J.; Dekker, C. Graphene nanodevices for DNA sequencing. *Nat. Nanotechnol.* 2016, 11, 127 EP –.
- [5] Rossini, A. E.; Gala, F.; Chinappi, M.; Zollo, G. Peptide bond detection via graphene nanogaps: a proof of principle study. *Nanoscale* 2018, 10, 5928–5937.
- [6] Civitarese, T.; Zollo, G. Gap Size Dependence of Atomistic-Resolved Peptide Bond Signals by Tunneling Current Across Nano-Gaps of Graphene NanoRibbons. *Computation* 2020, 8, 29.
- [7] Civitarese, T.; Zollo, G. Triggering Amino Acid Detection by Atomistic Resolved Tunneling Current Signals in Graphene Nanoribbon Devices for Peptide Sequencing. *ACS Appl. Nano Mater.* 2021, 4, 363–371.
- [8] Zollo, G.; Rossini, A. E. Vibration assisted electron tunneling through nano-gaps in graphene nano-ribbons for amino-acid and peptide bond recognition. *Nanoscale Adv.* 2019, 1, 3547–3554.
- [9] Son, Y.-W.; Cohen, M. L.; Louie, S. G. Energy Gaps in Graphene Nanoribbons. *Phys. Rev. Lett.* 2006, 97, 216803.
- [10] Li, Y. Y.; Chen, M. X.; Weinert, M.; Li, L. Direct experimental determination of onset of electron–electron interactions in gap opening of zigzag graphene nanoribbons. *Nat. Comm.* 2014, 5, 4311 EP –.

- [11] Phillips, J. C.; Braun, R.; Wang, W.; Gumbart, J.; Tajkhorshid, E.; Villa, E.; Chipot, C.; Skeel, R. D.; Kale, L.; Schulten, K. Scalable Molecular Dynamics with NAMD. *J. Comput. Chem.* 2005, 26(16), 1781–1802.
- [12] Feliciano, G.; Sanz-Navarro, C.; Coutinho-Neto, M.; Ordejón, P.; Scheicher, R. H.; Rocha, A. R. Capacitive DNA Detection Driven by Electronic Charge Fluctuations in a Graphene Nanopore. *Phys. Rev. Appl.* 2015, 3, 034003.
- [13] Soler, J.; Artacho, E.; Gale, J.; Garcia, A.; Junquera, J.; Ordejón, P.; Sánchez-Portal, D. The SIESTA method for ab initio order-N materials simulation. *J. Phys. Condens. Matter* 2002, 14(11), 2745–2779.
- [14] Datta, S. *Electronic Transport in Mesoscopic Systems*; Cambridge Studies in Semiconductor Physics and Microelectronic Engineering; Cambridge University Press, 1995.
- [15] Stokbro, K.; Taylor, J.; Brandbyge, M.; Ordejón, P. TranSIESTA - A Spice for Molecular Electronics. *Ann. N. Y. Acad. Sci.* 2003, 1006(1), 212–226.
- [16] Iannone, F.; Ambrosino, F.; Bracco, G.; De Rosa, M.; Funel, A.; Guarnieri, G.; Migliori, S.; Palombi, F.; Ponti, G.; Santomauro, G.; Procacci, P. CRESCO ENEA HPC clusters: a working example of a multifabric GPFS Spectrum Scale layout. 2019 International Conference on High Performance Computing Simulation (HPCS). 2019; pp 1051–1052.



ISBN: 978-88-8286-458-3